THE STRUCTURE AND PROPERTIES OF ZINC-ALUMINIUM BASED BEARING ALLOYS

TEMEL SAVAṢKAN

Ph.D. THESIS

THE UNIVERSITY OF ASTON IN BIRMINGHAM

November 1980

SUMMARY

Temel Savaşkan

Ph.D. 1980

A series of zinc-aluminium based binary and ternary alloys which may be suitable for bearing purposes have been produced by casting. Their structures have been investigated by optical and electron microscopy and by X-ray diffraction, in the as-cast and heat-treated conditions.

The ageing response of the alloys was monitored using hardness and quantitative X-ray diffraction techniques and the kinetics of the decomposition of the supersaturated α/α' and β phases were determined and related to the structural changes. This allowed the most suitable heat-treatments to be deduced.

Some mechanical properties relevant to the application of these alloys as monolithic bushing materials have been determined, i.e. impact properties, creep and tensile properties at ambient and elevated temperatures.

It was shown that the creep data may be correlated by a parametric method which allows the estimation of stress to a certain strain under different conditions.

A comparison of the wear resistance of selected alloys with cast iron and phosphor bronze was carried out, and it was shown that certain of these alloys were comparable or superior to these.

KEY WORDS: Zinc alloys, heat-treatment, creep and

bearings

LIST OF CONTENTS Page

LIST OF TABLES

LIST OF FIGURES

Page

Page

Page

Page

Page

Page

1. LITERATURE SURVEY

1.1 Introduction

A bearing is a means of supporting a load between surfaces moving relative to each other, with as little friction as possible. The plain bearings used in the car, aircraft and other engineering industries, consist of two surfaces: the shaft and the bearing, generally separated by a film of lubricant.

Bearing alloys usually feature a two phase structure, one phase hard and the other soft. In lubricated wear, the load from the rotating shaft is transmitted by the oil film to the hard constituent, which supplies the resistance to wear. The soft constituent transmits and distributes the load into the bulk of the bearing and thus to its supporting structure. The soft phase allows limited plastic deformation to take place and thus permits the assembly to accommodate slight misalignment between the shaft and bearing. This is the important property of conformability. The soft phase has the added advantage of allowing hard, foreign particles in the oil stream to become safely embedded in the bearing which prevents scoring of the shaft.

Alloys, utilized for bearing purposes, have also to satisfy some primary requirements such as:

1 - A suitable chemical composition giving rise to a desirable and stable phase structure with adequate corrosion resistance for the chosen application.

2 - A certain range of physical properties such as melting point, density, thermal conductivity, etc.

3 - Adequate mechanical properties such as tensile strength, fatigue strength, creep resistance, modulus of elasticity and damping characteristics.

Besides these, it is necessary to comply with certain service requirements, such as wear and seizure resistance, conformability and embeddability.

The usual bearing materials of the Babbit and the bearing bronze type contain tin as a primary ingredient. Tin is a costly (1) and imported material and this fact has led to the development of some substitute bearing alloys, which have little or no tin.

One such alloy which has had little commercial development contains only zinc and aluminium with a little copper. All these metals are readily available and since the copper content is low the alloy is cheap to produce. The development of this and similar alloys will now be considered in detail.

1.2 Historical Development of Zinc-Based Bearing Alloys

The zinc-aluminium-copper bearing alloys were originally developed in Germany during World War 2, when Continental countries were confronted with an acute shortage of primary materials necessary for the production of traditional bearing alloys, such as phosphor bronze, leaded bronze and white metal (2). Consequently development was concentrated on a new range of alloys utilizing primary materials readily available at that time. As a result of such research, alloys containing tin and copper were replaced to a certain degree by new ones containing zinc and aluminium as the main constituents.

Early development work at the Max-Planck Institut für Metallforschung in the immediate post-war period showed the possibilities of these alloys (3) but dimensional instability problems were found to be a serious drawback. Following this work the manufacturing and selling rights were sold to a German firm but the alloys were not developed further. With the reversion of German patents to the Allies after the war, development virtually ceased.

Inevitably, as the prices of copper and tin spiralled and the prices of aluminium and zinc remained comparatively stable, a fresh demand for re-opening the original development work on the zinc-aluminium-copper alloys became apparent.

A bearing alloy based on zinc-aluminium with small amounts of copper appeared subsequently in an Austrian patent as Alzen 305 (4,5). This alloy proved highly successful in many applications, but still suffered from dimensional instability problems. The patent was taken up by Fry's Metals Ltd., and is at present manufactured in the U.K. to a limited extent.

Development work in the U.K. has largely been confined to a search for suitable applications, but recently the company have reduced the copper content of their commercial alloy.

1.3 Phase Equilibria

1.3.1 The Binary Zinc-Aluminium Phase Diagram

Nayak (6) produced a phase diagram of the binary zinc-aluminium system based on data from thermal and quantitative thermal analysis. The solidus and liquidus temperatures were compared with those from the prior phase diagrams of Raynor (7) and Presnyakov et al (8) and were found to correlate well in certain regions. However the liquidus curve appeared to lie above the curve obtained in earlier work. The values obtained by Nayak and earlier workers are shown in the phase diagram of Fig. 1.

Nayak found that the maximum solid solubility of aluminium in zinc at the eutectic temperature was 0.84% (2 at -%). The eutectoid was at 21.6% Al (40 at -% Al), and 236°C.

For many years the possibility of a peritectic reaction in zinc-aluminium system has been a subject of contention, with conflicting interpretations being presented, e.g. (9 and 10).

The most important recent work on the zinc-aluminium system is that is Ellwood (11,12) the Russian group

Presnyakov et al (8), and Goldak and Parr (13) all of whom used high-temperature X-ray cameras to measure lattice parameters.

Ellwood did not state the method of preparation and final purity of his alloys, but the zinc and aluminium components used were of the order of 99.995% pure. The alloys were heat treated at 375°C for 3 weeks to establish equilibrium, and filings were made immediately following a water-quench. Ellwood mentioned that the solid solution was not retained in quenched alloys containing more than 55% zinc. These filings were encapsulated in a silica tube before X-ray analysis. Lattice parameters were measured in a high-temperature Debye-Scherrer camera, and the total estimated error, including errors due to temperature and composition uncertainties, was 0.0007 Å.

Ellwood's work failed to provide any evidence of a peritectic reaction.

Presnyakov et al made their alloys from 99.99% aluminium and 99.96% zinc by crucible melting and casting into graphite moulds. Subsequently, the alloys were homogenised at 350°C for 168 hours, deformed by rolling to 50% cross-section, and finally heated at 350°C for 2 hours. The alloys were not analysed to check their purity.

Lattice parameters of alloy filings were measured in a back-reflection, high-temperature camera. The camera atmosphere was air, so presumably the filings were enclosed in silica tubes, but no details are given in their papers.

Temperatures were controlled to ± $2^{\circ}C$. The estimated error in parameter measurement was stated to be 0.0004 Å.

The phase diagram of Presnyakov et al with β relabelled as γ is reproduced in Fig. 2. Their lattice parameter/ temperature curves and the derived lattice-parameter isotherms are given in Figs. 3 and 4. The discontinuities in the isotherms indicate the narrow $(\alpha'-\gamma)$ field shown on their diagram. From their X-ray data, they deduced that a eutectoid reaction occurred at $340^{\circ}C$.

They concluded that in the zinc-aluminium system a pertitectic transformation took place at $443^{\circ}C$, and involved a discontinuity in solubility. A second eutectoid decomposition of the α´ phase into α + γ occurred at $340^{\circ}C$, with the eutectoid point at about 70% zinc.

Goldak and Parr (13) later studied the zinc-aluminium system in the region 40-75% zinc.

Their alloys were made from 99.999% zinc and aluminium by levitation-melting and casting into a copper mould. one of their finished alloys was analysed by a wet-chemical method and it contained 70% zinc and 30% aluminium. A spectrographic analysis of the same alloy revealed the following impurities: Cu 10 ppm, Pb 8 ppm; Ca, Mg and Si trace.

A high-temperature, high-precision diffractometer was constructed for their work. For lattice-parameter measurements the specimen housing was evacuated to 4×10^{-6} mm Hg and back-filled with high-purity helium. Subsequently the specimens were homogenised in the unit at 350°C for 24 hours. The alloy was then brought to the desired temperature and one hour allowed for the establishment of equilibrium. The diffraction angle of the {422} reflection of each phase was measured by continuous scanning at a fixed speed, while the diffracted intensities were determined by a Geiger counter and recording potentiometer. Determinations on each alloy were made at ∼10°C intervals from ∼290°C to 400°C.

They stated that the principal error that affected the accuracy of their work were those due to composition and temperature uncertainties, and those arose in X-ray measurement. Their estimated errors in composition were of the order of 0.00005 Å per 0.05% zinc, which was regarded as the maximum likely error in analysis. Temperature errors systematically displaced all lattice-parameter/temperature curves. The greatest deviation from the curve of best fit for the lattice-parameter/temperature curve was 0.0002 Å. This value was taken as the maximum total error in measurement.

Their plot of the {422} diffraction angle versus temperature for 57.1% zinc alloy is shown in Fig. 5. The two pronounced cusps on this curve clearly indicate the presence of transformation horizontals at those temperatures. The lower cusp was due to the well-known eutectoid reaction, however the second cusp provided direct evidence for the $\alpha' \rightarrow (\alpha+\gamma)$ transformation at 340°C, which was indirectly inferred by Presnyakov et al.

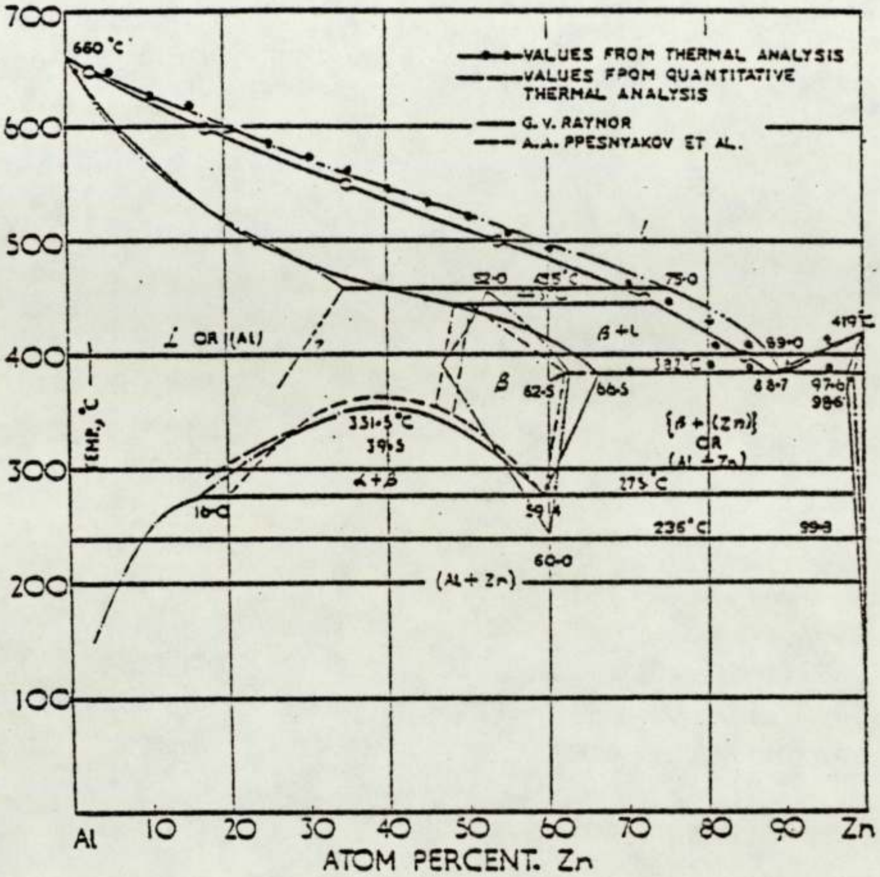

Fig. 1 The phase diagram al Al-Zn binary system (after Nayak $^{(6)}$).

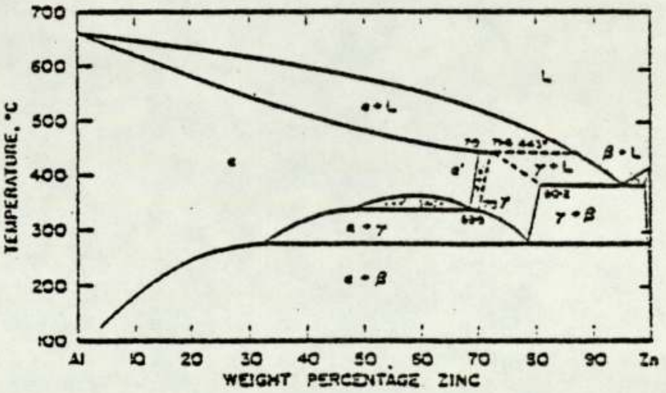

Fig. 2 The Al-Zn binary diagram according to Presnyakov et al $^{(8)}$

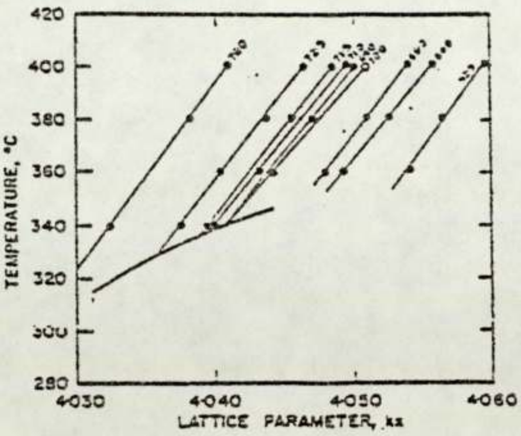

Fig. 3 Lattice-parameter/temperature curves of Presnyakov et al (8).

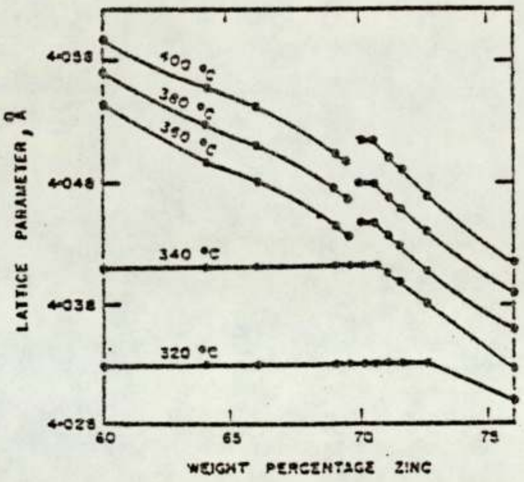

Fig. 4 Lattice-parameter isotherms of Presnyakov et al (8).

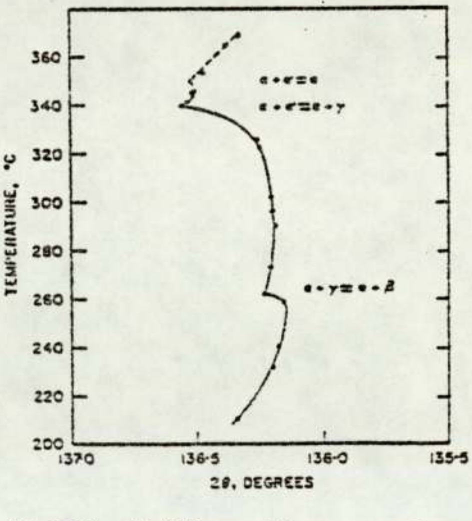

Fig. 5 {422} diffraction angle plotted against temperature for 57.1% zinc alloy, according to Goldak and Parr (13).

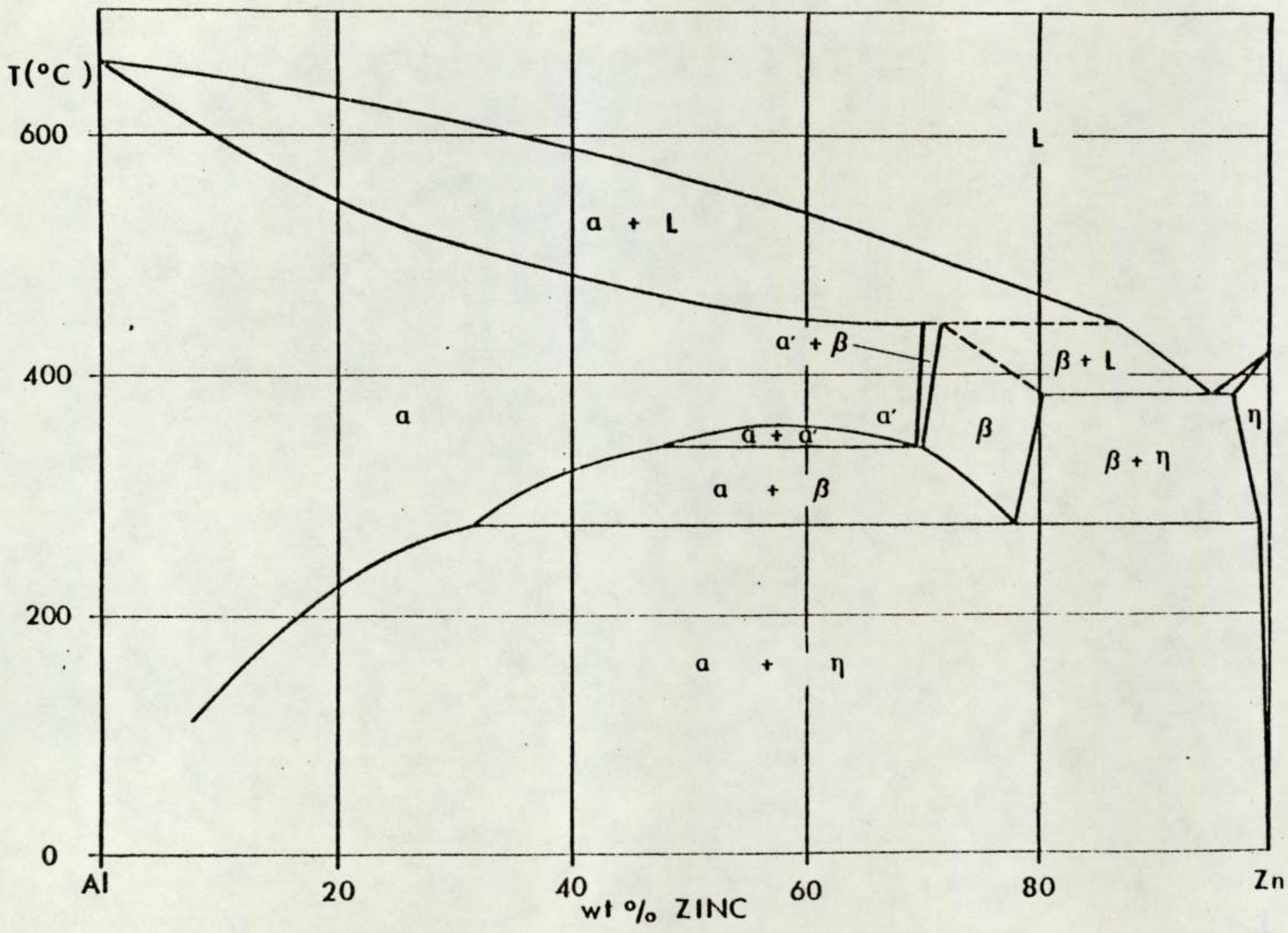

Fig. 6 Accepted phase diagram of Al-Zn system.

Their lattice-parameter/composition isotherms showed distinct discontinuities which defined the boundaries of an (α+γ) field in explicit confirmation of the results of Presnyakov et al.

In the original Russian work, the peritectic product was called β, and this nomemclature will now be used for the γ of the other workers, in this review. All of the high-temperature phases α, α' and β, were face-centred cubic but differed in lattice parameter.

The binary (α'+β) field was found to be approximately 1% wide and extended from an eutectoid point at 69.5% zinc to a peritectic horizontal at 443°C.

The work of Goldak and Parr provided confirmation of the results of the Russian workers and defined the limits of the (α+β) phase field more closely.

It is considered that the phase diagram of Presnyakov et al as modified by Goldak and Parr is probably the most accurate representation of the binary diagram to date as reproduced in Fig. 6.

1.3.2 The Ternary Zinc-Aluminium-Copper Phase Diagram

Köster and Moeller (14) were among the first to investigate the zinc-aluminium-copper ternary system by means of microscopic and X-ray analysis. The work reported in their first paper was concerned with the constitution and volume changes of the system and was restricted to only one temperature, that of 350°C. The result of their work is shown in Fig. 7. In addition to the phases present in the binary systems, one ternary phase (T) was found, stable within a narrow strip from 56% to 58% copper containing from 10% to 30% zinc.

The equilibrium between the phases γ, η, $\theta(Al_2Cu)$ and T in the complex region of the diagram between 55% to 80% copper was determined microscopically and full analysis of the phases present was undertaken to facilitate the construction of the ternary diagram.

In later papers Köster and Moeller (15,16) extended their work to include the temperatures of 400°C, 500°C, 600°C and 700°C.

In these later papers increased emphasis was placed on the high-copper half of the system, particularly the homogeneous connection between the η-phase in the copper-aluminium system and the δ phase in the copper-zinc system through the ternary cubic phase T.

Later Köster (17) investigated the liquidus surface and determined the equilibrium state of the Zn-Al-Cu system as shown in Fig. 8. He also summarised his results by giving the reaction sequence for the binary and ternary system down to 272°C as given in Fig. 9.

A ternary eutectic alloy containing 89.2% Zn, 7.0% Al and 3.8% Cu was reported by Gebhardt (18) to solidify at 377°C in close agreement with Köster's results.

The copper-rich areas of the ternary phase diagram, including β, γ and η phases, were investigated by Bauer and Hansen (19,20) and by Fletcher and Thomas (21). In the isothermal sections, the aluminium-zinc side at 20 to 55% Cu has been mainly studied by Gebhardt (18,22,23,24).

Gebhardt (22) and Strawbridge et al (25) showed that the solid solubility of copper in aluminium increased with the addition of zinc. The latter reported an increase in the solubility from 2.8 wt.% Cu with 0% Zn to about 3.4 wt½% Cu with 8 wt.% Zn at 460°C.

Solubilities of aluminium and copper in the Zn-phase have been determined by Gebhardt (22), Burkhardt (26) and Löhberg (27). These mutual solubilities are at a maximum along the locus of the Zn corners of the Al + ε + Zn phase field, with about 1.3 wt.% Al and 2.8 wt.% Cu soluble at 377°C and with 0.8 wt.% Al and 1.7 wt.% Cu soluble at 275°C.

The structures of the T phases in both the Zn-Al-Cu and Al-Cu-Ni systems have been investigated by a number of workers. In fact, the T phase was first observed in the Al-Cu-Ni system by Bingham and Houghton (28), but its structure was not determined.

Bradley and Lipson (29) investigated that system using X-ray diffraction and found that the T phase had a structure based on a deformed b.c.c. cell. The composition of the T phase was given as Al_6Cu_3Ni. Köster and Moeller (14,15) found a T phase isomorphous with Al_6Cu_3Ni in the Zn-Al-Cu ternary system. This phase had an ordered CsCl-type b.c.c. structure at high temperatures. At temperatures below 450°C the aluminium-rich end of the single-phase field (at approximately Al_5Cu_4Zn) had a structure of lower symmetry. The other end of the phase field corresponding to approximately $Al_{3.5}Cu_{4.5}Zn_2$ retained the CsCl structure. Köster suggested that at low temperatures the large difference in radius of the Cu and Al atoms renders the CsCl structure unstable, but that Zn atoms of intermediate size help to stabilise that structure. Köster denoted the CsCl structure as T phase and called the lower-symmetry structure T´.

Bown (30) examined crystals of T-phase extracted from slowly-cooled ingots of Al-Cu-Ni alloys, and established that two distinct structures were present, both based on the CsCl structure. One of these (T_1) had a rhombohedral structure with $a = 13.53$ Å, $\alpha = 17^\circ 27'$. The rhombohedral structure was based on eight b.c.c. cells joined corner to corner. With two adjacent heavy-metal atom sites per cell, the ideal formula, was given as $Al_8(Cu_1Ni)_6$, but it was suggested that there is only partial occupancy of other atom sites.

Later work (31) has shown that the T phase in Al-Cu-Ni can exist in many variants, all rhombohedral and based on the CsCl cell. Those examined by Bown (30) were but two of those variants.

In a recent investigation (32) the structure of the T´ phase in equilibrium with α and η of the Al-Cu-Zn system has been determined by electron and X-ray diffraction. It was established that T´ has a rhombohedral structure with:

$$a = 8.676 \text{ Å and } \alpha = 27.41^\circ$$

This structure is a superlattice based on assembly of five small CsCl-type cells, joined corner to corner along [111], so that Al and Cu atoms alternate in a linear array. The central atom site in the cell is vacant.

It was suggested that the zinc replaces aluminium in the T´ lattice.

The simultaneous occurrence of both phases (T and T´) depends on the composition of the alloy and the transformation temperature (17). Arndt and Moeller investigated the decomposition of the T phase in Zn-Al-Cu alloys with high copper contents within the temperature interval 200° - 300°C (33) and above 500°C.

Köster and his associates continued their intensive investigations in the years 1941 and 1942 as a result of which most of the phase diagram became known, but the solid-state phase changes in the low Cu region were not studied closely. Gebhardt (22) produced 350°, 300° and 240°C isothermal sections in this region and summarised the solid-state reactions.

There are minor discrepancies between this work and the earlier work of Köster (16), for example the solubility of Cu in the β phase was shown to reach 5% by Gebhardt but only 1.5% by Köster. Gebhardt hypothesised that a series of Class II four-phase reactions occurred below 300°C:

First T´ reacts with β to form α + ε. Then β reacts with ε to form α+η. The narrow (α+β+η) three-phase field contracts towards the binary edge and disappears at the binary eutectoid line. Finally α reacts with ε to form T´ + η, and the two three-phase fields which result are those observed at 240°C.

In a later work on this system, that of Arndt and Moeller (33,34), an alternative scheme similar to the original one of Köster was presented.

The first reaction is between β and ε to produce T´ + η. One of the observed low temperature three-phase fields is produced directly from this reaction (η+T´+ε). Next a narrow (α+β+η) field is generated from the eutectoid on the binary edge and contracts the β phase field away from the binary edge. β finally disappears by a Class I ternary eutectoid reaction to yield the observed (α+T´+η) phase field.

Recently Murphy (35) investigated the low-copper part of the Zn-Al-Cu phase diagram using electronprobe microanalysis and determined some of the solid-state phase reactions.

Fig. 10 shows the 350°C isothermal section. The phase boundaries agree best with those of Gebhardt; but the solubility of Cu in α was found to be significantly higher and the (ε+β) phase was somewhat broader.

The 290°C isothermal section is very similar to the 300°C isotherm of Gebhardt and is shown in Fig. 11. The T´ phase in the phase-field (α+β+T´) was found to be too small to analyse accurately but the β composition was measured and found to be very close to that in the (β+T´+ε) phase field. The (T´+β) region is very narrow whereas the (ε+β) region is still quite wide. Clearly the next phase reaction would be $T'+\beta \rightleftharpoons \alpha\ \varepsilon$ to yield (α+T´+ε) and (α+β+ε) three-phase fields, and these new three-phase fields are seen in the 280°C isothermal section of Fig. 12.

In Fig. 13 at 270°C, the (α+T´+ε) phase field is present, but the β-phase has disappeared and the (α+ε+η) phase field has taken its place. Furthermore the (α+ε) phase field is very narrow indeed, indicating that the four-phase reaction, $\alpha+\varepsilon \rightleftharpoons T'+\eta$ is imminent. In one alloy Murphy found that all four phases co-existed. This showed that the transformation temperature must be at 269° or 268°C.

At 250°C Fig. 14 the large (α+T´+η) three-phase field was observed.

Murphy found that the first and third four-phase reactions hypothesised by Gebhardt did occur: the first $\beta+T' \rightleftharpoons \alpha+\varepsilon$ at

$\sim 288^\circ C$ and the $\alpha+\varepsilon \rightleftharpoons T'+\eta$ at $\sim 268^\circ C$ or $269^\circ C$. The reaction proposed by Arndt, and Moeller was proved not to take place.

The actual reaction sequence found by Murphy is given in the diagram of Fig. 15.

The exact nature of the reaction whereby the β is eliminated at about $275^\circ C$ was not established. There are two possible mechanisms. The first is that proposed by Gebhardt. This would be initiated by a Class II reaction at some temperature above $275^\circ C$. The narrow $(\alpha+\beta+\varepsilon)$ phase field would then diminish to a line at the eutectoid temperature on the binary edge.

If on the other hand, copper stabilised the β-phase at low temperatures, the binary eutectoid reaction might occur first. The β phase field would then move away from the binary edge and finally disappear by a Class I ternary eutectoid reaction $\beta \rightleftharpoons \alpha+\varepsilon+\eta$. Which is these mechanisms is correct was not resolved.

The shape of the β phase field was found to change drastically as the temperature was altered, contracting from a broad field with a range of zinc content of nearly 9% at $350^\circ C$, to an extremely narrow field at $280^\circ C$, Fig. 16. This might significantly alter the relative proportions of the phases in the eutectoid-based bearing alloys on cooling.

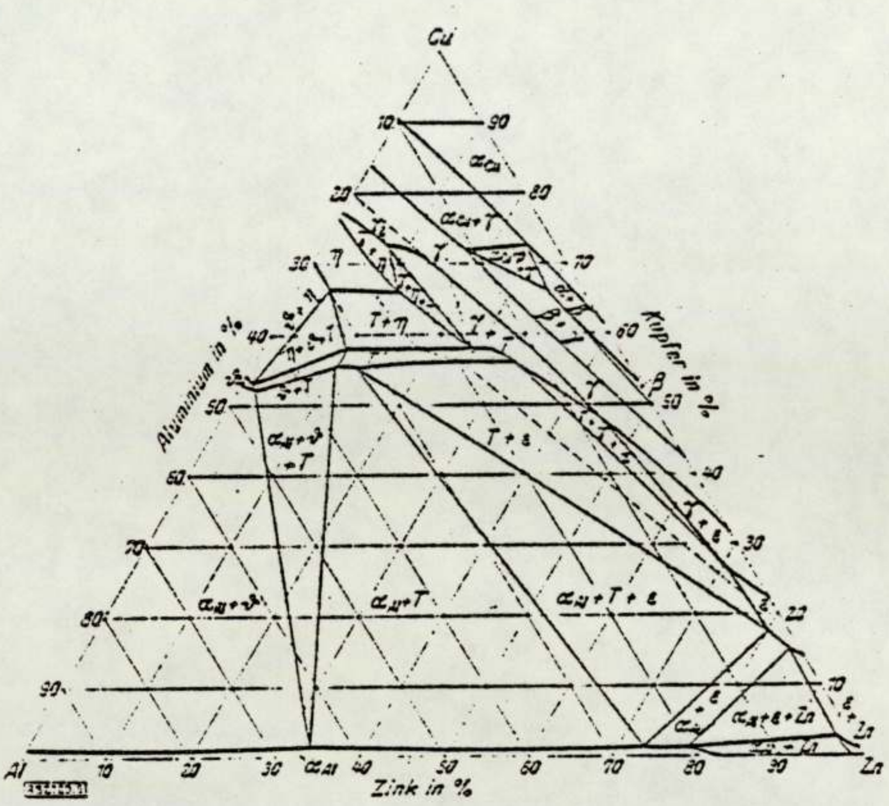

Fig. 7 Isothermal section of Zn-Al-Cu ternary system at 350^{O}C, according to Köster and Moeller (14).

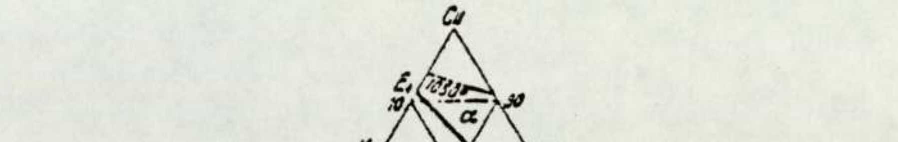

Fig. 8 Liquidus surface of the Zn-Al-Cu system according to Köster (17).

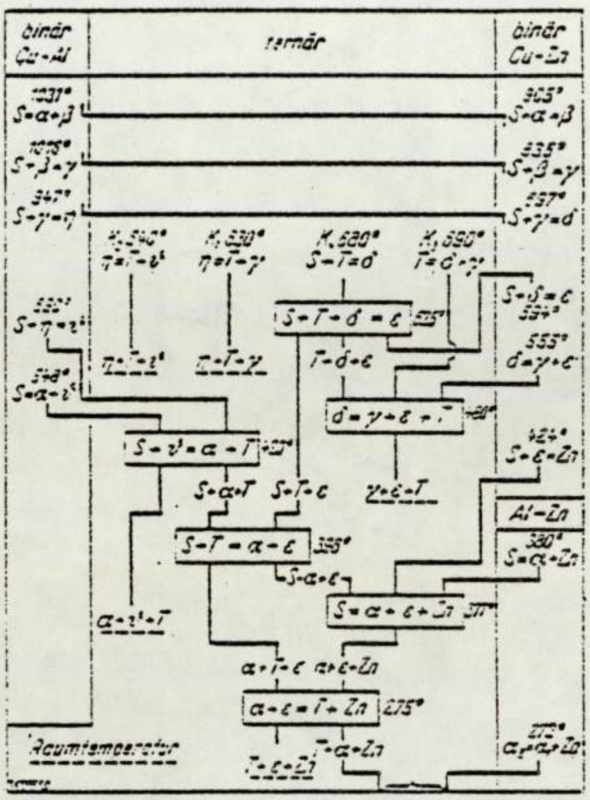

Fig. 9 Reaction sequences for the binary and ternary systems down to 272°C (after Köster$^{(17)}$).

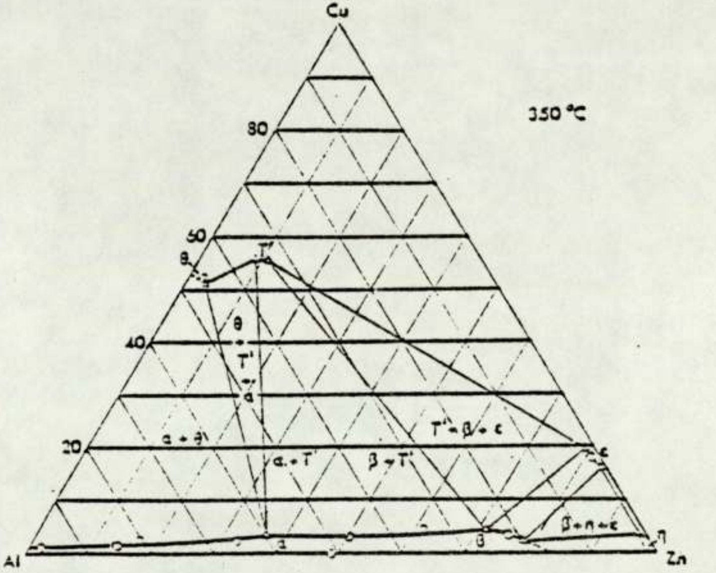

Fig. 10 Isothermal section of Zn-Al-Cu system at 350°C according to Murphy $^{(35)}$.

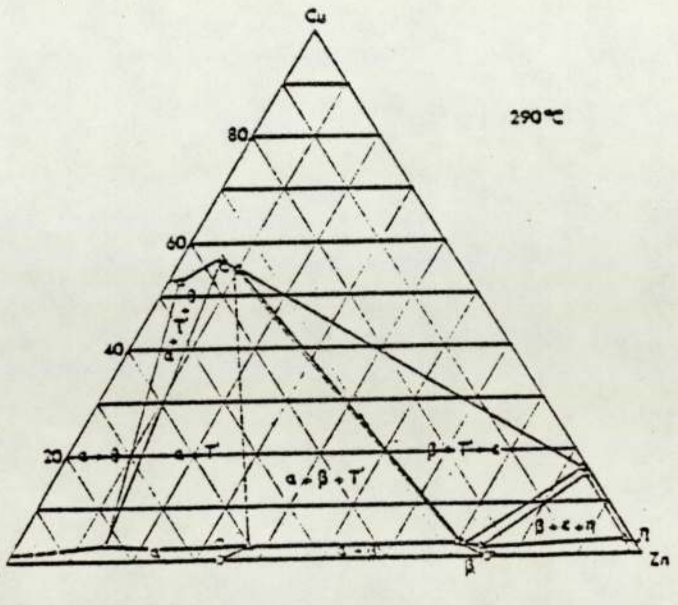

Fig. 11 Isothermal section at 290°C (after Murphy (35)).

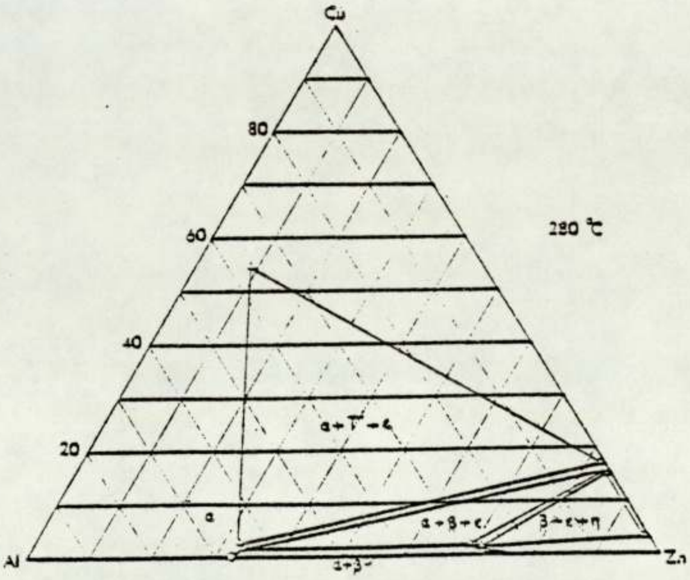

Fig. 12 Isothermal section at 280°C (after Murphy (35)).

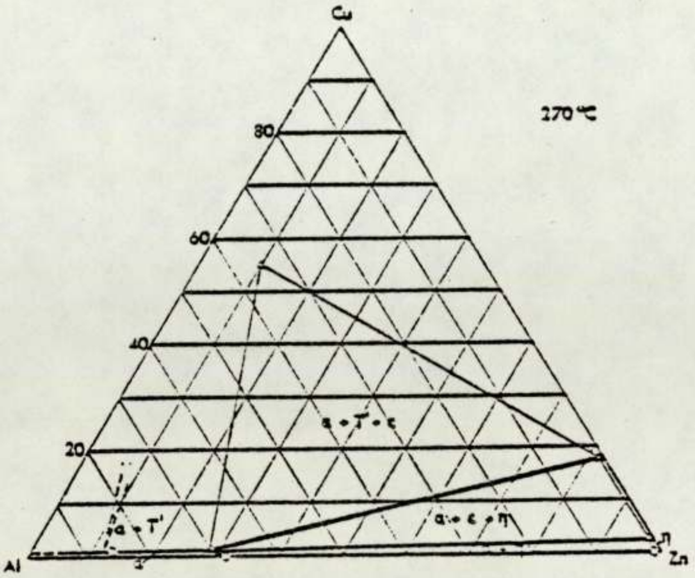

Fig. 13 Isothermal section at 270°C (after Murphy (35)).

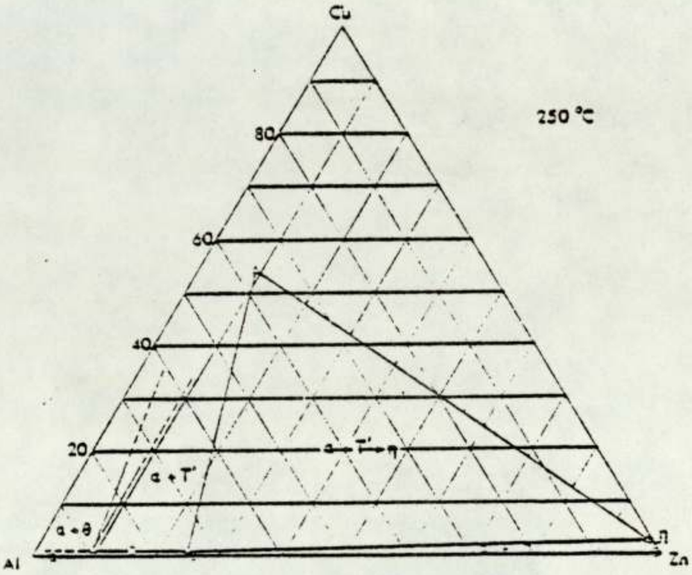

Fig. 14 Isothermal section at 250°C according to Murphy (35).

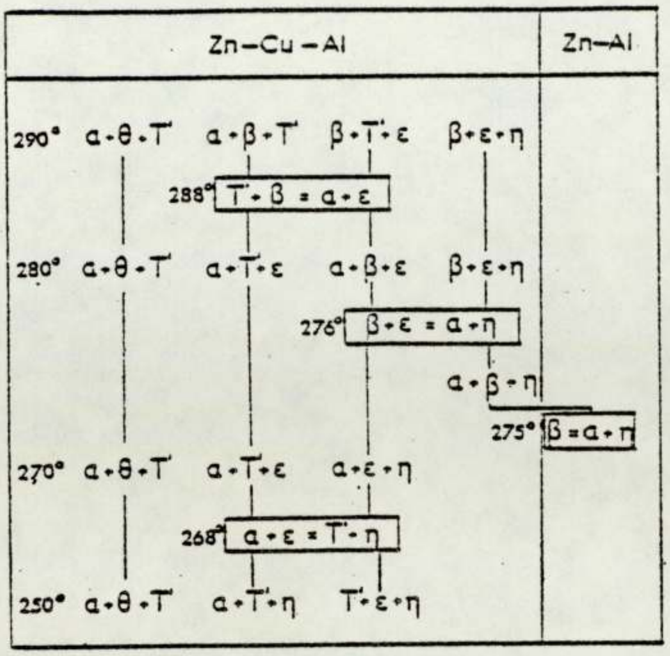

Fig. 15 Solid-state reactions in the low-copper part of the Zn-Al-Cu system according to Murphy (35).

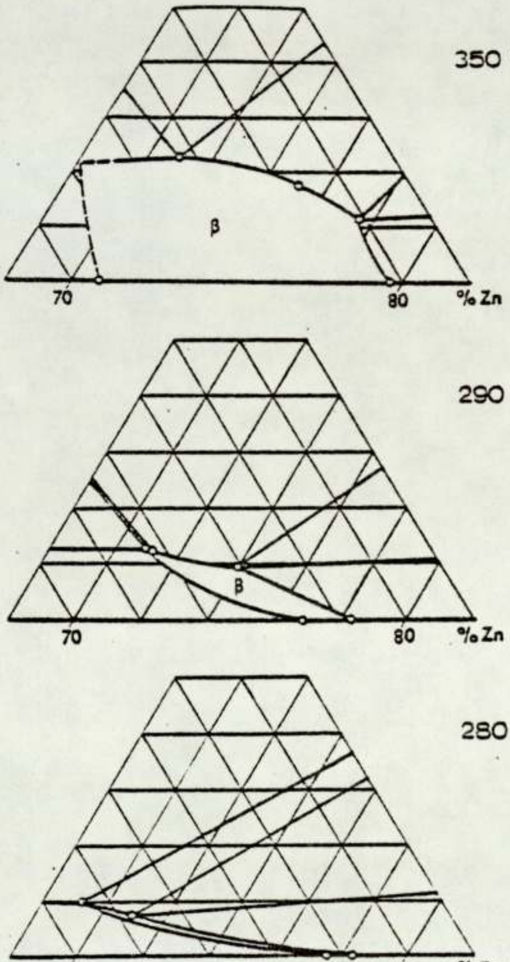

Fig. 16 The shapes of the β-phase field at 350, 290 and 280°C (after Murphy (35)).

1.4 Phase Transformations

1.4.1 Structural Changes in the Binary System

The extensive solid solution of zinc in aluminium has been subjected to a large number of detailed investigations, mainly from the point of view of transformation and cellular precipitation. The solid solution extends to about 82.5% Zn and occurs in three different isostructural modifications, designated α, α' and β in the Zn-Al phase diagram (Fig. 6).

Slow cooling of any of these single phase alloys results in the ultimate formation of zinc and aluminium, the latter with a comparatively low zinc content. Rapid cooling retains the zinc in super-saturated solid solution and on subsequent ageing the decomposition of these solutions forms a series of transitional phases. Studies of these transformations have been made using low angle X-ray scattering, electron microscopy, hardness and electrical resistivity measurements.

The exact nature of the transformation depends on the zinc content of the quenched alloys. Low-zinc alloys (up to 30% Zn) were studied by a large number of workers (36-45) who proposed the following decomposition sequence: Spherical G.P. zones → rhombohedral α' → cubic α' → zinc. The rhombohedral α' phase is precipitated in the form of plates and distorted by coherency strains (36,37,38,39). It differs only slightly in lattice parameter (a = 4.005Å) (40) from the cubic α' phase (a = 3.992Å). The final precipitate is zinc with the lattice parameter of $a = 2.859\text{Å}$ and $c = 4.947\ \text{Å}$ (40).

X-ray and electron microscopic investigations showed that the habit plane of the α′ particles was parallel to $\{111\}_\alpha$ of the matrix (36,37,38,40). The orientation relationship between zinc precipitate and aluminium matrix was determined (36,44) as:

$$(111)_{Al} \ // \ (0001)_{Zn};\ [1\bar{1}0]_{Al} \ // \ [100]_{Zn}$$

Although there have been some conflicting reports it is now generally agreed (38-45) that on quenching low-zinc aluminium-zinc alloys from the single phase region to room or sub-zero temperatures, fully coherent G.P. zones form rapidly (38-45). The zones are spherical (45) to start with and on reaching a critical diameter (∿60Å at room temperature) (41) they undergo a rhombohedral distortion to R-phase. The zinc content of the zones was estimated from the values of integrated intensities of low-angle X-ray lines to be around 85% at room temperature. The actual value is dependent on the ageing temperature. R-phase is formed at higher temperatures either on direct quenching or by zone reversion. The kinetics of its formation are appreciably faster on reversion than on quenching and this partly coherent metastable precipitate has a rhombohedral structure derived by a simple compression in a direction perpendicular to the matrix {111} planes. The possible existence of two different reversion temperatures for the G.P. zones and the R-phase respectively has been conceded by several investigators (46,47,48) but only recently on the basis of experimental data from a large number of workers, have two different metastable miscibility gaps (Fig. 17) been established (49,50).

The more concentrated aluminium-zinc alloys have been investigated less thoroughly. Graf and Lenormand (51) showed that an aged Al-40% Zn alloy exhibited X-ray "side-bands", which are often associated with spinodal decomposition (52). Rundman and Hilliard (53) used X-ray small angle scattering to obtain evidence that the same alloy does in fact decompose spinodally at room temperature. There has been some discussions (54,55) on interpretation of their results.

Ardell et al (56) found that rapid decomposition of concentrated, non-eutectoid zinc-aluminium alloys lead to the formation of "modulated" structures, not necessarily as a result of spinodal decomposition.

An aluminium-50% zinc alloy on quench-ageing above 25°C, showed mixed, discontinuous and continuous decomposition products (57). The discontinuous (or cellular) precipitation occurring in an aluminium-48.5% zinc alloy, on quench-ageing at temperatures above ambient, was studied by Ramaswamy et al (58). It was observed that the cellular reaction started at grain boundaries and proceeded at a linear growth rate, with the cell interface advancing steadily into the matrix containing the metastable precipitates. The interlamellar spacing and the rate of growth varied as a function of temperature. The results were interpreted on the basis of Turnbull theory (59) of cellular precipitation; which suggests that the cell boundary is the rate controlling factor in this system. The theory was modified to include the retarding effect of continuous precipitation in the matrix. The authors of this investifation found that the growth kinetics of the cellular reaction in this alloy were consistent with a mechanism controlled by cell-boundary diffusion and could not be explained in terms of models based on volume diffusion ahead of the cellular interface. They also reported that multiplication of lamellae within cells occurred by a branching mechanism.

More recently the observed growth rates for the cellular precipitation in the same alloy (Al-48.5% Zn) were reinterpreted by using the G.P. zone solvus below 125°C and the R-phase solvus above (60). This interpretation led to a significantly better agreement with the theoretically predicted growth rates based on a modified Turnbull theory of decomposition.

As a result of these investigations, the following sequence of precipitation which occurs concurrently with the dis-

continuous reaction during decomposition of quenched aluminium-zinc alloys has been established:
Supersaturated solid solution → spherical G.P. zones → rhombohedral R-phase → cubic α' → zinc.

Alloys with a composition corresponding to the β-phase field decompose on slow cooling by a eutectoid reaction which is seen in the binary phase diagram of Fig. 6. This reaction has been studied by Garwood and Hopkins (61) who showed more than one type decomposition product depending on the transformation temperature.

Decomposition of the eutectoid alloy during slow cooling or isothermally transforming at high temperatures produced a typical lamellar structure. However decomposition at room temperature after a rapid quench produced a fine (∿1 μm) mixture of equiaxed zinc-rich and aluminium-rich grains (56,62). This change was interpreted in terms of spinodal decomposition which takes place at about room temperature (56,62).

Recently Toldin et al (63) examined the results of decomposition of different, concentrated Zn-Al solid solutions in different ways. Quench-ageing, isothermal transformation and slow cooling to the transformation temperatures were all studied. Alloys with zinc contents between 40 and 60% were called AlZnII and an alloy with 73% Zn, close to the eutectoid composition, was called AlZnIII.

High temperature isothermal transformation of AlZnII produced small, lamellar precipitates of R-phase after one minute. Cellular decomposition started after two minutes, forming the equilibrium zinc phase. Low-temperature isothermal transformation produced R-phase, followed by spheroids of zinc, R-phase disappeared as the zinc spheroids grew.

Slow-cooling to a transformation temperature of less than $275^{o}C$ caused large, lamellar precipitates of metastable α' to form; the zinc did not appear until transformation had been going for 2 hours.

High-temperature isothermal transformation of the near eutectoid alloy resulted in the formation of a low zinc α_1 phase after one minute. After 4 minutes cellular decomposition developed in the matrix with the formation of zinc.

Quench ageing results in the formation of G.P. zones, probably during the quench. AlZnII quenched, then rapidly heated to $240^{o}C$, produced R-phase precipitates first, followed by zinc.

Cellular decomposition occurred on quench-ageing in the range $20\text{-}275^{o}C$, but was only observed when the grains exceeded 100 nm in diameter. If cellular decomposition did not take place, the R-phase transformed to large, lamellar precipitates of α'.

The results of this work, and that of previous workers, were generalised by Toldin et al into eleven sequences of phase transformation, which depend on composition, cooling rate and heat treatment temperature. Their scheme of transformation is shown in Fig. 18.

The kinetics of cellular transformation of the eutectoid alloy have been studied in some detail. The initial work by Garwood and Hopkins resulted in the production of the first isothermal TTT diagram for the alloy (62).

Isothermal-transformation and directional growth in the eutectoid alloy were later studied by Cheetham and Ridley (64). Their work was concerned with the measurement of growth rates and interlamellar spacings during decomposition of this alloy under isothermal conditions over a range of temperatures 125° - 250°C. Analysis of their data showed that the growth of the lamellar eutectoid decomposition product was controlled by interfacial diffusion. The results of their measurements showed that the growth rate passed through a maximum at ∿175°C, but that at higher reaction temperatures, the rate of growth appeared to decrease with time, while at lower temperatures, where the reaction proceeded rapidly, it was essentially constant.

They found that the interlamellar spacing decreased with decreasing temperature of transformation and the relationship between the spacing, s, and the undercooling, ΔT, is such that $s \alpha \Delta T^{-0.9}$. At all transformation temperatures investigated, the interlamellar spacing of the initial decomposition product was essentially constant with time, but the initial lamellae were later consumed and replaced by a coarse, secondary, lamellar product. Their experiments also showed that it was possible to produce alignment in the initial transformation product, but the replacement of this by the coarse, secondary product made a rigorous examination of the conditions for alignment impossible.

More recently Smith and Hare (65) investigated the isothermal transformation of the eutectoid alloy in considerable detail by standard techniques of metallography, dilatometry, calorimetry, hardness change, and electrical conductivity and produced a fuller TTT diagram (Fig. 19). Their tests were extended in temperature to sub-zero values and prolonged in time to a year.

As seen in the fuller diagram, they regarded the transformation as occurring in four stages:

I : The quenched condition

II : Breakdown of $\beta(\alpha')$ to products of intermediate composition

III : Adjustment of these products to α and η of equilibrium chemical composition

IV : Adjustment of structure to virtual physical stability.

Smith and Hare also studied the effect of varying aluminium content on the time-temperature-transformation characteristics of zinc-aluminium alloys, and found that the quickest transformation reaction took place with 18% Al, and explained this on the basis of extrapolation of α/α' (β) phase boundary on the zinc-rich side of the monotectoid in the equilibrium diagram to 20°C.

1.4.2 Structural Changes in the Ternary and Higher Systems

There is comparatively little information available on the structural changes in the zinc-aluminium based ternary (Zn-Al-Cu) and higher (Zn-Al-Cu-Mg) systems.

Work carried out in this field has been mainly concerned with the effect of small alloying additions on the structure and transformation characteristics of the binary zinc-aluminium alloys.

However the phase transformations in the ternary zinc-aluminium-copper system have been investigated by several workers and as a result the phase diagram of this system is partly established, as discussed in (1.3.2).

In the low-copper alloys used for bearings the T-phase forms by means of a four-phase transformation:

$$\alpha + \varepsilon \rightleftharpoons T + \eta \quad (35).$$

This transformation is slow and requires from several months to several years to be completed at room temperature. According to Köster (17) this transformation causes an increase in the volume of the sample up to 4 per cent. Gebhardt (23) reported an increase of 0.53 per cent in the linear dimensions of the sample during the $\alpha + \varepsilon \rightleftharpoons T + \eta$ transformation, occurring at the temperatures lower than that of decomposition of β phase. The same author (22) when investigating zinc-based alloys containing 4 to 30% aluminium with 2 to 16% copper found that on ageing, the dimensional increase of the samples was larger at higher copper contents, while their hardness, impact and tensile strength were lowered. Gebhardt's data also showed that the largest expansion occurred in alloys with compositions near 80% Zn, 10% Cu.

Structural changes occurring during the transformations of the supersaturated solid solutions in the low-copper zinc-aluminium-copper alloys were later investigated by a number of Polish workers.

Krupkowski and Ciach (66) investigated the kinetics of phase transformations in zinc-aluminium-copper alloys containing 2% Cu and either 60% Zn or 24%. They found that copper greatly retarded the decomposition of the supersaturated solid solutions on ageing. Low-zinc solid solutions quenched from the α-phase field, decomposed much more slowly than α' solid solutions with 60% Zn. A high cooling rate resulted in the retention of much more supersaturated α-phase in castings, and the slow decomposition of this phase gave rise to dimensional instability for long periods of time.

Ciach et al [(67)] later studied the structural changes during the ageing of supersaturated solid solutions in 78% Zn-Al-(1 to 3)% Cu alloys by means of hardness, dilatometric, microscopic and X-ray investigations. They found that the phase transformations in these alloys caused an increase in the hardness and length of the samples, as shown in their diagrams of Figs. 20 and 21. The effect of copper content on these changes is clear from these diagrams.

More recently Krol and Tasior [(68)] made an investigation of quench-ageing in the eutectoid-based zinc-aluminium alloys by X-ray, microscopic and dilatometric methods. Their alloys contained from 17 to 22% Al and 1 to 10% Cu. The alloys were solution treated, quenched and aged at 50° and 100°C for the investigations.

They concluded from measurements of the relative quantities of the phases present during ageing that transformation in the Zn-Al-Cu alloys occur according to the formulae:

$$\beta \rightarrow \alpha + \eta + \varepsilon, \quad \alpha + \varepsilon \rightleftharpoons T + \eta$$

Their work shows the complexity of the phase transformations, and provides useful information on the kinetics of phase transformations in the low-zinc part of the Zn-Al-Cu system. It is significant that the four-phase reaction which they deduced on ageing is one of the reactions found in the equilibrium diagram by Murphy [(35)]. The β phase decomposition may also occur in the equilibrium phase diagram.

Smith and Hare (65) investigated the influence of other alloying elements, especially magnesium and copper on the isothermal transformation properties of the binary eutectoid alloy. They found that of all the elements tested none stabilised the high-temperature β phase completely but many retarded the transformation, magnesium having by far the greatest effect. They also considered copper, silver, silicon, iron, manganese, nickel, and lithium. Copper, on which considerable work has been done, affected the time-temperature-transformation diagram markedly but to much lesser extent than magnesium. The authors of this work calculated that copper was one-fifteenth as effective as magnesium in retarding the eutectoid transformation. A TTT diagram for a eutectoid-based alloy containing nominally 0.5% Cu and 0.15% Mg (Zn-Al-0.5%Cu-0.15%Mg) produced by Smith and Hare is given in Fig. 22. The major retardation was due to the presence of magnesium and occurred below 190°C. Transformation, instead of starting after one minute at room temperature, started after one week, as seen in the above diagram. Their TTT diagrams for the binary and higher systems were used to show the suitable heat treatments to lead to various microstructures, including superplastic ones.

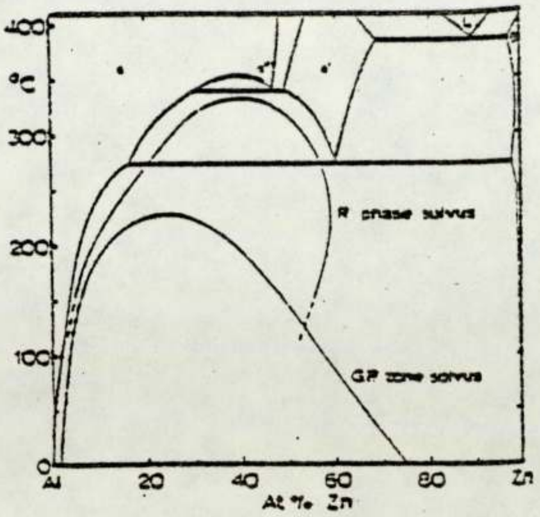

Fig. 17 The aluminium-zinc phase diagram with proposed metastable miscibility gaps for the G.P. zones and the R-phase (from Anantharaman and Satyanarayana (49)).

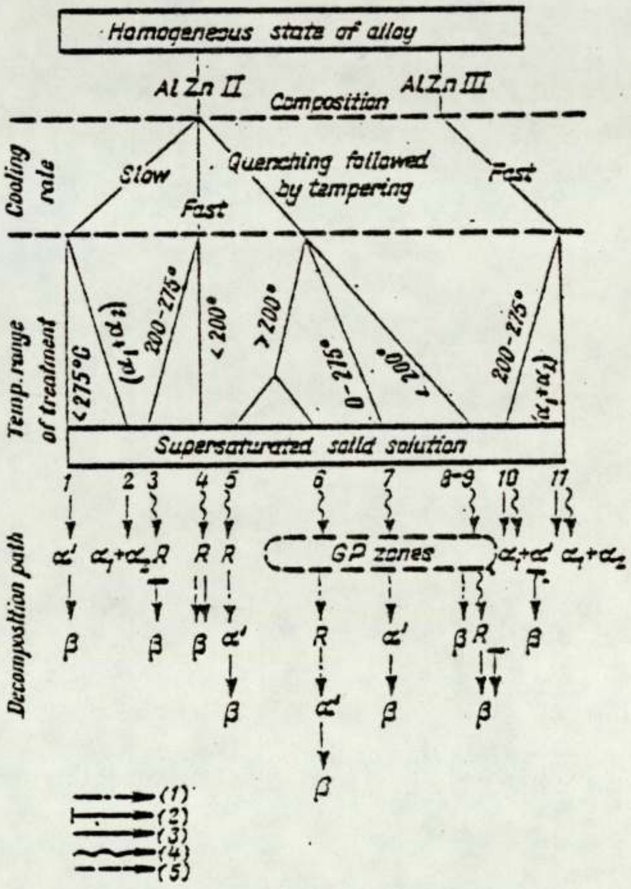

Fig. 18 R - intermediate rhombohedral phase; α' - supercooled high temperature α_2 phase (f.c.c. lattice); α_1 and α_2 - high temperature equilibrium phases (f.c.c. lattice); β - final equilibrium phase (h.c.p. lattice);, 1 - homogeneous rearrangement, 2 - cellular decomposition, 3 - nucleation, 4 - spinodal decomposition, 5 - nucleation at critical defects.

A scheme of transformation in Al-Zn alloys according to Toldin et al (63)

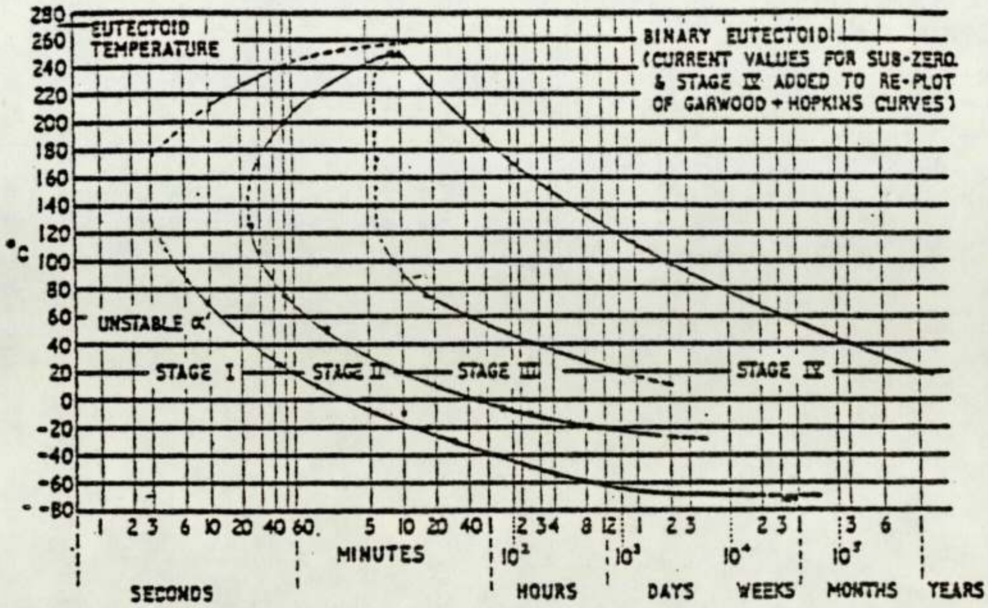

Fig. 19 TTT diagram for zinc-aluminium eutectoid alloy according to Smith and Hare (65).

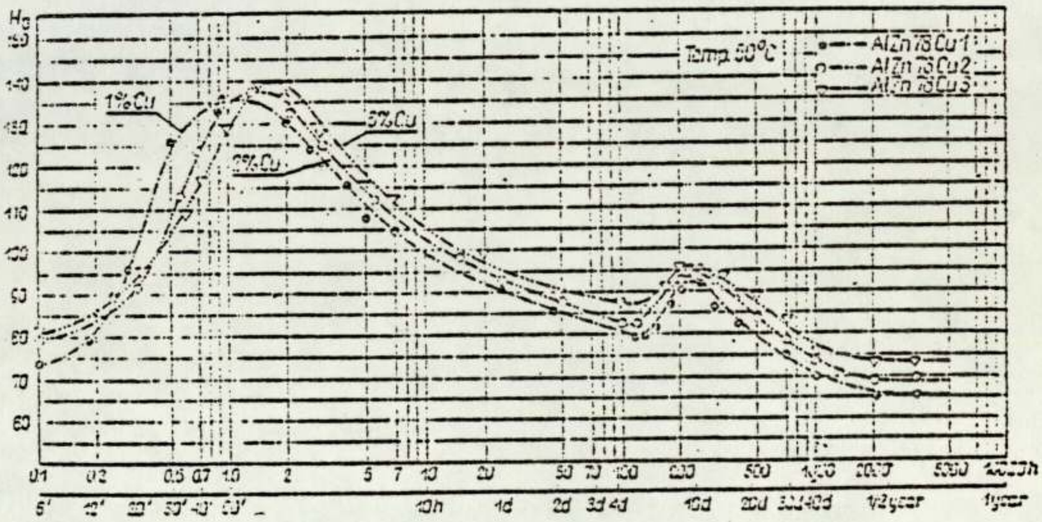

Fig. 20 Hardness change of 78% Zn-Al-(1-3)%Cu alloys on quench-ageing at 50°C (after Ciach et al (67)).

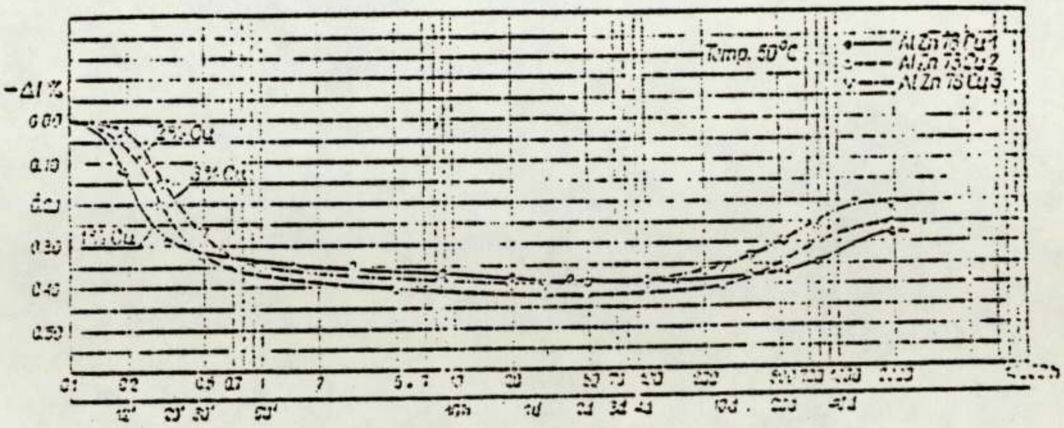

Fig. 21 Changes in the length of the samples of 78% Zn-Al-(1-3)%Cu alloys on quench-ageing at 50°C (after Ciach et al (67)).

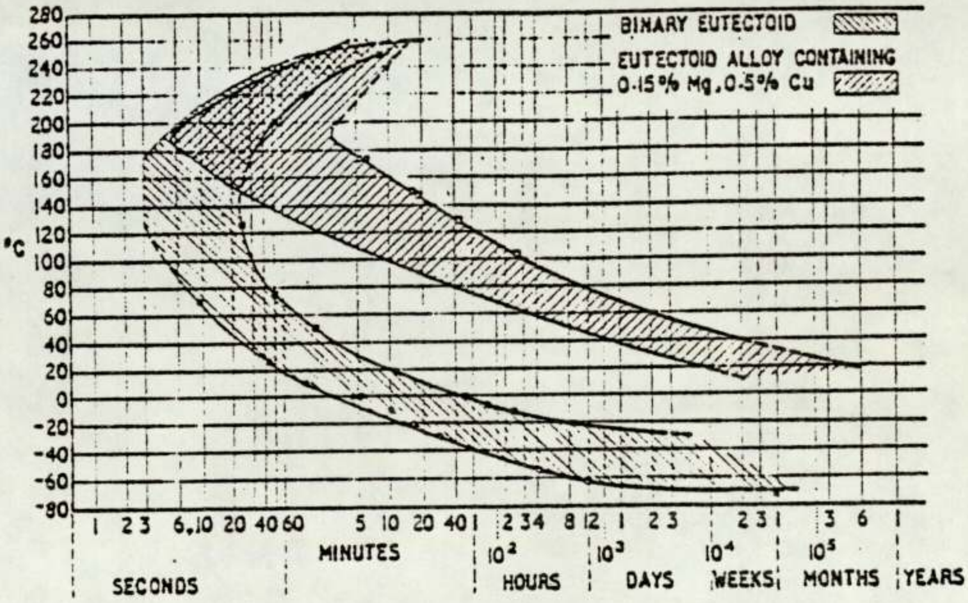

Fig. 22 Comparison of stage II TTT diagrams in binary and quaternary alloy (after Smith and Hare (65)).

1.5 Mechanical Properties of Zinc-Based Alloys

1.5.1 Tensile and Compression Properties

1.5.1.1 Binary Zn-Al Alloys

Most published work on the mechanical (especially tensile) properties of zinc-based alloys has concentrated on the binary zinc-aluminium eutectoid alloy in the superplastic condition.

There is little information available on either the off-eutectoid binary alloys or zinc-aluminium based ternary alloys, especially in the as-cast condition.

The tensile properties of extruded Zn-40% Al and Zn-50% Al alloys at different temperatures up to 270°C, were investigated and correlated with their microstructure by Melton and Edington (69). They observed that slip made a small but significant contribution to the deformation process in the Zn-40% Al alloy although the principle deformation process is grain-boundary sliding. In their discussion they state that the room temperature tensile strength of the Zn-Al alloys increases with increasing Al content. However the non-uniform microstructure produced by hot extruding the Zn-50% Al alloy provided a practical limit to the Al content of Zn-Al alloys as parts of the heterogeneous structure were not truly superplastic, at least in alloys made superplastic by extrusion. In a later investigation it was shown that raising the deformation temperature to 300°C overcame this problem in the 50% Al alloy, even though the alloy was in the $\alpha+\beta$ phase-field at that temperature (70).

Nuttall (71) studied the room-temperature deformation characteristics of the as-quenched Zn-22% Al eutectoid alloy. His work was mainly concerned with the determination of the effects of cold rolling and subsequent annealing on the room-temperature deformation properties of this alloy. The true-stress/true-strain relationships were determined at constant strain rates. An example of a true-stress/true-strain curve and corresponding strain ratio (R) obtained at a strain rate of 0.25 min^{-1} is shown in Fig. 23. This graph indicates that stress is essentially independent of strain, and the strain ratio (R) is ∿1 and exhibits little variation with strain. This is taken as evidence that the alloy is still characteristically superplastic even at room temperature, despite the fact that total ductility is small.

In addition to the behaviour mentioned above, a softening effect was observed during tensile testing of this alloy, as demonstrated by a decrease in hardness towards the fracture in the necked region of the test pieces. However the hardness remained fairly constant along the fractured gauge-length.

The observation that cold-rolling of the eutectoid alloy produced a decrease in hardness or U.T.S. (Fig. 24) was taken as evidence of superplastic behaviour although microstructure and deformation texture were found to be similar to those of normal metals. The formation of subgrains was noted in the highly-deformed material and correlated with the development of superplastic characteristics, i.e. the effective-grain size is that of the sub-grains, not the elongated grains bounded by high-angle boundaries. The extent of superplasticity varied with grain-size and with strain rate in the expected manner, but the effect of competing deformation mechanisms prevented a detailed explanation of the effects observed.

The deformation characteristics of the quenched-eutectoid alloy, below the transformation temperature (275°C) have been widely studied. Ball and Hutchison (72) proposed that grain-boundary sliding and grain-rotation are the predominant mode of deformation of this alloy. Kaybyshev and Kazakov (73) put forward intragranular slip in the zinc-based η phase as the controlling mechanism during deformation. The sudden increase in plasticity at 250°C was attributed to the change from single to multiple slip. Later in a detailed investigation Naziri et al (74) proposed that the deformation of the fine-grained eutectoid alloy at $m \simeq 0.3$, is predominantly due to the diffusion of the zinc-rich η-phase. Their work also confirmed that the above proposed mechanisms operate to a greater or lesser extent during superplastic deformation of this alloy.

Nuttall (75) found that testing at 250°C showed the typical characteristics of superplasticity. However at 290°C the superplastic behaviour gradually diminished with time. This effect was attributed to the gradual reversion of the fine-grained $\alpha + \eta$ structure to the β phase above the eutectoid temperature.

Recently Mohamed et al (76) studied the factors influencing ductility in the eutectoid alloy. In common with previous workers, they found that the maximum attainable ductility in tension in this alloy depends critically on the imposed strain rate, the testing temperature, and the initial grain size. However the highest ductilities were observed at intermediate strain rates, and there was a decrease at both higher and lower rates of strain. It was also shown that:

(i) the maximum ductility occurred at higher strain rates as the temperature was increased and/or the initial grain size was decreased, and

(ii) the maximum attainable ductility increased with increasing temperature and/or decreasing initial grain size.

Mechanical properties of alloys with zinc contents greater than the eutectoid composition have received little attention, except in the case of die-casting alloys with small amounts of aluminium. However, Feng (77) investigated a Zn-11% Al alloy and found it to be more strain-rate sensitive and stronger in tension than the eutectoid alloy at all temperatures below 279°C.

The tensile fracture characteristics of the Zn-Al alloys have been studied by several workers.

Gemmell and Grant (78) showed that a single-phase aluminium-20% zinc alloy exhibited intercrystalline fracture at 260°C and transcrystalline fracture as the testing temperature was raised; the transition was attributed to the ease with which grain-boundary migration and general recovery occur at higher temperature.

A similar alloy, used in a detailed investigation (79) of triple-point fracture at 260°C, was tested in tension, at a strain rate of $1.33 \times 10^{-4}s^{-1}$, over the range of temperature in which the material is single-phase. The work-hardening rate was low and decreased smoothly with increasing temperature. The fracture was entirely intercrystalline between 260° and 280°C and completely transcrystalline above 350°C. It was also found that a rise in temperature was accompanied by an increase in fracture strain. Metallographic examination of specimens tested at 300°C showed that, although the main fracture was transcrystalline, some intercrystalline triple point cracks were present; such cracks were very blunt when compared with similar ones at 260°C. It was suggested that there are two main factors opposing crack nucleation and growth; namely, the ease of grain-boundary migration and ease of recovery of the material around the growing crack tip. The nucleation of a crack should thus be controlled both by the recovery and migration rate and the growth mainly by the recovery rate, unless the time allowed for migration is sufficient to completely remove the grain-boundary from the crack.

In his latter paper Williams (80) concluded that failure of this alloy (Zn-20% Al) arises as follows; at 260°C, the stress concentrations produced by grain-boundary sliding cannot be fully relaxed, either by migration or recovery, and intercrystalline triple-point cracks nucleate and grow. As the testing temperature is increased the work hardening rate decreases, migration occurs more readily, and any triple-point cracks that do form will be blunted at the crack tip by the reduced work-hardening rate; this blunting will lead to an increased effective energy and accompanying slow growth rate. However, above 350°C the very low work-hardening rate and high grain boundary mobility inhibit both triple-point crack and cavity nucleation and the failure is then entirely transcrystalline.

Ball and Hutchison (72) reported that the zinc-aluminium eutectoid alloy with a grain size of $\sim$1.1 μm became brittle below -100°C when tested at a strain rate of $4.2 \times 10^{-5}s^{-1}$, whereas alloys with grain sizes of 2.5 and 4.5 μm failed in a ductile manner at -196°C. The ductile-brittle transition is thus seen to depend on grain-size and, probably, on alloy composition.

A recent metallographic examination of fractured tensile specimens of the quenched eutectoid alloy revealed the presence of extensive cavitation after deformation at low strain rates and room temperature (81). The authors of this work proposed that the fracture of this alloy, at low-strain rates, occurred by a combination of external necking and internal linkage of voids by an intergranular void sheet process.

It appears that tensile properties of the zinc-aluminium alloys are dependent on the alloy composition, heat treatment temperature, cooling rate, grain-size, test temperature and deformation rate.

Determination of compressive properties could provide useful information in designing the optimum forming conditions in the production of zinc-aluminium alloys. However, in this context, there is little work available in the literature.

The deformation characteristics of the Zn-Al eutectoid alloy during compression in the temperature range -268.8° to 357°C were investigated by Komnik et al (82). They determined the true-stress (σ) vs. true-strain (ε) curves for the alloy under compression at the rate of $2 \times 10^{-4} s^{-1}$ after three prior heat treatments. These were: quenching from the cast state, quenching after homogenization at 367°C for 70 hours, and tempering (70 hours at 227°C followed by slow cooling, 30°C/hour, to room temperature). In their investigation it was observed that the alloy remained plastic down to -268.8°C, but in the range 27° - 357°C the plastic deformation was irregular. They also found that at 27°C the internal stress (σ_i) either diminished or did not vary with ε, whatever the prior heat treatment. They concluded that the effective stress

($\sigma^* = \sigma - \sigma_i$) for the first heat treatment did not depend on ε; for the second it diminished as ε increased and for the third it increased with ε.

1.5.1.2 Ternary and Higher Alloys

The addition of small amounts of other component elements to the binary eutectoid alloy has been widely investigated, especially in efforts to develop superplastic alloys with adequate mechanical properties.

Naziri and Pearce (83) studied the influence of copper additions on the mechanical properties of the binary eutectoid alloy. Their tensile test results showed that the addition of up to 1% copper had no significant effect on the stress required to deform the binary alloy above about 175°C. They also found that copper additions up to 1% slightly altered the dependence of strain-rate sensitivity on the strain-rate at different temperatures.

Smith and Hare (65) later reported that the addition of copper and magnesium raised the mechanical strength of the eutectoid alloy to a useful industrial level.

Nuttall (84) investigated the effect of ternary additions on the mechanical properties of a Zn-22% Al binary eutectoid alloy. The alloys studied contained 0.2% Mn, 1% Si or 4% Cu. The silicon-containing alloy cracked on hot rolling or swaging and little work was carried out on this material.

Fig. (25) shows the relationship between true-stress and true-strain-rate for the copper and manganese-containing ternary alloys at 250^{o}C, together with the results for the as-quenched binary eutectoid alloy. It can be seen from this graph that the important features of ternary alloys were that the highest m value ($\sim$0.5) occurred at high strain rates (0.1 - 1.0 min^{-1}), and that m gradually decreased to 0.3 at low strain rates. At a given strain rate, the flow stress of the ternary alloys was higher than that of the binary alloy, particularly at low strain rates. This effect persisted at all temperatures between 25 and 250^{o}C (298 and 523 K) as can be seen from the temperature-dependence of the flow stress for the as-quenched alloys in Fig. 26.

The room-temperature tensile properties and hardnesses of the binary and the two ternary alloys in a number of conditions, determined by Nuttall, are given in Table 1. It can be seen from the table that manganese-containing alloy is superior to the copper-containing alloy. Only a marginal improvement in room-temperature strength properties over the binary alloy was achieved in the case of copper containing alloy.

The alloy containing 4% copper showed no significant improvement in room-temperature mechanical properties compared with previous results obtained on 1% copper alloy (85).

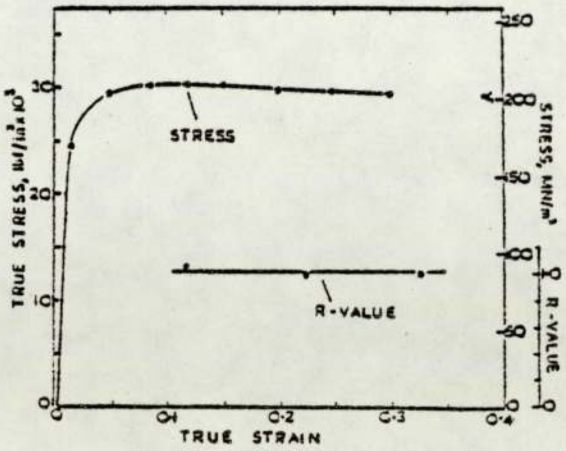

Fig. 23 True-stress/true-strain relationship at constant rate and R-value for the as-quenched binary eutectoid alloy (after Nuttall$^{(71)}$).

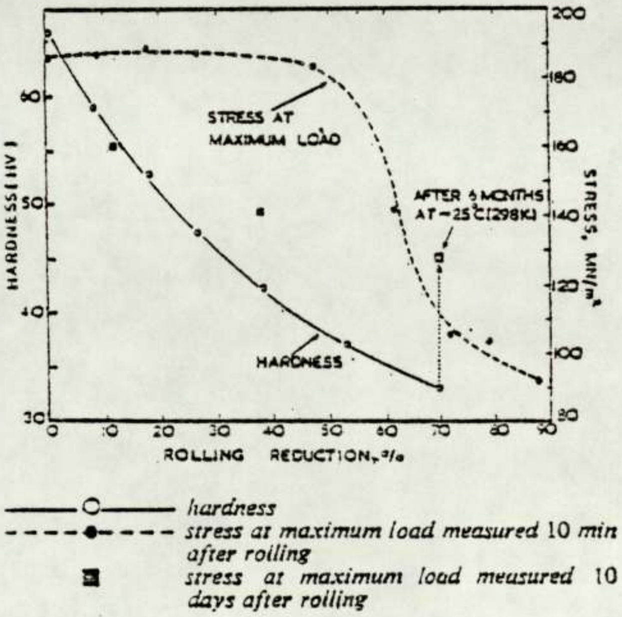

Fig. 24 Effect of cold rolling on hardness and tensile stress at maximum load (after Nuttall $^{(71)}$).

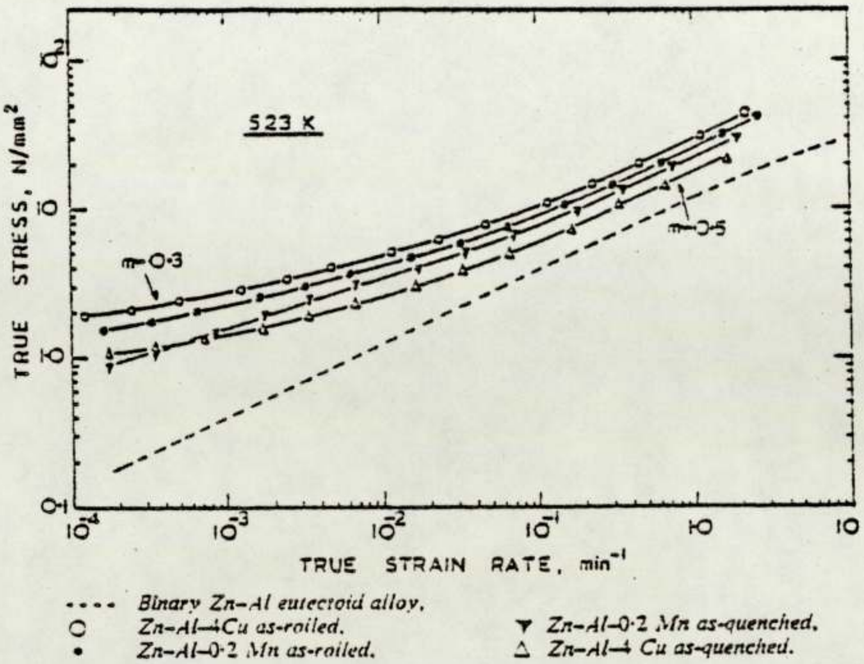

Fig. 25 Flow stress/strain rate relationships for the binary and ternary alloys at 250°C (after Nuttall (84)).

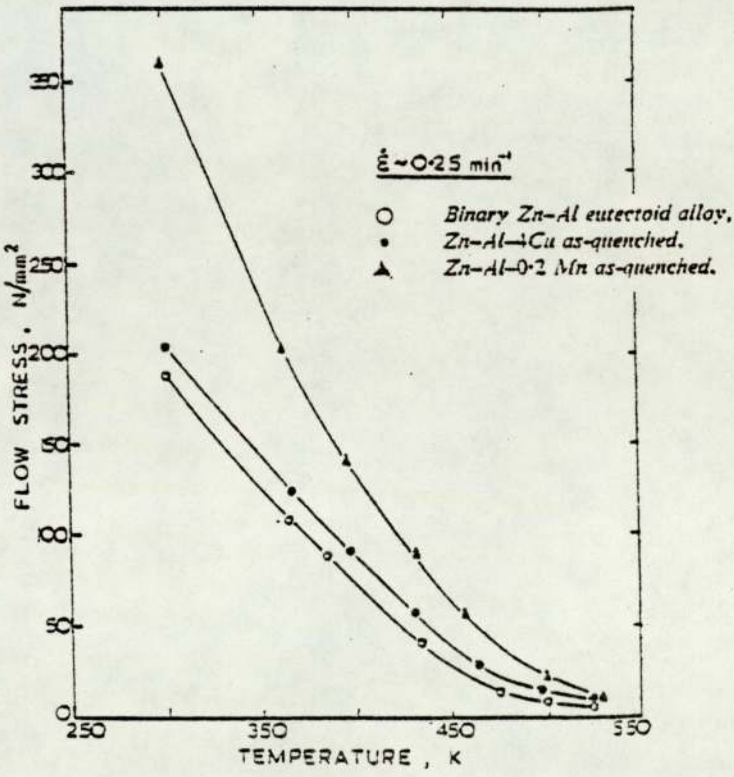

Fig. 26 Temperature-dependence of the flow stress for the as quenched alloys (after Nuttall (84)).

Very little work has been reported on the deformation mechanisms and fracture properties of the zinc-aluminium based ternary and quaternary alloys.

Loosemore (85) studied the deformation and fracture properties of a zinc-aluminium eutectoid-based quaternary alloy (Zn-21.9% Al-1.03% Cu-0.095% Mg) during tensile testing in the temperature range of -196° to 20°C. His work showed that the failure of this alloy occurred by a mixture of ductile and brittle fracture.

In his investigation it was found that this alloy had a temperature-insensitive flow stress at cryogenic temperatures, enhancing low-temperature ductility, since the crack propagation stress, 490 N/mm^2, was not reached by the yield stress at -196°C until the strain-rate exceeded 0.1/s.

1.5.2 Creep Properties

1.5.2.1 Correlation of Creep Data

An important objective in recent work on the creep of metals has been to try to develop a "universal" equation which applies to the creep behaviour of all metals (86).

Several methods of rationalisation of creep data have been suggested in recent times. These proposals have usually been developed from empirical equations for the stress (σ)-dependence of secondary or steady-state creep rate ($\dot{\varepsilon}_s$) of the form:

$$\dot{\varepsilon}_s = A\sigma^n \exp(-Q_c/RT) \quad \ldots\ldots\ldots\ldots\ldots\ldots(1)$$

A is a structure-sensitive parameter. In pure metals and simple alloys n is often found to be in the range 4-5. Q_c is close to the activation energy for self-diffusion (Q_D). R is the gas constant and T the absolute creep temperature. Such expressions are applicable to high-temperature climb-controlled creep in which deformation mainly occurs by the diffusion of vacancies.

In the development of a "universal" equation, the work of McLean and Hale (87) was significant in showing that the creep rates of pure metals could be better rationalised by dividing stress by the modulus of the material at the appropriate temperature. Sherby (88,89) extended this approach by dividing the creep rate by the diffusion coefficient, D, and taking into account the stacking-fault energy (γ_s) of the metal. The resultant expression (89,90) has the form

$$\dot{\varepsilon}_s/D = A'\gamma_s^{3.5} (\sigma/G)^n \quad \ldots\ldots\ldots\ldots\ldots\ldots(2)$$

with A′ a constant and G the shear modulus.

This equation as was pointed out by Mukherjee et al (86) is dimensionally unbalanced. Also they considered that the activation-energy term should be stress-dependent. Their alternative equation has the form:

$$\dot{\varepsilon}_s kT/DGb = A'' (\sigma/G)^n \quad \ldots\ldots\ldots\ldots\ldots\ldots(3)$$

where k is the Boltzmann constant, b is the Burgers vector, and A′′ is a function of γ_s.

Use of this equation to correlate data obtained from the creep of simple metals gave a pronounced scatter band in the results (86).

Hancock et al (91) considering the even wider variation in the important variables for real engineering alloys, concluded that the development of a true "universal" creep equation was unlikely.

Despire this, Wilshire and his co-workers (92,93,94) proposed an equation of the form:

$$\dot{\varepsilon}_s = A^*(\sigma-\sigma_o)^p \exp(-Q_c^*/RT) \qquad \text{..........(4)}$$

The importance of which is the introduction of the concept that the effective stress is the applied stress reduced by a friction stress (σ_o). The friction stress represents the part of the applied stress supported by substructural features other than the dislocations contributing to creep deformation. With the introduction of σ_o, the exponent p in eqn. (4) is not found to be $\sim$4 irrespective of whether the data are for simple or complex materials. Q_c* can be related to an appropriate activation energy for diffusion (usually Q_D). On this basis it was suggested that creep-controlling mechanisms are similar (92-94) irrespective of the degree of material complexity.

As a result of experimental work of their own, and a survey of a published data, Evans and Harrison (95) proposed the equation:

$$\dot{\varepsilon}_s = B\left(\frac{\sigma-\sigma_o}{\sigma_{0.05}}\right)^{3.5} \qquad \text{....................(5)}$$

with $B \simeq 2.5 \times 10^{-5}$/s independent of material, crystal lattice, microstructure and temperature. $\sigma_{0.05}$ is the 0.05% proof stress. In this equation, the effective-stress is normalised by the proof stress or yield stress of the alloy at the creep temperature. This normalisation gives rise to the independence of B on material parameters.

A later version of this equation (96) incorporates an additional term which alloys the equation to be used to correlate primary and secondary (general) creep data. This has the form:

$$\dot{\varepsilon}_s = A^*(\sigma-[\sigma_o]t)^p \exp(-Q_c^*/RT) \quad \ldots\ldots(6)$$

For initial creep, $[\sigma_o]$ is replaced by $[\sigma_o]_{in}$ which is obtained by extrapolation of secondary creep data to zero applied stress. This equation was shown to correlate well the data obtained from creep of Nimonic 90.

1.5.2.2 Creep in the Binary Alloys

It is now generally recognised (97,98) that when a material deforms under creep conditions, it can fail either by cavitation or by triple point fracture (or an apparent combination of both). Density measurements have been used (99,100) to study the nucleation and growth of cavities during a creep test, and there appears to be clear evidence (100) that cavity nucleation occurs throughout a test. All of the mechanisms for the nucleation of creep cracks, i.e. cavities or triple point cracks, rely on grain-boundary sliding to produce large stress concentrations for initial nucleation of a crack nucleus (101,102).

The creep properties of the binary zinc-aluminium alloys at any test condition, largely depend on composition (Zn/Al ratio), heat treatment, cooling rate and grain size.

Congleton and Parkins (103) investigated the creep properties of Al-rich alloys with up to 4.9% Zn. They found that substitutional strain-ageing occurred during creep of some supersaturated alloys and resulted in a dramatic reduction of the creep rate. They suggested that if the initial ratio of $\dot{\varepsilon}/\varepsilon$ is too high, strain-ageing effectively lowers the creep rate only after enough transient creep has occurred to reduce the $\dot{\varepsilon}/\varepsilon$ ratio into the critical range. In alloys that strain-age very rapidly, the initial value of $\dot{\varepsilon}/\varepsilon$ was less than the critical values calculated from the equation:

$$\dot{\varepsilon}/\varepsilon \simeq 40 \exp(-Q/kT) \quad \ldots\ldots\ldots\ldots\ldots\ldots (7)$$

and good creep resistance was maintained until dislocations could break away and move more freely through the alloy.

Congleton and Parkins also found that the activation energy relevant to the strain-ageing process in low-zinc-aluminium alloys is $\sim$46 KJ/mol., in good agreement with Mott's (104) estimate of $^1/3$ the activation energy for self-diffusion of the parent metal. Hence they proposed that the ratio of $\dot{\varepsilon}/\varepsilon$ at the onset of strain-ageing could be used to determine the binding energy.

The nucleation and growth of triple point cracks in a single-phase Zn-80% Al alloy during creep at 262°C, was studied by Williams (105). It was proposed that the nucleation and growth of triple point cracks could be related to the combined effects of grain-boundary sliding and applied stress.

As a result of previous investigations it has been established that the high-temperature creep deformation especially in the Al-rich Zn-Al alloys usually proceeds by a combination of dislocation motion within grains and grain-boundary sliding (105,106).

Since grain-boundary sliding is the predominant mechanism for the deformation process, a large grain-size reduces creep. This was shown by Marshall et al (107) who demonstrated a marked reduction in creep rate for the furnace-cooled eutectoid alloy.

Chin et al (108,109) studied in detail the role of diffusion in determining the creep mechanisms in Zn-Al solid solutions. In their investigation the creep behaviour of solid solutions (α, α' and β) in the binary system over a composition range of 0 to 78.4% Zn were studied in order to experimentally verify the theoretical diffusion coefficients.

As a result of their work, it was suggested that glide may be the controlling creep mechanism in Zn-Al solid solutions near the miscibility gap composition (61.3% Zn).

In the second part of their study (109) the stress exponents and activation energies for a number of Zn-Al alloys containing from 17.4 (8) up to 78.4% Zn (60 at - %Zn) were measured in order to determine the composition range over which glide controls the creep process.

The stress exponent and activation energy measurements indicated that a transition from climb-controlled to glide-controlled creep occurred as the zinc-concentration increased. As a result they suggested that the creep behaviour of these alloys could be explained by a combination of climb and glide controlled creep processes. Glide creep is dependent on the chemical diffusivity which approaches zero at the miscibility gap composition 61.3% Zn (∿39.5 at % Zn). This causes a minimum in the creep rate at the miscibility gap composition, as shown in Fig. 27.

Chin et al concluded that the absolute magnitude of the observed creep rate could be rationalised for all compositions by a simple equation:

$$\frac{1}{\dot{\varepsilon}_{total}} = \frac{1}{\dot{\varepsilon}_{cl}} + \frac{1}{\dot{\varepsilon}_{gl}} \quad \ldots\ldots\ldots\ldots(8)$$

The temperature and stress dependences of steady-state strain-rates in the Zn-22% Al eutectoid alloy were studied (110) by tensile and creep testing using double shear-type specimens in a normalised stress range of 5×10^{-7} to 5×10^{-3}. The stress-dependence of the strain-rate showed three separate regions with stress exponents of:

(i) 0.87 ± 0.12;
(ii) 1.99 ± 0.15;
(iii) 3.73 ± 0.17.

Table 1

Alloy	Condition	0·2% Proof Stress, N/mm^2	UTS, N/mm^2	Elongation, % on 25 mm	Strain-Rate Exponent, *m*	Hardness, HV
Zn–Al	As-quenched	158	186	90	0·18	64
Zn–Al–4 Cu	As-rolled	167	191	105	0·12	73
Zn–Al–0·2 Mn	As-rolled	232	335	60	0·11	100
Zn–Al–4 Cu	As-quenched	172	201	78	0·14	84
Zn–Al–0·2 Mn	As-quenched	305	361	23	0·1	108
Zn–Al–4 Cu	As-quenched† aged at 250° C (523 K) for 20 min	203	242	88	0·13	90
Zn–Al–0·2 Mn	As-quenched† aged at 250° C (523 K) for 20 min	377	410	25	0·1	115
Zn–Al–0·2 Mn	As-quenched† aged at 22° C (295 K) for 100 h	392	462	21	0·1	127
Zam‡	—*	354–420	384–680	4–17	—	~115
Presal*†	—*	232–310	310–386	—	—	—

* Depending on composition and thermomechanical history.

† Strain rate unknown.

The room temperature tensile properties and hardnesses of binary and two ternary alloys (after Nuttall (84))

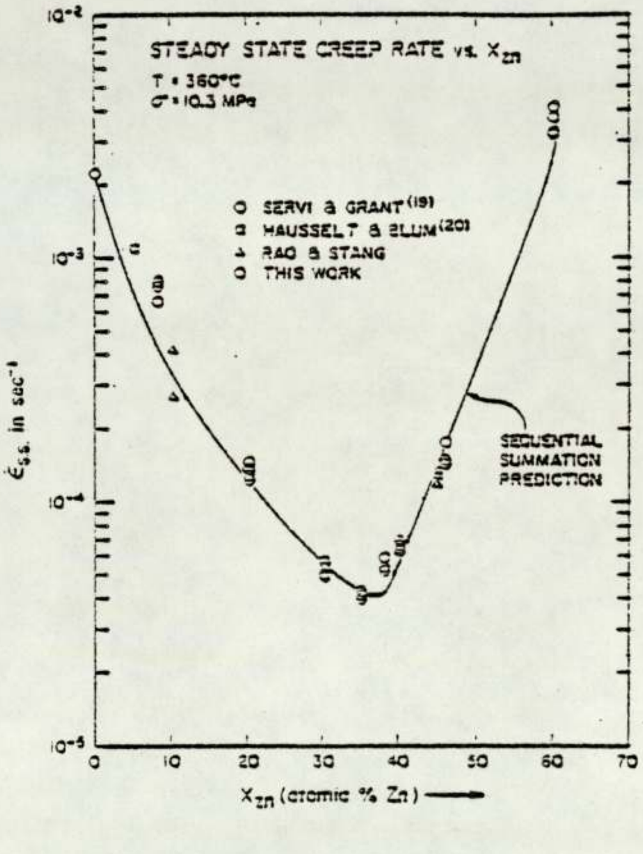

Fig. 27 Comparison of the steady state creep rates for Zn-Al solid solutions with the sequential summation prediction at 360°C (after Chin et al (109).

The activation energy for deformation in regions I and II was identified as that for grain-boundary diffusion, while that in region III was approximately equal to the self-diffusion value. Dislocation climb and Coble creep were found to be the controlling mechanisms in regions III and I respectively. The results in region II were in close agreement with predictions based on the Ball-Hutchison (72) model for superplasticity.

1.5.2.3 Creep in the Ternary and Higher Alloys

Many workers have studied the effect of alloying additions on zinc-aluminium alloys, mainly with the intention of improving their creep resistance.

Naziri and Pearce (83) reported that the addition of up to 1% copper continuously improved the room-temperature creep resistance of slightly hypereutectoid (Zn-20% Al) alloys and at 1% the improvement was one hundred and forty-fold.

The work of Swanson (111) showed that the presence of up to 0.05% Mg had a profound effect on the secondary creep rate of the binary eutectoid alloy without seriously impairing its superplastic properties. He also showed that much of the benefit was obtained with a magnesium addition of 0.005%.

Later Nuttall (84) investigated the room-temperature creep properties of two Zn-Al eutectoid-based ternary alloys (74% Zn-22% Al-4% Cu and 77.8% Zn-22% Al-0.2% Mn). His work was carried out on these alloys after various heat treatments by measuring the secondary creep rate at a stress of 35 MN/m^2. His results indicated that although the copper addition significantly increased the room temperature creep resistance of the binary eutectoid alloy, there was no improvement in increasing the copper content from 1 to 4%. However, the creep resistance of the manganese-containing alloy was substantially better than that of any of the alloys containing copper. Therefore it was suggested that the zinc-aluminium eutectoid alloy containing small additions of manganese could form the basis for an alloy with both excellent formability at moderate temperatures and acceptable room-temperature strength and creep properties.

In addition to copper, manganese and magnesium, nickel is also claimed to be a useful alloy addition (112,113), its effects being in many ways similar to those of copper.

Mulvania et al (114) studied the effects of additions of single elements (titanium chromium, manganese, copper and magnesium) on the room-temperature creep resistance of the binary eutectoid alloy. Their work showed that in general, creep resistance of the binary eutectoid alloy was improved by alloying. As a result of these observations it was suggested that alloy additions which improved creep resistance in zinc die-castings also improved the creep resistance of the binary eutectoid alloy.

The highest creep strength was obtained with an addition of 0.018% Mg. However the optimum high creep strength and low superplastic flow stress was obtained by copper additions.

They also found that the creep resistance of an alloy containing 0.42% Cu and 0.002% Mg was similar to that of a commercial zinc die-casting. The superplastic flow stress (or forming stress) in this quaternary alloy increased by only a factor of two.

It can be concluded that the combination of copper and magnesium alloy additions greatly improves the creep resistance of the binary eutectoid alloy without seriously affecting its processing or forming properties.

1.5.3 Damping Characteristics

Bearing bushes are used to support rotating or oscillating shafts. Vibrations caused by out of balance forces are transmitted through the bush into the structure of the machine. If the structure resonates in sympathy with the vibration this may result in excessive noise, discomfort or even fatigue failure of the structure or attached components.

Damping of vibrations is usually effected by use of high hysteresis elastomers interposed between the machine structure and its supports. However Zn-Al based alloys posses a substantial capacity for damping under certain conditions, and this property is an especially valuable one as vibration can be attenuated close to its source.

Damping is characterised by anelastic behaviour (115), i.e. the non-linearity between stress and strain caused by time dependent relaxation of applied stress. Anelastic materials subjected to cyclic stress will produce a hysteresis loop on a stress-strain diagram. The area of this loop represents the elastic strain energy dissipated by damping in one cycle.

The mechanisms of damping in metals have been listed by Burdett and Queen (116) as solute ordering, grain-boundary viscosity, thermo-elastic damping, magnetic damping, and dislocation damping. Of these grain-boundary sliding and possibly dislocation damping may be important in the zinc-aluminium alloys.

Grain-boundary sliding was discovered by Ke (117) who found an internal friction peak in relaxation spectrum of polycrystalline aluminium which was absent in single crystals. The effect occurs when the temperature is sufficiently high for disordered material in the grain boundaries to be rearranged to reduce the boundary shear stresses. The process is thermally activated and results in a relative sliding motion between the adjacent grains. Energy is dissipated by grain-boundary sliding and reaches a peak in the temperature range where viscosity of the boundary region is low enough to allow energy dissipation but not so low that strain energy remains stored.

Dislocation damping occurs when partially pinned dislocations vibrate back and forth between pinning points. Energy dissipation occurs if some frictional effect obstructs the motion of the dislocation line. Such effects may be interaction with point defects, solute atoms or similar feeble pinning features.

Specific work on Zn-Al alloys has been reported over a number of years. Postnikov and Zolotukhin (118) studied the effect of cyclic heat treatment on the damping capacity of Zn-Al alloys containing 10, 20, 30, 60, 80 and 98% Zn. They determined the damping capacity of these alloys as shown in Fig. 28 . Damping capacity is defined here as resonance curve breadth factor, Q^{-1}. It can be seen from this figure that the height of the peaks which corresponds to the damping capacity (Q^{-1}) increases with the zinc concentration. Thermocycling has practically no effect on the position of the peak on the temperature axis but it broadens it considerably and increases the height.

Nuttall (119) later investigated the damping characteristics of the Zn-Al eutectoid alloy in the superplastic and non-superplastic condition. In his investigation the damping capacity of the alloy was measured in terms of both logarithmic decrement (δ) and specific damping capacity (SDC), defined as the fractional vibrational energy lost during one cycle of stress, using torsional free decay. It was found that in the superplastic condition, δ increased rapidly with increase in temperature to a frequency-dependent peak ($\sim$1.2) at $\sim$200°C, while in the non-superplastic condition δ rose more moderately with temperature to a maximum (∿0.8) at the phase-transformation temperature of 276°C, as seen in Fig. (29). In the single-phase β region both as-quenched and slow-cooled material showed an initial decrease in δ, which then remained relatively constant with further increase in temperature.

In both conditions the rapid decrease in δ occurred at ∿300°C, compared with the equilibrium eutectoid isotherm of 276°C. This temperature difference is associated with a reverse transformation hysteresis, which is commonly observed in eutectoid transformations, and has been reported in the section on mechanical properties (75).

Measurements of SDC in the superplastic condition showed a variation with temperature similar to that for δ; however little dependence of SDC on surface shear stress was found at any temperature, (Fig. 30).

Nuttall concluded that high damping in the Zn-Al eutectoid alloy was associated with superplasticity and arose from grain-boundary sliding. The effect was greatest in the temperature range 200-276°C. Although the SDC was essentially independent of strain amplitude, a small frequency dependence was observed.

In the non-superplastic condition the lamellar microstructure gave rise to a continuously rising damping capacity up to the eutectoid temperature. This was explained by the coupled relations between interface; a concept used by Nowik (120) to explain his observations of an apparently indefinite rise in damping with temperature in an Zn-60% Al alloy after discontinuous precipitation of zinc.

In a more recent investigation it was found the binary Zn-Al eutectoid alloy in superplastic condition at room temperature exhibited a damping capacity of 3.27%, compared with 2.15% in a Zn-Al-Cu ternary alloy, Alzen 305 (121).

The major advantage of the Zn-Al alloys is that their damping behaviour is not stress dependent, they can produce high damping at minimal stress. The Zn-Al-Cu alloy, Alzen 305, exhibited relatively higher damping at elevated temperatures, i.e. 13.11% at 150°C. The Alzen 305 exhibits a fairly high damping capacity when given a similar heat treatment to the binary Zn-Al, except that the soaking time is three hours, longer than this appears to produce a decrease in damping capacity.

There is a possibility that Zn-Al based bearings could be produced with moderate damping capacity at their operating temperature. This would be a positive advantage sonce conventional copper-based or aluminium-based bearing alloys have negligible damping capacity (121,122,123).

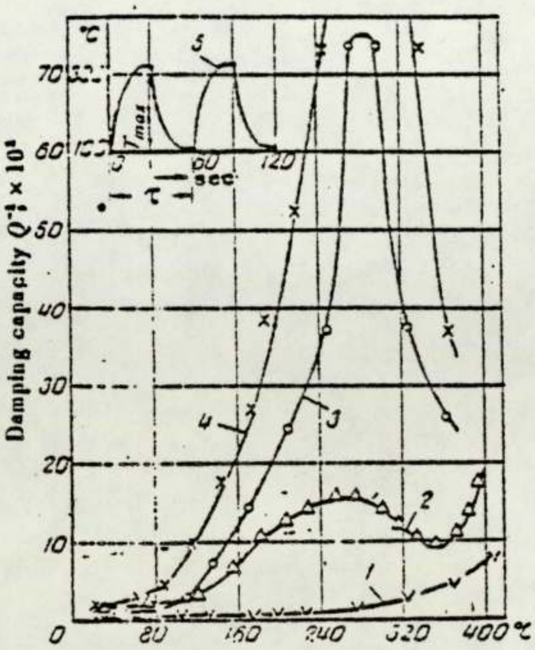

Fig. 28 1) 20% Zn, 2) 60% Zn, 3,4) 80% Zn
5) shape of thermocycle;
1, 2, 3 - n = 0, 4 - n = 180,
Tmax = 330°C, τ = 60 s.

Effects of temperature and temal cycling on the damping capacity of aluminium-zinc alloys (after Postnikov and Zolotukhin (118)).

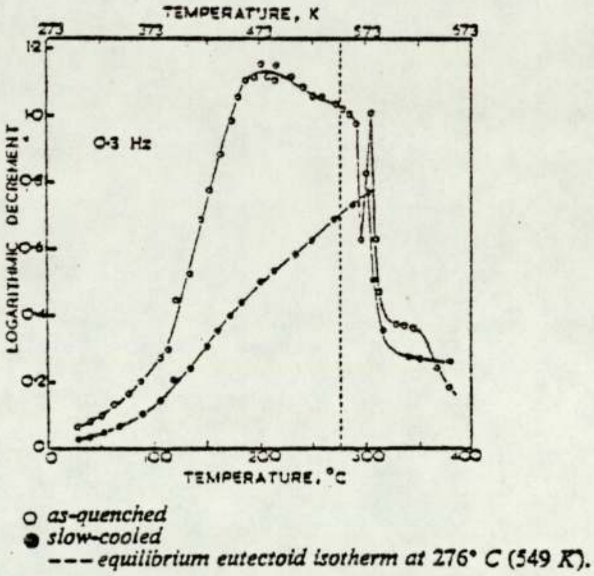

Fig. 29 Logarithmic decrement (δ) vs. temperature for as-quenched and slow-cooled binary eutectoid alloys at a frequency of 0.3 Hz (after Nuttall (119)).

1.6 Formability and Machinability of Zinc-Based Alloys

In the production of commercial bushings the material is conveniently formed by extrusion or casting and machining. It has been reported that Zn-Al based bearing alloys, consisting of 38 to 75% Al, 0 to 4.8% Cu, 0.05 to 2.8% Ni, 0 to 0.05% Mg and balance Zn, in the as-cast state could be either cold shaped or hot shaped at 200 to 400°C (124).

However the superplasticity associated with zinc-aluminium based alloys could be used to great advantage in production provided that the properties, particularly creep properties, are not adversely affected.

Forming in the superplastic condition compared with casting and machining or extrusion would give important commercial advantages of low forming pressures requiring cheaper presses, lower die cost, longer die life, excellent detail, better surface finish and fewer secondary operations (114).

Generally, for a given alloy the degree of superplasticity is dependent upon the value of strain-rate-sensitivity index (m) in the equation $\sigma = K\dot{\varepsilon}^m$; a higher value being associated with greater superplastic deformation. The value of m varies with strain-rate and has a maximum between 0.4 to 0.8. Forming operations should be carried out at the strain rates near to that for which m is a maximum.

However the application of superplastic formation of monolithic bushes for bearing purposes would be in modes where compression and shear predominate, and the strain-rate is high, e.g. extrusion. Under such conditions the advantage of low power requirements may be offset by the low production rates dictated by the strain-rate dependence of superplasticity.

The superplastic condition may be produced, as discussed in the previous section, either by plastic deformation, or quench-ageing.

The deformation conditioning of ternary Zn-Al-Cu and Zn-Al-Cu with less than 0.05% Mg, alloys to show superplastic behaviour by utilising an homogenising heat treatment, followed by hot working at a temperature between 205°C and 250°C was reported (125). The hot working consisted of hot rolling to a reduction of 80 to 95% or hot extrusion followed by drawing. A Zn-Al based alloy consisting of 74.5 to 81.9% Zn, 18 to 24% Al and 0.1 to 1.5% of a third component, mainly of Ni was also reported to have high-strength and ductility and could be shaped conveniently by extrusion (125). The third component of this alloy could also be titanium, copper, iron and/or silicon.

Stewart (127) investigated the superplastic forging of binary Zn-22% Al and ternary Zn-20% Al-2% Cu alloys. His work was concerned with the upset forging and closed die forging of these alloys. Cylindrical specimens were upset to a reduction in height of 97% and also were forged into a complex part with thin web sections.

His work showed that the optimum superplastic forging conditions of these alloys were obtained at a forging rate of less than 2.1 mm/s, and at a temperature as close to the transformation as possible. The effect of temperature on forging stress is shown in Fig. 31 and of forging rate in Fig. 32. Good lubrication during forging was obtained with teflon sheet, a grease-molybdenum-disulphide mixture, or colloidal graphite.

Stewart concluded that large deformations at low stresses could be obtained in Zn-Al and Zn-Al-Cu alloys under actual forging conditions and a complex shape could be forged with excellent die fill under relatively low loads, but at low deformation rates.

Closed die forging of a Zn-Al eutectoid-based commercial alloy (ZAM) containing up to 2% Cu and 0.05-0.2% Mg was investigated at temperatures of 230-270°C by Belk (182). It was found that the low flow stress of this alloy at these temperatures enabled split multi-sectioned dies to be used thereby permitting complex shapes to be formed that, with conventional materials, could only be produced by machining or casting. The product had a uniform fine-grained equi-axed structure which exhibited little or no directionality and therefore, had a better combination of properties than a cast product. As a result it was suggested that closed die forging was particularly suited to medium-length production runs, where neither machining nor die castings were economic.

Extrusion, either conventional or superplastic, is not necessarily the only process by which bearings are made. Thin-wall, steel-backed bushings might conceivably be made by deep drawing of sheet. The utilisation of superplasticity in this context has been more widely investigated, and details are available for several ternary and quaternary alloys similar to bearing alloys.

It has been established that small amounts of alloy additions which have been used to improve the mechanical properties, do not seriously affect the forming properties of the basically binary eutectoid alloy (77,83,84,111,129,130).

Johnson et al (131) investigated the superplastic forming techniques and strain distribution in a zinc-aluminium eutectoid alloy, containing 0.15% copper. In their investigation "bubbles" and "top-hats" of this alloy were formed at low pressures at temperatures ∿250°C by various methods. Their work showed that friction played a large part in restricting the flow of this material. For this reason they suggested that the deep parts could not be produced by simply forming into female moulds, as variations in thickness would be too great. As a result of their observations it was proposed that multi-stage operations are the most efficient in producing parts of fairly uniform thickness distribution because of their ability to take advantage of friction.

Deep drawing of superplastic materials has received little attention, although it is capable of producing components having high aspect ratios. At temperatures <0.3 Tm, where Tm is the absolute melting point, the majority of superplastic materials exhibit ductilities similar to, or even lower than, those of conventional materials and so exhibit similar press-forming characteristics. If the deformation temperature is increased, the ductility increases dramatically and the limit of deformation should also be increased.

The deep drawing of superplastic materials at >0.5 Tm, however, poses problems, because, in order to draw in the flange, the material in contact with the punch nose must first work harden and so must the material forming the cup walls. At such deformation temperatures, superplastic materials do not work harden, and in the absence of work hardening, the blank will not draw and the process will be more akin to stretch forming. There are, however, a number of ways in which the problems of deep drawing superplastic materials can be overcome (132).

Oshita and Takei (133) studied the effect of strain-rate and drawing temperature on the deep drawing of a superplastic Zn-Al alloy. It was established that there were upper and lower limits to the strain rate for deep drawing this material. High strain rates caused failure because of insufficient ductility, at low strain rates premature failure occurred because of the reduced strength. The maximum draw ratio was, however, only 2.1, even at 250°C and the optimum strain rate.

Hawkins and Belk (132) investigated the deep drawing characteristics of a zinc-aluminium eutectoid based commercial alloy (ZAM) containing additions of 1% copper and 0.1% magnesium, which exhibits superplastic properties between 230°C and 270°C. By optimising the drawing parameters, a draw ratio in excess of 3.75 was achieved.

However it is unlikely that these forming techniques could give satisfactory dimensional accuracy, and therefore machining becomes necessary. There is little information available on the machinability of the zinc-aluminium based bearing alloys.

Some Zn-Al based alloys containing the intermetallic compound Bi_2Mg_3 were reported to exhibit good machinability (134). The alloy composition range which was claimed to give the best mechanical and machining properties was Zn-22 to 27% Al-0.05 to 1.5% Cu-0.05 to 0.6 Mg-0.2 to 1.5% Bi, the ratio of Mg to Bi being adjusted to give the intermetallic compound.

A high-strength stable zinc-aluminium based quaternary alloy with excellent machinability characteristics was reported by Dollar et al (135). The alloy contained Zn, 20 to 28% Al, 0.1 to 3.5% Cu and 0.01 to 0.5% Mg.

It seems that the use of superplastic forming techniques is applicable to possible commercial bearing alloys and should result in substantial economies in production cost, if satisfactory production rates can be achieved.

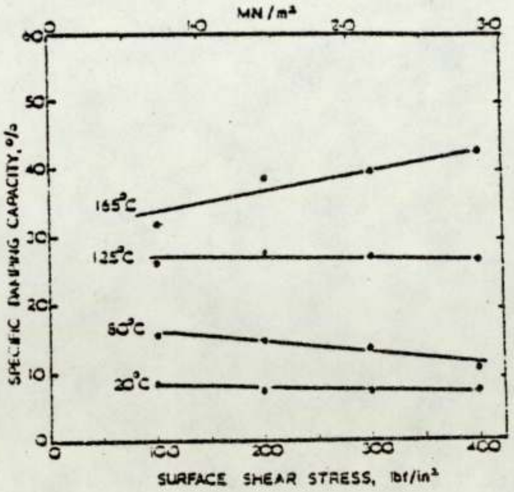

Fig. 30 Variation of specific damping capacity with surface shear stress for the as-quenched binary zinc-aluminium eutectoid alloy (after Nuttall (119))

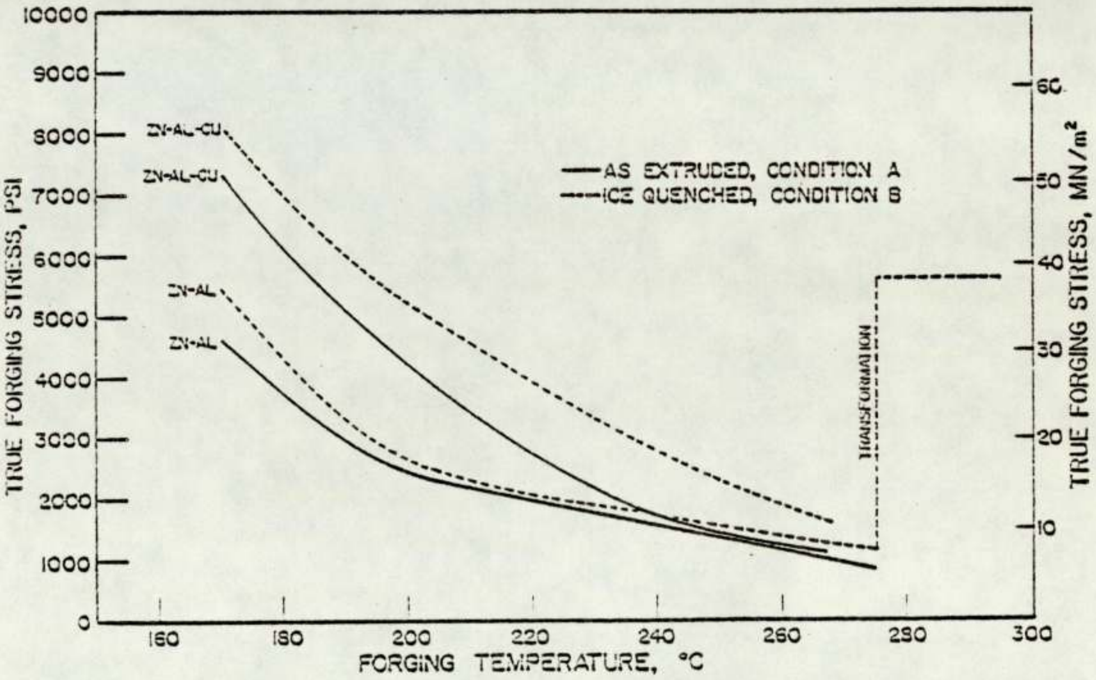

Fig. 31 True stress vs forging temperature at a forging height of ∿51 mm and a forging rate 1.3 mm/s for the alloy and condition shown (after Stewart (127))

1.7 Corrosion Behaviour of Zn-Based Alloys

Extreme corrosion in zinc-aluminium alloys usually occurs by intergranular attack, with or without an applied stress (136).

Truszkowski et al (137) made a detailed study of intergranular corrosion of as-cast and heat treated Zn-Al alloys containing 10 to 90% Zn. Corrosion in their study was measured by its effect upon impact and tensile properties. The lowest resistance to intergranular corrosion was found for the as-cast alloys containing 35 to 65% Zn, i.e. in the central part of the miscibility gap of the equilibrium phase diagram. On quench-ageing, such alloys formed fine particles of Zn within the grains and in the grain boundaries and the corrosion resistance was considerably improved.

Alloy with zinc-content in the range 65 to 82% showed little as-cast segregation in the dendrites and had good corrosion resistance. This was improved as the Zn content was increased, and improvement was attributed to the increase in the amount of fine-grained interdendritic eutectic.

Intergranular corrosion in the superplastic Zn-Al alloys has received some attention. Tennant (138) demonstrated the extreme susceptibility of the eutectoid alloy to intergranular corrosion in a steam/water environment and noted the improvement could be obtained by small copper additions.

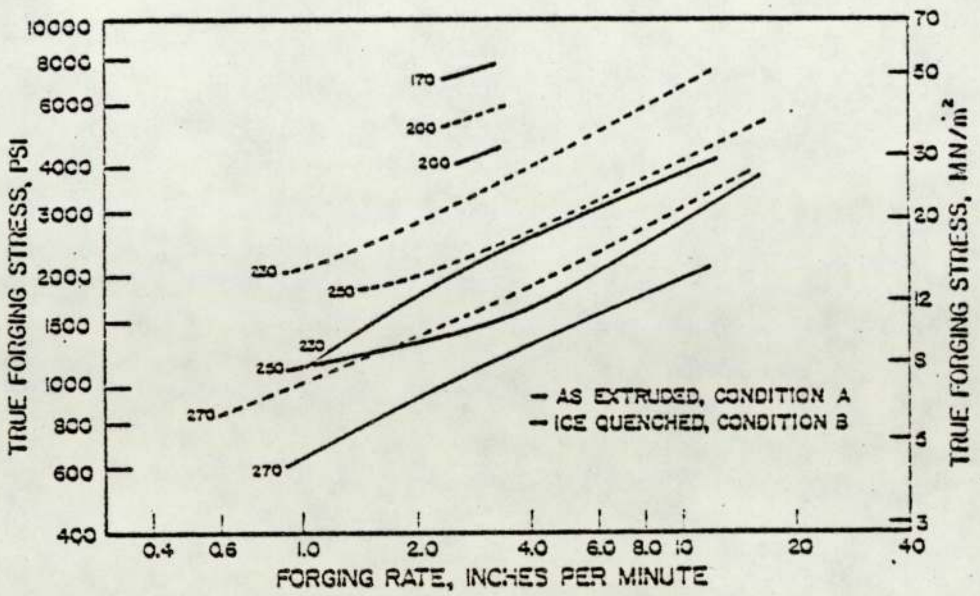

Fig. 32 True stress vs forging rate for the Zn-20% Al-2% Cu alloy at a forging height of ∿51 mm at the temperature and condition shown (after Stewart (127))

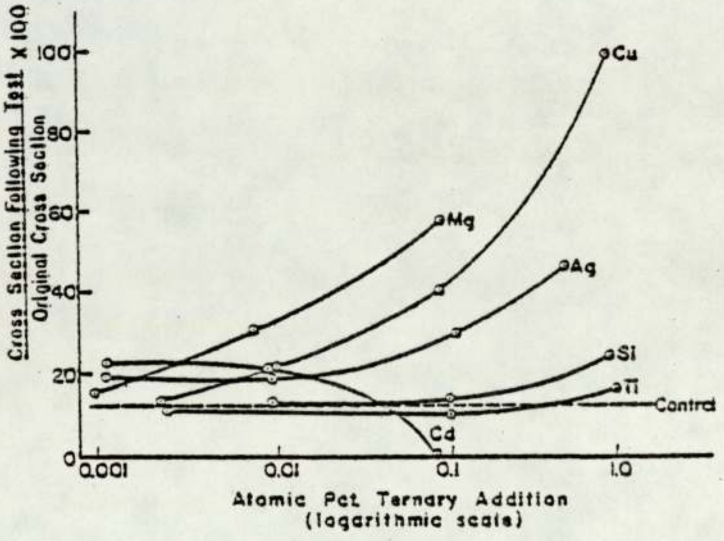

Fig. 33 Effects of ternary additions on the corrosion behaviour of the superplastic zinc-aluminium eutectoid alloy (after Dollar et al (139))

Dollar et al (139) made a more quantitative assessment of the effect of ternary additions to the eutectoid alloy. Their graph (Fig. 33) summarises the results obtained from all of the alloys evaluated. It was shown that copper additions appeared to be the best solution to the intergranular corrosion problem of the binary eutectoid alloy, and cadmium was the only ternary addition which exhibited an adverse effect to the corrosion of this alloy.

Melton and Edington (140) later investigated the effect of increasing Al content on the boiling water corrosion resistance of Zn-Al alloys with 50 to 78% Zn. They concluded that increasing the aluminium content reduced the susceptibility to catastrophic failure and gave better room-temperature strength to the alloy whilst retaining good superplastic behaviour.

The apparent discrepancy between this work and that of Truszkowshi et al is probably due to the very different physical state of the materials. Melton's alloys were solution-treated and air-cooled, stabilised at 250°C and then extruded at the same temperature. A much more uniform structure would be obtained by such treatment.

Higher zinc-alloys such as are used for gravity castings suffer seriously from corrosion when small amounts of certain impurities are present. Pollard and Edwards (141) examined the effect of Sn and Pb on the intergranular corrosion of alloys containing 88 and 96% Zn. Sn was found to be deleterous in amounts above 0.001% and Pb above 0.01%. Individually Cu and Mg were found to have no significant effect, but in combination with Sn or Pb the effect was complicated. In certain composition ranges they severely reduced the corrosion resistance.

1.8 Bearing Properties of Zinc-Based Alloys

Marczak and Ciach (142) reviewed Polish work on a series of zinc-based alloys containing approximately 40% Al and 2% Cu. It was reported that these alloys exhibited good tribological properties. These properties were attributed to the formation of aluminium and zinc oxides on the bearing surfaces. Alumina is hard and gives good wear resistance. Zinc oxide is much softer and has an hexagonal crystal structure which allows it to act as a lubricant under near-seizure conditions.

Comparative tests of Zn-38% Al-2% Cu against a Cu-30% Pb alloy showed that the zinc-based alloy had better seizure resistance at loads less than 175 N. Above this load, the better performance of the copper-lead alloy was obtained because the lead provided lubrication by melting, whereas the oxide layers were wiped off the surface of the zinc-based alloy. Good running-in properties and excellent embeddability were also demonstrated. Maximum bearing loads in clean or contaminated oils were found to lie between those for aluminium-10% tin and bearing bronze, both of which are high-performance bearing alloys.

Zinc-based alloys are susceptible to dimensional changes during service, but Marczak and Ciach developed a heat treatment which stabilises the structure, such that no distortion occurred after five years in service.

Detailed wear properties for other zinc-aluminium based alloys are not available in the literature. In a recent patent, alloys consisting of 38 to 75% Al, 0 to 4.8% Cu (with the maximum Cu content amounting to 6.5% of the Al content), 0.05 to 2.8% Ni, 0 to 0.05% Mg and balance Zn were described as suitable for bearing bushes (124).

Another alloy containing 50 to 75% Al, 0 to 3% Cu, 0.3 to 1.5% Mn, 0 to 1% Ni, 0 to 0.5% Cr and 0 to 0.1% Li was reported (143). Manganese is stated to increase the wear resistance and high-temperature hardness.

The Alzen alloys as developed by Vöest A.G. (4,5) consist of a zinc-base containing 27 to 70% Al, 0 to 5% Cu and 0 to 5% Si. It is claimed that these alloys compare well with the tin-bronzes in their general wear characteristics, and especially under poor lubrication conditions. Of this range of alloys, that containing 30% Al and 5% Cu, Alzen 305, has been manufactured in the U.K. Experience with this alloy shows that it may be substituted for bronzes in a wide range of applications. Plain bearings, hydraulic parts, spindle nuts and general construction parts represent some applications where Alzen 305 has been used extensively. It may also be used for worm wheels, roller bearing cages and track bearing plates for heavy tracked vehicles. Although successful in poorly lubricated conditions especially where seizure could cause catastrophic failure, it may also be used in well lubricated applications where it is found that under light loadings wear rate is negligible. Fig. 34 shows the comparative behaviour of Alzen 305 in a sliding wear test (4).

In use, Alzen bushings require a slightly larger clearance than for other materials since they have a high coefficient of expansion and may also suffer an expansion with time unless carefully heat treated at temperature lower than 250°C. For most applications the maximum operating temperature is about 100°C.

In another patent (144) a range of abrasion resistant zinc-aluminium based bearing alloys containing 17 to 27% Al, 2 to 4% Si, with additions of 0.1 to 0.5% Ti or 0.3 to 1.0% Zr were reported. The alloys had an average hardness of about 75 V.P.N. and coefficient of friction between 0.02 and 0.06 and exhibited very low abrasive wear.

In addition to zinc-aluminium based alloys, straight aluminium-based alloys are widely used in industry. For example an Al-11% Si alloy is produced in the form of a thin-wall steel-backed shell bearings by Glacier Metal Company. Aluminium-silicon alloys have also been used for many years as thick-wall bushings, and in some instances engine castings in Al-Si have been precision bored to form an integral bearing surface.

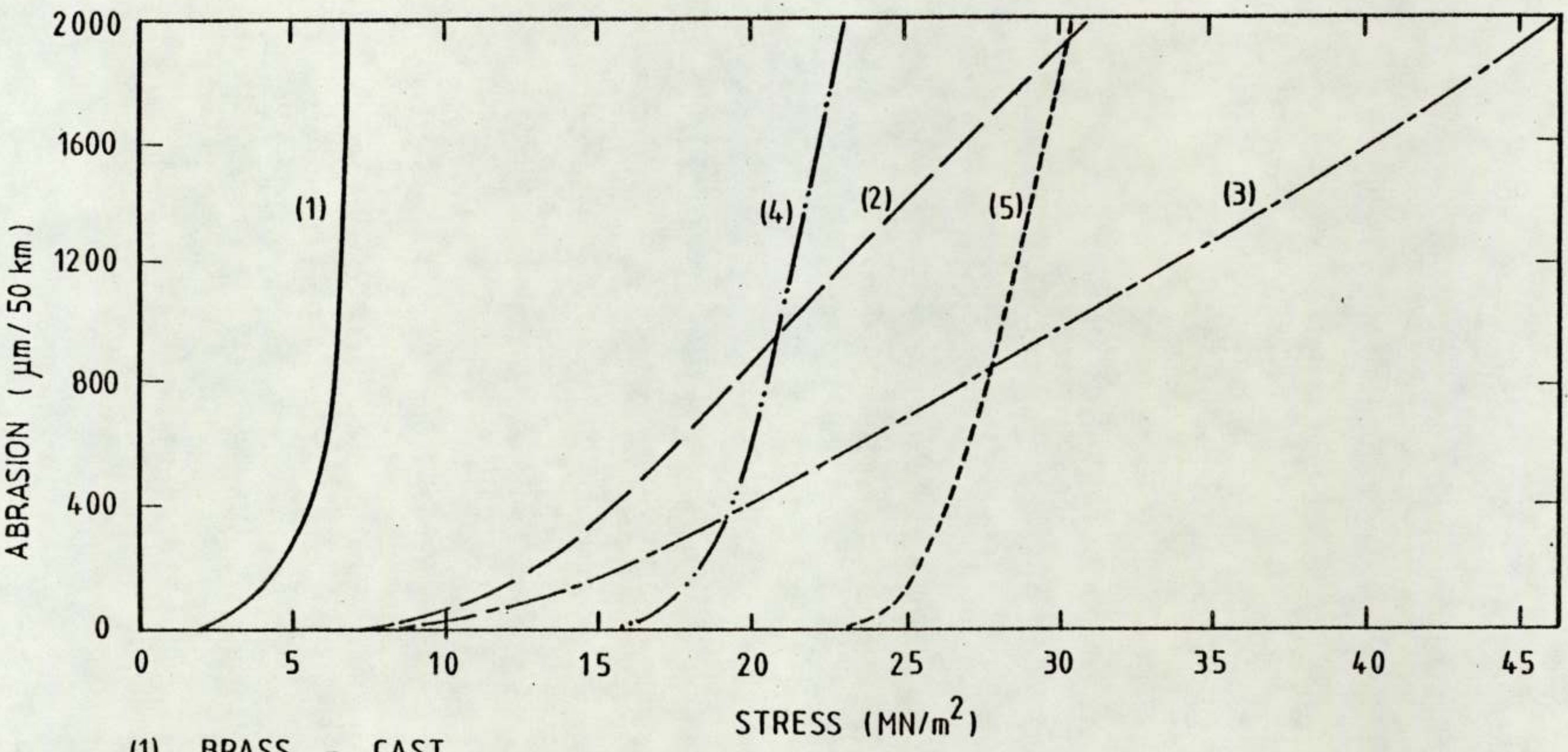

Fig. 34 Comparison of wear behaviour of Alzen 305 with bronze at a sliding speed of ∿3 m/s. (from Vöest A.G. of Austria reported by Kaye (4)).

1.9 Summary

Zinc-aluminium based alloys appear to be viable as bearing materials. Previous Polish work on a series of zinc-based alloys containing 40% Al and 2% Cu has shown that these alloys have good tribological properties mainly due to the formation of aluminium and zinc oxides.

It has been shown that the Alzen 305 type zinc-aluminium-copper alloys compare well with the tin-bronzes in their general wear characteristics. Experience with the Alzen also shows that it may be substituted for bronzes in a wide range of applications.

Some other zinc-aluminium based ternary and higher alloys containing additional elements singly or in combination, such as copper, magnesium, manganese, nickel and silicon, have also been reported to have good mechanical and bearing properties. However the detailed wear properties of these alloys are not available in the literature.

In order to assess the bearing alloys it is necessary to know their structure and properties (physical, mechanical and tribological). However there is little published work on the general properties of the zinc-aluminium based ternary alloys.

Since the structures of dilute ternary alloys are approximately similar to that of the equivalent zinc-aluminium alloys, the binary alloys aid in the interpretation of the more complex structures of the ternaries.

After a series of investigations, the equilibrium phase diagram of the binary zinc-aluminium system has finally been established. Structural changes arising from the phase transformations in this system, have been found to be dependent upon the zinc content, heat treatment temperature and cooling rate. The solid solution of zinc in aluminium extends to about 82.5% and occurs in three different isostructural modifications, designated α, α´ and β. Slow cooling of any of these single-phase alloys results in the ultimate formation of zinc and aluminium, the latter with a comparatively low-zinc content. In this case the structure mainly appears in supersaturated solid solution and on subsequent ageing the decomposition of these solutions forms a series of transitional phases. The transformation rate of these alloys on ageing increases with increasing temperature and zinc content.

Since the addition of small amounts of alloying elements does not significantly change the structure and mechanism of transformations, previous workers mainly used the binary phase diagram in order to explain their observations on the zinc-aluminium based ternary alloys. However research work on the zinc-aluminium-copper system has shown that phase transformations in this system are more complex than that of the binary system, and θ ($CuAl_2$), T´ or ε phases may be formed depending on temperature and zinc content. The equilibrium phase diagram of the zinc-aluminium-copper ternary system has not yet been fully established, however, there is considerable information now available on the low-copper part of the system due to the early German work and the work of Murphy.

The zinc-aluminium eutectoid-based alloys have been widely investigated, especially in efforts to develop superplastic alloys with adequate mechanical properties. These alloys can be made superplastic by either hot working or by quenching from above the eutectoid temperature. Superplasticity may also be obtained in alloys with a much higher aluminium content, and these have much better room-temperature strength than the eutectoid alloy.

However the binary alloys, especially the eutectoid one, have two main disadvantages:

(1) Their mechanical properties are probably inadequate for monolithic bearing applications, and

(2) they are susceptible to catastrophic intergranular failure in a steam/water environment.

As a result of a large number of investigations it has been established that the additions of other alloying elements improve the mechanical and corrosion properties of the binary alloys without significantly changing their forming properties. Copper, magnesium, manganese and nickel are claimed to be major useful alloy additions.

The presence of a third component has also a marked effect on the transformation characteristics of the binary alloys. It has been found that the alloying additions do not stabilise the β phase of the binary system, but greatly retard its transformation. Among the additional elements magnesium is found to be the most effective one in retarding the eutectoid transformation. Therefore the magnesium-containing alloys require a longer period of heat treatment in order to stabilise their structure and properties. It appears that although magnesium increases the mechanical properties of the binary alloys, it is not as beneficial as copper in the production of zinc-aluminium based bearing alloys.

The zinc-aluminium alloys in the non-superplastic condition exhibit much better mechanical properties. For example engineering properties (particularly tensile and creep) of these alloys could be substantially improved by furnace cooling after forming. This heat treatment, however, is expensive, time consuming and limits the applicability of the alloy and therefore this is not a preferable method for a large scale commercial production.

These alloys in the superplastic condition have poorer mechanical strength but advantageous forming properties. Superplasticity associated with zinc-aluminium based alloys could be used to great advantage in production provided that the properties, particularly creep properties are not adversely affected and adequate forming rates can be achieved. Therefore the addition of alloying elements is the better method of obtaining optimum properties, since zinc-aluminium based ternary and higher alloys exhibit moderate strength, good creep and corrosion resistance and advantageous forming properties.

As a result of previous development work it appears that the zinc-aluminium-copper alloys provide a cheap alternative to conventional tin or copper-based bushing materials, because of their advantages in price, availability, ease of production, formability and excellent bearing properties under poor lubrication condition. An added advantage of the zinc-based alloys is that they can be heat treated to give a useful degree of vibration damping.

However the zinc-aluminium based alloys have some disadvantages, the main problem limiting their application is the instability of some physical and mechanical properties, particularly the dimensional instability problem. The exact cause of the instability problem has not been fully ascertained, it must be explained in terms of the equilibrium phase diagram and the rate of the phase transformations on ageing. In this context a determination of the kinetics of transformation is necessary in understanding the problem.

There is no detailed information available on the properties and use of these alloys in the as-cast condition.

It is therefore, the object of the present research to investigate the structure and properties of a number of zinc-based binary and ternary alloys (Zn-Al, Zn-Al-Cu and Zn-Al-Si) in order to assess their use as bearing materials.

The structure of as-cast and heat treated alloys must be determined and correlated with strength, creep and bearing behaviour. In order to avoid the instability problem phase changes following bearing production have to be minimised. To do this the kinetics of the transformation of the β phase must be established.

It is possible that for optimum properties the alloys may be produced in superplastic condition but creep cannot be tolerated. Hence the kinetics of creep deformation at different temperatures and under various applied stresses must be investigated, so that the safe working conditions can be established.

To assess the relative bearing performance of zinc-aluminium based alloys in the as-cast and heat treated conditions compared with conventional materials a simple practical wear test must also be carried out.

2. EXPERIMENTAL PROCEDURE

2.1. Production of Alloys

Five zinc-based alloys were prepared by melting and casting. Ingots of the binary eutectoid alloy were prepared from high purity (99.99%) zinc and aluminium only.

To prepare the alloy the calculated amount of aluminium was first melted in either a fireclay or alumina crucible, in a gas-fired furnace at about 700°C. After melting the aluminium the temperature was dropped to approximately 600°C and zinc was added accompanied by vigorous stirring. 2% excess zinc was added to the melt in order to meet losses due to volatilization. The melt was then degassed using a commercial degasser (Zincrex) again accompanied by vigorous stirring.

The resultant alloy was then chill-cast into mild steel moulds as either round bars or flat ingots. The pouring temperature was about 600°C.

The ternary alloys were cast in the form of 600 g ingots.

To produce the ternary zinc-aluminium-copper alloys a pre-prepared master alloy of Cu-50% Al was melted in a fireclay crucible in a gas-fired furnace at about 900°C. The aluminium was added to the melt accompanied by vigorous stirring. At this stage the melt was degassed using only the proprietary Foseco degassing compound. For these alloys the melt temperature was dropped to approximately 700°C and the zinc was added, again with vigorous stirring. Again 2% more zinc was added in order to meet the losses of zinc during melting. The melt was then degassed using Foseco and Zincrex.

The resultant alloy was chill-cast into mild steel moulds as either round bars or flat ingots. Again the pouring temperature was about 600°C. The three different zinc-aluminium-copper alloys were produced in this way.

One zinc-aluminium-silicon alloy was produced for this investigation. Again 600 g ingots of the alloy were cast. A master alloy of Al-22.2% Si was first prepared from high purity (99.99%) aluminium and silicon. For each ingot 270 g of master alloy was required and this was melted in a crucible at about 900°C in a gas-fired furnace. On melting the temperature was dropped to approximately 700°C and the zinc added to the melt. Again 2% excess zinc was added to the melt. The melt was then degassed and stirred vigorously.

The resultant alloy was chill-cast into mild steel moulds and a number of round and flat shaped ingots of the alloy were produced.

The moulds were kept dry and cold (room temperature) for each cast.

2.2 Heat Treatments

The zinc-based binary and ternary alloys were investigated in the as-cast and heat-treated conditions. Heat-treated alloys were first hot-rolled at 350°C (~0.9 Tm) to an approximately 20% reduction in diameter or thickness in order to facilitate diffusion of the alloy constituents and hence to promote uniformity of structure. They were then homogenized in an argon atmosphere at 350°C for 48 hours and furnace cooled to room temperature to eliminate microsegregation and produce a more uniform structure. The temperature of the furnace used for both hot-rolling and homogenization treatments was maintained within an accuracy of ± 2°C.

Machining was carried out on the homogenized and furnace cooled alloys to produce the required test specimens.

To obtain the high-temperature phases, the specimens were solution-treated at 350°C for 3 hours and immediately quenched into cold water. Again the temperature of the furnace was controlled to ± 2°C.

Ambient temperature ageing was carried out in air. Heat-treatments at 60°C, 80°C, 100°C and 150°C were carried out in thermostatically controlled oil-bath or fluidised-bed furnaces controlled to ± 2°C. Boiling water was also used for short time heat-treatments at 100°C. The 200°C heat-treatment was carried out in an air-circulation muffle furnace controlled to ± 2°C. Following ageing the samples were quenched into cold water.

2.3 Metallography

2.3.1 Optical Microscopy

Specimens from each alloy in different conditions were examined by optical microscopy to study the structures and the effect of heat-treatment.

In order to avoid any structural change produced by heating during hot mounting, the specimens were embedded in Araldite. All specimens were ground and polished by standard metallographic techniques on silicon carbide papers to a 6 µm finish followed by hand polishing on a soft cloth (sylvyt) with Silvo.

Zinc-based binary and ternary alloys required a long, careful hand polishing in order to obtain a scratch-free mirror surface. Silvo was found to be quite a suitable polishing compound for most of these alloys in most conditions.

Alloy 4B (Zn-38% Al-2% Cu) in the as-quenched condition proved to be particularly difficult to prepare for examination, as all polishing compounds tried produced chemical attack giving stress-corrosion problems, and releasing particles from the sample which caused further scratches on the surface.

However it was found possible to produce satisfactory specimens by electropolishing in a solution of 15% perchloric acid in butoxyethanol or methyl alcohol at about -50°C.

The structure was revealed by etching the polished specimens in 1% Nital for about 5 to 10 s. depending on the composition and condition of the alloy. The specimens were then examined under the light microscope and microphotographs were taken on either Reichert or Vickers projection microscopes.

2.3.2 Electron Microscopy

To obtain better resolution of fine structures than was possible with the light-optical microscope some work was carried out on polished and etched samples in the scanning electron microscope. The specimens were mounted in conducting bakelite or a current leak-path was made with Aquadag. The instrument used was a Cambridge Instruments SEM 150, operated at a beam energy of 20 keV.

The SEM 150 was also used to examine the fracture surface of mechanical test pieces after failure. To do this the fracture sections were cut from the gauge length and ultrasonically cleaned. The specimens were then stuck on aluminium stubs with double sided adhesive tape and a conducting path made with Aquadag.

Detailed examination of the structure of these alloys was made in the transmission electron microscope using thin foils. The thin foils were prepared in three stages:

(1) A cylinder 3 mm in diameter was removed from the specimen by spark-erosion in a Servomet spark-erosion machine. This was then cut into thin slices again by spark-erosion.

(2) The slices were wet-ground by hand on 600 mesh paper to <100 μm thickness, grinding was carried out on both sides alternately, using a small jig.

(3) The circular foil-blank so produced was electropolished in a disc-jet machine using a potential of 15 to 30 V depending on the specimen. Twin jets acting on both sides of the specimen eroded a concave hollow on each side. When penetration occurred, usually near the middle, the machine was switched off to stop the process. The electrolyte used was 15% perchloric acid in dibutoxylthylene and it was kept below -20°C and continuously pumped to the jet machine during polishing. This was found a suitable method as the window technique did not produce satisfactory specimens. Some of the thin-foils were prepared by an ion-beam etching technique; this produced foils of more uniform thickness, but was very slow.

Thin foils were examined in two different transmission electron microscopes, a JEOL 100B at 100 keV and a high-voltage AEI EM7 at 1 MeV. In the former penetration of rather thick-foils was poor but thin-foils produced reasonably good results.

2.4 Investigation of Transformation Behaviour on Quench-Ageing

Three principle techniques were used to study the transformation of the high-temperature phases during ageing. These were metallography, hardness testing and quantitative X-ray diffraction. In each case measurements and examinations were made at room temperature after ageing for a certain time at the chosen temperature. The metallographical examination was carried out as described earlier in (2.3).

2.4.1 Hardness Testing

Flat-shaped hardness specimens with parallel surfaces were machined from the homogenized alloys. They were then ground to 6 μm finish and polished using either Silvo or diamond polishing compounds. Heat-treatment was carried out as described earlier, but the specimens were lightly repolished after heat-treatment before the hardnesses were determined. The Vickers hardness was measured for different time intervals during ageing at chosen temperatures (i.e. room temperature ($\sim 20^{\circ}C$), $60^{\circ}C$, $100^{\circ}C$, $150^{\circ}C$ and $200^{\circ}C$). A 5 kg load for the binary and a 10 kg load for the ternary alloys were used.

Usually four specimens were used to determine the hardness change at each temperature. At least five measurements were taken for each time and the mean values of hardness and standard deviation were calculated.

The data obtained in this manner were then plotted to show the hardness change with time for each alloy at each ageing temperature.

2.4.2 Quantitative X-ray Diffraction

A quantitative X-ray diffraction technique was used to study the transformation characteristics of the metastable high-temperature phases in quenched zinc-based binary and ternary alloys during isothermal ageing. The metastable phases are β (1B and 2B), $\beta+\varepsilon$ (3B) and α (4B).

To do this the crystal structures and lattice-parameters of these phases were first determined by an X-ray diffraction technique. A Philips diffractometer utilising Ni-filtered CuK_α radiation with a wavelength of $\lambda = 1.542$ Å was used for the work.

Samples were prepared in the form of discs 3 mm thick and 10 mm diameter. These were ground before heat-treatment. Following quenching into cold water, the discs were polished on 600 grade paper then placed immediately in the diffractometer which was scanned through a suitable range of angle usually from 20° to 180° 2θ. The diffraction peaks of the alloys were recorded on a chart. The Bragg angle (2θ) and Miller indices ($hk\ell$) of each diffraction peak were measured and the crystal structures were determined by standard X-ray analysis.

Lattice parameters were calculated using the data obtained from each peak. An extrapolation technique was used for data from cubic crystals to determine the lattice parameter to high precision. This involved plotting "a"-value deduced from each peak for angles (θ) larger than 60°, versus either $\cos^2\theta$ or $\sin^2\theta$ and extrapolating the graph to $\theta = 90^\circ$.

These results allowed the selection of the appropriate angular range corresponding to the diffraction peaks suitable for following the transformation of the metastable high-temperature phases on quench-ageing.

X-ray specimens again 3 mm x 10 mm discs were prepared, heat-treated and quenched. They were then quickly polished on 6 μm grade paper and placed in the diffractometer which was programmed before the test. The diffractometer was automatically scanned at a fixed speed through a pre-determined range of angle corresponding to certain diffraction peaks of the phases present, and this was repeated for a number of scans, until the transformation was completed. Account was taken of the elapsed time between quenching and the first scan.

To follow the transformation during ageing at temperatures above ambient, the specimens after quenching were placed in a furnace which was maintained at a constant temperature. After ageing for a selected period of time the specimens were removed from the furnace and plunged into cold water to stop the reaction. They were then quickly placed in the diffractometer which was again automatically scanned through a pre-determined range of angle. As soon as scanning finished the specimen was taken out and put in the furnace again for a further period of ageing. This procedure was repeated until decomposition was completed.

An oil-bath and boiling water were used for ageing treatments above ambient, and these were kept close to the diffractometer to minimise room-temperature ageing during the test. The temperature of the oil-bath was measured with a potentiometer and three thermocouples, connected to different zones inside the bath, and an accuracy of ± 2°C was achieved.

The data obtained from both strip charts and counter printouts were used to determine the fraction transformed factors (f). The areas of the diffraction peaks were measured with a planimeter on the chart and the changes in the area due to transformation of the phases were determined. Integrated intensities of the diffraction peaks were also calculated from the data print-out, and hence the change in the intensities with transformation time were determined.

2.5 Investigation of Mechanical Properties

2.5.1 Notched-Bar Impact Test

The notched-bar impact tests were carried out in order to determine the impact strength and influence of temperature. Alloys in the as-cast and heat-treated conditions were tested on a standard Charpy machine.

V-notched Charpy test pieces were produced from the homogenised and cast alloys by machining accurately to the standard dimensions.

The homogenised specimens were solution-treated and quenched. They were then aged at 100°C for one hour in boiling water and plunged into cold water for one minute to stop the reaction.

To obtain the test temperatures the specimens were treated in the following ways:

Temperature (°C)	Heat-transfer Medium	Time of stay (min)
-196	Liquid nitrogen	20
0	Ice + distilled water	20
∿20(Room temperature)	Air	30
100	Boiling water	10
200	Air in re-circulating furnace	10

The energy of fracture was measured at each temperature in order to determine the variation of energy absorbed with temperature.

It was found that the energy absorbed as measured by the standard Charpy machine for alloy 3B was very low, approaching zero, but the variation with temperature was estimated from the scale. Therefore, to determine the values of energy absorbed for alloy 2A and 2B a smaller capacity Hounsfield impact machine was used. The shape and dimensions of these test pieces were different from those of standard Charpy. The energy values obtained in this way were still very low and the variation with temperature was quite small.

2.5.2 Creep Testing

Creep tests were performed with the alloys in the as-cast and heat-treated conditions. The heat-treatment was 2 hours ageing at 200°C. The tests were carried out at various temperatures from 60°C to 180°C (0.5 to 0.7 Tm) at a number of different stress-levels.

The alloys were machined to accurate dimensions in order to produce suitable test pieces. A creep test piece with 10 mm diameter and 50 mm gauge-length is shown in Fig. 35.

Suitable weights were prepared for the creep machine. These were calculated by taking into account the Lever arm ratio (L.A.R.) of the machine, in order to obtain the selected load and therefore stress level on the gauge-length of the test piece.

The calibration for the balance of the creep machine was checked before each test.

The temperature of the specimen inside the furnace was measured by a potentiometer using chromel/alumel thermocouples. These were attached to three different points between the ridges of the sample in order to check that there was no temperature gradients along the gauge length. Temperature changes were limited to a maximum of ± 2°C during the test by careful setting and adjustment of the furnace and also by allowing a reasonably long time for the temperature to stabilise.

Creep extensions were measured by transducers located in extensometers which were attached to the ridges on the specimens, as shown in Fig. 36. The transducers were connected through a unitmeter to a chart recorder for enabling continuous record of extension to be taken. Both the transducers and the recorder were calibrated for each test. The creep extension during the test was continuously recorded by selecting suitable recorder scale and adjustment of the whole measurement system.

Creep strain and corresponding time values were obtained from the recorder chart and therefore the creep curves (creep strain versus time) for each alloy at a selected temperature and stress were determined.

Total creep extensions (up to fracture) of some of the heat-treated alloys could not be determined accurately as they exceeded the range of the measurement system. However this was not significant for the purpose of this investigation, since the interest was principally in the secondary creep region.

2.5.3 Hot-Tensile Testing

Tensile tests were carried out mainly to determine the proof-stress ($\sigma_{0.05}$) and friction-stress (σ_o) for the correlation with the secondary creep rate ($\dot{\varepsilon}_s$) of these alloys. The tests were performed at various temperatures on a Mand tensile machine at a cross-head speed of 6.83×10^{-3} mm/s, on specimens similar to those used for the creep work.

The temperature of the specimen was measured with a potentiometer and three chromel/alumel thermocouples which were attached to the gauge-length. Temperature was controlled to $\pm$ 3^{o}C during the test.

Extension measurement was made continuously by extensometer, transducer and recorder set as described earlier for creep. Another chart recorder was used to determine the applied loads continuously and therefore the corresponding stress values.

Applied stress and corresponding strain values were calculated from the data obtained from both charts and finally engineering stress-strain (σ vs. ε) curves of the alloy at each test temperature were determined.

The friction-stress was measured at appropriate creep temperature using the stress-relaxation test technique. To do this, the specimen was deformed in the tensile machine at a constant cross-head speed of 6.83×10^{-3} mm/s. until a steady stress level was reached. The crosshead was then stopped to hold the specimen length constant and the ensuing relaxation of the load was monitored. The stress was then observed to decay to a limiting value which was taken as the friction stress (145).

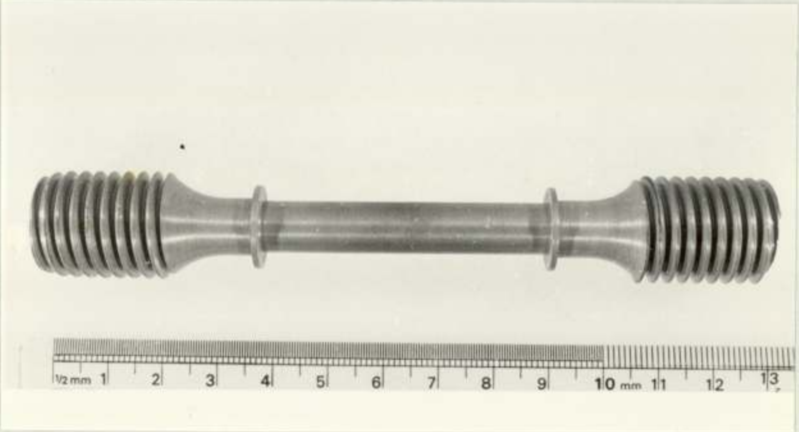

Fig. 35 A creep specimen

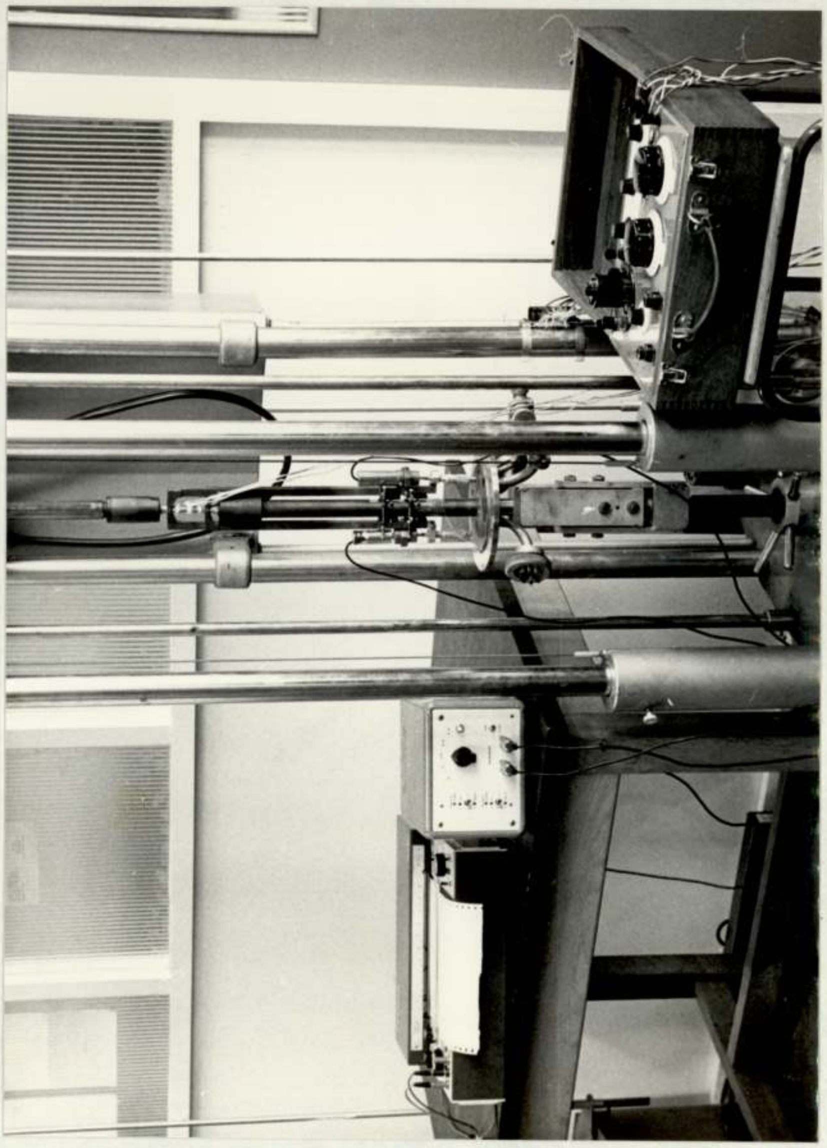

Fig. 36 Creep test apparatus

2.6 Wear Test

The zinc-aluminium based alloys in the as-cast and heat-treated conditions were tested as bushings in order to determine their bearing properties.

To do this the valve rockers of an 850 cc four-cylinder, water cooled engine were bored out and bushed with some of the experimental alloys and fitted to a high mileage works test car. This application was chosen because a variety of materials could be tested together under closely similar conditions. For comparison purposes two of the eight rockers were furnished with cast iron and phosphor-bronze. The rockers operated on a hardened and ground steel shaft, under a copious flow of lubricating oil, at temperatures not higher than 100°C.

The heat-treated alloys were rolled, homogenized, solution-treated and quenched, then aged at 150°C for 2 hours in an air-circulating furnace in order to complete the decomposition process. Temperature variations during the heat-treatments were limited to a maximum of ± 2°C.

Accurately machined bushes were produced from these alloys and were press-fitted in the rockers as seen in Fig. (37a). They were then ultrasonically cleaned and accurately weighed.

The rockers were placed on the shaft (Fig. 37b) and the shaft assembly was fitted in the engine of the test car. The lubricant used for the test was a normal SAE 20/50 engine oil to BS 1905-1965.

After running the car for several thousand kilometres, the rocker shaft assembly was taken out and dismantled. Each rocker complete with its bush was again ultrasonically cleaned and accurately weighed. This process was repeated a number of times up to a certain mileage. As a result of these measurements the wear as a weight loss, at a certain running distance was determined. This wear includes a very small amount of wear of rocker tips which is assumed to be the same for all rockers.

(a)

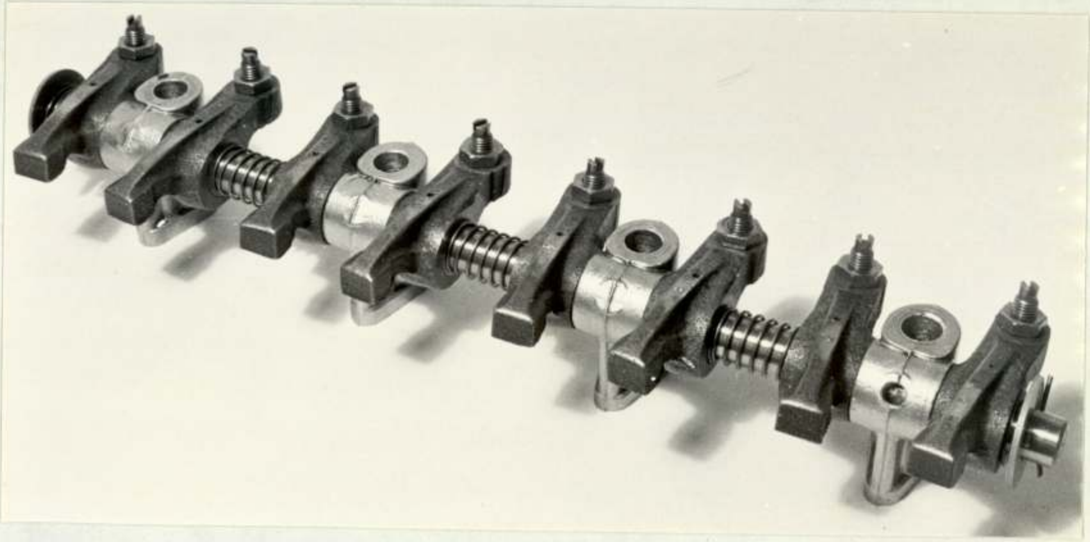

(b)

Fig. 37 (a) A rocker fitted with experimental alloy bush

(b) Bushed rockers assembled on the shaft

3. EXPERIMENTAL RESULTS

3.1 Chemical Composition of the Alloys

The composition of the cast alloys was determined by a wet-chemical method and by electron-probe microanalysis. The results are given in Table 2.

TABLE 2

Composition of the Alloys

Method of Analysis	Composition (wt.-%)					Alloy Number	
	Zn	Al	Cu	Si	Other	As-cast	Heat-treated
N	78	22				1A	1B
W	77.8	22.2					
E	77.4	22.6					
N	70	27	3			2A	2B
W	69.9	27.1	3.0				
E	69.6	27.3	3.1				
N	77	19	4			3A	3B
W	76.8	19.3	3.9				
E	76.3	19.9	3.8				
N	60	38	2			4A	4B
W	60.1	38.0	1.9				
E	59.9	38.1	2.0				
N	55	35		10		5A	5B
W	56.0	35.6		8.4			
E		87.7		11.5	Fe 0.4 Mg 0.4	6	

N : Nominal composition, W : Wet-Analysis, E : Electron-probe microanalysis.

Alloy 5 could not be analysed accurately by electron-probe to determine the overall composition since the silicon was present as large discrete particles in the zinc-aluminium matrix. An overall measurement could be obtained by using a line or area scan, but since the correction procedures are not applicable to coarse mixtures of separate phases a true concentration cannot be calculated.

The composition of the high-temperature solid solutions in the quenched and aged condition was mainly determined by electron-probe microanalysis and the results are given in Table 3. The α/α' and β phases decomposed into a multi-phase mixture before analysis but this was so fine (∿1 μm) that the correction procedure was applicable.

TABLE 3

Composition of the heat-treated alloys

Alloy	Phase	Composition
1B	β	79.9% Zn - 22.1% Al
2B	β	69.8% Zn - 27.1% Al - 3.1% Cu
3B	β	80.0% Zn - 18.0% Al - 2.0% Cu
	ε	83.4% Zn - 16.6% Cu
4B	α/α'	59.9% Zn - 38.1% Al - 2.0% Cu

3.2 Metallography

3.2.1 Alloy 1 (Binary Zinc - 22% Aluminium)

In the as-cast condition the binary alloy consisted of aluminium-rich cored dendrites with a zinc-rich interdendritic phase as a semi-continuous network as seen in Fig. 38. This undesirable metallographic structure was completely eliminated by homogenization at 350°C for 48 hours. The homogenized structure after furnace cooling to room temperature had a lamellar morphology, Fig. 39. The packets of lamellae appeared to be nucleated on prior β grain-boundaries and grew into the grain. β grains were not entirely replaced by the lamellar products, the grain centres apparently decomposed into a non-lamellar mixture of zinc and aluminium. A high magnification micrograph, Fig. 40, shows branched, irregular lamellae, particulate products, and some unresolved material.

Air cooling following homogenization and a further 3 hours solution treatment at 350°C produced a much finer lamellar product, Fig. 41. Again in some areas pronounced degeneration of the lamellae was seen as in Fig. 42.

Isothermal transformation at 200°C following solution treatment produced more degenerate lamellae than for air cooling. Fig. 43 is an optical micrograph of a typical area, and Fig. 44 shows the same structure in secondary electron image mode in the scanning electron microscope.

Quenching and ageing at room temperature produced an entirely non-lamellar structure, Fig. 45. Ageing at 60°C and 200°C, Figs. 46 and 47, produced successively coarser but otherwise identical structures. Increasing the time at 200°C likewise coarsened the structure, Fig. 48.

Transmission electron microscopy of thin-foils of the material aged at room temperature showed that the fine product barely resolvable in the optical microscope is a mixture of zinc and aluminium grains. The grain size was in the range 90 to 200 nm with some particles an order of magnitude smaller, Fig. 49. The structure was essentially the same as that produced by ageing at higher temperature.

3.2.2. Alloy 2 (Ternary Zn - 27% Al - 3% Cu)

Alloy 2 in the as-cast condition possessed a cored-dendritic structure. This comprised a zinc-rich interdendritic eutectic phase mixture which surrounded the aluminium-rich dendrites as shown in Fig. 50. The light-coloured eutectic mixture consisted of zinc and ε phase, possibly with β solid solution which decomposed during cooling.

The dendritic structure of this alloy was fully eliminated by the homogenization at 350°C for 48 hours. As observed in alloy 1, the homogenized structure after furnace cooling had a lamellar morphology, Fig. 51. The lamellae were again nucleated on the prior β grain-boundaries and grew into the grains. This micrograph shows the general structure as consisted of different lamellar products; some straight lamellae with some branching and others showing pronounced curvature. Solution treatment followed by air cooling produced a similar but much finer lamellar product as shown in Fig. 52.

Isothermal transformation at 200°C for one hour, following the solution treatment produced more degenerated lamellae than for slow cooling. Fig. 53 is an optical micrograph of a typical area, and the SEM micrograph, Fig. 54, shows the same structure at higher magnification.

Solution treatment followed by quenching and subsequent ageing for 2400 hours at room temperature produced a typical equiaxed and fine-grained structure as shown in Fig. 55. Increasing the ageing time to 22000 hours showed no further change. Ageing at 200°C coarsened the structure without changing its morphology, Fig. 56. Increasing the ageing time at 200°C greatly coarsened the structure and small lamellar groupings of zinc and aluminium grains were also observed as seen in Fig. 57. In Figs. 55-57, but especially in Fig. 57, small, rounded grains are visible which appear to be different to the α and η phases. These are not visible in the binary alloys and are presumed to be copper-rich.

Transmission electron microscopy of the thin foils of the homogenized and furnace-cooled alloy showed the general structure consisting of straight lamellae with loops and branches, (Fig. 58). The transmission electron micrograph of Fig. 59 shows the different morphologies of decomposition products on slow cooling. The large particles embedded in the zinc-aluminium lamellae may be ε phase, zinc or aluminium, although no useful diffraction patterns were obtained.

An electron micrograph from a thin foil of the quenched alloy aged at room temperature for approximately 5 hours, showed zinc and aluminium phases with possibly small precipitate particles, Fig. 60.

Ageing at 200°C for 2 hours produced a mixed structure with small precipitate particles as seen in Fig. 61. A high magnification micrograph, Fig. 62, shows zinc lamellae growing from one of the particles. The mixed lamellar and equiaxed structures suggest that zinc forms by continuous and discontinuous modes of decomposition during transformation of quenched β phase on isothermal ageing at higher temperatures, i.e. 200°C.

3.2.3 Alloy 3 (Zn - 19% Al - 4% Cu)

In the as-cast state electron-probe microanalysis showed that alloy 3 consisted of cored, aluminium-rich dendrites (Fig. 63a) and a zinc and copper-rich interdendritic phase (Fig. 63b). A typical light-optical micrograph of the structure is shown in Fig. 64. The small round particles were identified by electron probe microanalysis and X-ray diffraction as ε phase.

Homogenization at 350°C fully eliminated the cored cast structure of Fig. 64. On furnace cooling after homogenization a lamellar matrix was produced with large ε phase particles in irregular rows, corresponding to the copper and zinc-rich interdendritic regions of the prior cast structure, Fig. 65.

Solution treatment followed by air cooling produced a much finer lamellar structure similar to that of Fig. 52 but with rounded ε particles embedded in it.

Isothermal ageing at 200°C for one hour following the solution treatment produced finer but more degenerate lamellar structures, as shown in Fig. 66.

Solution treatment followed by quench-ageing at room temperature produced a visible decomposition product for light microscopy only after about 700 hours. After 4400 hours a non-lamellar fine-grained matrix structure was produced as in Fig. 67.

Ageing at 60°C produced a similar fine-grained structure as in Fig. 68. Increasing the ageing temperature and time produced coarser structures as shown in the optical micrographs of the specimens aged at 200°C for 20 hours and 88 hours (Figs. 69 and 70).

The above optical micrographs showed that the ε phase of this alloy was present in all conditions examined except for ageing at high temperatures, i.e. 200°C, for long times, when it gradually dissolved.

The transmission electron micrograph of Fig. 71 shows the general structure of the homogenized alloy after furnace cooling at higher magnification.

A TEM micrograph of Fig. 72 obtained on the quenched alloy after ageing at 200°C for 2 hours, shows the general structure containing mixed zinc and aluminium grains. Another TEM micrograph, Fig. 73 taken on the same thin-foil showed branched and bifurcated lamellae in small patches.

3.2.4 Alloy 4 (Zn - 38% Al - 2% Cu)

The cast structure of alloy 4 consisted of aluminium-rich dendrites and zinc-rich interdendritic material as seen in Fig. 74. This cored structure is essentially the same as the cast structures of alloys 2 and 3, except that there is a greater volume fraction of dendrites.

The dendritic structure of this alloy was eliminated by homogenization at 350°C for 48 hours. Furnace-cooling following the homogenization, produced small rounded or U-shaped particles as seen in Fig. 75. Fig. 76 shows the same structure in secondary electron image made in the SEM. This is a quite different structure from the lamellae obtained on furnace cooling of alloys 1, 2 and 3.

The transmission electron micrograph of Fig. 77 shows the structure of the homogenized and furnace cooled alloy in detail. Light particles are aluminium-rich α phase and dark particles are zinc-rich η phase, formed by eutectoidal decomposition of the α' and β solid solutions. Another transmission electron micrograph, Fig. 78, obtained from the same thin foil at higher magnification shows the same structure with some precipitate particles. Some of the precipitate particles in the α phase are angular, and have been formed by precipitation in the solid state. Other particles are plate-like but may have been formed by precipitation or by a co-operative growth mechanism.

Isothermal transformation at 200°C for 2 hours following solution treatment produced a mixed lamellae structure consisting of very fine and large degenerate lamellae, Fig. 79.

Solution treatment followed by water quenching produced a large-grained α/α' solid solution, as shown in the optical micrograph of Fig. 80. On ageing this produced fine products which could not be resolved in the optical microscope but clearly represented decomposition initiated at grain boundaries and within the grains. Fig. 81 shows the product formed after 190 hours at room temperature. However transmission electron micrograph of Fig. 82 showed that 4400 hours ageing of the quenched alloy at room temperature produced very fine zinc or intermetallic precipitate particles 100-150 nm in diameter. The diffraction pattern obtained from the above area showed only the f.c.c. structure of the aluminium matrix in a $<1\bar{1}2>$ zone. An electron diffraction pattern from a similar area of the same foil is shown in Fig. 83, with its indexing. The major reflections are from two aluminium matrix zones separated by an angle of about 6.5 degrees signifying a slightly curved crystal lattice. The third zone represented a crystal with interplanar spacings of 2.10, 2.10, 1.37 and 1.61 Å. These correspond to interplanar spacings of the ε phase ($CuZn_5$). The interplanar angles confirmed that this was indeed ε phase with zone axis $<12\bar{1}>$. A stereographic projection showing the aluminium zones and the ε phase zone was drawn and is shown in Fig. 84. The projection shows that the orientation relationship between the ε phase and aluminium matrix is given within the accuracy of measurement by:

$$[0\bar{1}0]_\alpha // [0001]_\varepsilon$$

$$(001)_\alpha // (1\bar{1}00)_\varepsilon$$

$$(100)_\alpha // (\bar{1}\bar{1}20)_\varepsilon$$

Ageing of the quenched alloy at 200°C for 10 minutes initiated precipitation on grain boundaries and on certain intragranular sites, Fig. 85. After 2 hours a mixed structure consisting of cellular material extending from the grain boundaries and precipitate particles in the remaining regions is seen in Fig. 86. The morphology of this mixture varies from place to place, but coarse aggregates appear to be associated with the α grain boundaries and a finer mixture of plates or needles of zinc and aluminium fills the grain interiors as seen in the transmission electron micrograph of Fig. 87. This micrograph shows plates which are thickened locally into sub-angular masses and form zig-zag semi-continuous chains in three dimensions.

In Fig. 88 a heavy grain-boundary precipitate borders a fine intragranular array of short needles, arranged in two or three principle directions. This does not appear to be the same product in a different orientation. Fig. 89 shows the fine structure of Fig. 86 together with coarse lamellae very similar to that seen in the eutectoid alloy. Rounded or subangular particles within the aluminium-rich phase are a distinguishing feature however. These may be copper-rich intermetallic particles or zinc. No diffraction pattern could be obtained from them to provide a positive identification.

3.2.5 Alloy 5 (Zn - 35.6% Al - 8.4% Si)

Alloy 5 in the as-cast condition exhibited a three-phase structure which consisted of a cored aluminium-rich matrix, interdendritic zinc and large primary silicon particles as seen in Fig. 90. It is a hypereutectic silicon alloy, and quite different from the binary aluminium-silicon alloy of the same silicon content.

The cored cast structure of the matrix was eliminated by homogenization at 350°C for 48 hours. Furnace-cooling of the homogenized structure produced small rounded or U-shaped particles of zinc and aluminium, Fig. 91, as observed with Alloy 4 in the same condition. Heat-treatment appeared to have no effect on the large silicon particles which were unchanged.

Alloy 1 (Zn-22%Al)

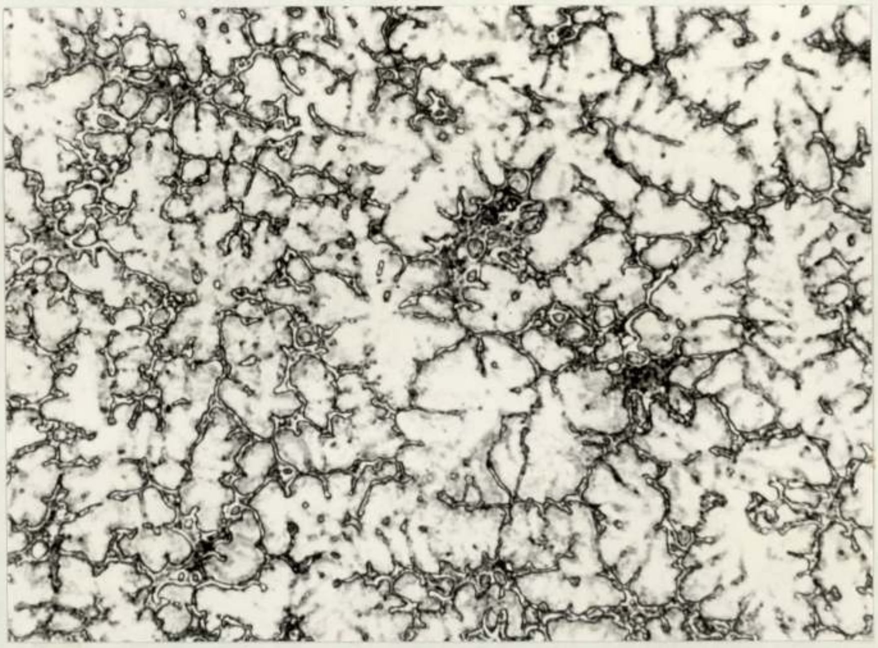

Fig. 38 Cored-dendritic structure of the as-cast binary eutectoid alloy (1A) x 280

Fig. 39 Optical micrograph showing the lamellar structure produced by furnace cooling after homogenization of alloy 1 x 280

Alloy 1 (Zn-22%Al)

Fig. 40 Optical micrograph showing the branched, irregular lamellae particulate products in the furnace-cooled alloy x 1600

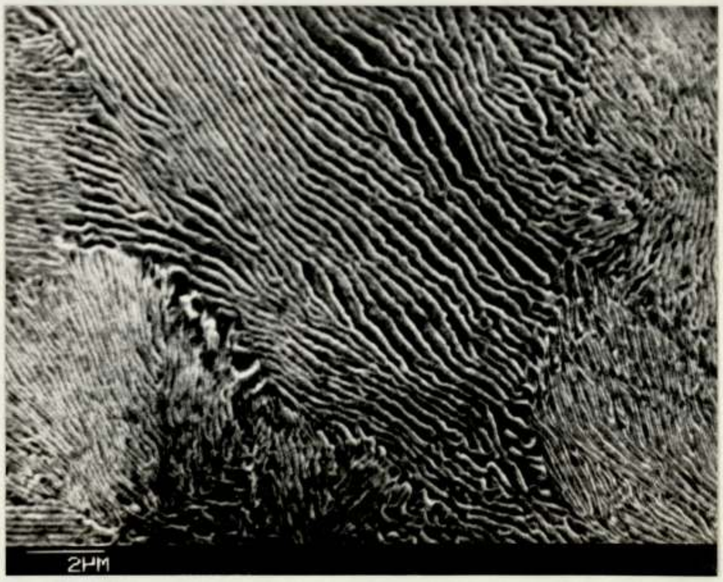

Fig. 41 Lamellar structure produced by air cooling after solution treatment

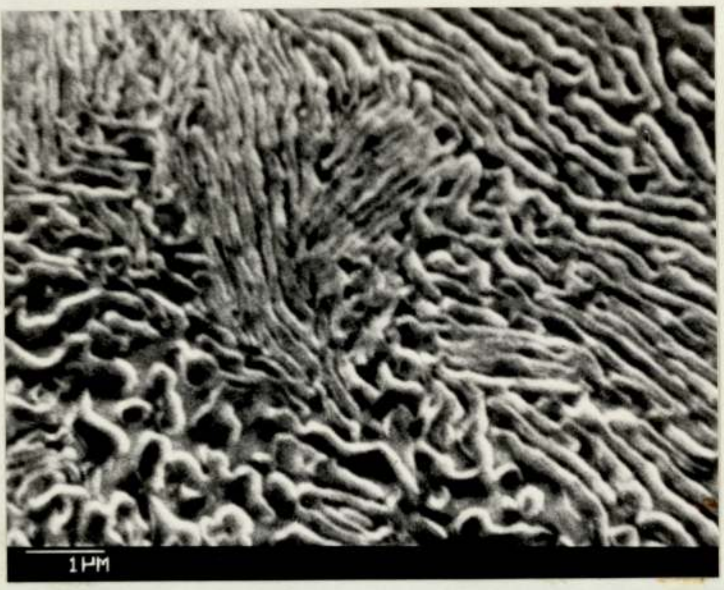

Fig. 42 Degenerate lamellar products in the air-cooled alloy

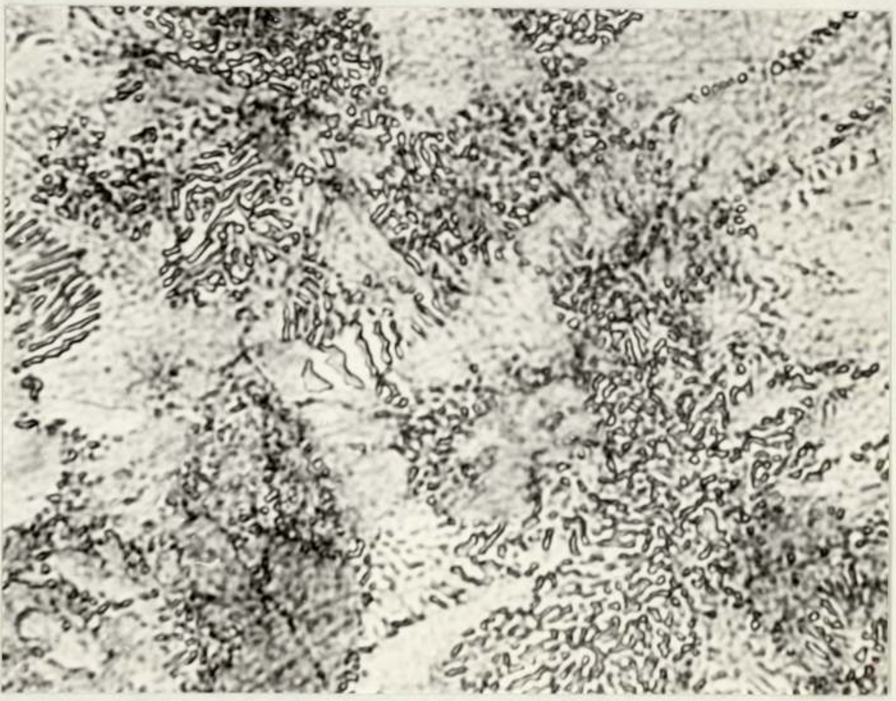

Fig. 43 Optical micrograph showing the degenerate lamellar products produced by isothermal transformation at 200°C for one hour following the solution treatment x 1200

Alloy 1 (Zn-22%Al)

Fig. 44 Scanning electron micrograph from the isothermally transformed alloy at 200°C

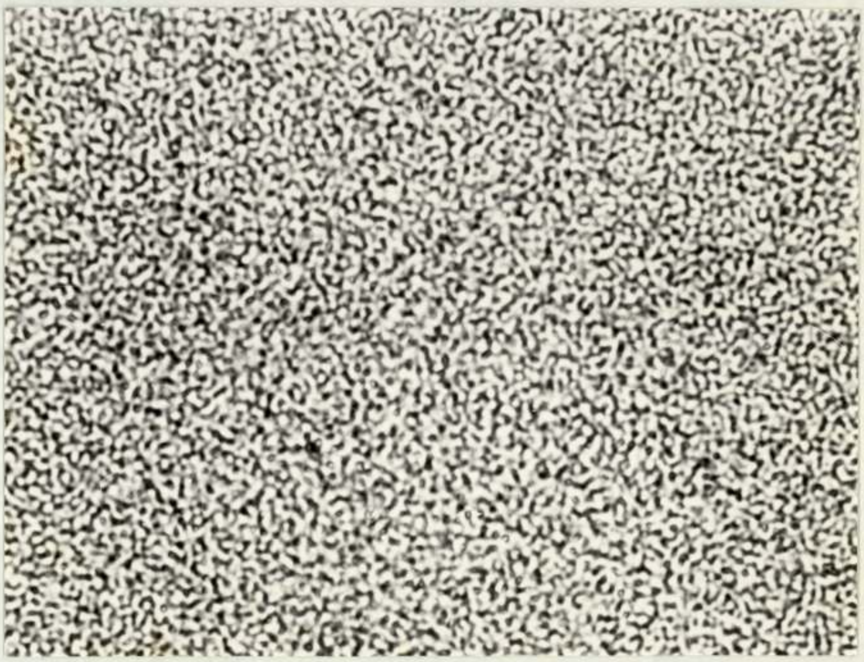

Fig. 45 Fine-grained structure produced by natural ageing of the quenched alloy at room temperature x 1200

Alloy 1 (Zn-22%Al)

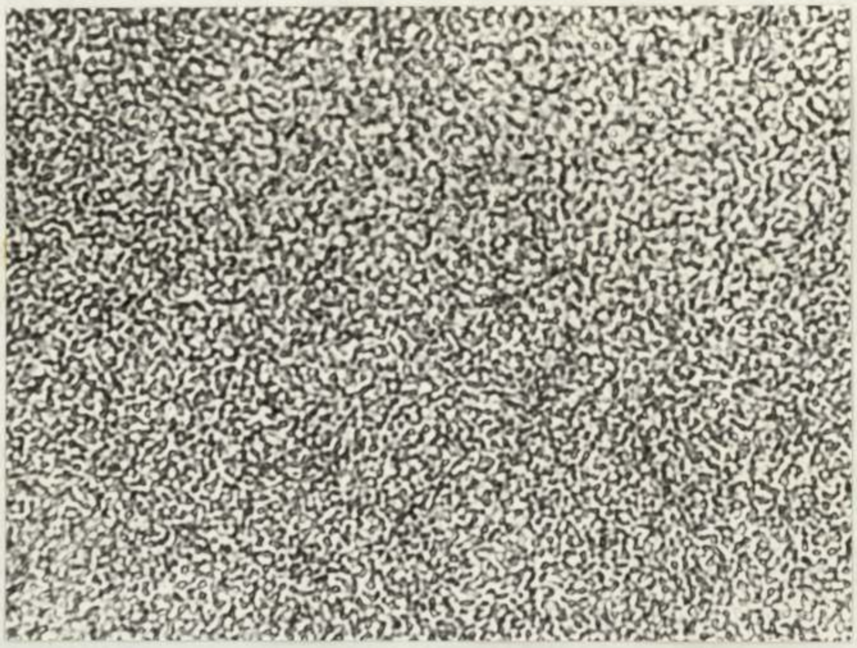

Fig. 46 Microstructure produced by ageing of the quenched alloy at 60°C for 792 hours
x 1200

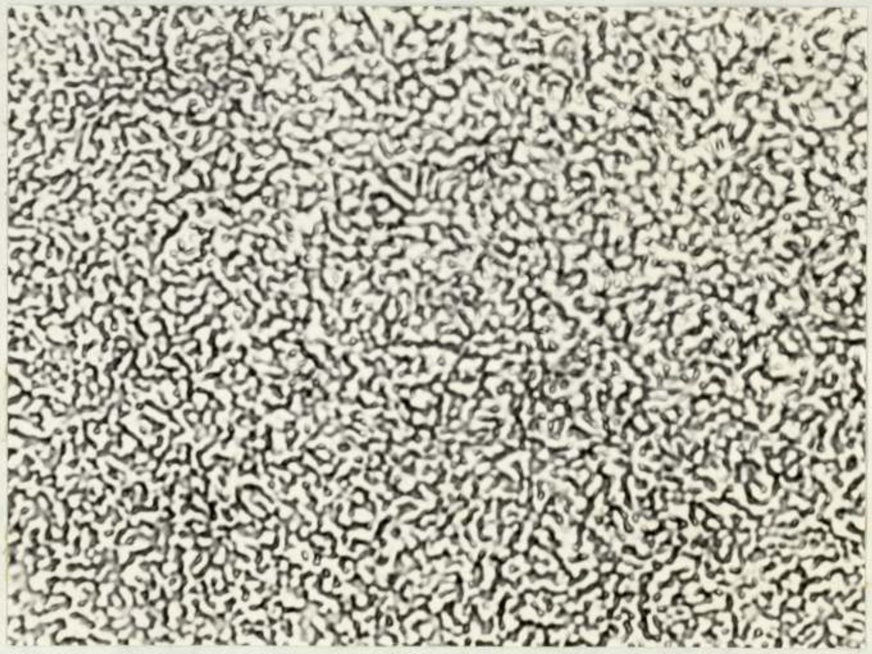

Fig. 47 Micrograph showing the structure produced by transformation at 200°C for 20 hours
x 1200

Alloy 1 (Zn-22%Al)

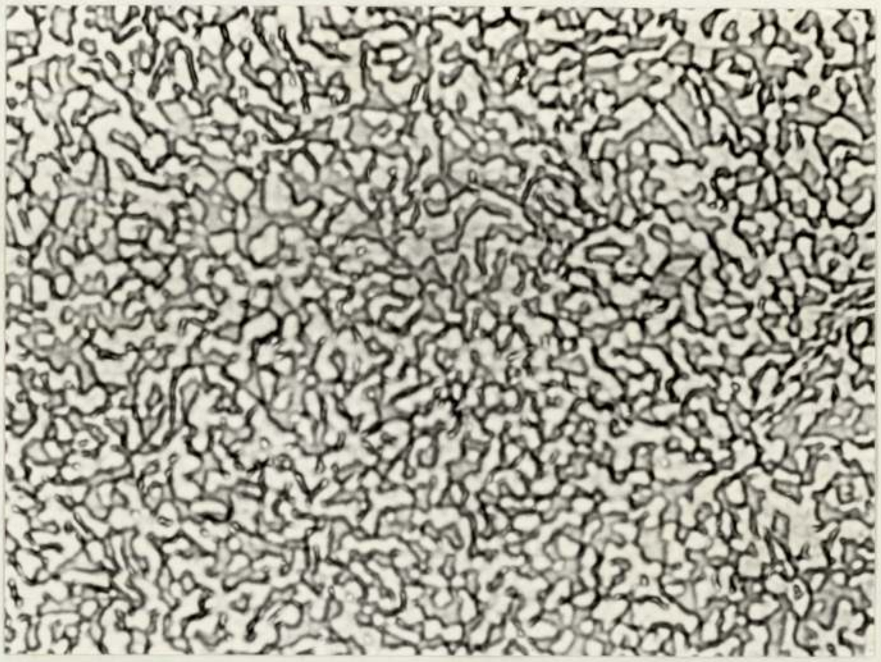

Fig. 48 Microstructure obtained on ageing at 200°C for 217 hours x 1200

Fig. 49 Transmission electron micrograph showing the mixture of fine zinc and aluminium-rich grains obtained on quench-ageing at room temperature x 118K

Alloy 2 (Zn-27%Al-3%Cu)

Fig. 50 Cored-dendritic structure of zinc-aluminium-copper alloy (2A) x 960

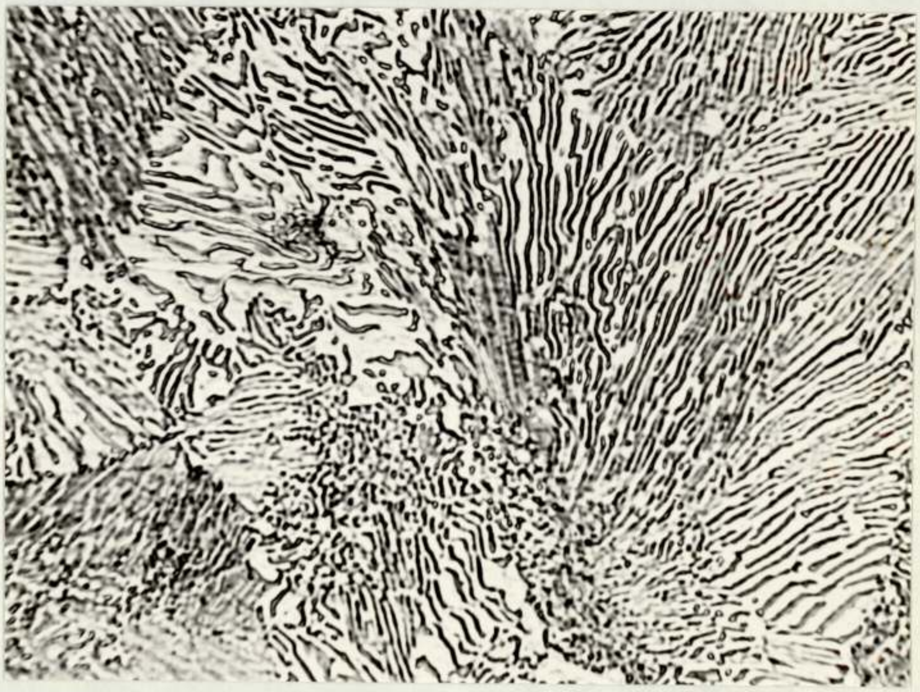

Fig. 51 Lamellar morphology produced by furnace cooling of the homogenized alloy x 960

Alloy 2 (Zn-27%Al-3%Cu)

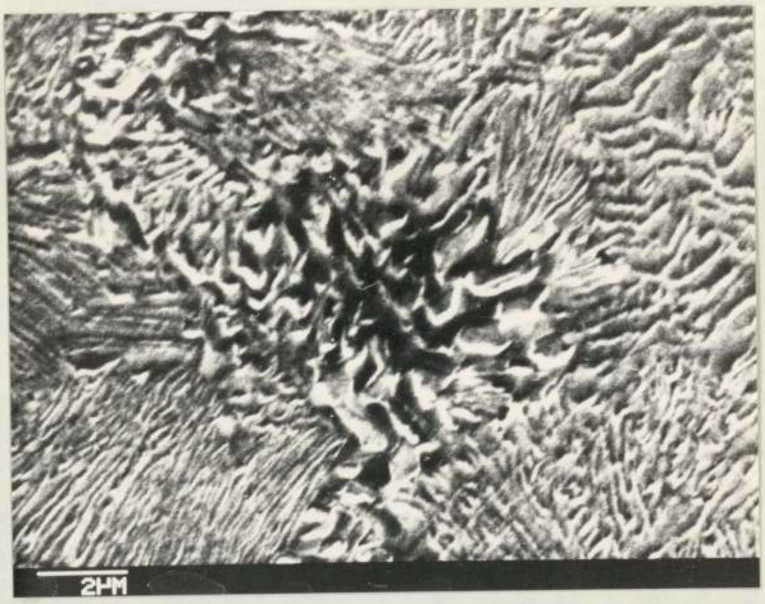

Fig. 52 Fine lamellar products obtained by air cooling from solution treatment temperature

Fig. 53 Degenerate lamellar structure produced by isothermal transformation at 200°C for one hour after solution treatment x 1200

Alloy 2 (Zn-27%Al-3%Cu)

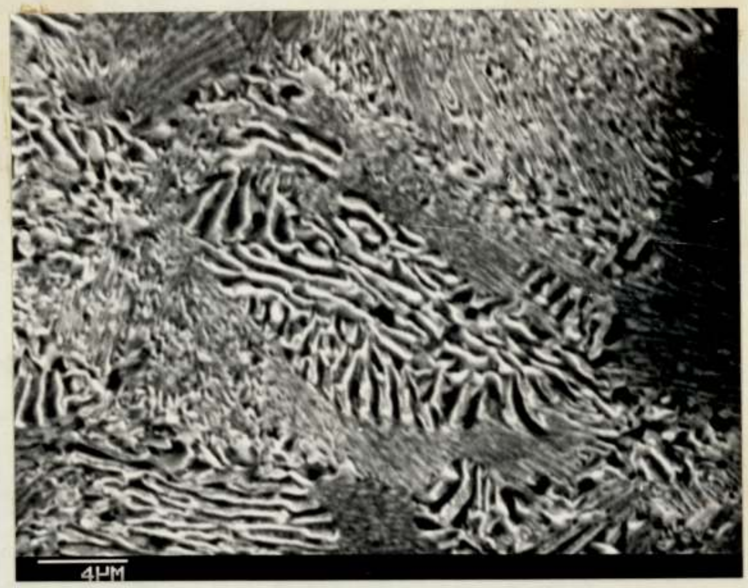

Fig. 54 Scanning electron micrograph showing products of isothermal transformation in detail

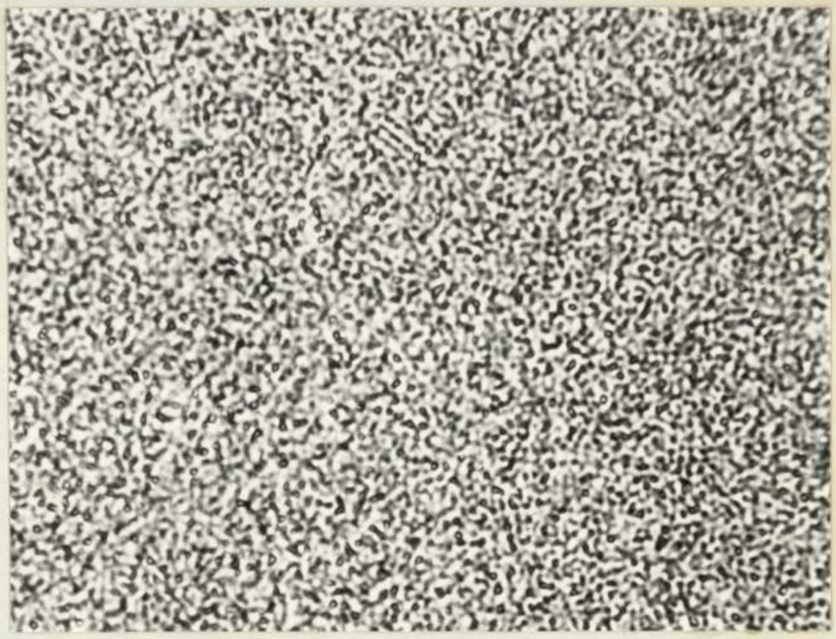

Fig. 55 Optical micrograph of typical equiaxed fine-grained structure obtained by water quenching from solution treatment and transformation at room temperature for about 2350 hours x 1200

Alloy 2 (Zn-27%Al-3%Cu)

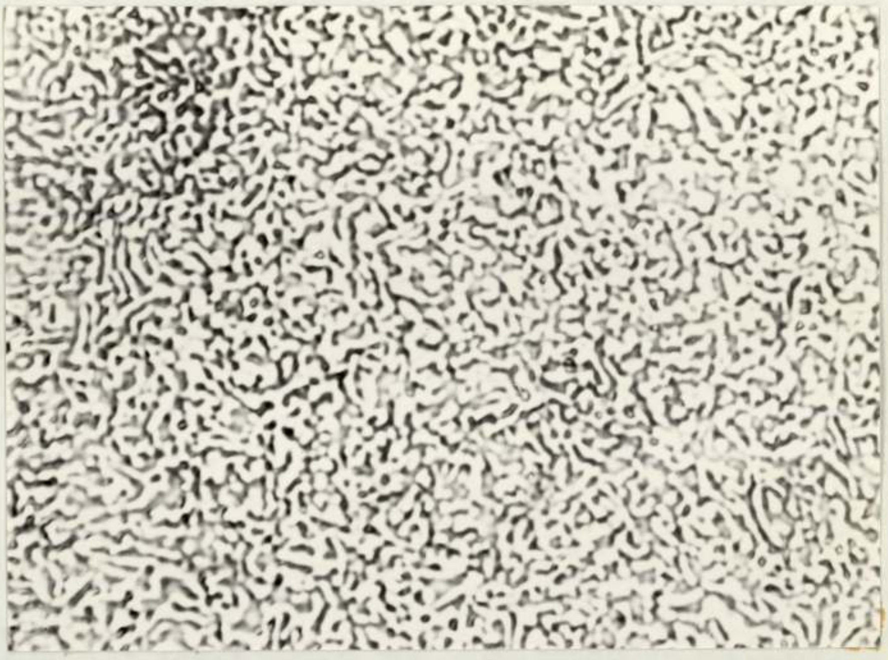

Fig. 56 Fine-grained structure obtained on quench-ageing at 200°C for ~34 hours x 1200

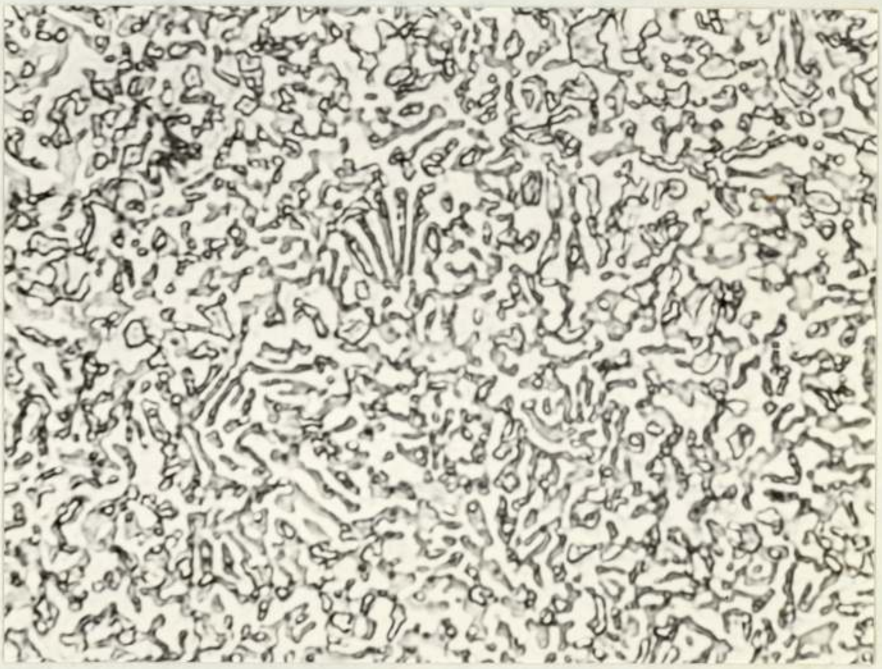

Fig. 57 Coarse structure produced by quench-ageing at 200°C for 218 hours x 1200

Alloy 2 (Zn-27%Al-3%Cu)

Fig. 58 Transmission electron micrograph of typical lamellar products of furnace-cooled alloy x 10.5K

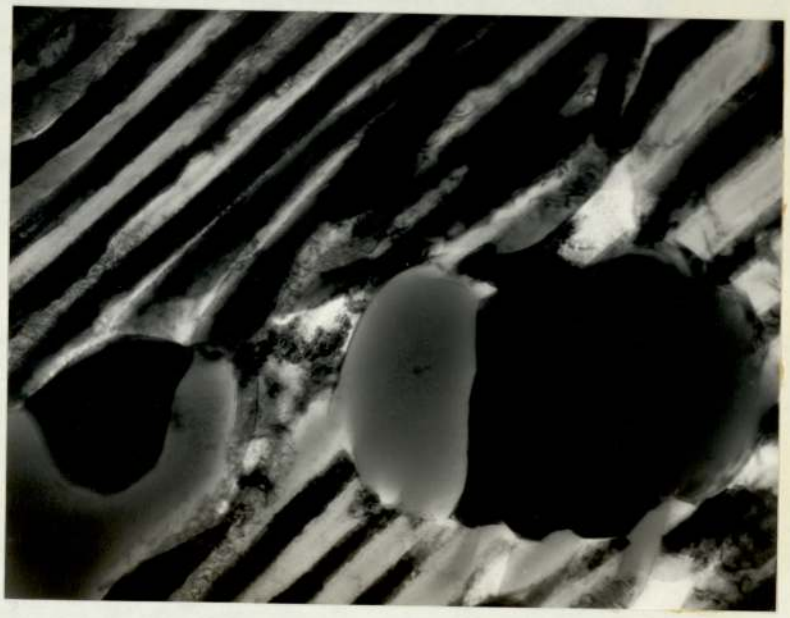

Fig. 59 Transmission electron micrograph showing the different morphologies of decomposition products obtained on furnace cooling x 15·5 K

Alloy 2 (Zn-27%Al-3%Cu)

Fig. 60 Transmission electron micrograph showing the zinc and aluminium-rich phases with small precipitate particles obtained on quench-ageing at room temperature for 5 hours x 50.4K

Fig. 61 Mixed structure produced by decomposition of the quenched alloy at 200°C for 2 hours x 20.6K

Fig. 62 Transmission electron micrograph showing the zinc lamellae growing one of the particles on ageing at 200°C x 33.4K

Alloy 3 (Zn-19%Al-4%Cu)

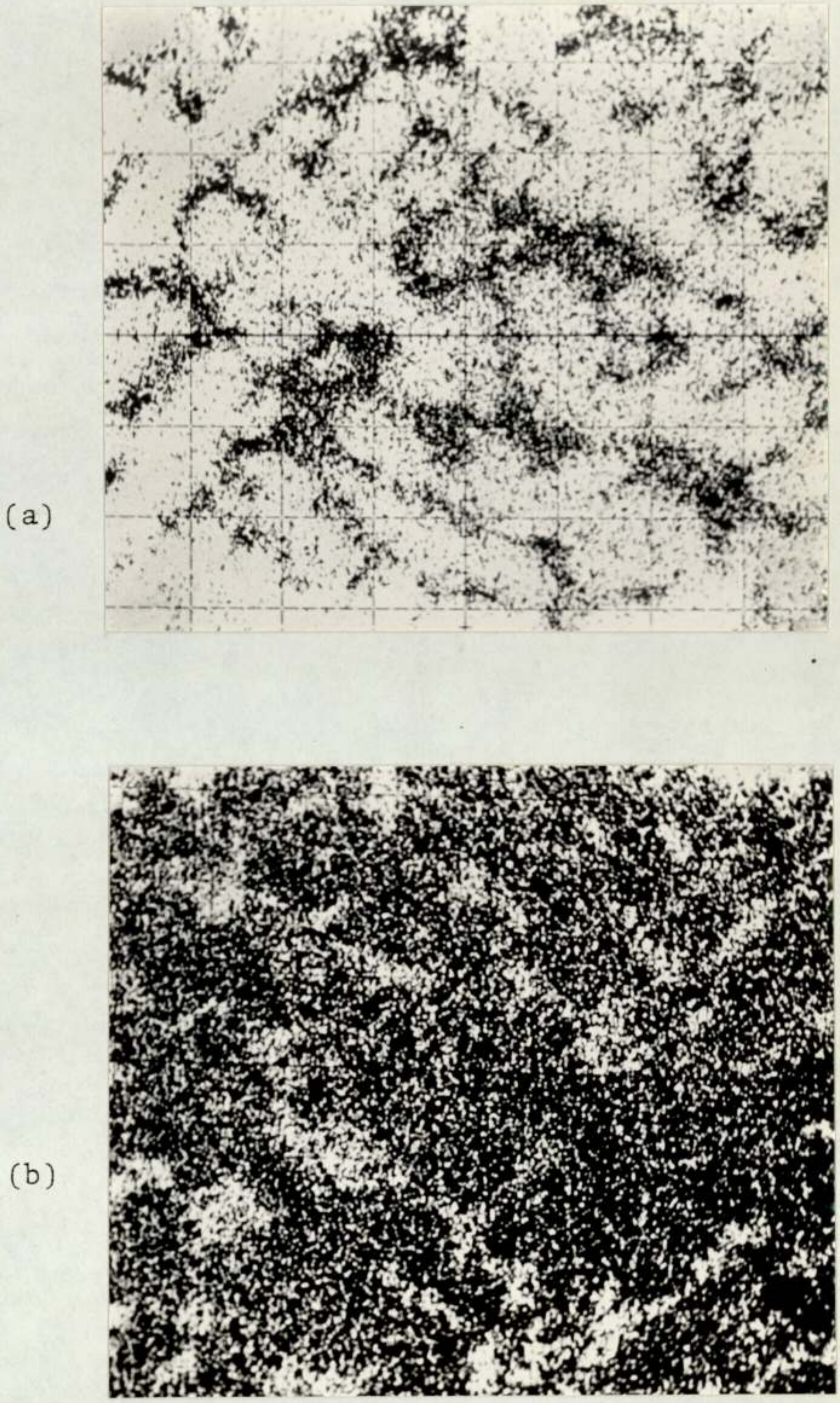

Fig. 63 X-ray micrographs of the as-cast structure of alloy 3A showing

(a) distribution of aluminium-rich dendrites, and

(b) copper-rich interdendritic phase

x 1130

Alloy 3 (Zn-19%Al-4%Cu)

Fig. 64 Optical micrograph of the as-cast structure of alloy 3A x 280

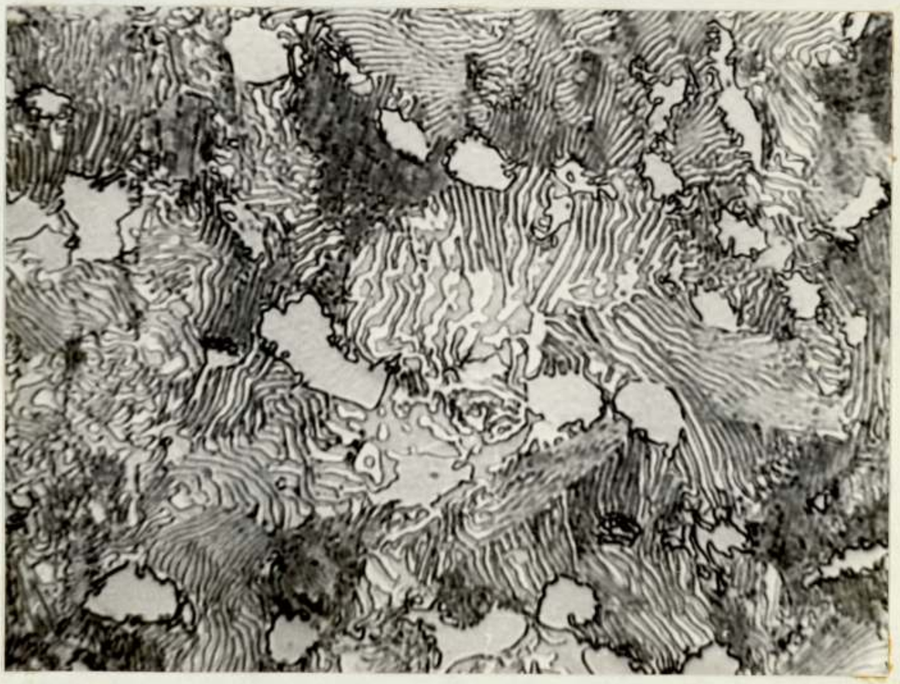

Fig. 65 Optical micrograph showing the lamellar structure and large ε-phase particles in the furnace-cooled alloy x 960

Alloy 3 (Zn-19%Al-4%Cu)

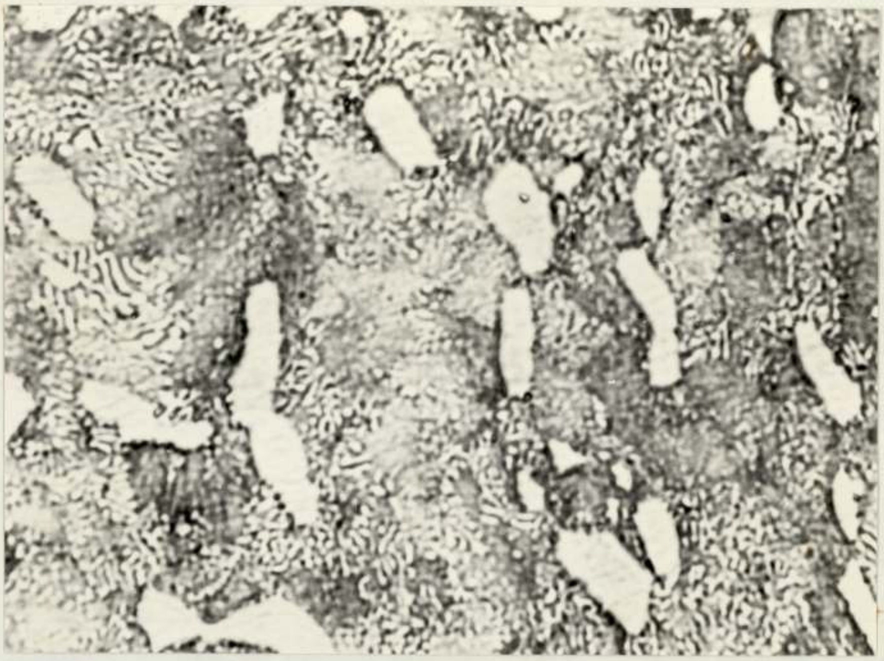

Fig. 66 Microstructure produced by isothermal transformation at 200°C for one hour following the solution treatment x 1200

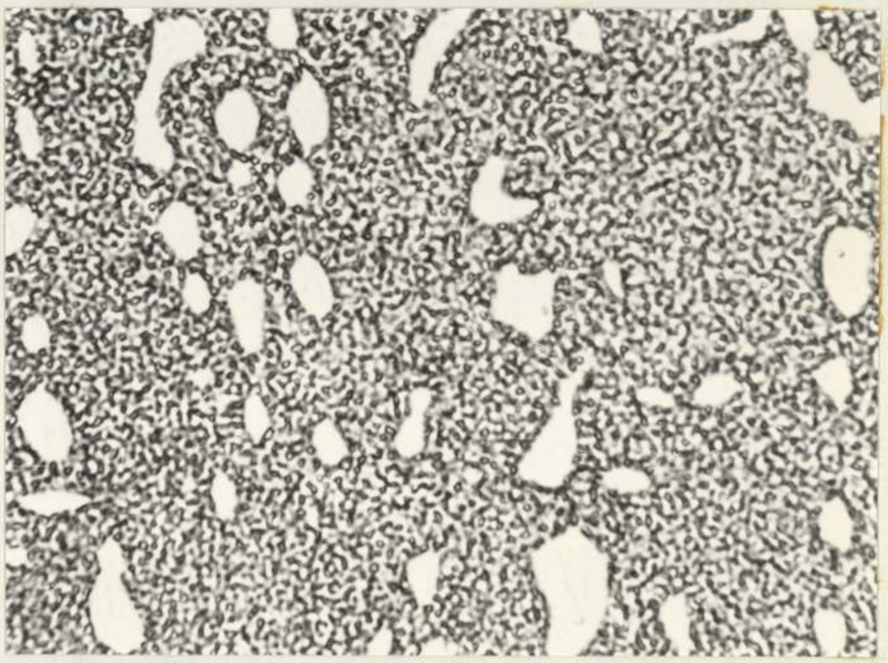

Fig. 67 Optical micrograph of fine-grained structure with ε-phase particles obtained by quench-ageing at room temperature for 4400 hours x 1200

Alloy 3 (Zn-19%Al-4%Cu)

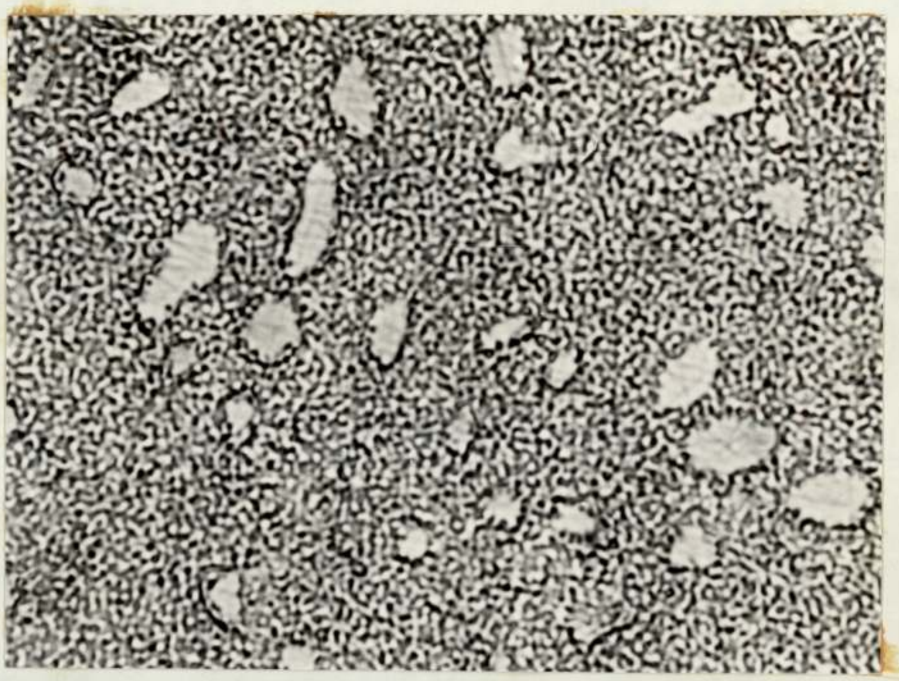

Fig. 68 Structure obtained by ageing at 60^{o}C for 840 hours after solution treatment and quenching x 1200

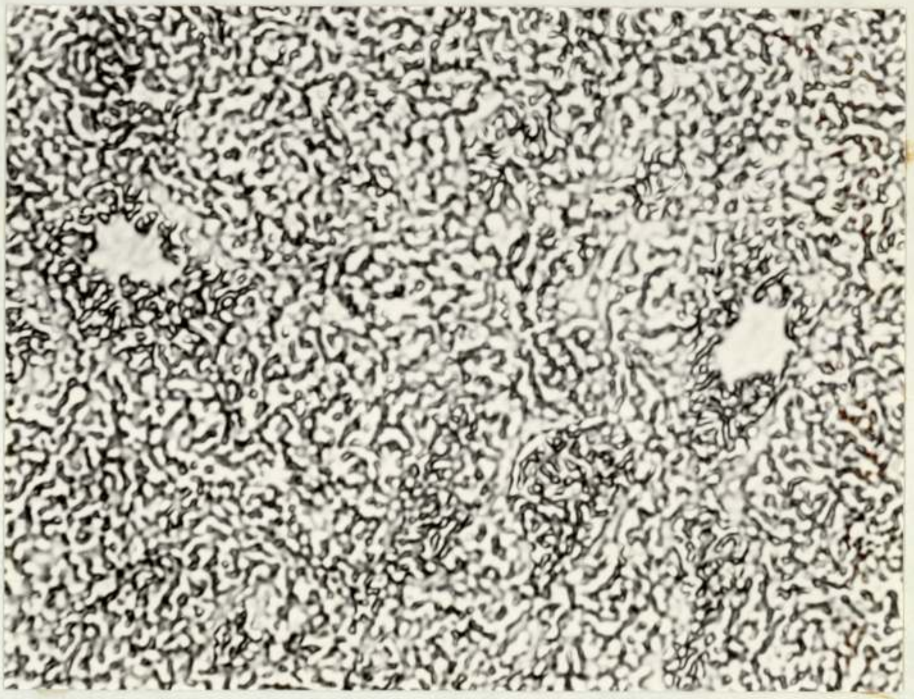

Fig. 69 Structure obtained on quench-ageing at 200^{o}C for 20 hours x 1200

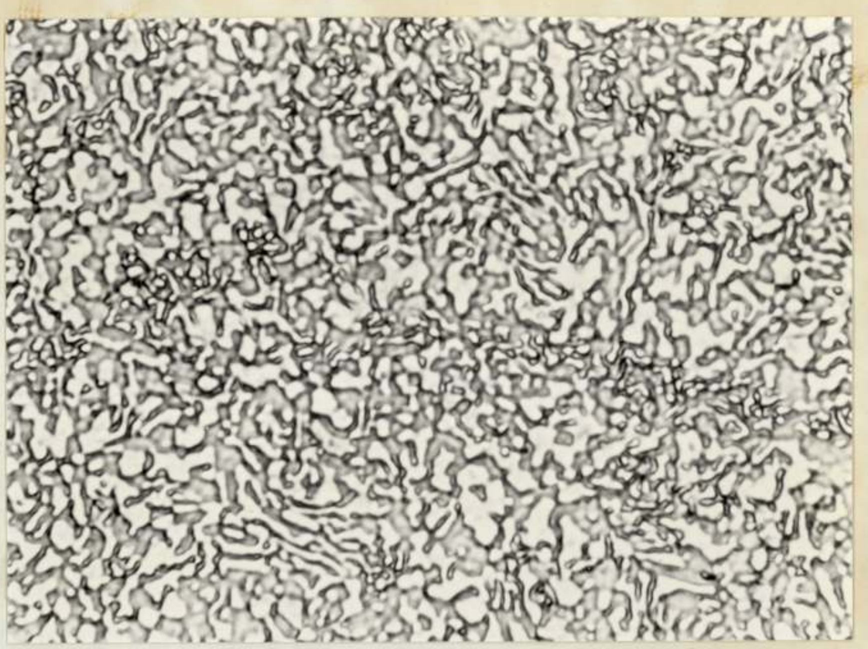

Fig. 70 Optical micrograph showing the coarse structure without ε-phase, obtained by ageing at 200°C for 90 hours x 1200

Fig. 71 Transmission electron micrograph of the general lamellar structure of furnace-cooled alloy x 7.5K

Alloy 3 (Zn-19%Al-4%Cu)

Fig. 72 Transmission electron micrograph of a mixed structure containing both zinc and aluminium-rich grains, obtained during quench-ageing at 200°C for 2 hours x 20.6K

Fig. 73 Transmission electron micrograph showing the branched and bifurcated lamellae in small patches in the alloy aged at 200°C for 2 hours x 20.6K

Alloy 4 (Zn-38%Al-2%Cu)

Fig. 74 As-cast structure of alloy 4 x 332

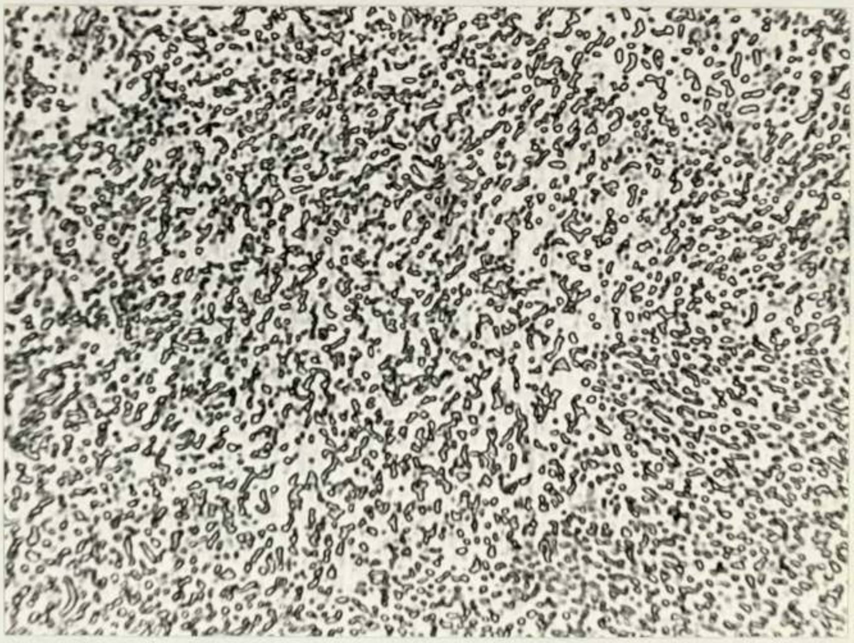

Fig. 75 Optical micrograph of the structure produced on furnace cooling x 960

Alloy 4 (Zn-38%Al-2%Cu)

Fig. 76 Scanning electron micrograph of the furnace-cooled alloy showing the zinc and aluminium-rich particles in detail

Fig. 77 Transmission electron micrograph showing the structure of the furnace-cooled alloy x 10.5K

Alloy 4 (Zn-38%Al-2%Cu)

Fig. 78 Transmission electron micrograph showing the aluminium-rich (α) and zinc-rich (η) phases together with some precipitate particles in the furnace-cooled alloy x 15.5K

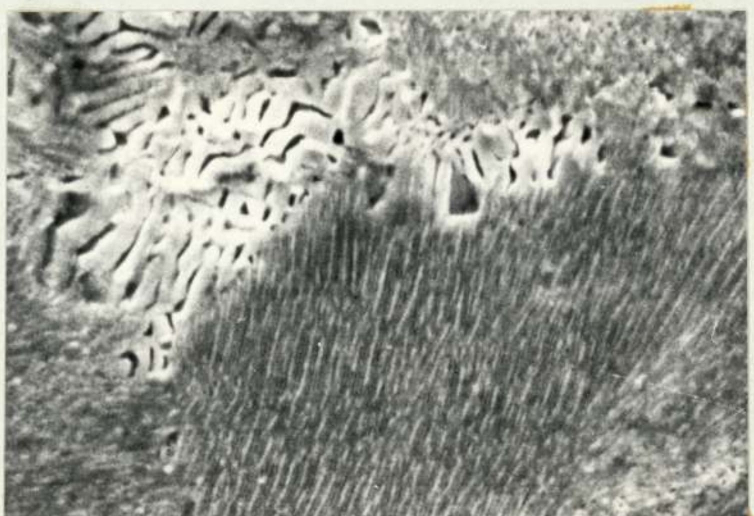

Fig. 79 Mixed lamellar structure produced by isothermal ageing at 200°C for 2 hours

Alloy 4 (Zn-38%Al-2%Cu)

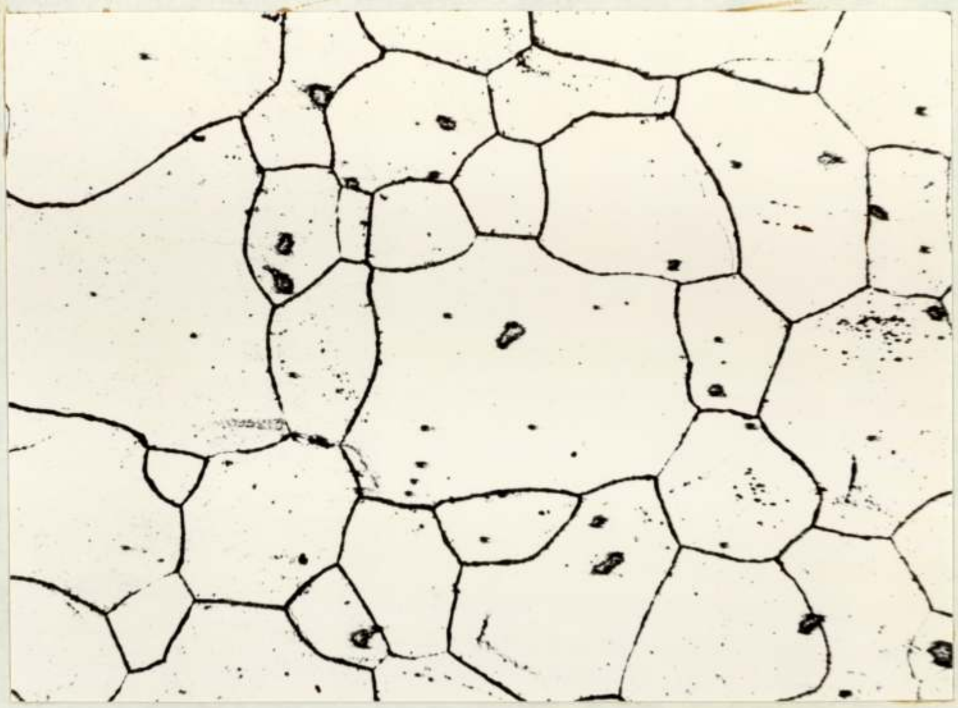

Fig. 80 Optical micrograph of the as-quenched alloy showing large grains of α/α' solid solution x 80

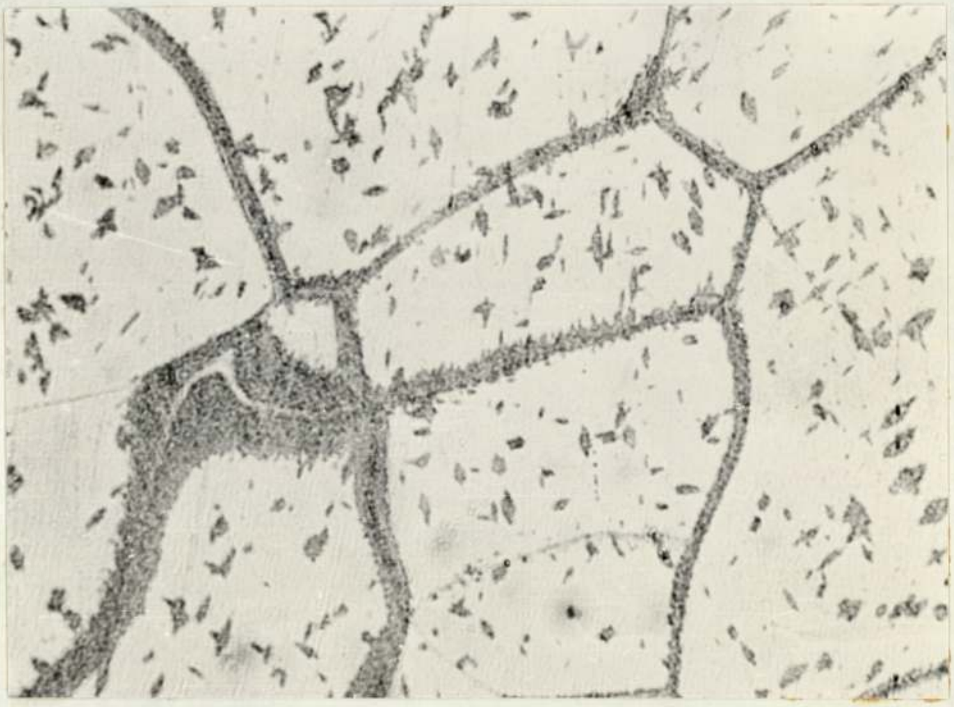

Fig. 81 Decomposition products at the grain-boundaries and within grains formed after ageing at room temperature for 190 hours x 280

Alloy 4 (Zn-38%Al-2%Cu)

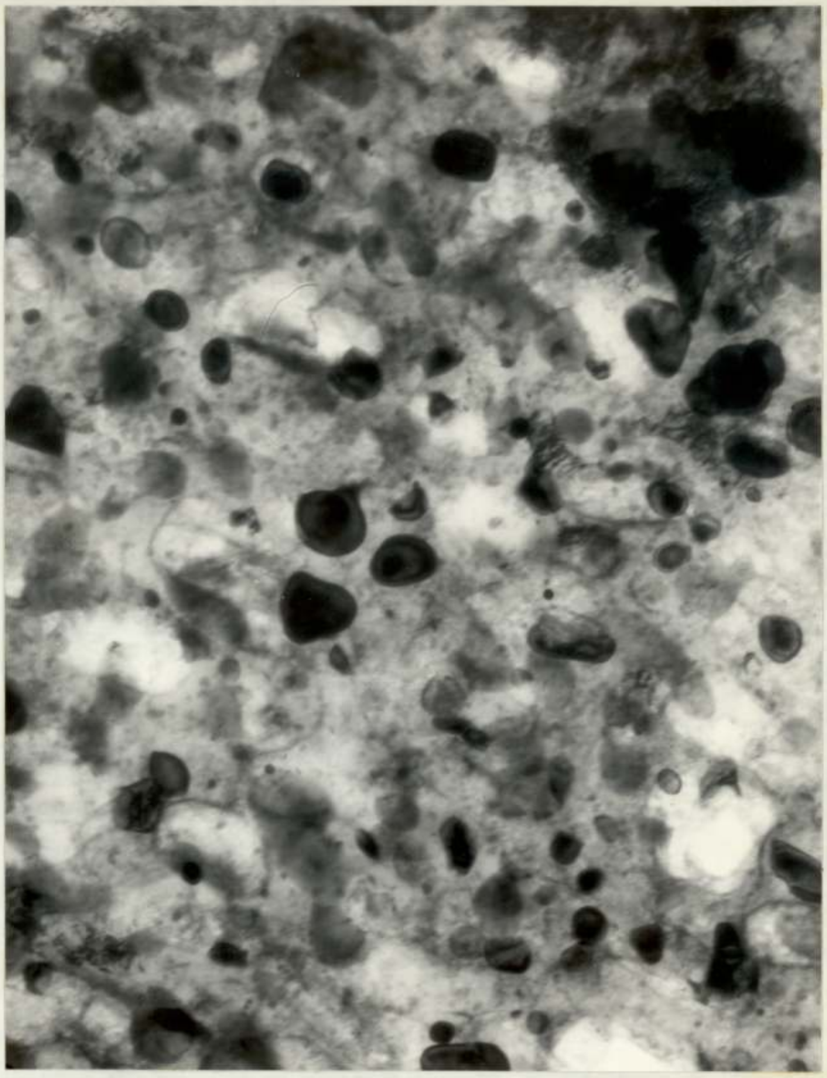

Fig. 82 Transmission electron micrograph showing the very small zinc or intermetallic precipitate particles formed during decomposition of the quenched alloy on ageing at room temperature for about 4400 hours x 33.4K

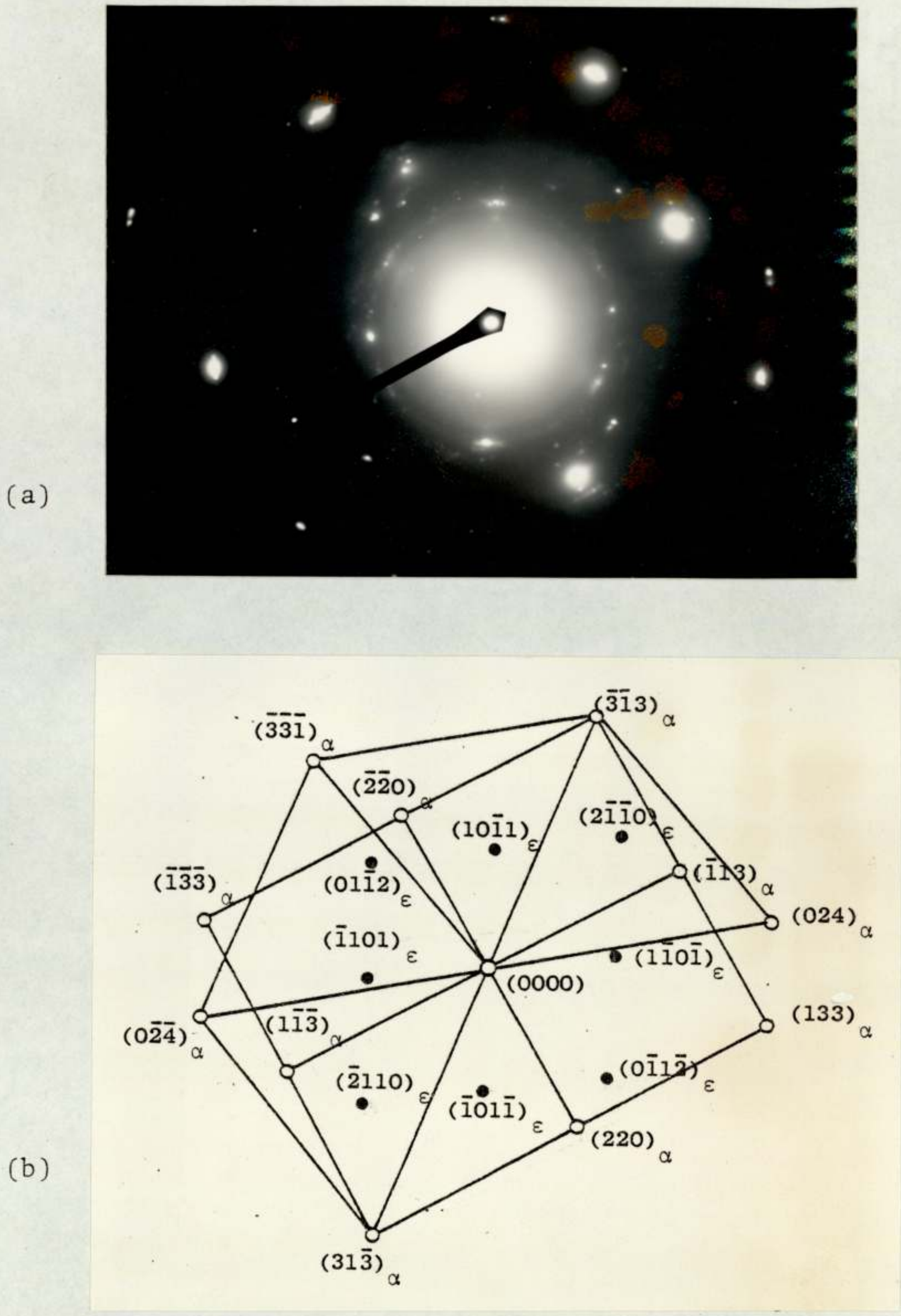

Fig. 83 (a) An electron diffraction pattern from the area shown in Fig. 82

(b) Indexing

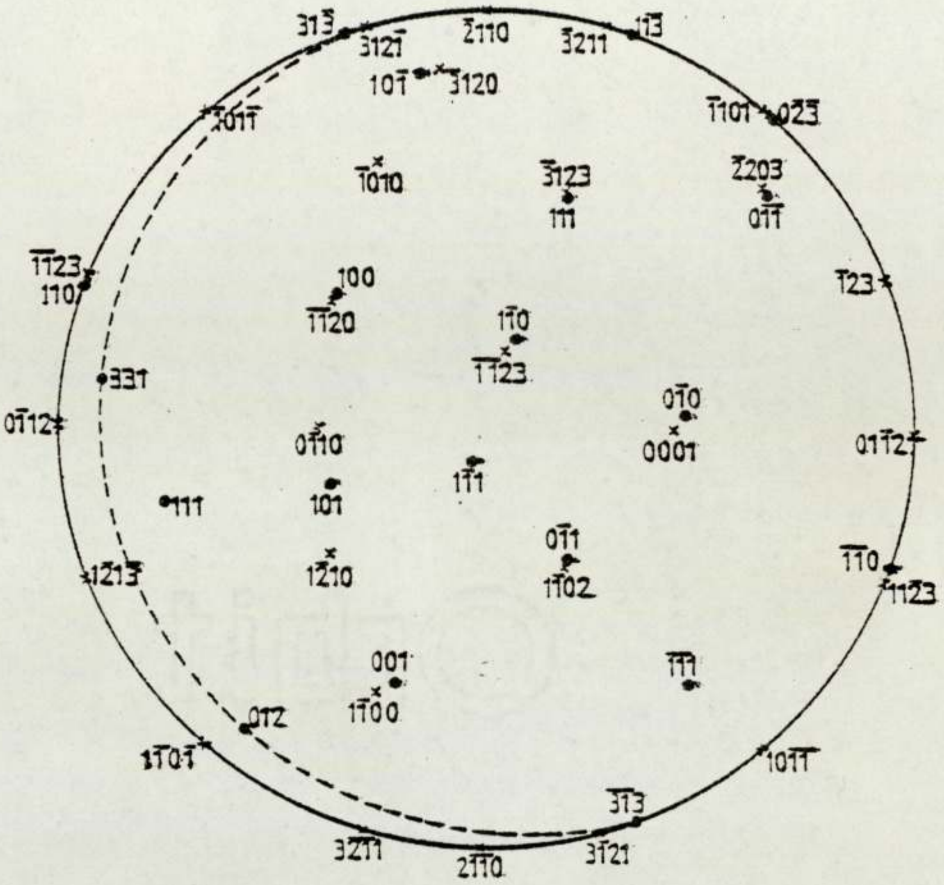

(h k ℓ) ● α phase indices

(h k i ℓ) × ε phase indices

Fig. 84 A stereographic projection showing the aluminium and ε-phase zones and their orientation relationship

Fig. 85 Optical micrograph showing the precipitation on grain boundaries and on certain inter-granular sites obtained on ageing at 200°C for 10 minutes x 200

Alloy 4 (Zn-38%Al-2%Cu)

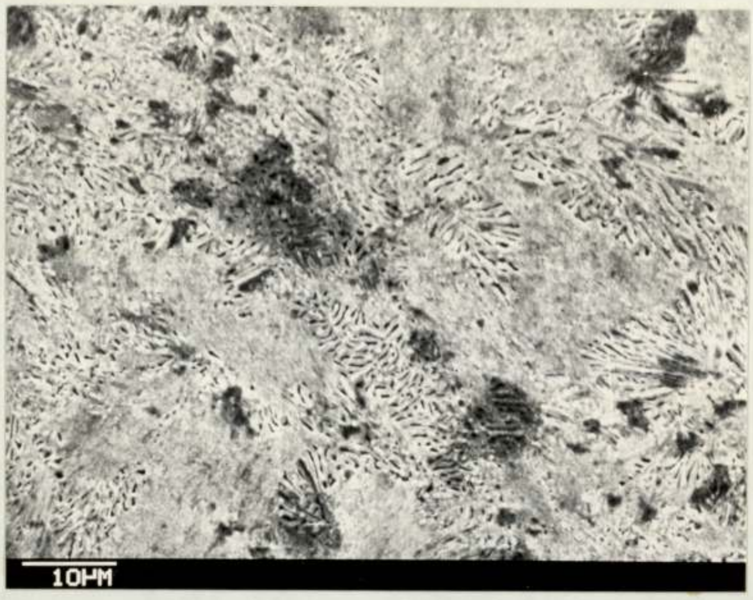

Fig. 86 Mixed structure consisting of cellular material and precipitate particles in the remaining regions, obtained after 2 hours ageing at 200°C

Fig. 87 Transmission electron micrograph showing the decomposition products obtained on quench-ageing at 200°C for 2 hours x 14K

Alloy 4 (Zn-Zn-38%Al-2%Cu)

Fig. 88 A mixture of precipitate particles formed after 2 hours ageing at 200°C x 14K

Fig. 89 Mixed structure consisting of fine and large lamellae and small rounded or subgranular particles within the aluminium-rich phase obtained by decomposition of the quenched alloy at 200°C for 2 hours x 14K

Alloy 5 (Zn-35.6%Al-8.4%Si)

Fig. 90 As-cast structure of Zn-Al-Si alloy (5) x 330

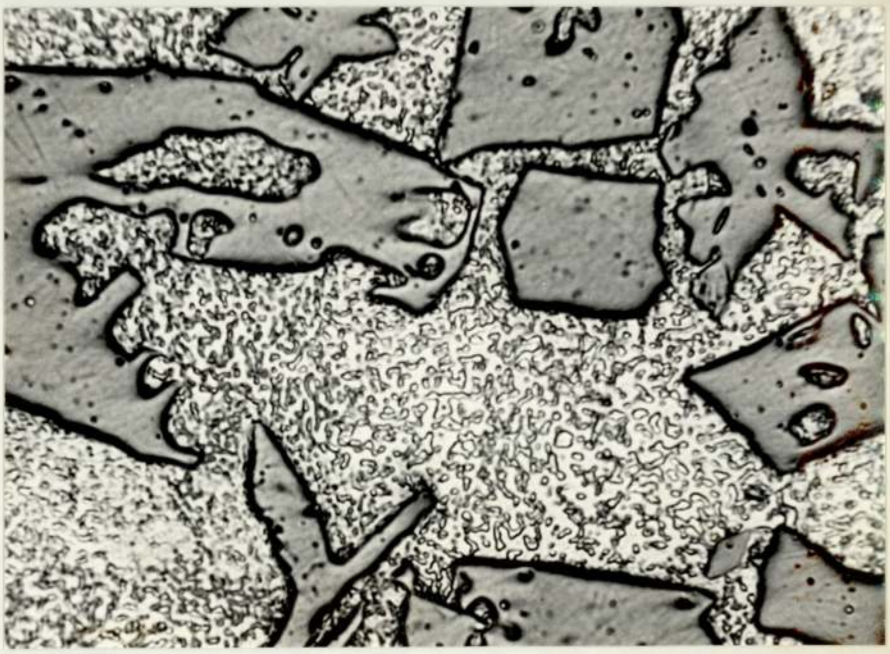

Fig. 91 Microstructure of alloy 5 produced by furnace-cooling after homogenization x 960

3.3 Decomposition of the Alloys on Quench-Ageing

3.3.1 Hardness

Hardness measurements were used to follow the decomposition of the quenched alloys on isothermal ageing.

The hardness results for alloys 1 to 5 obtained at different temperatures are plotted as hardness versus Ln time in Figs. 92, 93, 94, 95 and 96.

It can be seen from the diagrams that the set of curves for each alloy shows a similar behaviour. Initially hardness increased from the as-quenched value, reached a peak after a certain ageing time and then steadily and smoothly decreased in most cases. As the temperature increased the time to peak hardness decreased.

Comparison of the above figures shows that high-zinc alloys transformed faster than the low-zinc alloys. In the binary eutectoid alloy (1B) hardening occurred very quickly and this alloy reached its peak hardness in about 600 s at room temperature, Fig. 92. Therefore the hardness change during ageing prior to peak hardness, at temperatures above ambient could not be determined. The hardness curves obtained at temperatures above ambient show only the overageing or coarsening behaviour of this alloy. However the hardness changes in the ternary alloys (2B and 4B) on quench-ageing at temperatures up to 100°C were satisfactorily determined as seen in the above figures.

The activation energies for hardness change, on quench-ageing, of these alloys were determined by plotting either Ln (time to 50% peak hardness or Ln time to peak hardness) versus the reciprocal of absolute temperature. The data for these plots, obtained from the hardness curves of the zinc-aluminium-copper alloys are given in Table 4A. As this table shows, only two points were obtainable for the Ln (time to 50% peak hardness) versus $^1/T$ plots. However, the Ln (time to peak hardness) versus $^1/T$ plots for alloys 2B and 4B, were obtained with three data points, Fig. 97. The slopes of these plots, which are straight lines, were determined by a linear regression method and the activation energies were calculated from the expression:

$$H = At \exp(-Q/kT) \quad \ldots\ldots\ldots\ldots\ldots (9)$$

The results for alloys 2B, 3B and 4B are listed in Table 4b. This table shows the activation energies for hardness change on quench-ageing of the zinc-aluminium-copper alloys were in the range of 70 to 90 kJ/mol.

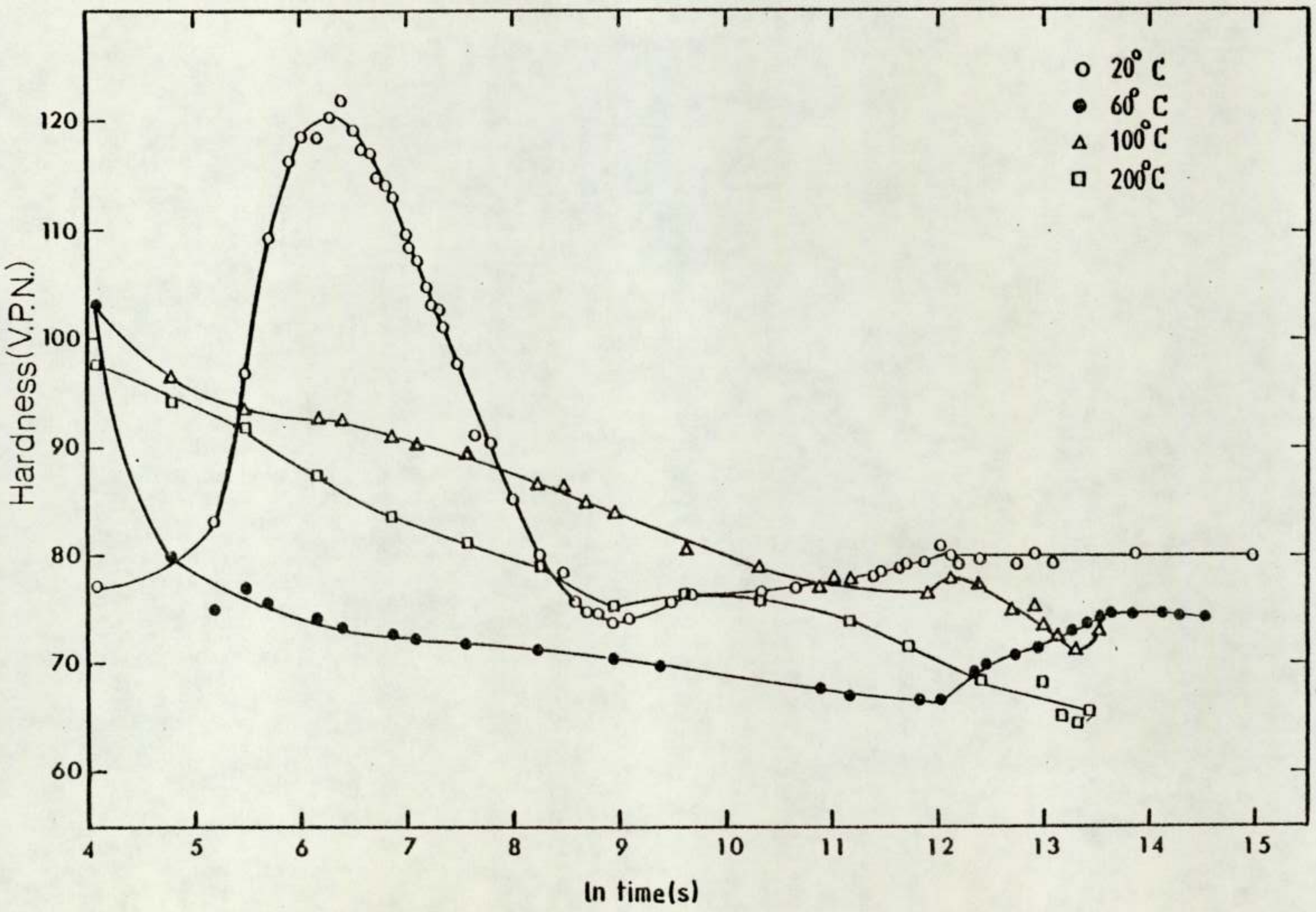

Fig. 92 Hardness change on quench-ageing of alloy 1B at ~20, 60, 100 and 200°C

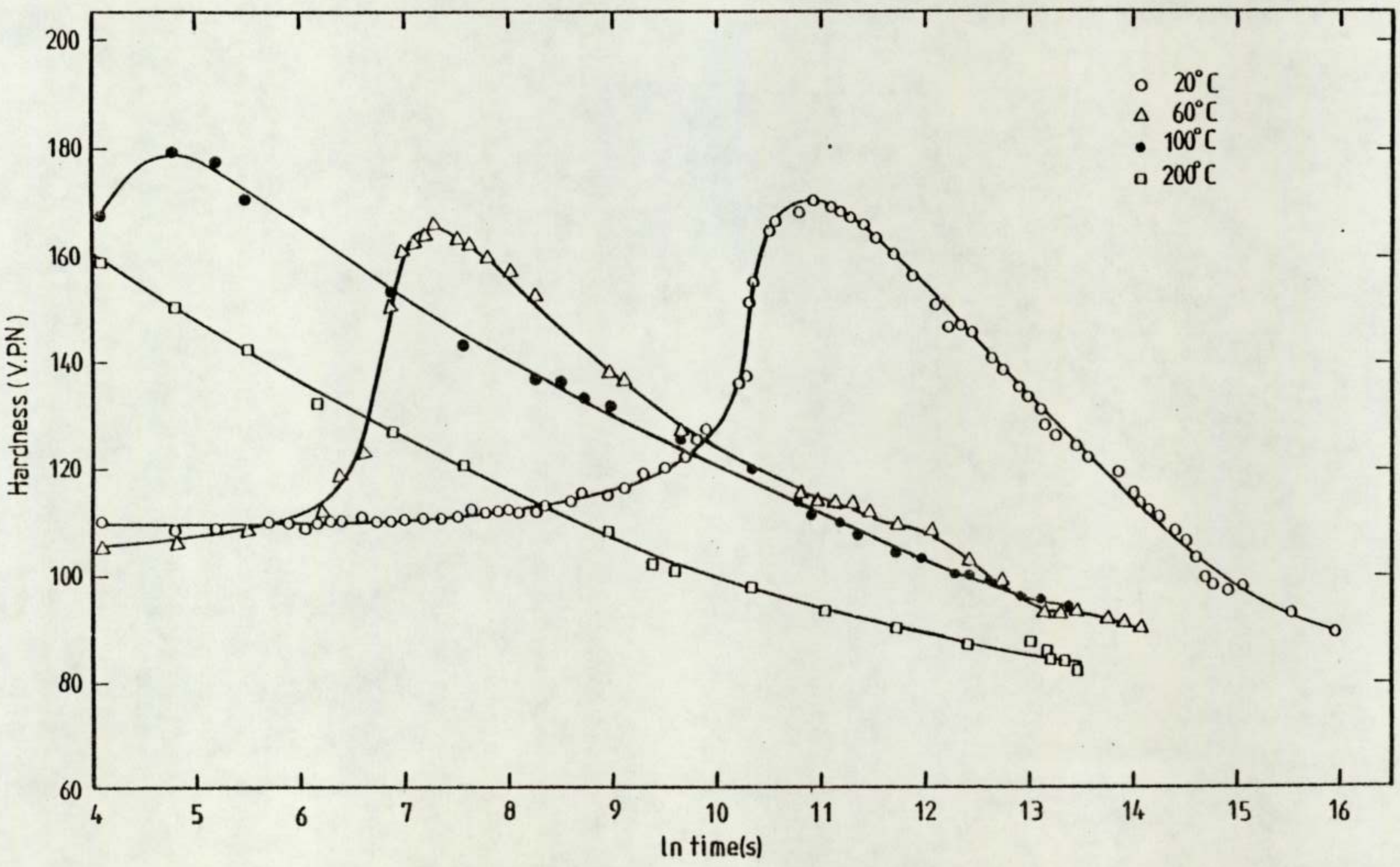

Fig. 93 Hardness change on quench-ageing of alloy 2B at ~20, 60, 100 and 200°C

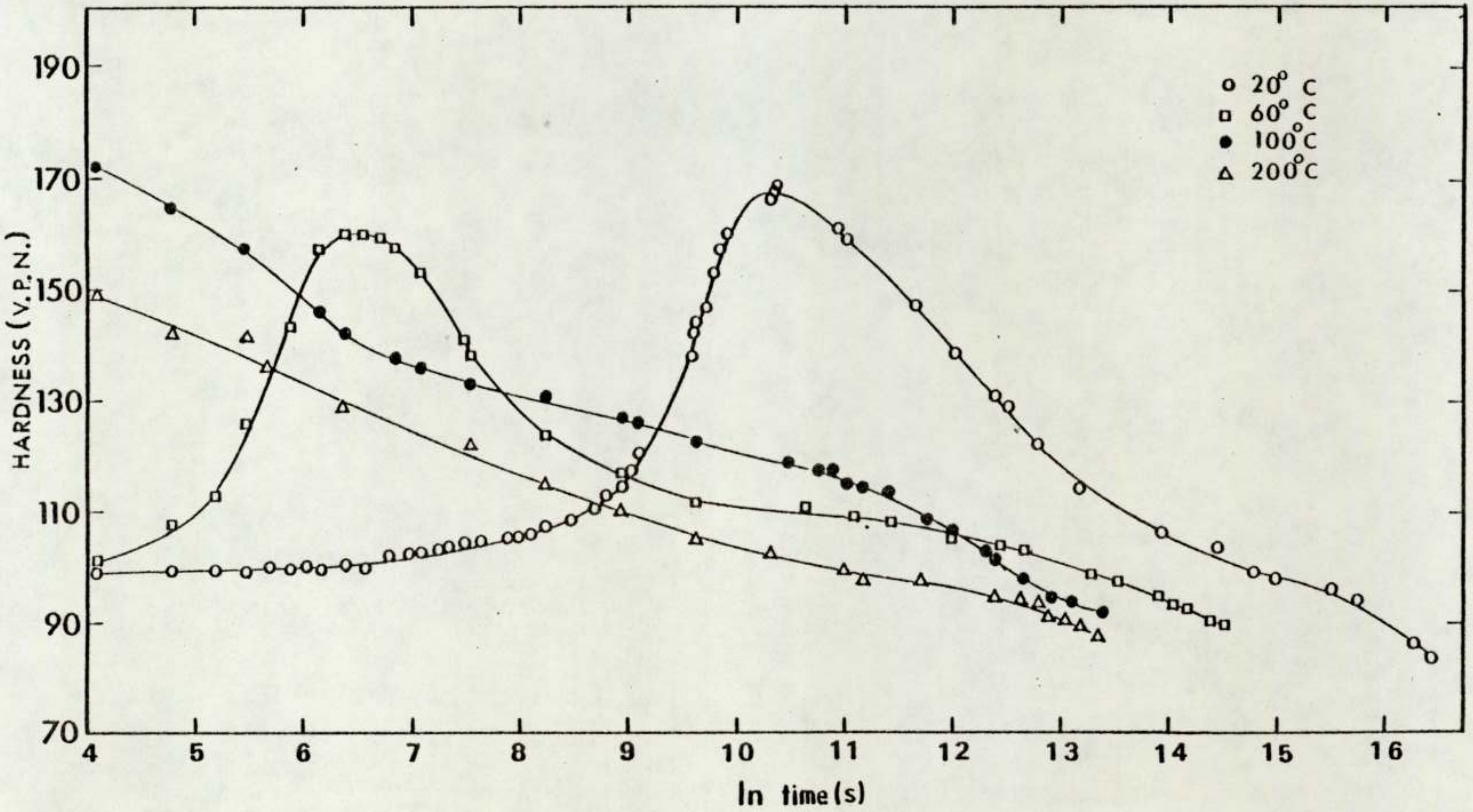

Fig. 94 Hardness curves for alloy 3B quenched and isothermally transformed at 20, 60, 100 and 200°C

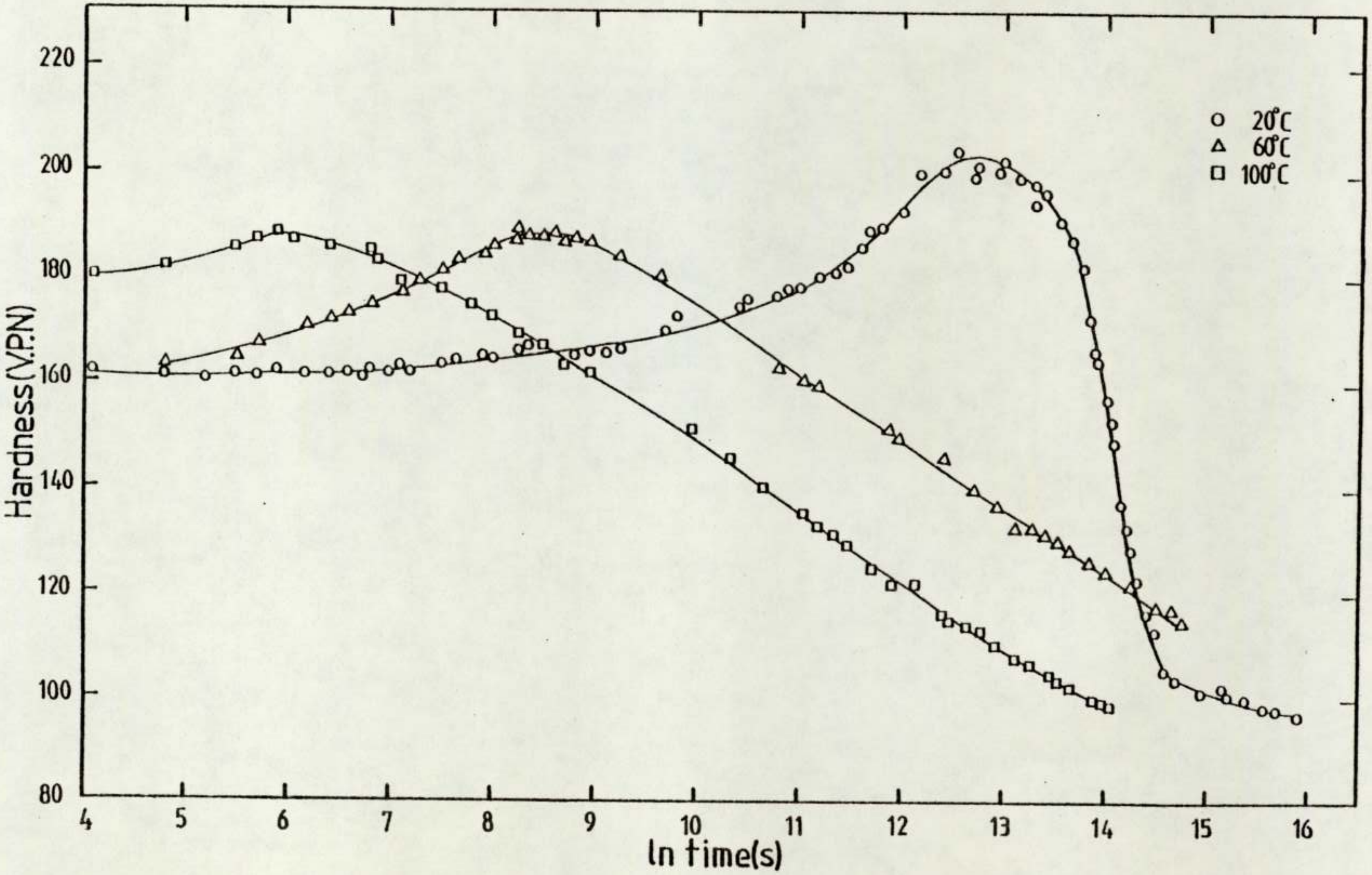

Fig. 95 Hardness change of alloy 4B during quench ageing at 20, 60 and 100°C

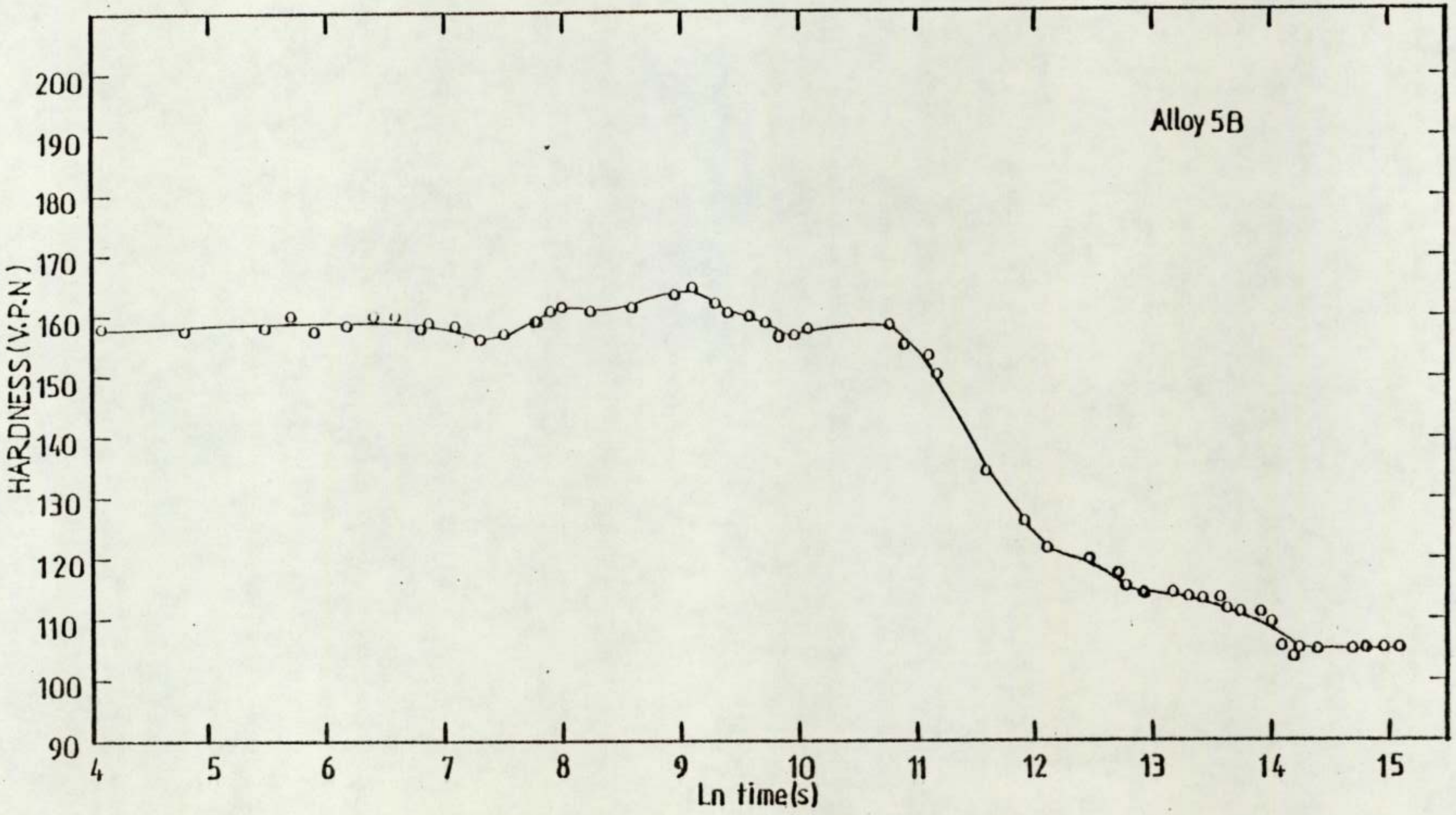

Fig. 96 Hardness change during quench-ageing of alloy 5B at room temperature

TABLE 4A

Data for Arrhenius plots obtained from the hardness curves of zinc-aluminium-copper alloys

Alloy	T(^{o}C)	$^{1}/T(K^{-1})$ x 10^{-3}	Ln time(s) to 50% peak hardness	Ln time(s) to peak hardness
2B	20	3.41	10.24	10.90
	60	3.00	6.71	7.27
	100	2.68	-	4.79
3B	20	3.41	9.41	10.31
	60	3.00	5.60	6.50
4B	20	3.41	11.36	12.70
	60	3.00	6.92	8.50
	100	2.68	-	5.90

TABLE 4B

Activation energies for hardness change on isothermal ageing of zinc-aluminium-copper alloys, determined from Arrhenius plots (Ln time to 50% peak hardness or to peak hardness versus $^{1}/T$)

Alloy	Hardness level	Slope (Q/k) x 10^{3}	Activation energy Q(kJ/mol)
2B	50% Peak hardness	8.6	72
	Peak hardness	8.4	70
	50% Peak hardness	9.3	77
	Peak hardness	9.3	77
4B	50% Peak hardness	10.8	90
	Peak hardness	9.4	78

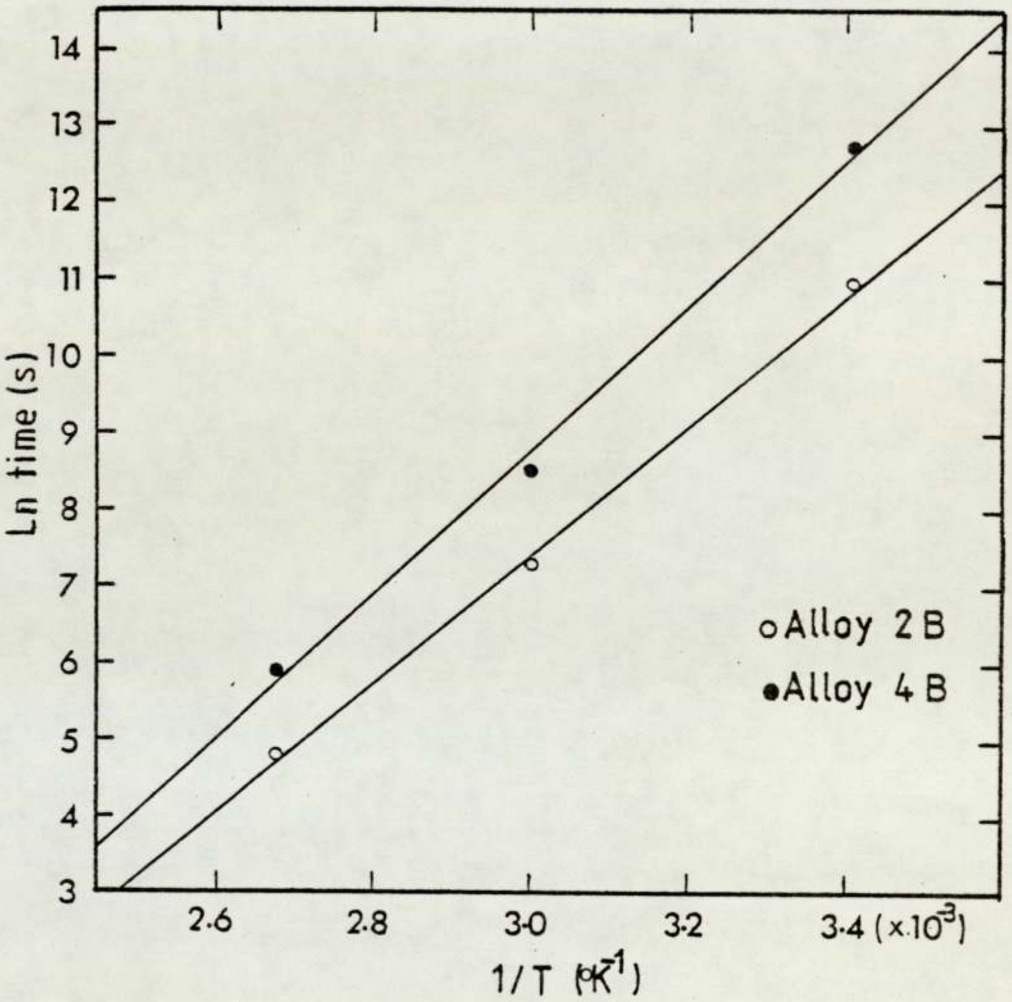

Fig. 97 Arrhenius plots for determination of activation energy for hardness change of alloys 2B and 4B during quench-ageing

3.3.2 X-ray Diffraction

The crystal structures and lattice parameters of the quenched high-temperature phases were determined by X-ray diffraction and the results are given in Table 5.

TABLE 5

Crystal structure and lattice parameter of the high-Temperature phases

Alloy	Phase	Crystal Structure	Lattice Parameter (Å)
2B	β	f.c.c.	a = 3.999
3B	β	f.c.c.	a = 3.995
	ε	h.c.p.	a=b=2.766, c=4.300
4B	α/α′	f.c.c.	a = 4.022

The lattice parameter of the β phase of the binary alloy (1B) could not be determined by this method, since diffraction peaks of this phase were found to overlap those of the aluminium even when first put in the diffractometer. This was due to the very rapid decomposition of the binary β phase at room temperature. In the ternary alloys the β phase peaks were easily measured prior to the start of decomposition.

The diffraction peaks which were large and sufficiently well separated to follow the transformation of the quenched alloys on isothermal ageing are given below:

Alloy	Decomposing Phase	Diffraction Peak
1B	β	$(10\bar{1}1)_{Zn}$
2B	β	$(200)_{\beta}$ and $(10\bar{1}1)_{Zn}$
3B	$\beta+\varepsilon$	$(200)_{\beta}$

Three diffraction peaks $(10\bar{1}1)_{Zn}$, $(200)_{\beta}$ and $(200)_{Al}$ were considered to follow the transformation of the quenched β phase of alloy 1B on ageing, the only useful peak was $(10\bar{1}1)_{Zn}$, as the two $(200)_{f.c.c.}$ peaks were superimposed and the change in each could not be measured due to the effect of the other.

The $(200)_{\beta}$ and $(10\bar{1}1)_{Zn}$ diffraction peaks were found useful to study the transformation of the quenched β phase of alloy 2B during isothermal ageing and the results obtained on both peaks are compared.

The only useful diffraction peak for alloy 3B was the $(200)_{\beta}$, as the $(111)_{\beta}$ was overlapped by the growing $(10\bar{1}0)_{Zn}$, and the $(10\bar{1}1)_{Zn}$ overlapped the $(10\bar{1}1)$ peak from the undissolved ε phase. This ε phase was found to be metastable at room temperature, as no detectable change in the intensity of its diffraction peaks was observed during decomposition of β phase.

The change in the size of diffraction peaks due to decomposition of β phase alloys 1B, 2B and 3B on quench-ageing at room temperature are shown in Figs. 98, 99 and 100.

The values of the fraction transformed (f) were calculated using the equations $f = \frac{I}{I_{max}}$ for the $(10\bar{1}1)_{Zn}$ peak, or $f = 1-\frac{I}{I_{max}}$ for the $(200)_{\beta}$, where I is the integrated intensity of the measured peak at any given moment and I_{max} is its maximum intensity.

Two methods of measuring the intensities were used: summing the peak counts from the numerical output of the X-ray diffractometer (called f_c), or measuring the peak area on a simultaneously drawing strip chart with a planimeter, f.

The values of the fraction transformed factor determined from the diffraction peak used for each alloy are listed in Tables, 6, 7 a, b, c, 8 a, b, and 9.

The data in the above tables are plotted as f versus Ln time in Figs. 101, 102, 103 a, b and 104 to show the transformation characteristics of these alloys. For one alloy (2B, Fig. 103a) f_c is plotted as a displaced scale. This shows that the data obtained by the different methods are essentially similar.

The activation energy for transformation was obtained in the usual way by plotting Ln (time to 50% transformation) versus the reciprocal of the absolute temperature. A

Good straight line was obtained for alloy 2B as seen in Fig. 105. The data for this plot and the result are given in Table 10.

It was found extremely difficult to investigate the decomposition of α/α' solid solution of alloy 4B on quench-ageing by this technique, due to irregular changes in the intensities of the diffraction peaks. This effect was thought to be a result of a large and variable grain size of this alloy in the as-quenched condition (Fig. 80). Therefore an experiment was carried out to attempt to obtain satisfactory data using specimens with a smaller and more uniform grain size. For this purpose the quenched specimens were cold rolled, and the grain size was reduced. However the results obtained were better but still not reproducible enough to determine the transformation curves (fraction transformed vs Lnt) of this alloy.

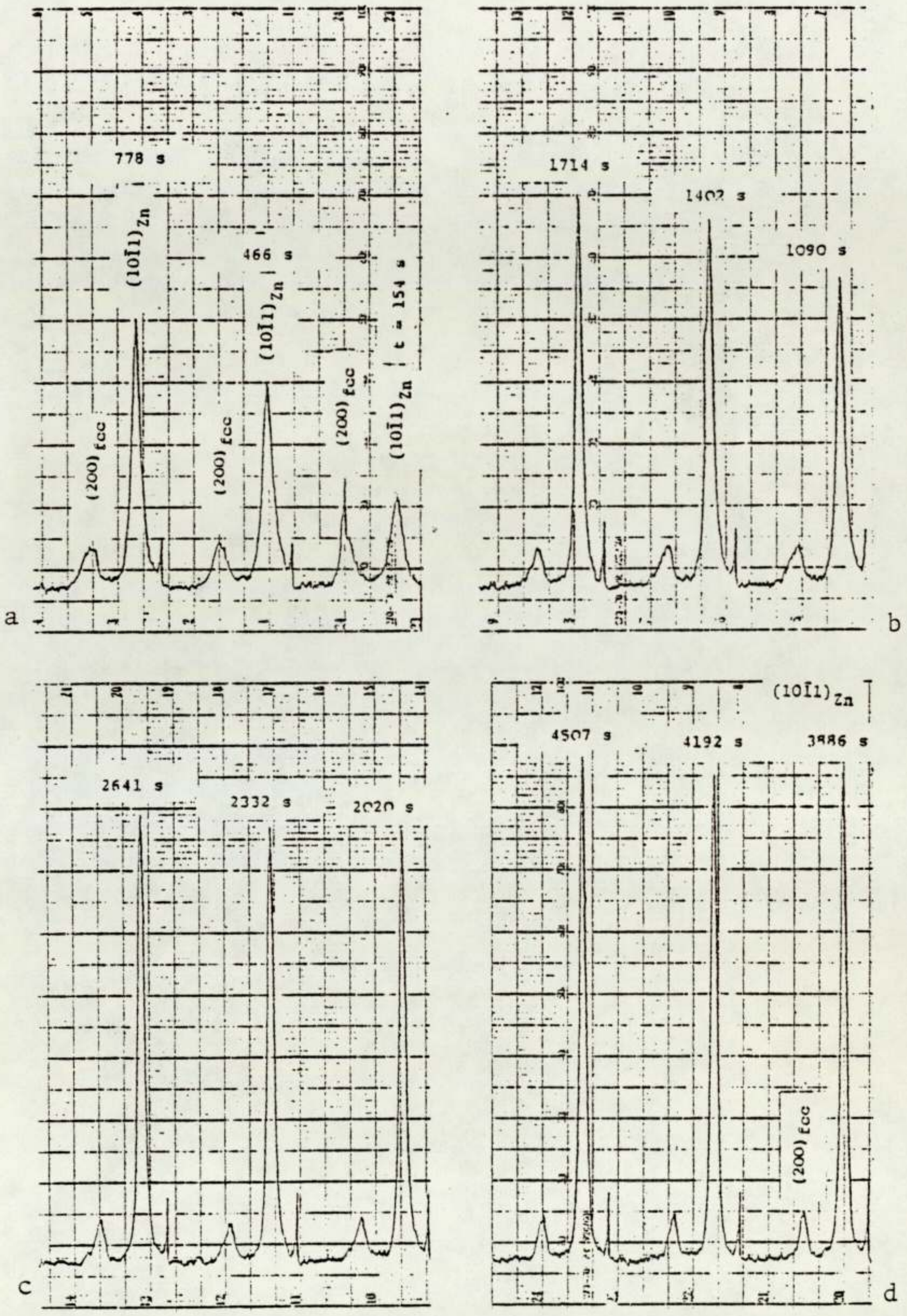

Fig. 98 Relative changes in the diffraction peaks of alloy 1B during transformation at room temperature

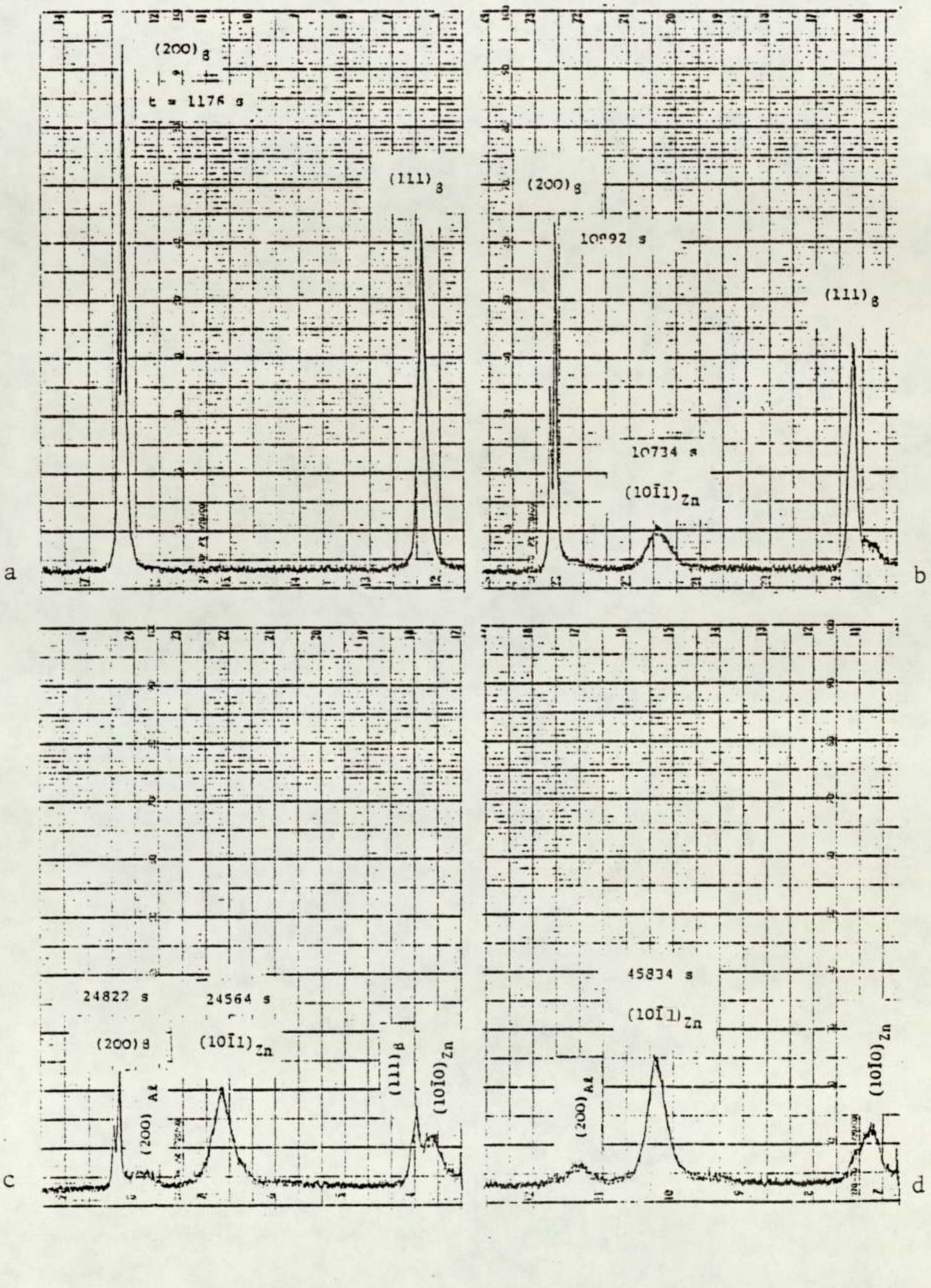

Fig. 99 Relative changes in the size of diffraction peaks of alloy 2B on quench-ageing at room temperature

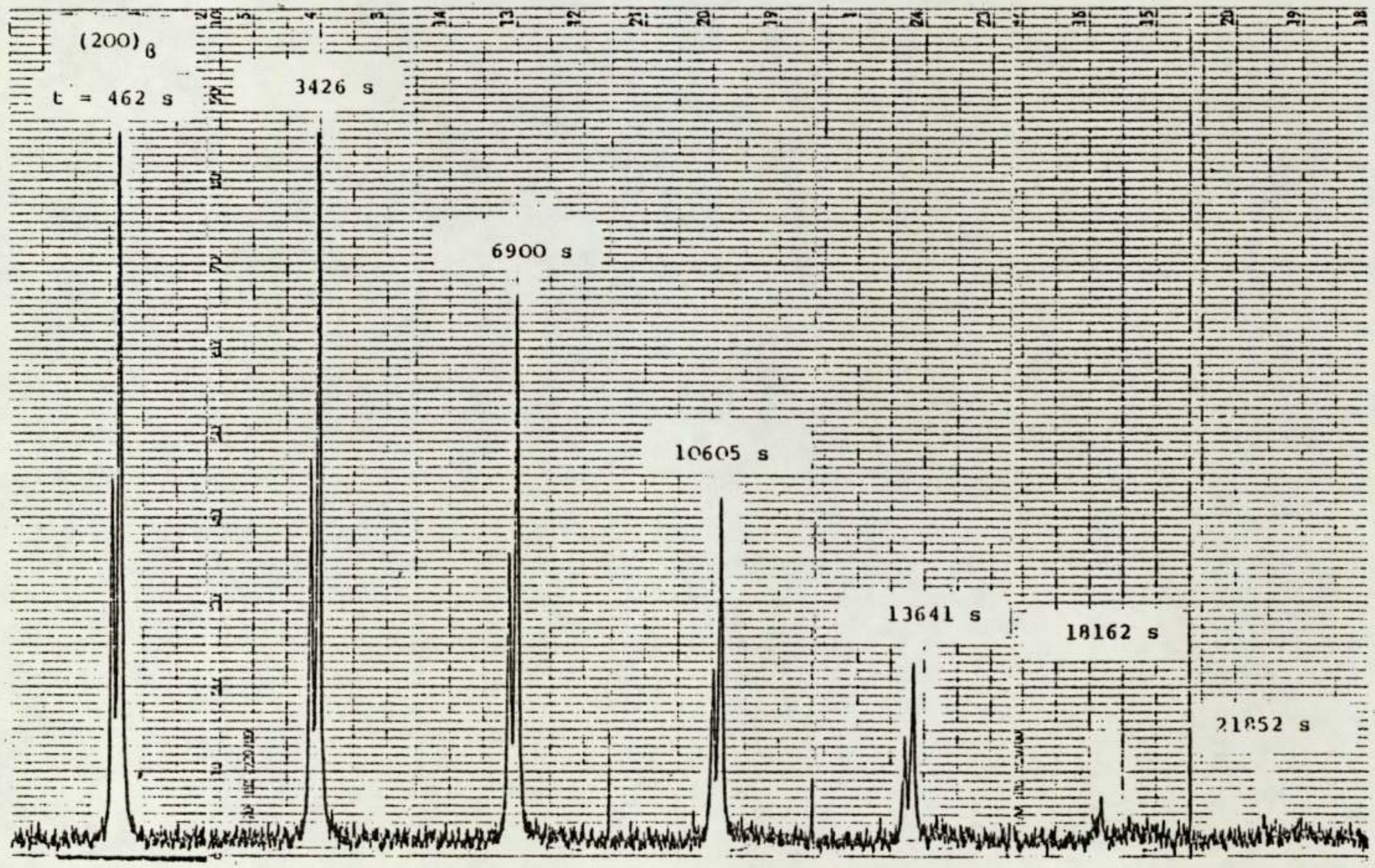

Fig. 100 Decrease in the size of $(200)_\beta$ diffraction peak of alloy 3B during transformation at room temperature

TABLE 6

Data for decomposition of the β phase of Alloy 1B on Ageing at ∿22°C (Room Temperature) Determined from the intensities of the $(10\bar{1}1)_{Zn}$ X-ray Diffraction Peak.

Time(s)	Ln time	Fraction Transformed f	Fraction Transformed f_c	$\ln\ln\frac{1}{1-f}$	$\ln\frac{f}{1-f}$
154	5.04	0.280	0.272	-1.113	-0.945
466	6.14	0.630	0.640	-0.006	0.532
778	6.66	0.700	0.733	0.186	0.847
1090	6.99	0.765	0.798	0.370	1.180
1402	7.25	0.820	0.856	0.539	1.516
1714	7.45	0.870	0.890	0.713	1.901
2020	7.61	0.900	0.930	0.834	2.197
2332	7.76	0.925	0.956	0.952	2.512
2641	7.88	0.950	0.983	1.097	2.944
2956	7.99	0.970	0.995	1.255	3.476
3265	8.09	0.985	0.998	1.435	4.185
3574	8.18	0.995	0.999	1.667	5.293
3886	8.27	∿1.000	1.000	∞	∞
4192	8.34	1.000	1.000	∞	∞

TABLE 7a

Decomposition of the β-phase of Alloy 2B on Ageing at ∼23°C (Room temperature) Determined from the intensities of $(200)_\beta$ X-ray Diffraction Peaks.

Time(s)	Ln time	Fraction Transformed		$\mathrm{LnLn}\,\frac{1}{1-f}$	$\mathrm{Ln}\,\frac{f}{1-f}$
		f	f_c		
1176	7.07	0.035	0.025	-3.335	-3.317
2268	7.73	0.070	0.050	-2.623	-2.587
3357	8.12	0.117	0.113	-2.084	-2.021
4446	8.40	0.165	0.155	-1.713	-1.622
5538	8.62	0.213	0.196	-1.429	-1.307
6630	8.80	0.261	0.249	-1.196	-1.041
7722	8.95	0.304	0.303	-1.015	-0.828
8814	9.08	0.348	0.347	-0.849	-0.628
9906	9.20	0.391	0.396	-0.701	-0.443
10992	9.31	0.435	0.426	-0.561	-0.262
12084	9.40	0.478	0.453	-0.431	-0.088
13176	9.49	0.513	0.479	-0.329	0.052
14268	9.57	0.539	0.496	-0.256	0.156
15357	9.64	0.561	0.526	-0.195	0.245
16449	9.71	0.583	-	-0.134	0.335
18270	9.81	0.652	0.603	0.054	0.628
19362	9.87	0.670	0.621	0.103	0.708
20454	9.93	0.696	0.638	0.175	0.828
21546	9.98	0.728	0.661	0.264	0.985
22638	10.03	0.764	0.686	0.367	1.175
23730	10.08	0.774	0.699	0.397	1.231
24822	10.12	0.800	0.727	0.476	1.386
25914	10.16	0.817	0.733	0.530	1.496
27006	10.20	0.835	0.748	0.589	1.622
28104	10.24	0.844	0.760	0.620	1.688

TABLE 7a (continued)

		Fraction Transformed			
Time(s)	Ln time	f	f_c	$\mathrm{LnLn}\,\frac{1}{1-f}$	$\mathrm{Ln}\,\frac{f}{1-f}$
29196	10.28	0.857	0.780	0.665	1.791
30288	10.32	0.870	0.791	0.713	1.901
31380	10.35	0.891	0.809	0.796	2.101
32472	10.39	0.900	0.804	0.834	2.197
33564	10.42	0.913	-	0.893	2.351
36273	10.50	0.930	0.829	0.978	2.587
37362	10.53	0.929	0.841	1.029	2.734
38454	10.56	0.948	0.847	1.084	2.903
38546	10.59	0.957	0.855	1.146	3.103
40632	10.61	0.963	0.860	1.193	3.259
41724	10.64	0.970	0.866	1.255	3.476
42759	10.66	0.974	0.870	1.295	3.623
43908	10.69	0.978	0.871	1.339	3.795
45000	10.71	0.983	-	1.405	4.057
46092	10.74	0.987	-	1.469	4.330
47184	10.76	0.991	-	1.550	4.702
75864	11.24	1.000	-	∞	∞
76956	11.25	1.000	1.000	∞	∞
78048	11.27	1.000	1.000	∞	∞

TABLE 7b

Decomposition of the β-phase of Alloy 2B on Ageing at 60°C Determined from the Intensities of $(200)_\beta$ X-ray Diffraction Peaks

Time(s)	Ln time	Fraction Transformed (f)	$\text{LnLn}\,\frac{1}{1-f}$	$\text{Ln}\,\frac{f}{1-f}$
60	4.09	0.316	-0.968	-0.772
120	4.79	0.105	-2.199	-2.143
240	5.48	0.316	-0.968	-0.772
300	5.70	0.290	-1.072	-0.895
360	5.89	0.342	-0.871	-0.654
420	6.04	0.368	-0.779	-0.541
480	6.17	0.211	-1.440	-1.319
540	6.29	0.368	-0.779	-0.541
600	6.40	0.526	-0.292	0.104
720	6.58	0.684	0.142	0.772
840	6.73	0.895	0.813	2.143
960	6.87	0.947	1.078	2.883
1080	6.99	0.974	1.295	3.623
1200	7.09	0.990	1.527	4.595
1440	7.27	1.000	∞	∞
1800	7.50	1.000	∞	∞

TABLE 7c

Decomposition of the β-phase of Alloy 2B on Ageing at 100°C Determined from the Intensities of $(200)_\beta$ X-ray Diffraction Peaks.

Time(s)	Ln time	Fraction Transformed (f)	LnLn $\frac{1}{1-f}$	Ln $\frac{f}{1-f}$
20	3.00	0.195	-1.528	-1.418
30	3.40	0.293	-1.059	-0.881
50	3.91	0.707	0.205	0.881
60	4.09	0.793	0.454	1.343
80	4.38	0.921	0.932	2.456
100	4.61	0.982	1.391	3.999
120	4.79	0.994	1.632	5.110
150	5.01	∼1.000	∞	∞
180	5.19	1.000	∞	∞

TABLE 8a

Decomposition of the β-phase of Alloy 2B on Ageing at $\sim 23^{\circ}$C (Room temperature) Determined from the Intensities of $(10\bar{1}1)_{Zn}$ X-ray Diffraction Peaks.

Time(s)	Ln time	Fraction Transformed		$\ln\ln \frac{1}{1-f}$	$\ln \frac{f}{1-f}$
		f	f_c		
2007	7.60	0.012	-	-4.417	-4.411
3093	8.04	0.041	0.034	-3.173	-3.152
4182	8.34	0.087	0.079	-2.397	-2.351
5274	8.57	0.134	0.116	-1.939	-1.866
6366	8.76	0.186	0.155	-1.581	-1.476
7458	8.92	0.238	0.186	-1.303	-1.164
8550	9.05	0.291	0.225	-1.067	-0.891
9642	9.17	0.337	0.261	-0.889	-0.677
10734	9.28	0.384	0.305	-0.725	-0.473
11826	9.38	0.430	0.358	-0.576	-0.282
12918	9.47	0.477	0.417	-0.434	-0.092
14010	9.55	0.512	0.465	-0.332	0.048
15102	9.62	0.547	0.497	-0.233	0.189
16188	9.69	0.581	-	-0.139	0.327
18012	9.80	0.643	0.599	0.030	0.588
19104	9.86	0.673	0.624	0.111	0.722
20196	9.91	0.698	0.660	0.180	0.838
21288	9.97	0.721	0.696	0.244	0.949
22380	10.02	0.744	0.698	0.309	1.067
23472	10.06	0.765	0.714	0.370	1.180
24564	10.11	0.780	0.730	0.415	1.266
25656	10.15	0.793	0.753	0.454	1.343
26748	10.19	0.802	0.775	0.482	1.399
27840	10.23	0.814	0.802	0.520	1.476
28932	10.28	0.826	0.818	0.559	1.558

TABLE 8a (Continued)

Time(s)	Ln time	Fraction Transformed		LnLn $\frac{1}{1-f}$	Ln $\frac{f}{1-f}$
		f	f_c		
30024	10.31	0.837	0.833	0.596	1.636
31116	10.35	0.849	0.844	0.637	1.727
32208	10.38	0.861	0.869	0.680	1.824
33300	10.41	0.872	-	0.721	1.919
36012	10.50	0.901	0.912	0.838	2.208
37104	10.52	0.919	0.921	0.922	2.429
38196	10.55	0.930	0.936	0.978	2.587
39288	10.58	0.942	0.950	1.046	2.788
40374	10.60	0.954	0.962	1.125	3.032
41466	10.63	0.965	0.968	1.210	3.317
42558	10.66	0.971	0.960	1.264	3.511
43650	10.68	0.977	0.975	1.328	3.749
44742	10.70	0.980	0.963	1.364	3.892
45834	10.73	0.983	0.985	1.405	4.057
46926	10.76	0.988	0.987	1.487	4.411
75618	11.23	0.994	0.980	1.632	5.110
76710	11.25	1.000	1.000	∞	∞

TABLE 8b

Decomposition of the β-phase of Alloy 2B on Ageing at 100°C Determined from the Intensities of $(10\bar{1}1)_{Zn}$ X-ray Diffraction Peaks.

Time(s)	Ln time	Fraction Transformed (f)	$\mathrm{LnLn}\,\frac{1}{1-f}$	$\mathrm{Ln}\,\frac{f}{1-f}$
60	4.09	0.5	-0.367	-0.000
120	4.79	0.688	0.153	0.791
180	5.19	0.727	0.261	0.980
240	5.48	0.748	0.821	1.088
300	5.70	0.766	0.373	1.186
360	5.89	0.781	0.418	1.272
420	6.04	0.797	0.467	1.368
480	6.17	0.813	0.517	1.470
540	6.29	0.828	0.566	1.572
600	6.40	0.844	0.620	1.688
720	6.58	0.875	0.732	1.946
840	6.73	0.891	0.796	2.101
960	6.87	0.906	0.861	2.266
1200	7.(o	0.920	0.927	2.442
1800	7.50	0.953	1.118	3.010
4200	8.34	0.970	1.255	3.476
6000	8.70	0.990	1.527	4.595
7200	8.88	1.000	∞	∞
9000	9.11	1.000	∞	∞
13800	9.53	1.000	∞	∞

TABLE 9

Decomposition of the β-phase of Alloy 3B on Ageing at ∿21°C (Room temperature) Determined from the $(200)_\beta$ X-ray Diffraction Peaks.

Time(s)	Ln time	Fraction Transformed (f)	LnLn $\frac{1}{1-f}$	Ln $\frac{f}{1-f}$
462	6.14	0.013	-4.336	-4.330
1203	7.09	0.033	-3.395	-3.378
1944	7.57	0.053	-2.910	-2.883
2685	7.90	0.079	-2.497	-2.456
3426	8.14	0.105	-2.199	-2.143
4164	8.33	0.132	-1.955	-1.883
4902	8.50	0.171	-1.674	-1.579
5643	8.64	0.211	-1.440	-1.319
6162	8.73	0.250	-1.246	-1.099
6900	8.84	0.303	-1.019	-0.833
7644	8.94	0.355	-0.824	-0.597
8382	9.03	0.408	-0.646	-0.372
9123	9.12	0.461	-0.481	-0.156
9864	9.20	0.513	-0.329	0.052
10605	9.27	0.579	-0.145	0.319
11343	9.34	0.638	0.016	0.567
12162	9.41	0.684	0.142	0.772
12903	9.47	0.724	0.253	0.964
13641	9.52	0.763	0.364	1.169
14379	9.57	0.803	0.485	1.405
15120	9.62	0.836	0.592	1.629
15861	9.67	0.865	0.694	1.858
16602	9.72	0.895	0.813	2.143
17340	9.76	0.917	0.912	2.402
18162	9.81	0.947	1.078	2.883

TABLE 9 (Continued)

Time(s)	Ln time	Fraction Transformed (f)	LnLn $\frac{1}{1-f}$	Ln $\frac{f}{1-f}$
18900	9.85	0.961	1.177	3.204
19638	9.89	0.974	1.295	3.623
20376	9.92	0.983	1.405	4.057
21114	9.96	0.990	1.527	4.595
21852	9.99	0.996	1.709	5.518
22590	10.03	0.999	1.933	6.907
24162	10.09	-	-	-
24900	10.12	-	-	-
25638	10.15	1.000	∞	∞
26376	10.18	1.000	∞	∞
27000	10.20	1.000	∞	∞

TABLE 10

Data for Arrhenius plot (Ln time vs $^1/_T$) used for determination of activation energy for transformation of alloy 2B on quench-ageing

T($^\circ$C)	T($^\circ$K)	$^1/_T$ (K^{-1}) x 10^{-3}	Ln time(s)
23	296	3.38	9.47
60	333	3.00	6.35
100	373	2.68	3.73

Slope (Q/k) = 8.2×10^3

Activation energy (Q) = 68 kJ/mol.

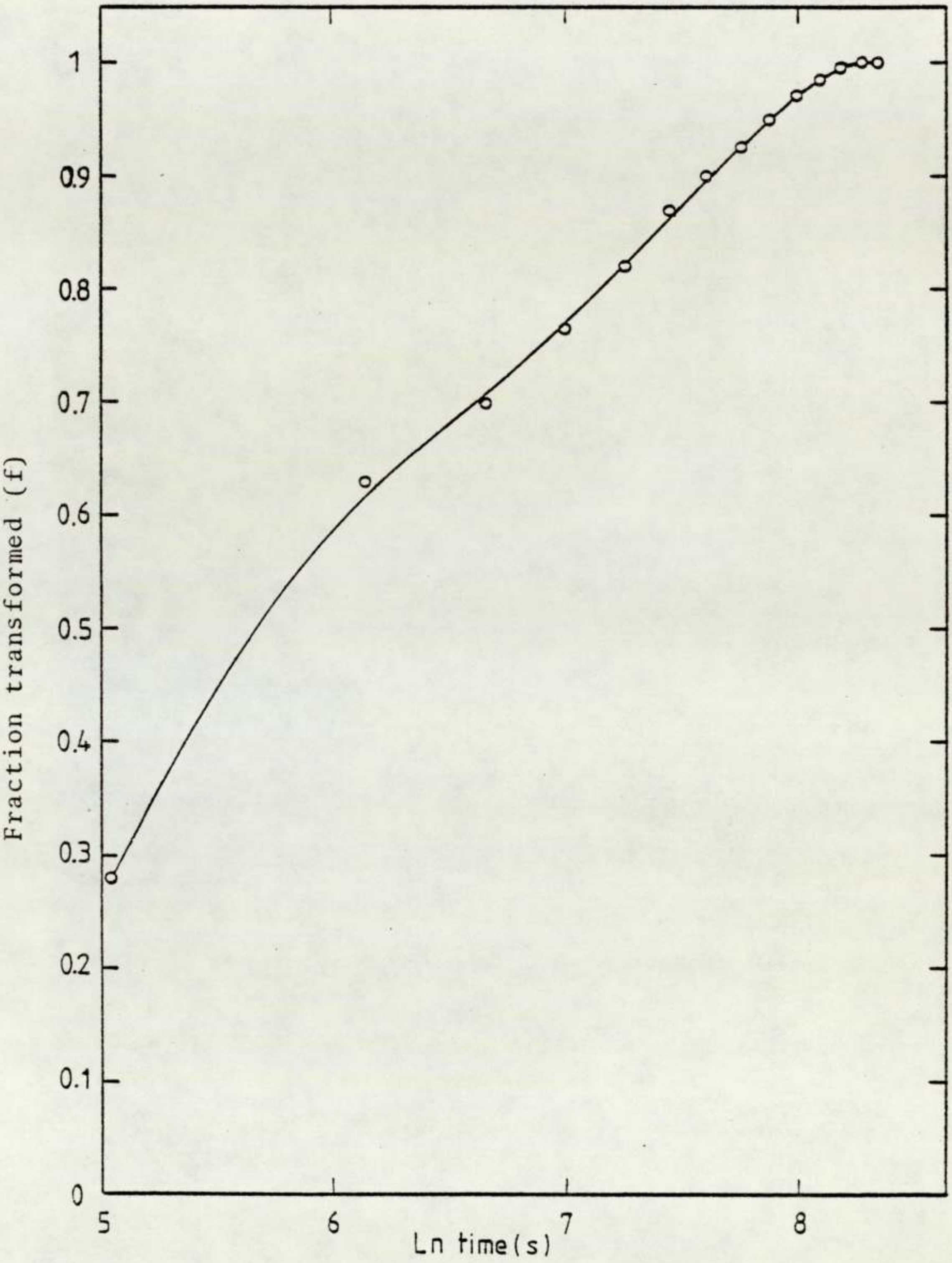

Fig. 101 Transformation curve of alloy 1B deduced from changes in the intensity of $(10\bar{1}1)_{Zn}$ diffraction peak at room temperature

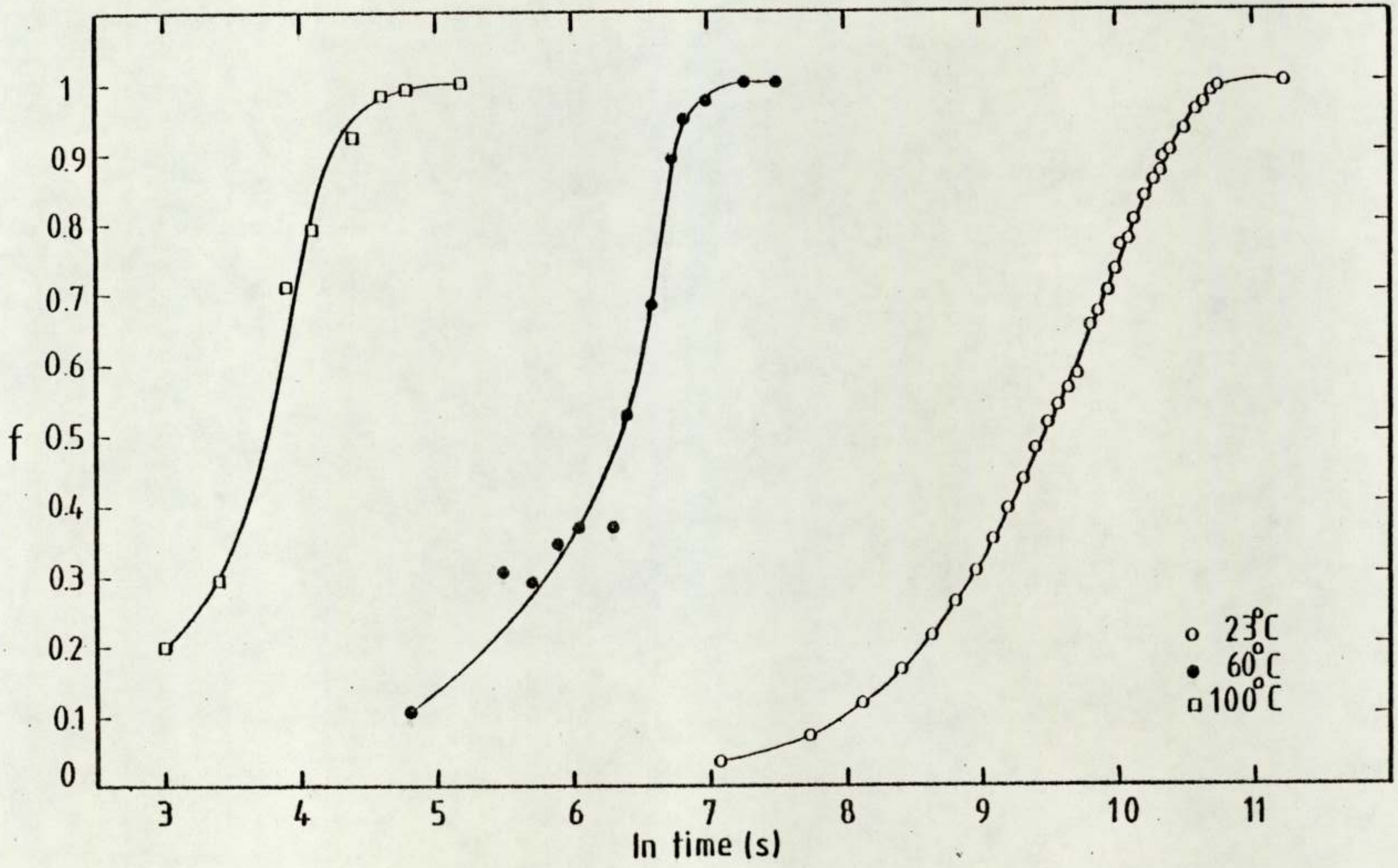

Fig. 102 Transformation curves of alloy 2B determined from the changes in the intensity of $(200)_\beta$ during quench-ageing at 23, 60 and 100°C

a)

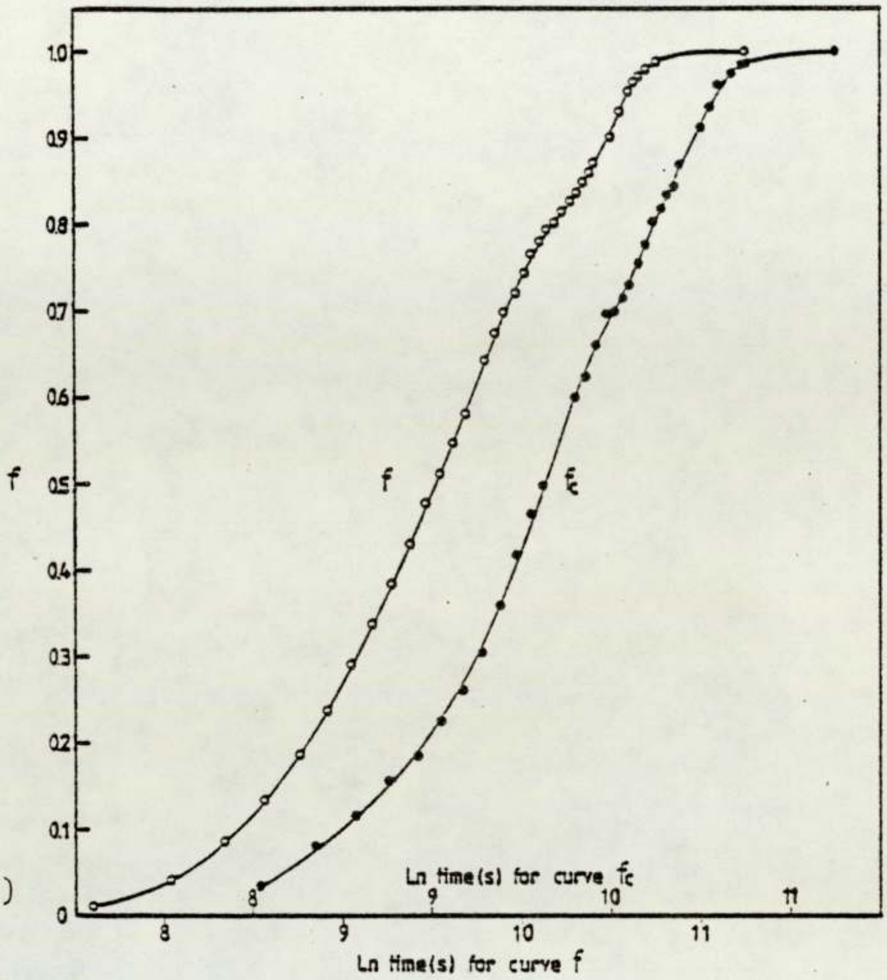

b)

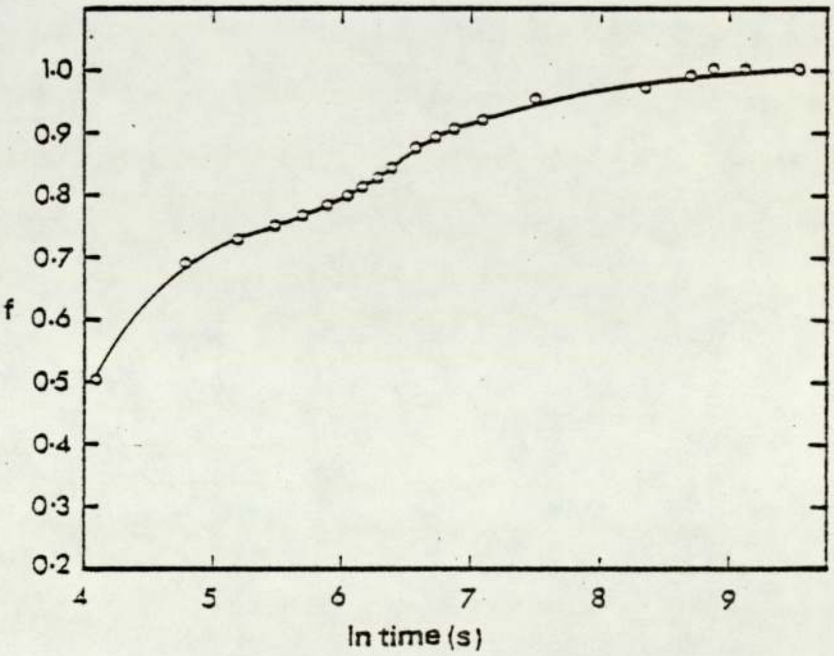

Fig. 103 Transformation curves of alloy 2B deduced from the change in the intensity of $(10\bar{1}1)_{Zn}$ diffraction peak a) at room temperature b) at 100°C

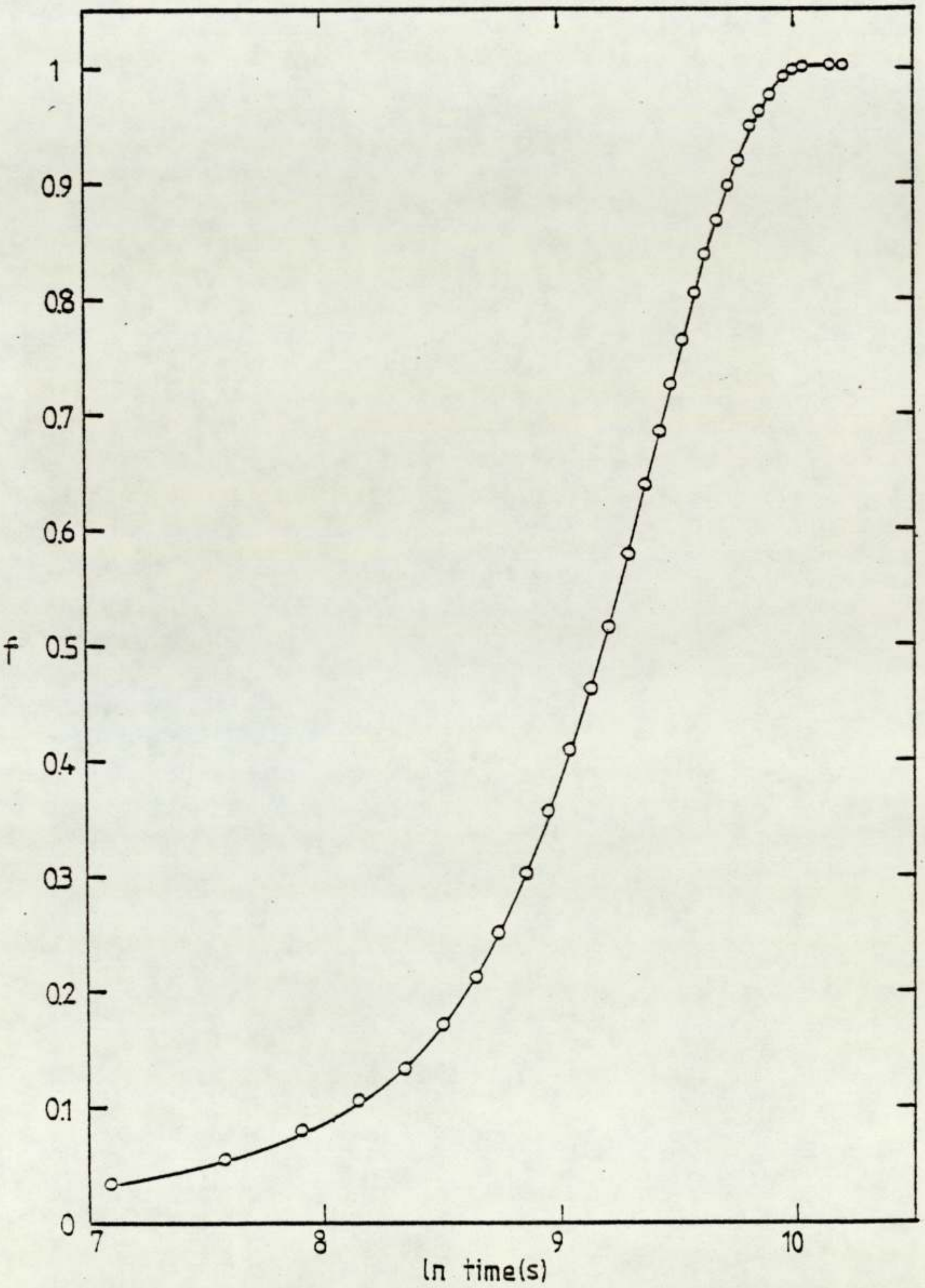

Fig. 104 Transformation curve of alloy 3B deduced from the change in the intensity of $(200)_\beta$ at room temperature

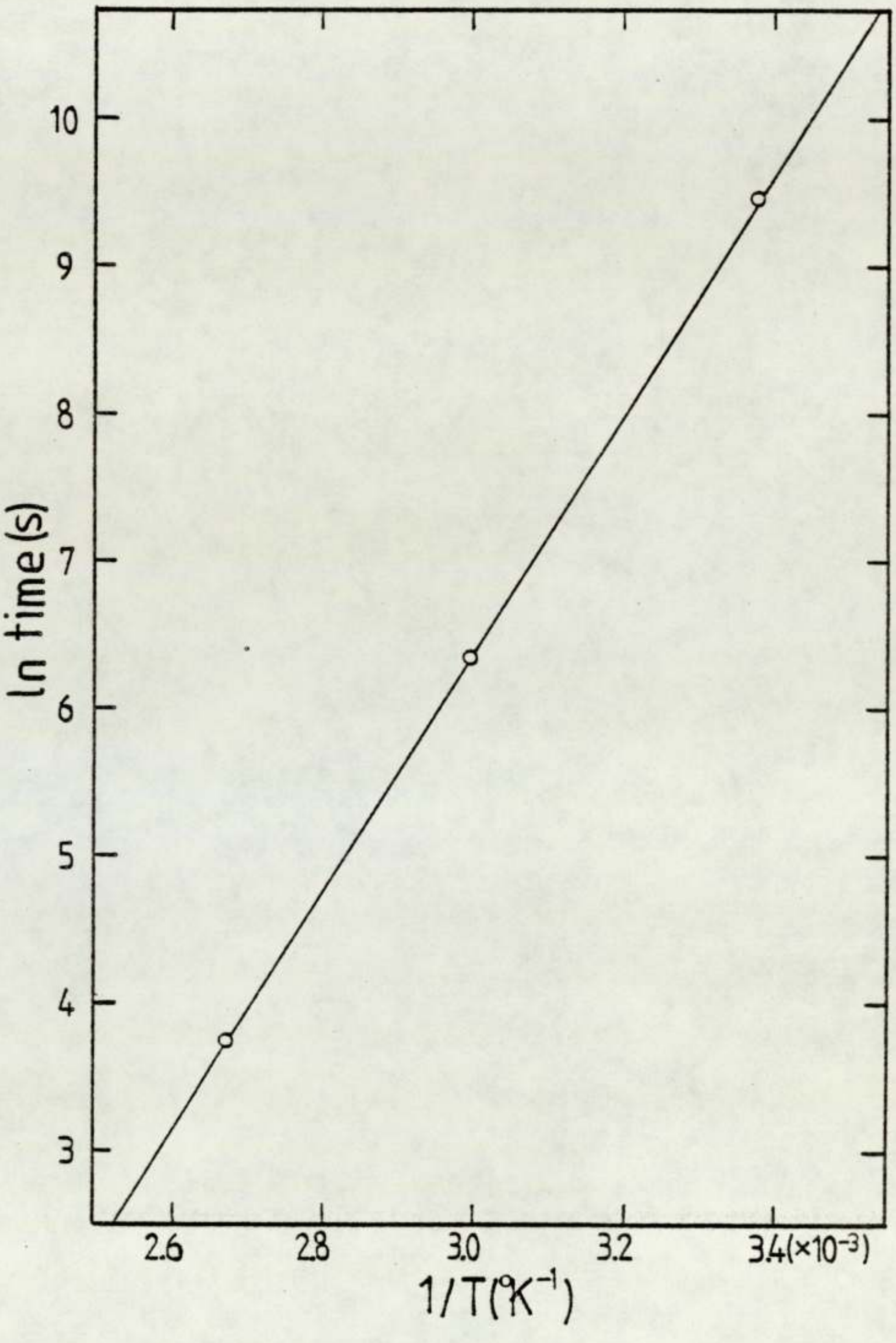

Fig. 105 Arrhenius plot for determination of activation energy for transformation of alloy 2B

3.4 Mechanical Properties

3.4.1 Impact

The results of impact tests obtained on alloys 2A, 2B and 3B are given in Table 11.

TABLE 11

Impact Results

Temperature (°C)	Energy to fracture (J)		
	Alloy 2A	Alloy 2B	Alloy 3B
-196	0.1	3.1	0.2
0	0.7	4.1	1.0
20	1.0	2.9	1.3
100	2.6	1.6	4.0
200	3.0	1.7	5.5

These results were used to plot the energy-temperature curves to show the effect of temperature on the energy absorbed in fracture, Fig. 106 and 107. Alloy 2B exhibited an unusual impact transition curve, as the energy absorbed decreased sharply above 0°C with increasing temperature (Fig. 106). This could be due to the effect of heat-treatment, since this alloy in the as-cast condition showed a normal transition curve from low to high temperature under the same conditions.

These results show that the zinc-aluminium-low copper alloys have poor impact strength as their energy absorbed values are much lower than the common engineering alloys. However this is not a great disadvantage for bearing applications, where impact loading is not an important service factor.

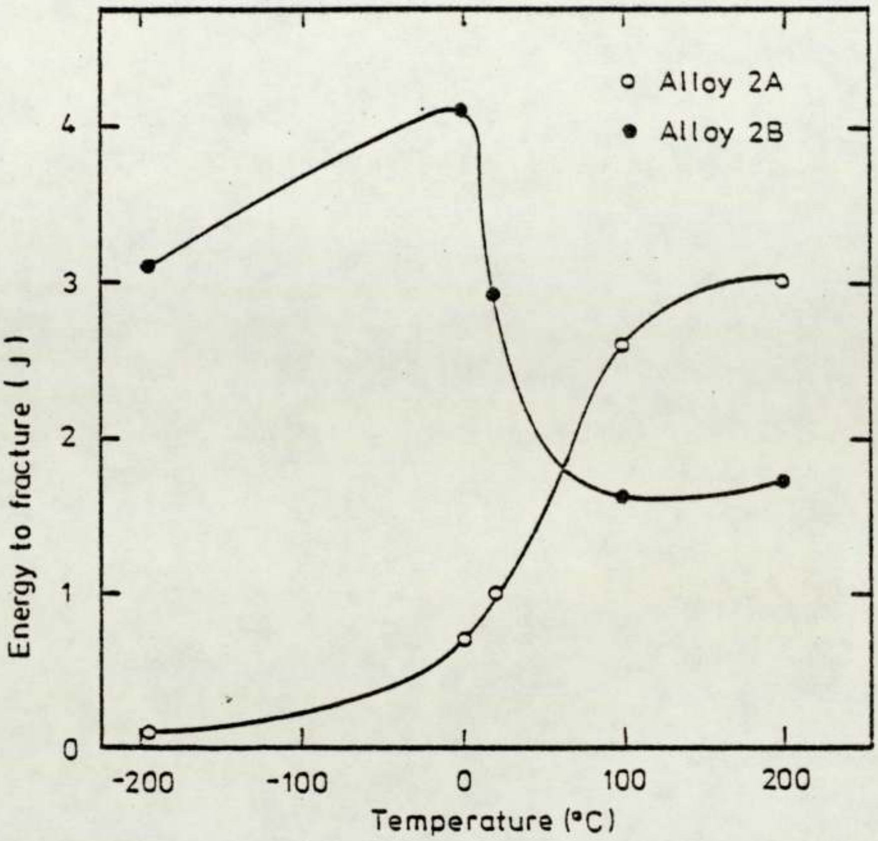

Fig. 106 Energy to fracture versus temperature curves for alloys 2A and 2B

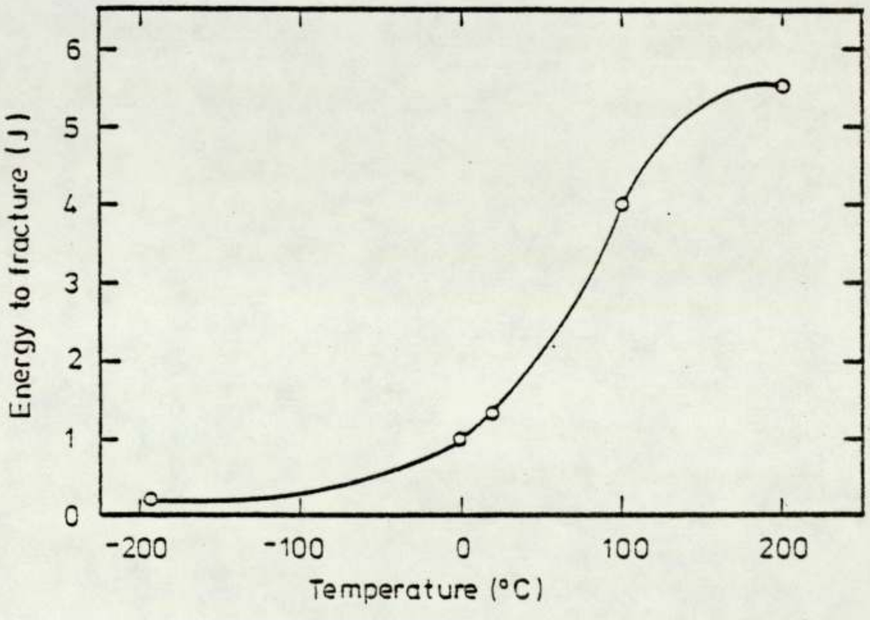

Fig. 107 Charpy impact ductile to brittle fracture transition curve for alloy 3B

3.4.2 Hot Tensile

Stress (σ) and strain (ε) measurements were obtained during tensile deformation of alloys 1A, 1B, 2A, 2B, 3A, 3B and 6, at different temperatures. The results were used to plot stress-strain curves of the alloys, Figs. 108, 109, 110, 111, 112, 113 and 114. The ultimate tensile strength (U.T.S.) and 0.05% proof stress ($\sigma_{0.05}$) were determined from the stress-strain curves and are given in Table 12. This table also includes the measured friction stress (σ_o) values of these alloys.

The results showed that as the temperature increased the ultimate tensile strength, 0.05% proof stress and friction stress of the alloys decreased. At any given temperature, the zinc-based alloys in the as-cast condition showed a much higher tensile strength and friction stress than the same alloy in the heat-treated condition.

The results also suggest that the tensile strength of the zinc-aluminium based alloys increased both with decreasing zinc content and with increasing copper additions. This is particularly true where the results obtained from the as-cast alloys are concerned. Only alloy 2B did not follow this trend at each temperature.

The aluminium-silicon commercial alloy showed much higher hot-tensile strength and friction stress than the zinc-based alloys.

It was observed that during hot-tensile testing of the zinc-based alloys, the stress in some cases, approached zero before the failure occurred. However the stress and strain values up to fracture were not plotted in the stress-strain curves in each case, since the work was carried out principally to establish proof stresses ($\sigma_{0.05}$) and friction stresses (σ_o). The heat-treated alloys showed higher total elongations than the cast alloys at most temperatures.

The zinc-based alloys in the as-cast condition showed a measurable friction stress, but in the heat-treated condition their friction stresses were found to be zero. An example of stress-relation shown as a stress versus time curve for alloy 3B at 80°C appears in Fig. 115.

The friction stress was found to be dependent on the strength of the alloy and temperature. Stronger alloys exhibited higher friction stress, and as the temperature increased the friction stress decreased. It was also observed that the relaxation time (the time required for the stress to reach the limiting value) increased as the strength of the material increased and decreased with increasing temperature.

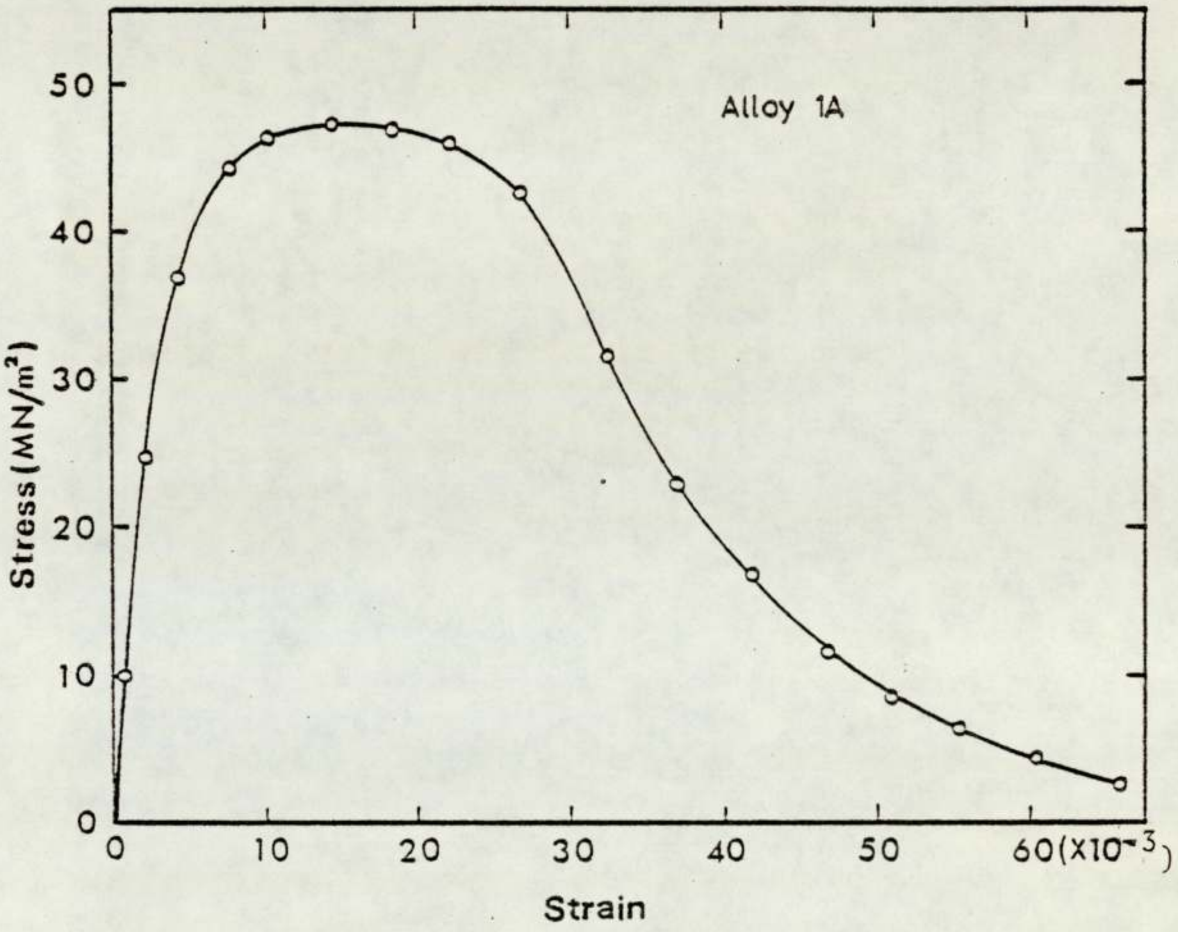

Fig. 108 Stress (σ) - strain (ε) curve for alloy 1A at 120°C

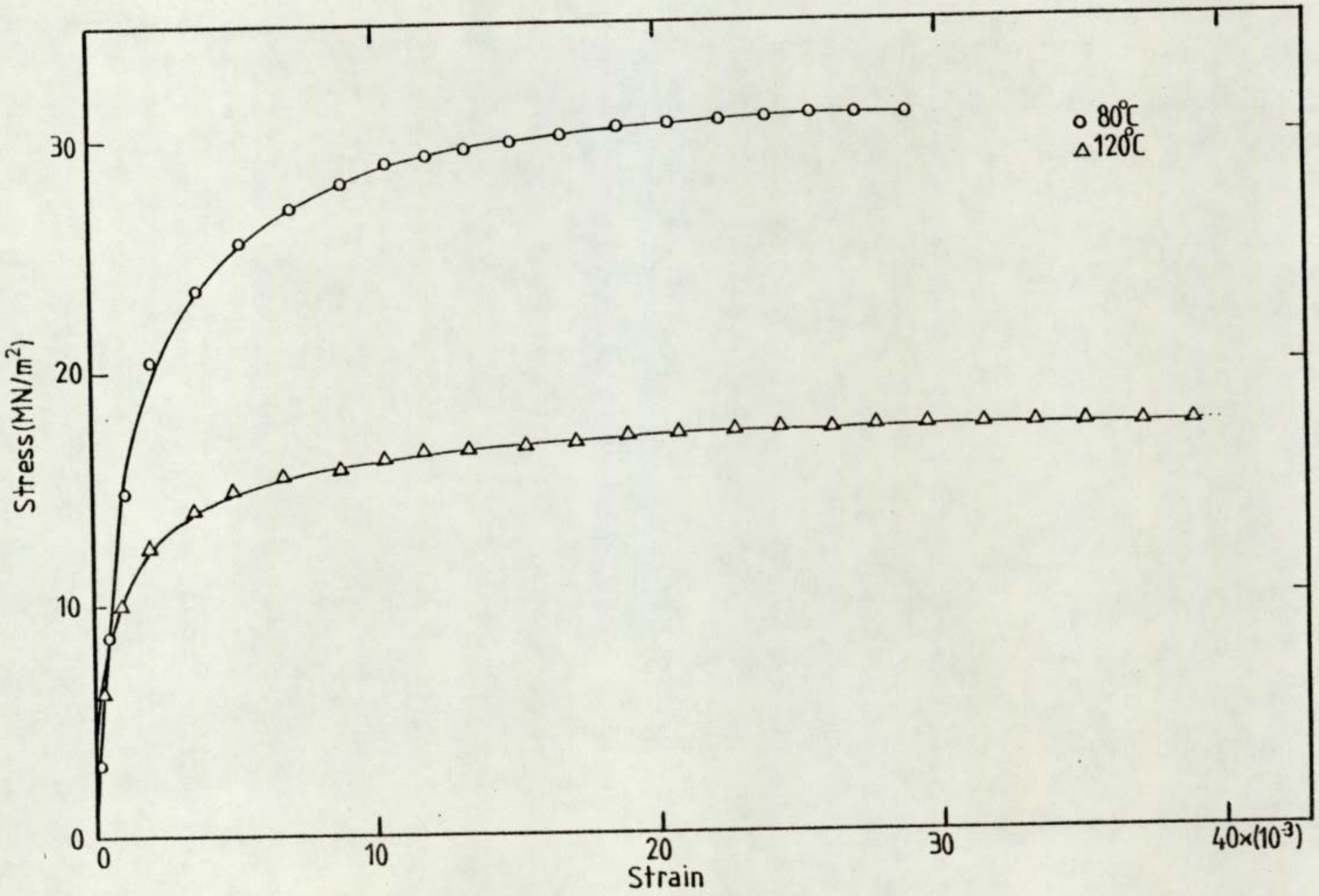

Fig. 109 Stress (σ) - strain (ε) curves of alloy 1B at 80^0 and 120^0C

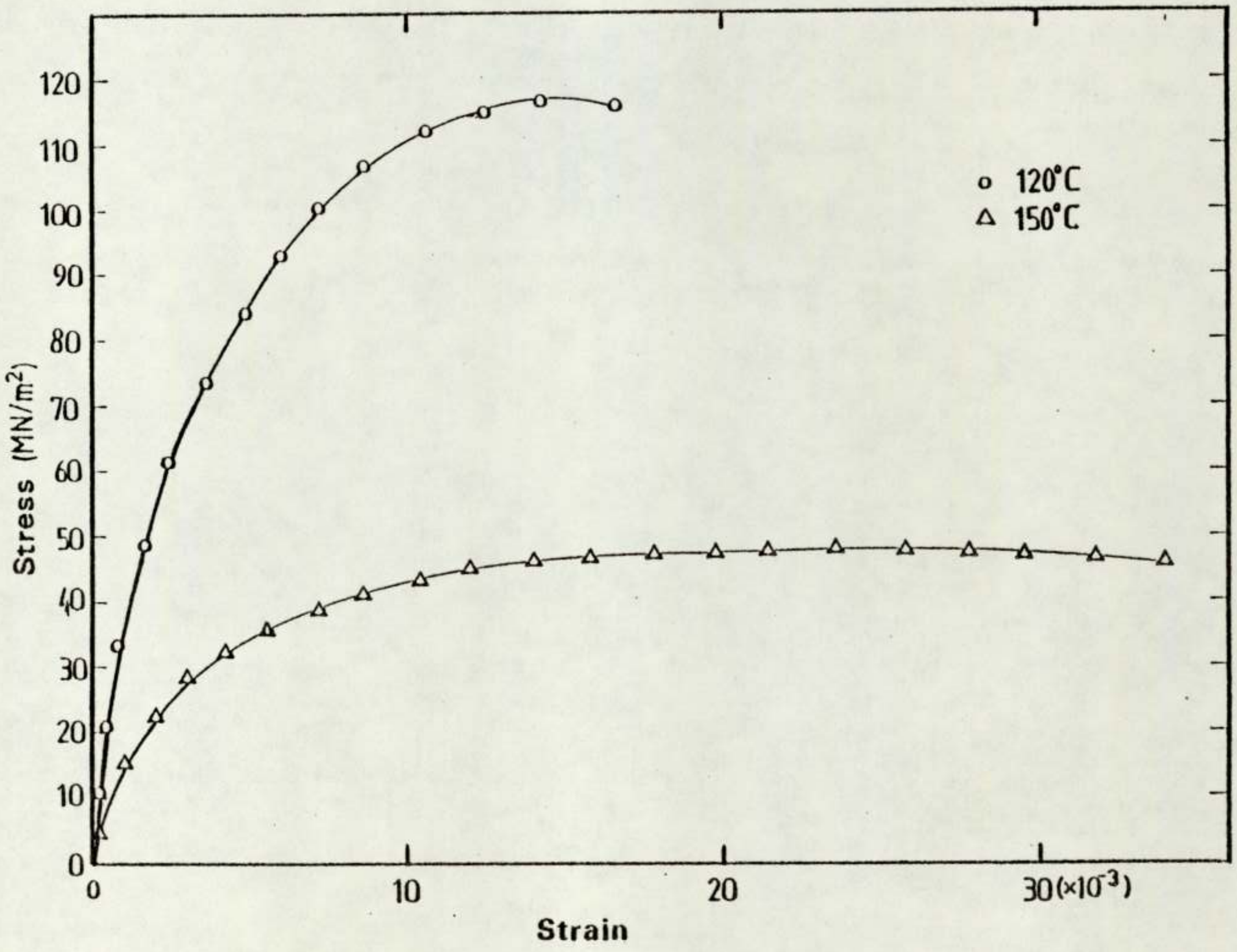

Fig. 110 Stress (σ) / strain (ε) curves of alloy 2A at 120°C and 150°C

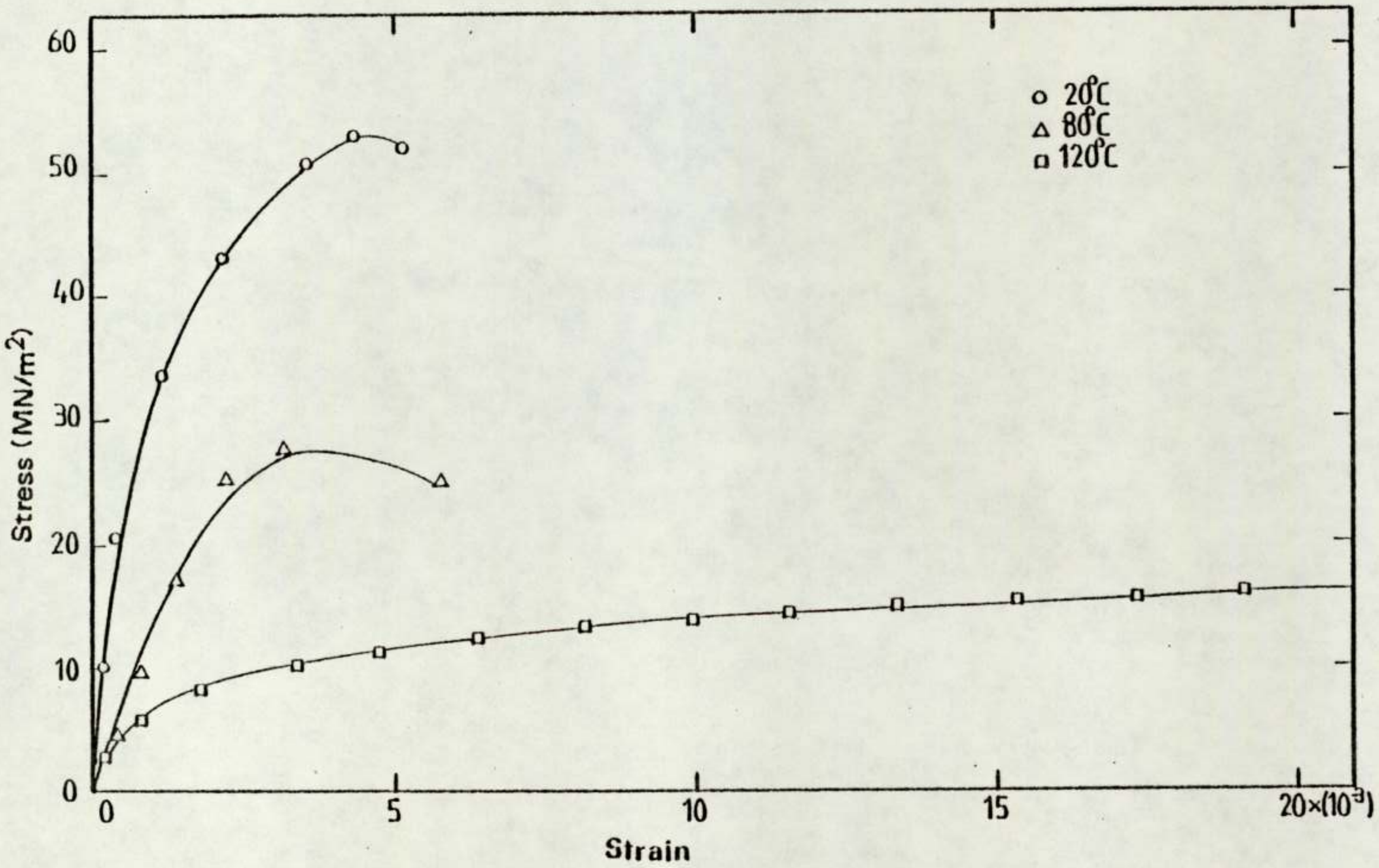

Fig. 111 Stress-strain curves of alloy 2B at 20, 80 and 120^{o}C

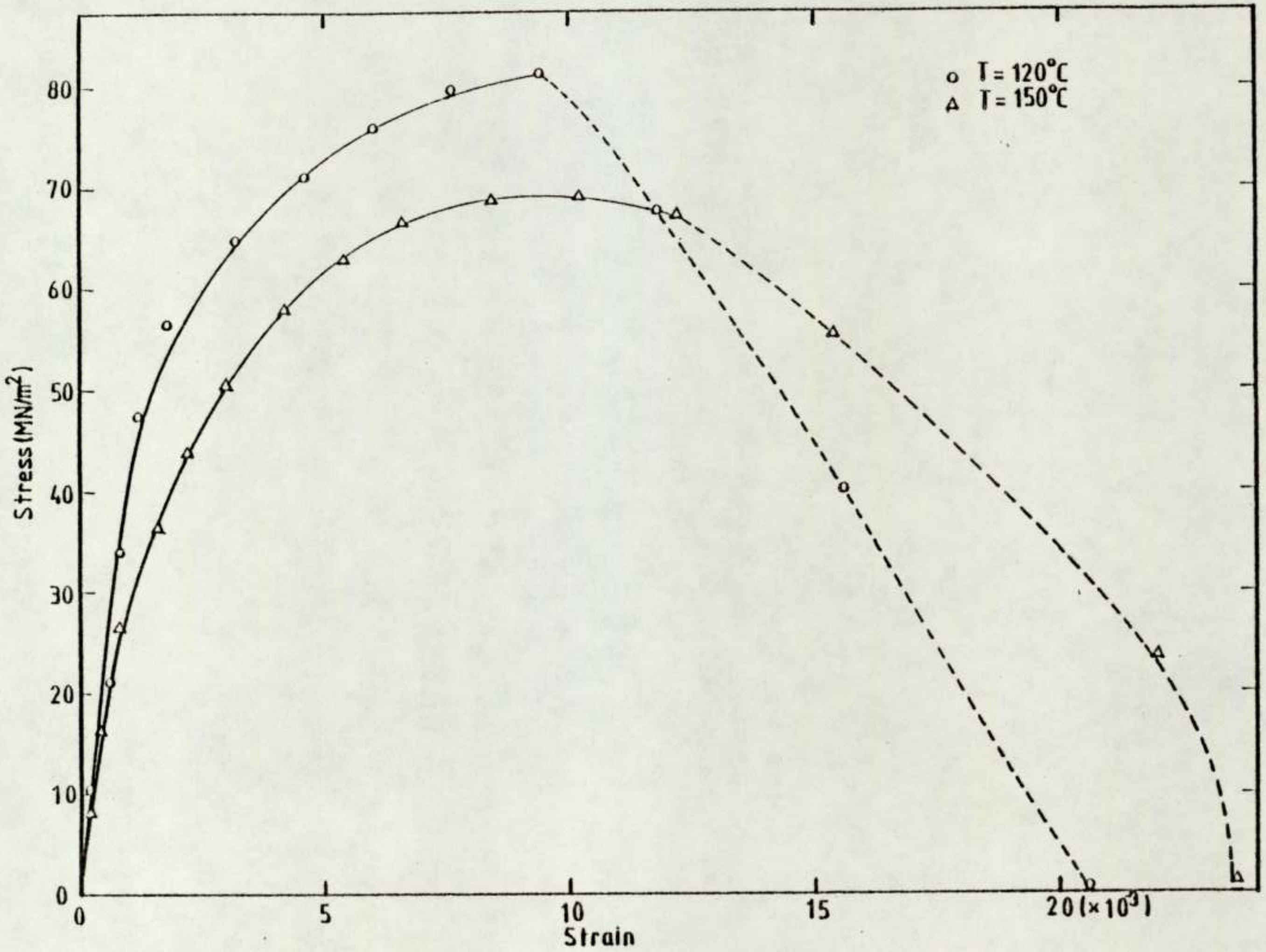

Fig. 112 Stress-strain curves of alloy 3A at 120 and 150^{o}C

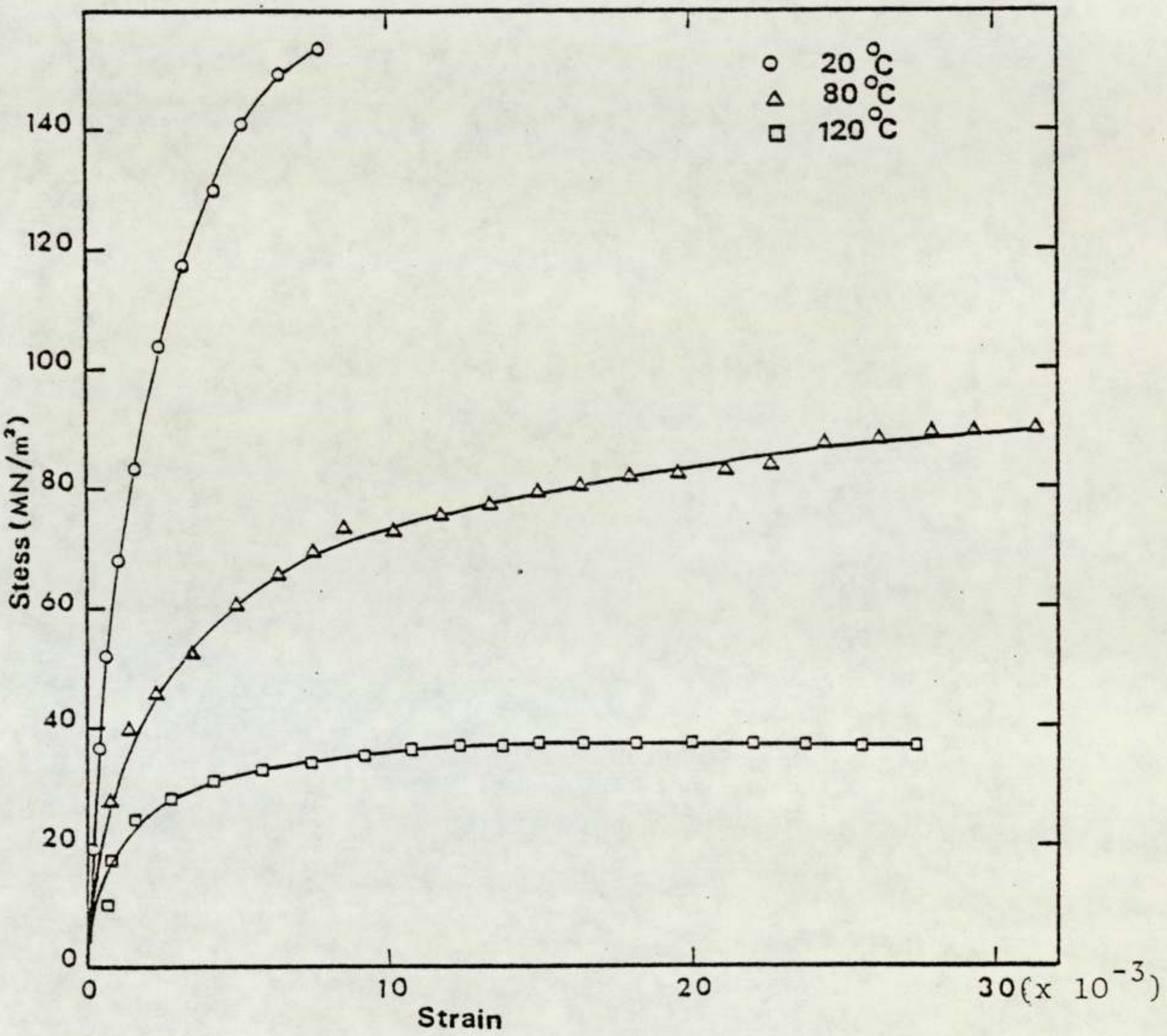

Fig. 113 Stress-strain curves for alloy 3B at 20, 80 and 120°C

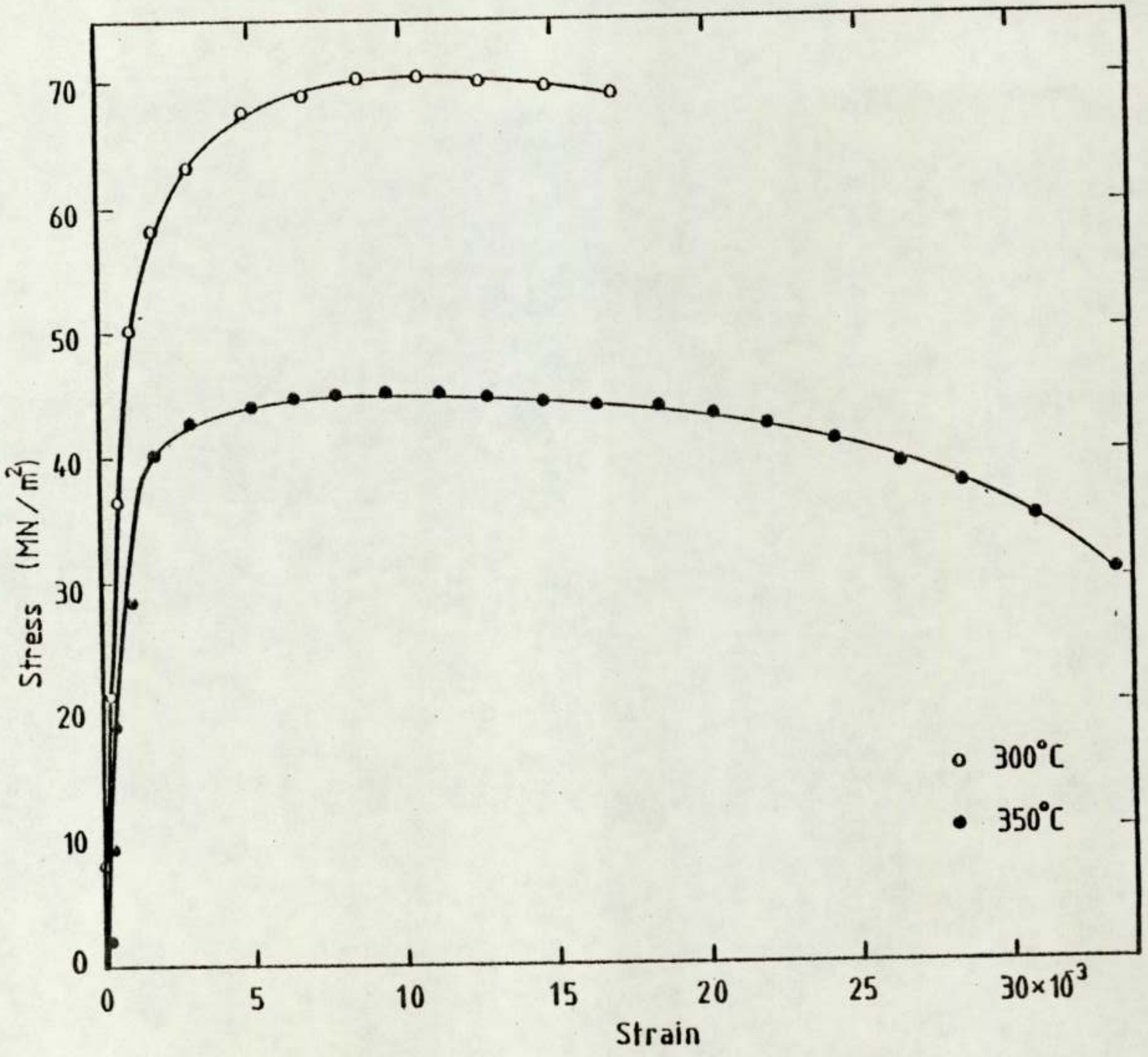

Fig. 114 Stress-strain curves of alloy 6 at 300°C and 350°C

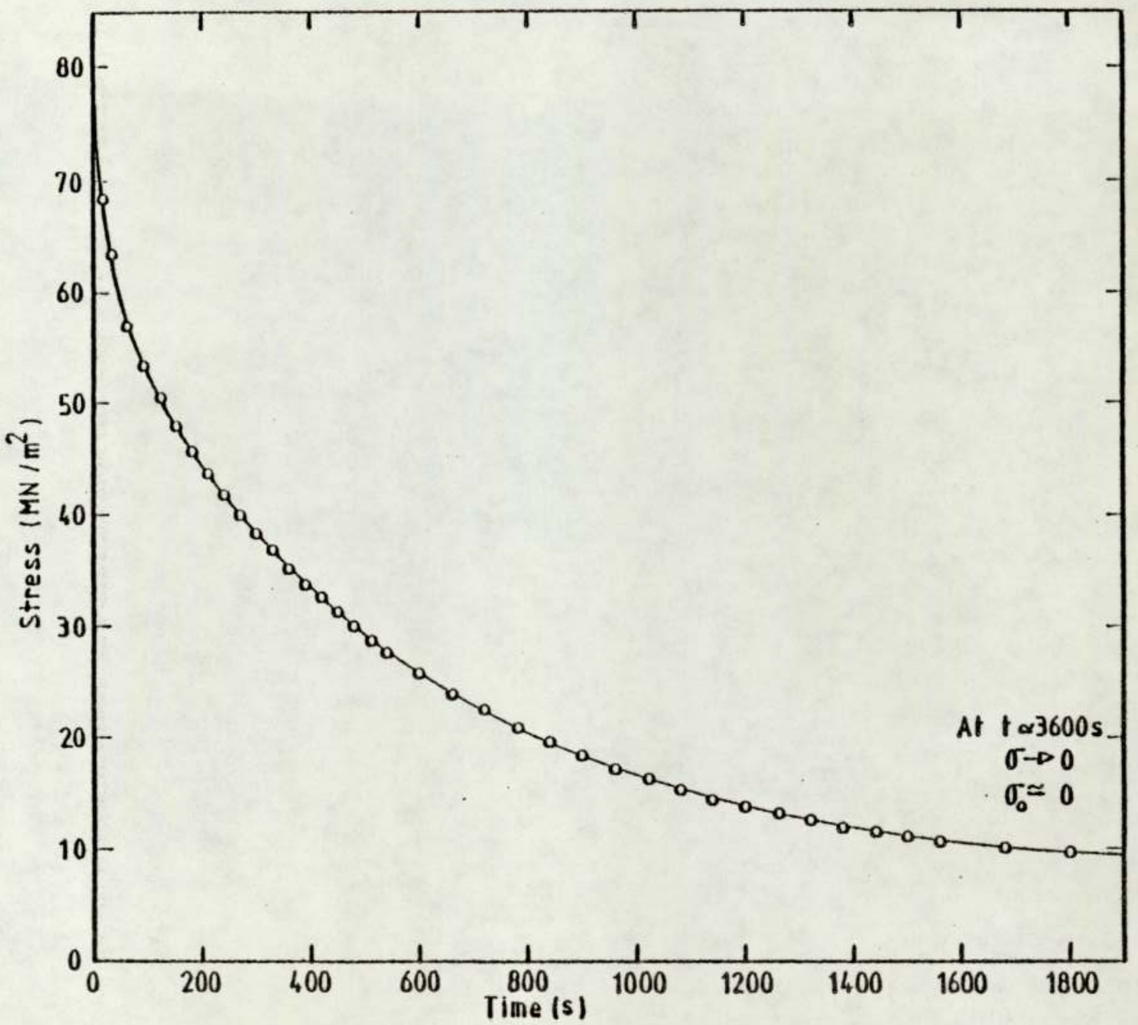

Fig. 115 Stress-relaxation curve of alloy 3B at 80°C

TABLE 12

Tensile Results of the Alloys Tested

Alloy	Temperature (°C)	$\sigma_{0.05}$ (MN/m^2)	UTS (MN/m^2)	σ_o (MN/m^2)
1A	120	24.5	47.2	7.7
1B	80	17.4	30.9	0
	120	9.9	17.4	0
2A	120	56.0	116.6	19.0
	150	21.5	48.1	7.8
2B	20	33.0	52.8	0
	80	20.5	27.2	0
	120	7.5	16.4	0
3A	120	51.0	81.2	18.0
	150	37.5	69.1	13.0
3B	20	85.0	153.7	0
	80	37.5	93.2	0
	120	21.0	37.3	0
6	300	57.0	70.5	18.5
	350	38.0	45.6	12.0

3.4.3. Creep

The variation of creep strain with time was measured for alloys 1A, 1B, 2A, 2B, 3A, 3B and 6 at various temperatures and stresses. The results were plotted as creep strain (ε) versus time (t) in Figs. 116, 117, 118, 119ab, 120, 121, 122, 123, 124, 125, 126ab, 127, 128, 129, 130ab, 131, 132, 133, and 134.

The secondary creep rates ($\dot{\varepsilon}_s$) determined from the steady state region of the curves are given in Table 13. It can be seen from this table that the as-cast alloys have much lower creep rates than the heat-treated alloys under the same test conditions.

The ternary alloys (2 and 3) in both as-cast and heat-treated conditions showed much higher creep resistance than the binary eutectoid alloy (1). This demonstrated the effect of copper additions and the zinc/aluminium ratio on the creep strength of the zinc-aluminium eutectoid alloys.

The ternary alloy with higher copper content in the as-cast condition (3A) showed lower creep rate than alloy 2A as the temperature increased. However the former in the heat-treated condition (3B) showed less creep resistance than alloy 2B.

At present there is not sufficient data available to establish the effect of composition on the creep behaviour of the zinc-aluminium based alloys. However the results suggest that the creep resistance of the heat-treated eutectoid alloys increased with decreasing zinc/aluminium ratio and with increasing copper content of their decomposed β phase.

The results in Table 13 also show that the creep properties of the zinc-based eutectoid alloys are inferior to that of the aluminium-silicon based commercial alloy (6).

The data obtained from the secondary creep stage provided useful information for the bearing applications of these alloys, where the linear dimensions are important and excessive creep deformation cannot be tolerated.

The creep rupture data which contains the time to fracture and total strain of the experimental alloys for each test condition is given in Table 14. This table allows a comparison to be made of the creep behaviour of the alloys with other materials for different applications. The creep rupture data is particularly useful for different applications, where the fracture is the main limiting factor rather than excessive deformation.

Heat-treated alloys exhibited higher total creep strain than the as-cast alloys under the same conditions (temperature and stress). Total strain of the as-cast alloys decreased as the temperature increased, but for most of the heat-treated alloys the total strain increased with temperature. A tendency was also observed for the total strain to decrease with increasing applied stress, but alloys 1B and 3B showed a maximum before decreasing sharply. These observations suggest that the total strain critically depends on creep rate and some structural factors such as grain size.

Failure of the as-cast alloys occurred without any noticeable external necking, as seen in Fig. 135. However, multiple necking occurred during the creep deformation of heat-treated alloys. Examples of the latter for alloy 3B at 80°C, 10 MN/m^2 and 150°C, 30 MN/m^2 are shown in Fig. 136. The observations suggest that the number of necks is proportional to the total strain.

Microscopic examination showed the presence of cavitation within the gauge length of the fractured specimens of the as-cast and heat-treated alloys. Figs. 137 and 138 show the polished longitudinal sections of alloys 2A and 3A, creep tested to failure at 120°C and 30 MN/m^2. Cavitation was more extensive in the heat-treated alloys as shown in the micrographs, Figs. 139, 140, 141ab and 142ab, obtained from the longitudinal sections of the fractured specimens of alloys 1B, 2B and 3B at different creep conditions.

These micrographs also show the coalescence of cavities in the necked regions where the fracture occurred. The cavity stringers were formed mostly normal to the stress axis as seen in Figs. 137, 140 and 141. However in alloy 1B the cavities were oriented parallel to the stress axis, Fig. 139 . The same observation for this alloy was reported earlier(81).

Microscopic examination also suggested that the number of cavities increased with decreasing stress and temperature. This can be seen in the micrographs, Figs. 141 and 142, which were obtained from specimens of alloy 3B fractured under different conditions (stress and temperature). It appears that the number of cavities is increased with decreasing creep rate.

These observations suggest that cavities play a great role in the creep failure of zinc-based alloys. Cavities are initially nucleated either at the second phase particles or along the grain-boundaries and can be oriented either normal or parallel to the stress axis during deformation. Failure eventually occurs in the particular necked region where growth and coalescence of these cavities is greatest.

The optical micrograph, Fig. 143, obtained from the fractured specimen of alloy 2A at 120^{o}C and 30 MN/m^{2}, shows the structural features after failure. It can be seen that cracks or cavities formed between the aluminium-rich dendrites, which are the weakest areas of the cast structure. The micrographs of the heat-treated alloys 1B and 3B (Figs. 144 and 145) near to the fracture surface, show their fine-grained structure and ε phase particles in the latter. These micrographs indicate that the fine grains of the heat-treated alloys remained essentially equiaxed during deformation. However the change in the grain size, if any, could not be determined.

Examination of the creep fracture surfaces in the scanning electron microscope showed the mixture of cavities and elongated cusps associated with ductile fracture behaviour. Fig. 146 shows the cavities, cusps, dimples and cracks in the fracture surface of alloy 3A obtained at 150°C and 20 MN/m^2.

The ductile creep fracture of the heat-treated alloys is mainly characterized by elongated cusps formed between cavities during final fracture. Examples of this for alloys 1B and 3B failed at 120°C and 20 MN/m^2 are shown in Figs. 147 and 148 respectively. These micrographs also show the fine zinc and aluminium-rich grains separating within the cusps.

As a result of these observations it may be concluded that the zinc-based eutectoid alloys, under creep conditions, fail by a typical ductile fracture in which the cavities and elongated cusps are the main features. The size of the cusps varies greatly from area to area, however a tendency seems to be evident for the size of the cusp to increase with increasing creep rate.

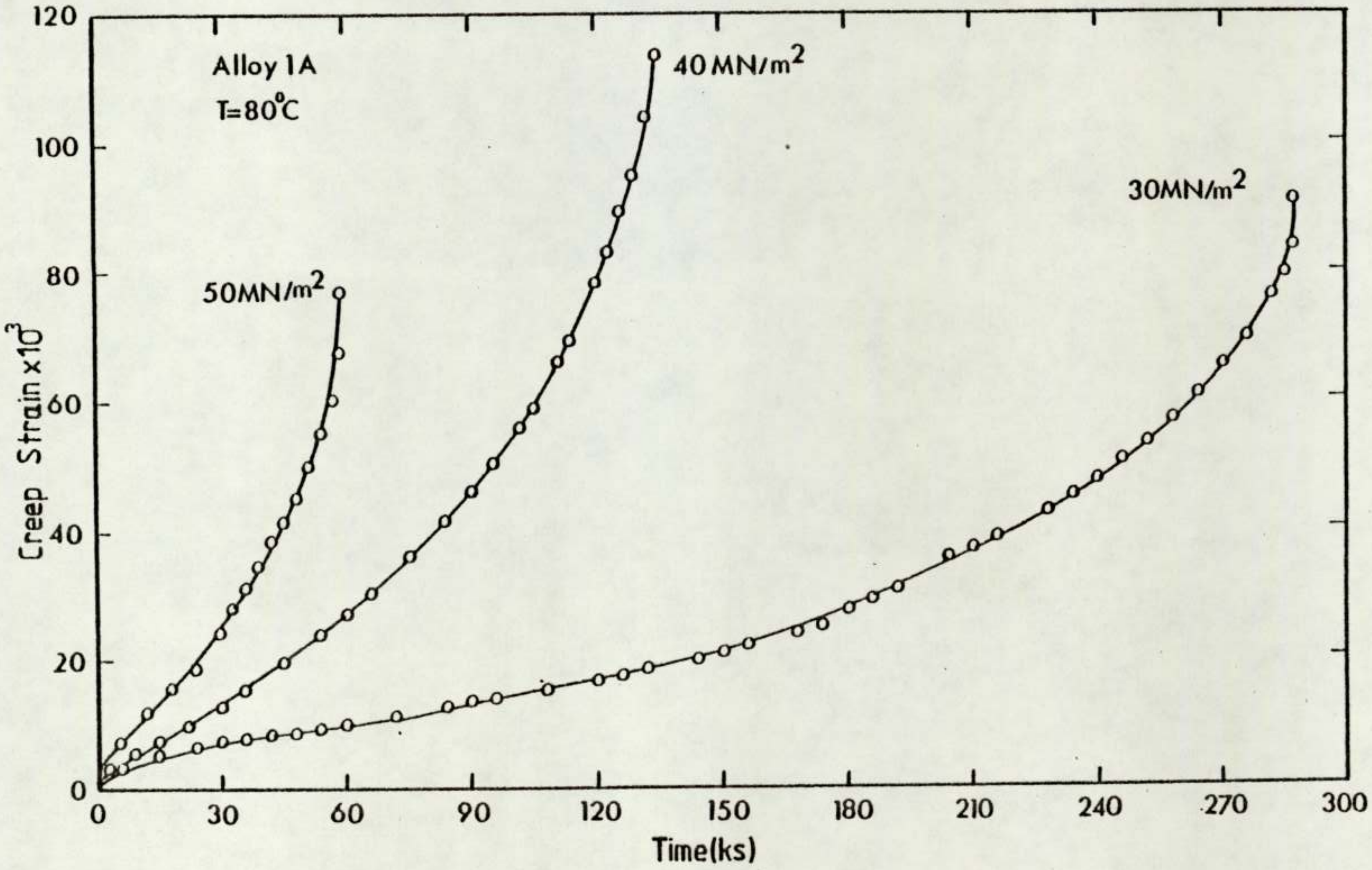

Fig. 116 Creep curves of alloy 1A at 80^{o}C and under stresses of 30, 40 and 50 MN/m^{2}

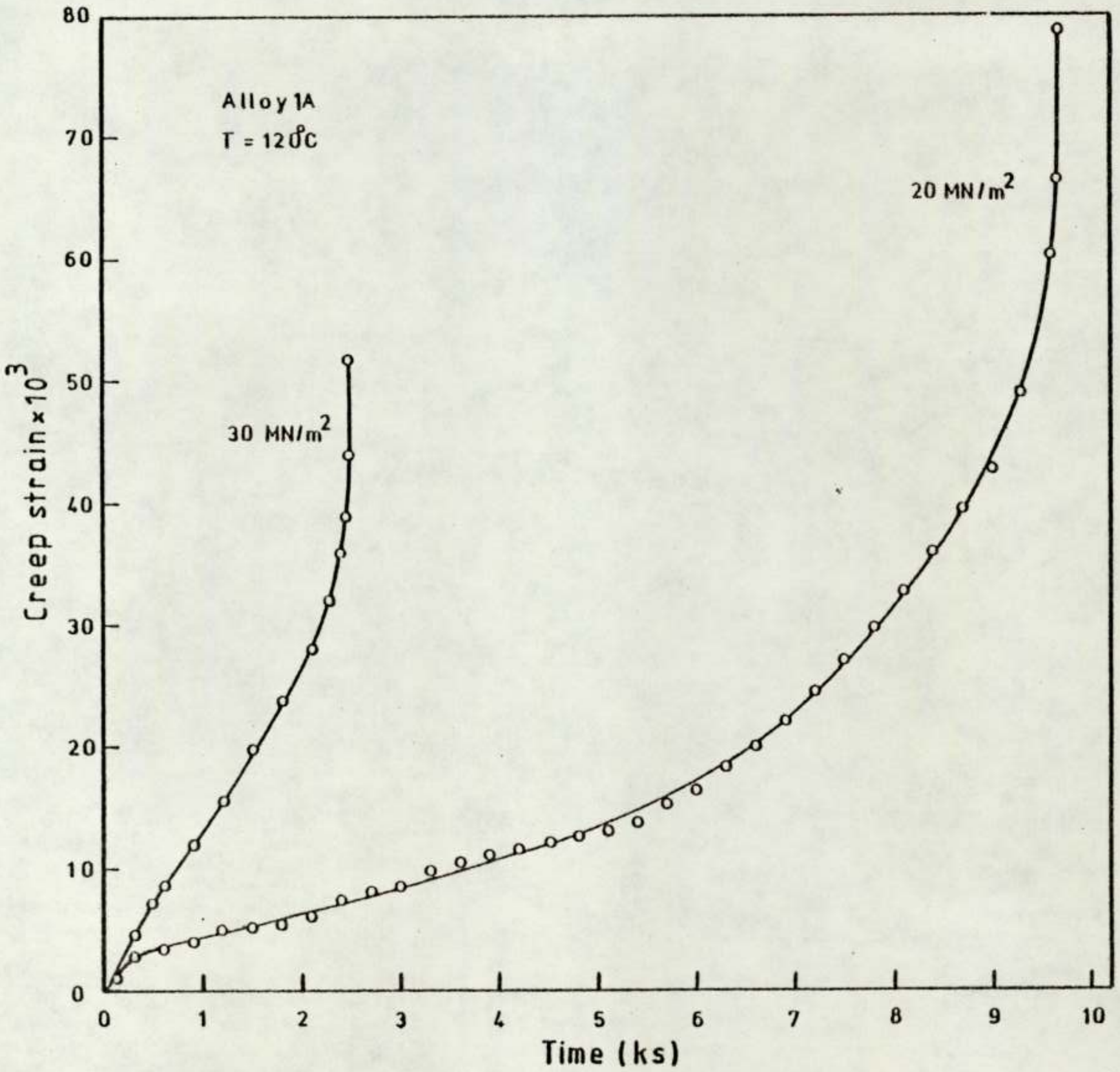

Fig. 117 Creep curves of alloy 1A at 120°C under stresses of 20 and 30 MN/m^2

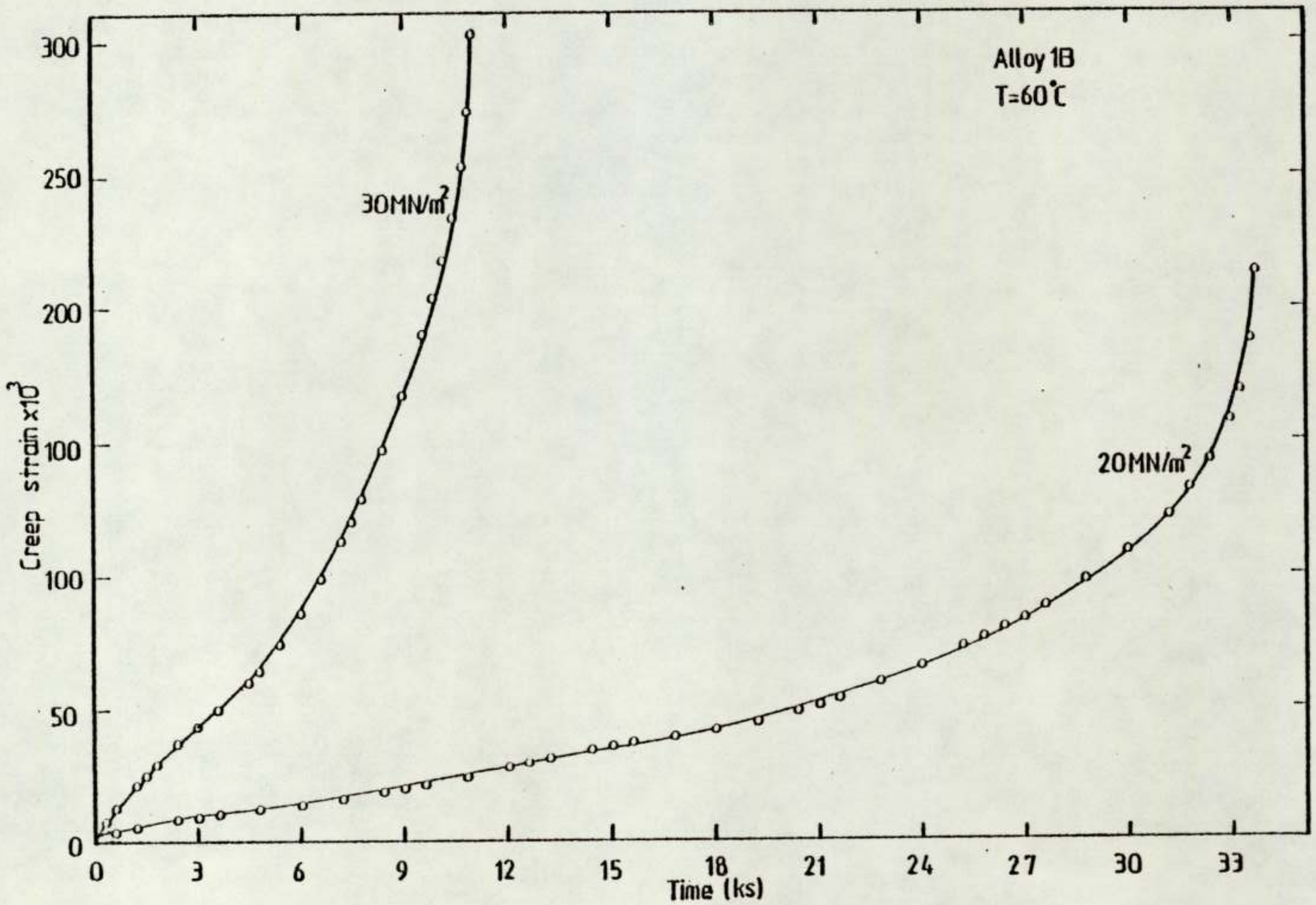

Fig. 118 Creep curves of alloy 1B at 60°C and under stresses of 20 and 30 MN/m^2

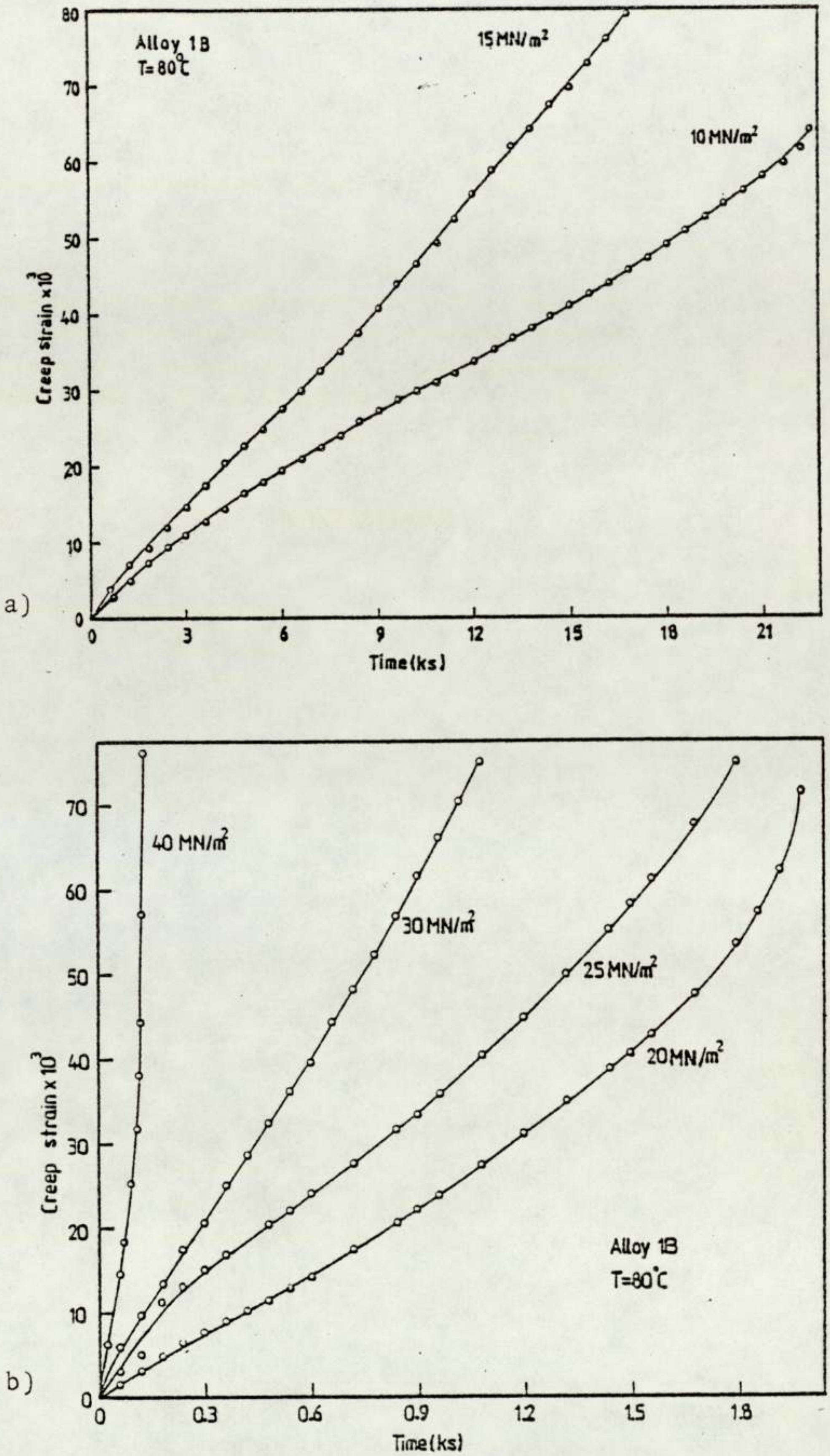

Fig. 119 Creep curves of alloy 1B at 80°C and under stresses of

a) 10 and 15 MN/m^2

b) 20, 25, 30 and 40 MN/m^2

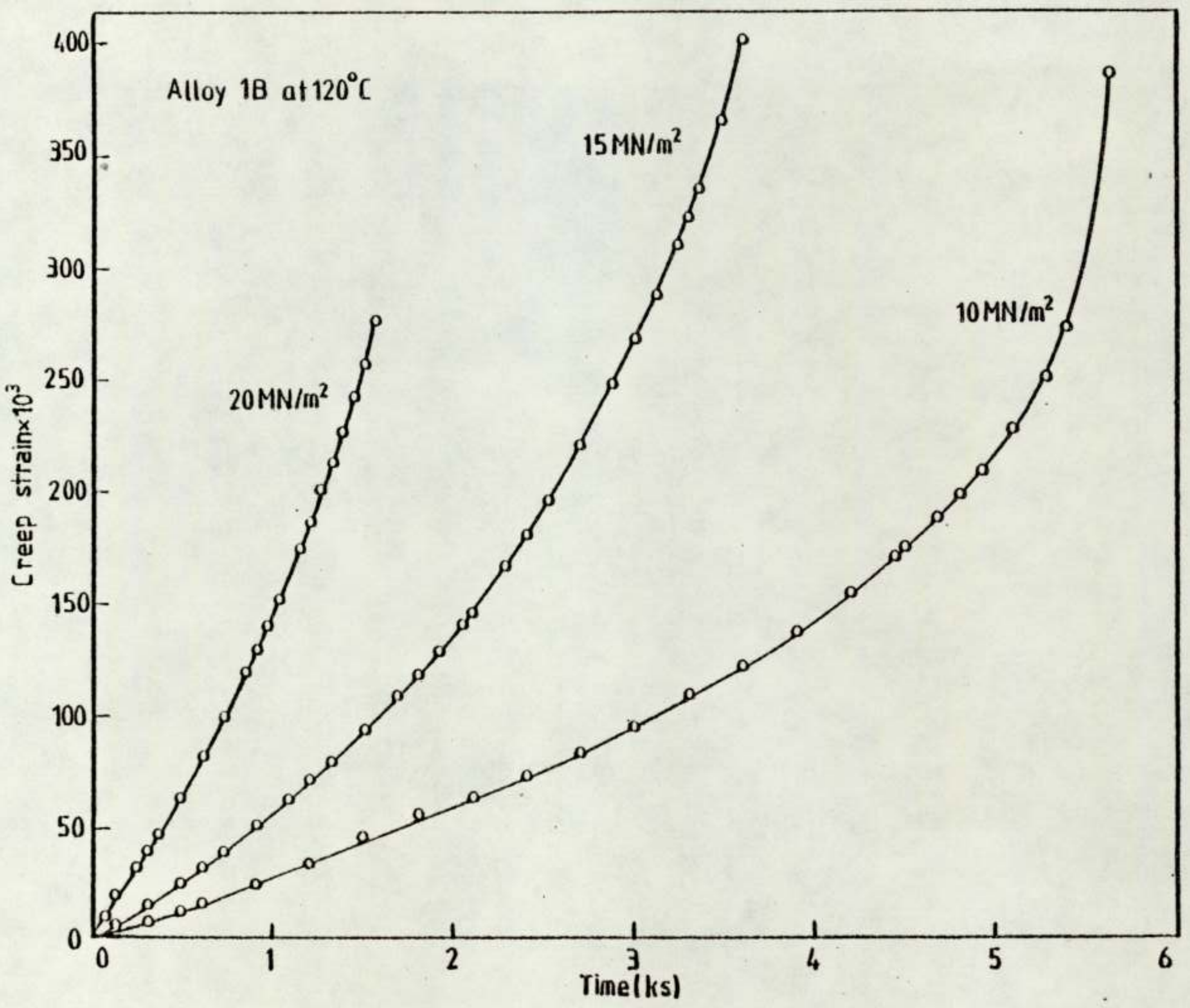

Fig. 120 Creep curves for alloy 1B at 120^{o}C and under the stresses of 10, 15 and 20 MN/m^2

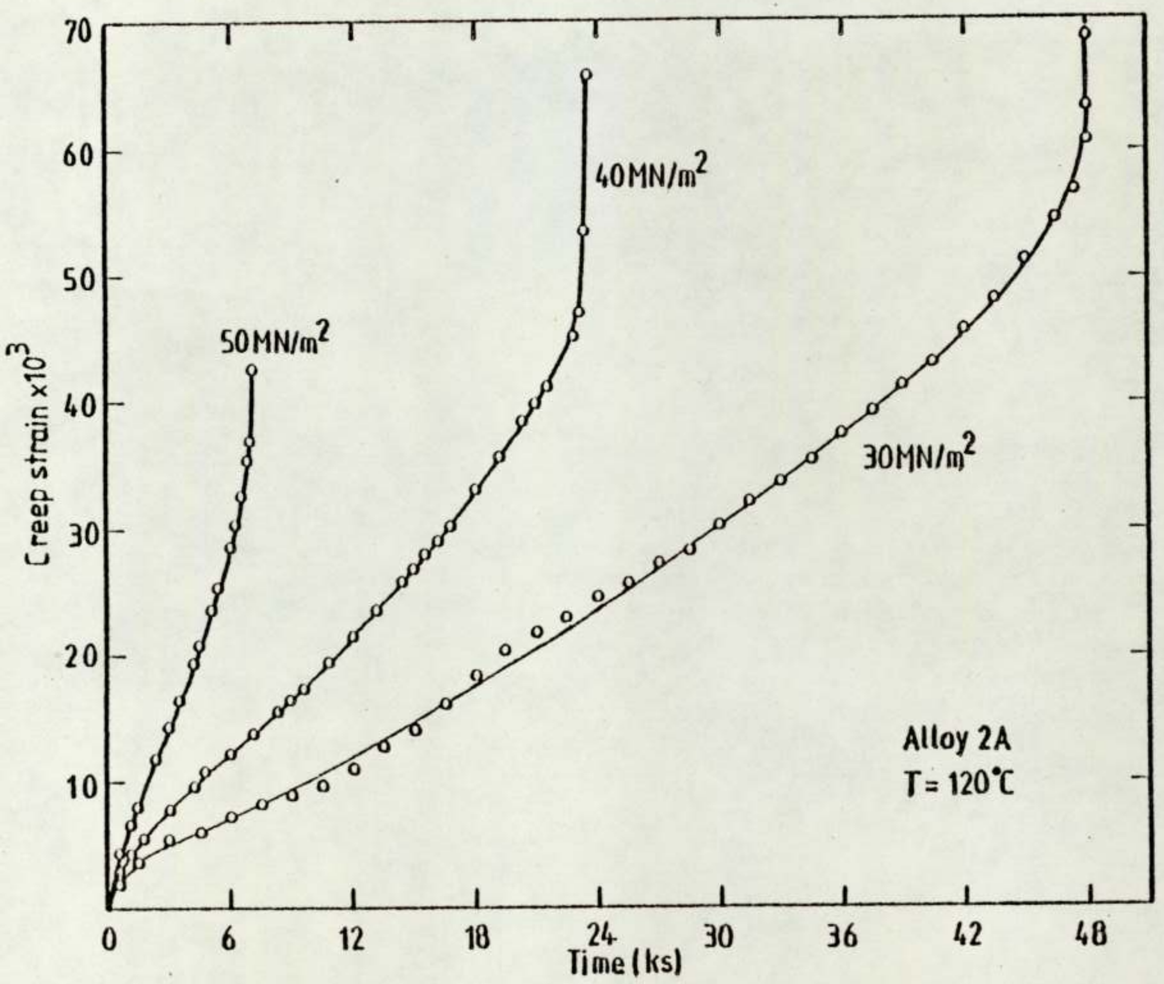

Fig. 121 Creep curves for alloy 2A at 120^{o}C and under stresses of 30, 40 and 50 MN/m^2

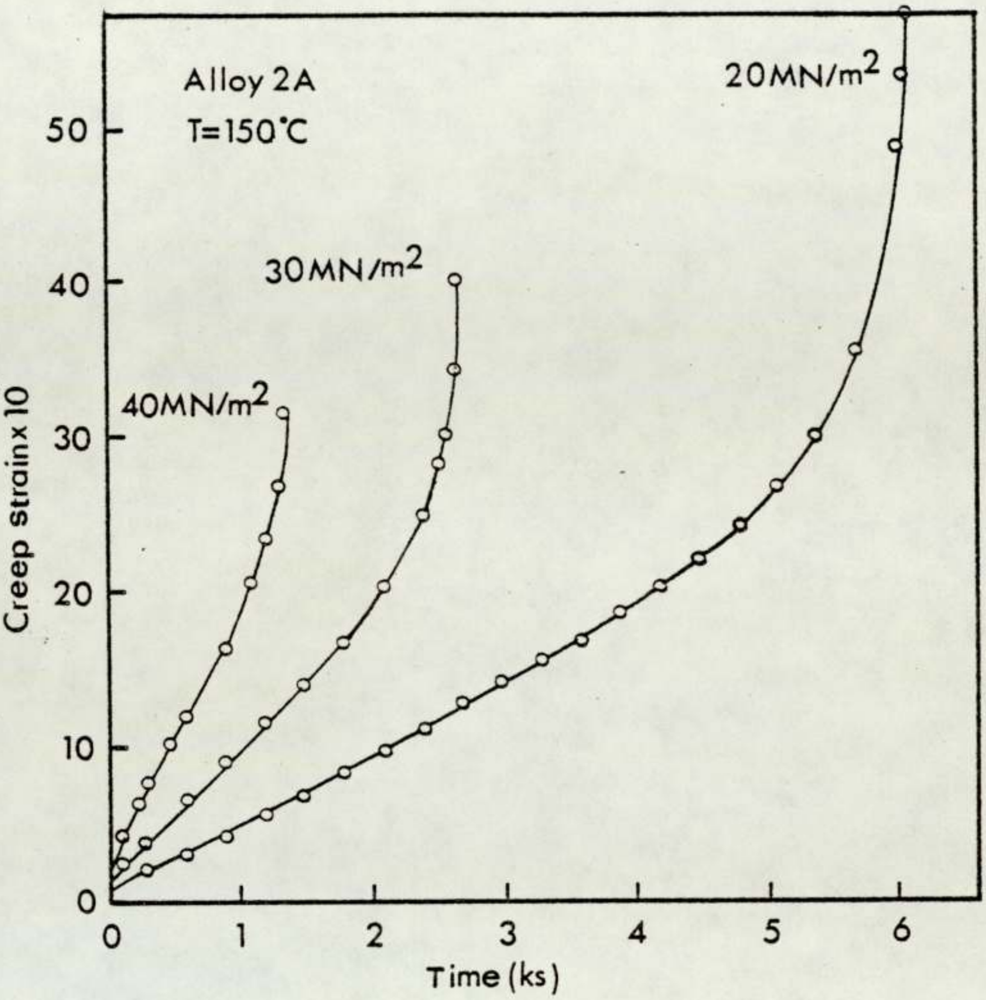

Fig. 122 Creep strain-time curves for alloy 2A at 150°C and at stresses of 20, 30 and 40 MN/m²

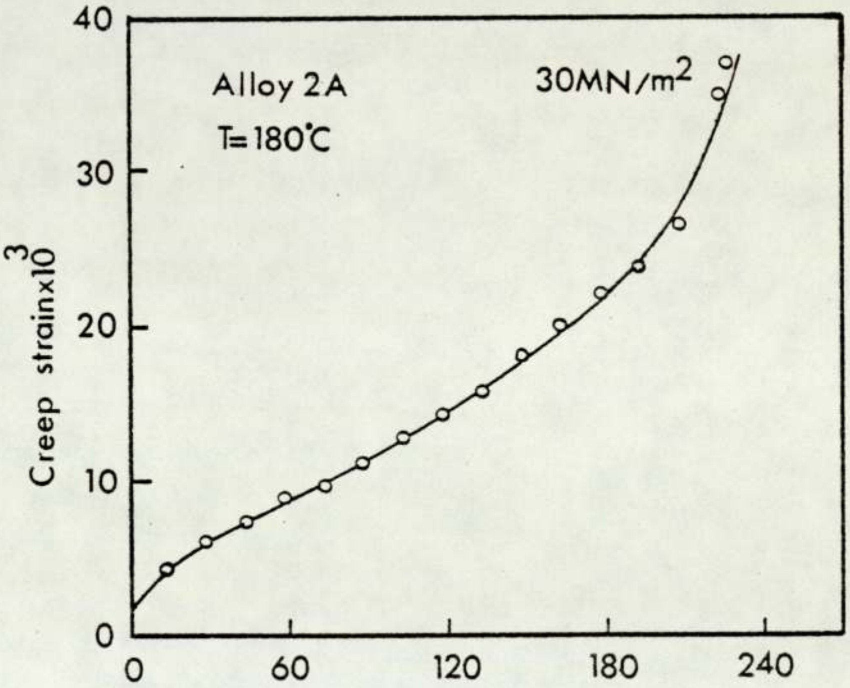

Fig. 123 Creep curve for alloy 2A at 180°C and 30 MN/m²

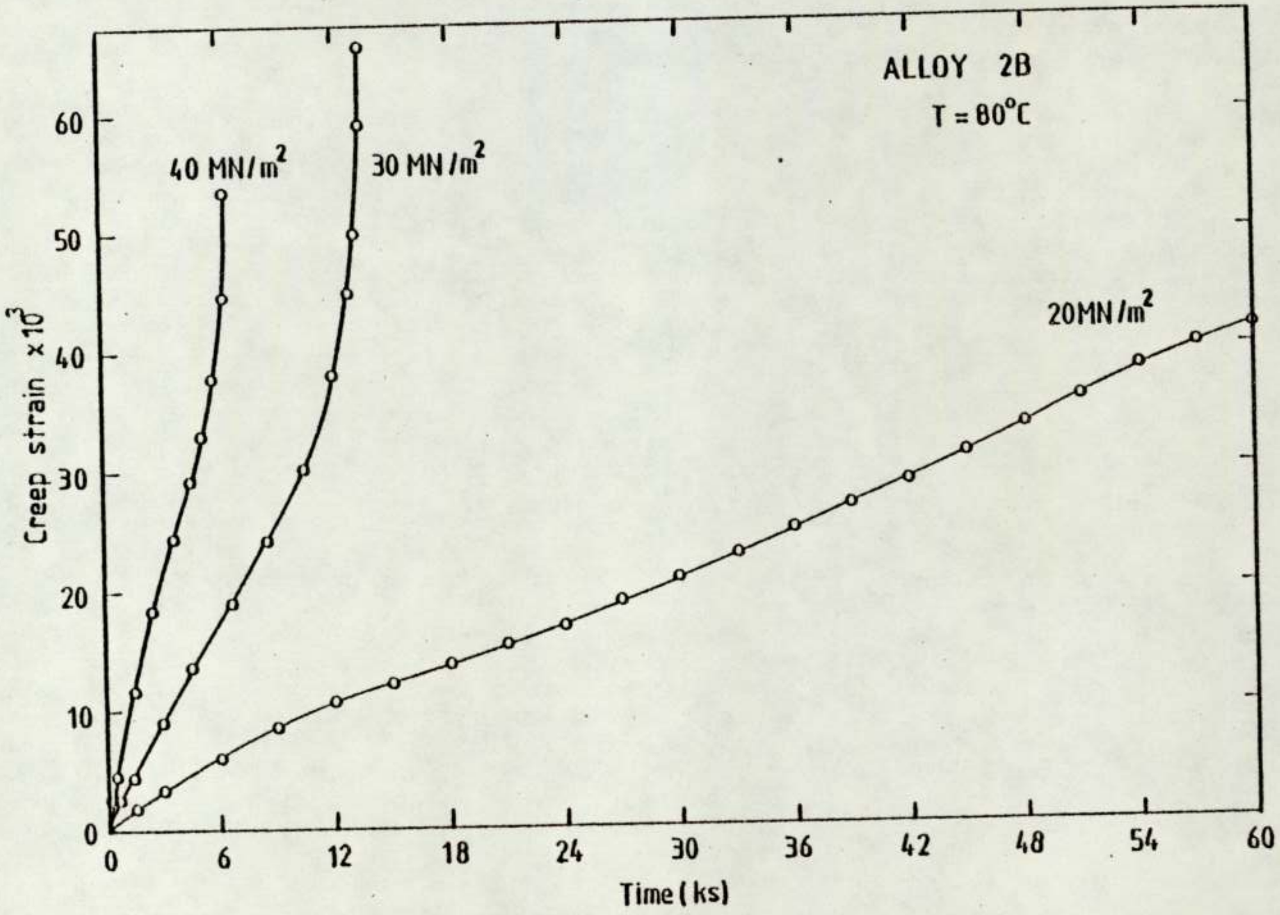

Fig. 124 Creep strain versus time curves for alloy 2B at 80°C and under stresses of 20, 30 and 40 MN/m^2

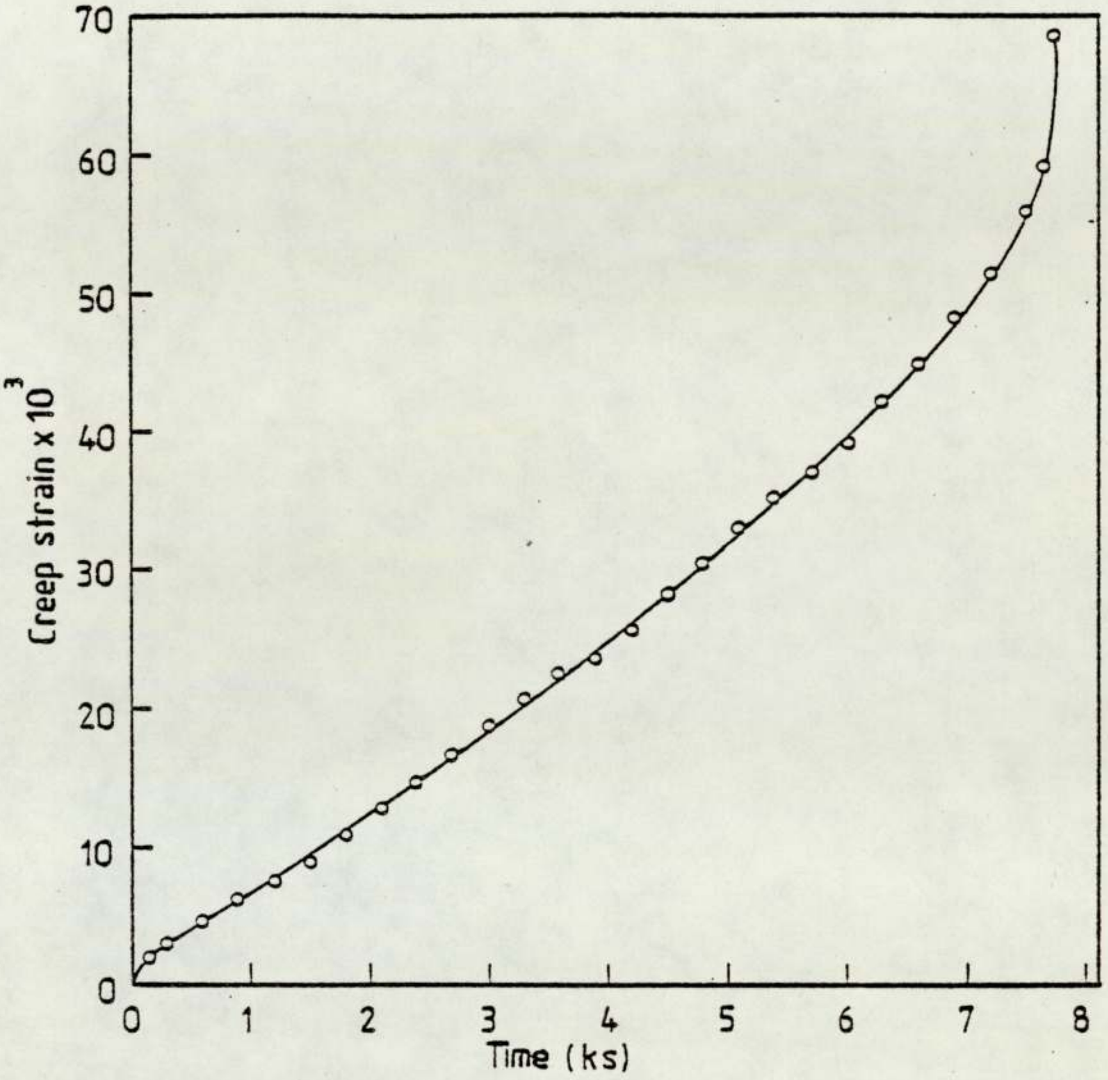

Fig. 125 Creep curve for alloy 2B at 100°C and 20 MN/m^2

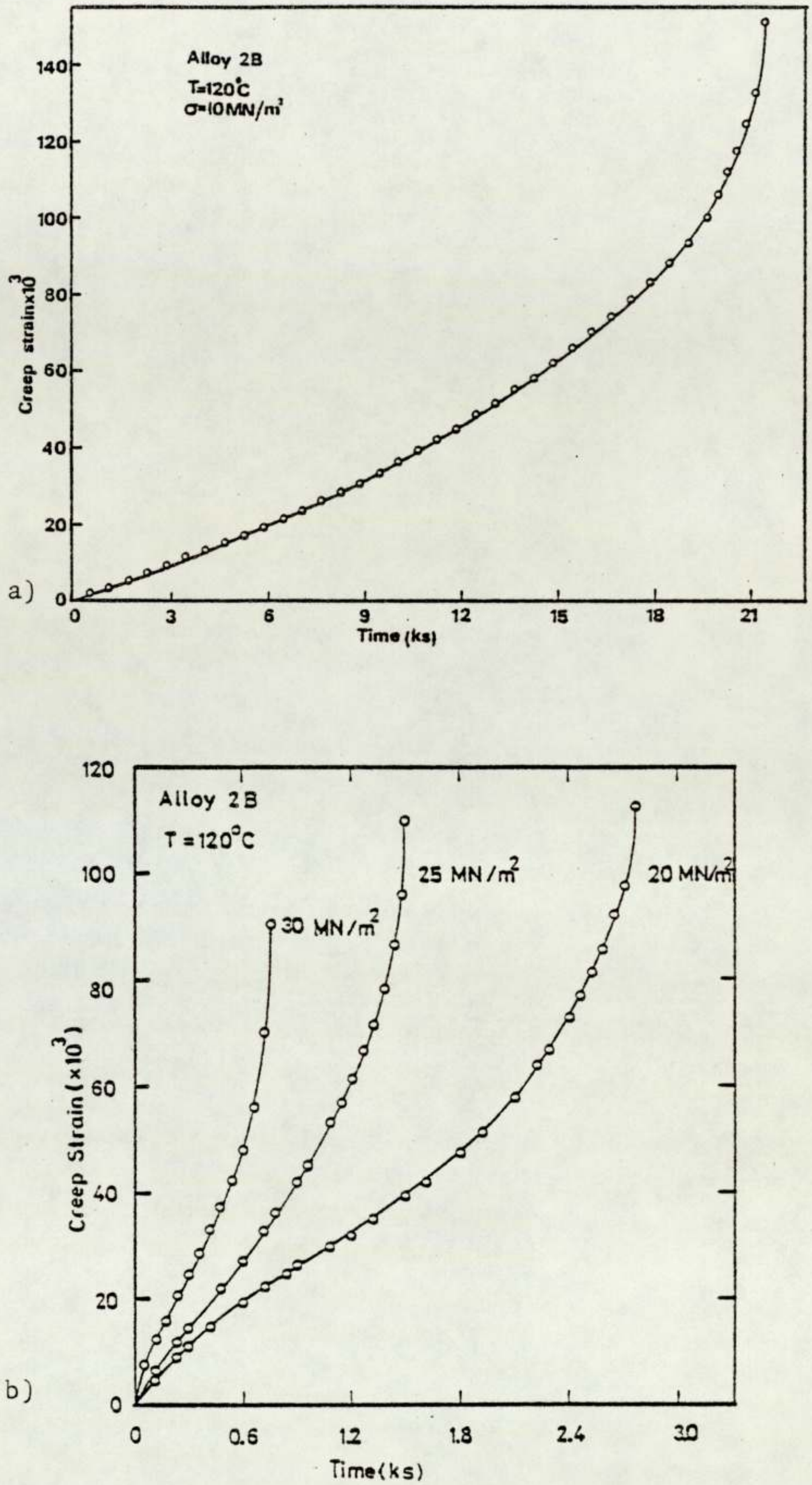

Fig. 126 Creep curve for alloy 2B at 120°C and under stress of

a) 10 MN/m^2

b) 20, 25 and 30 MN/m^2

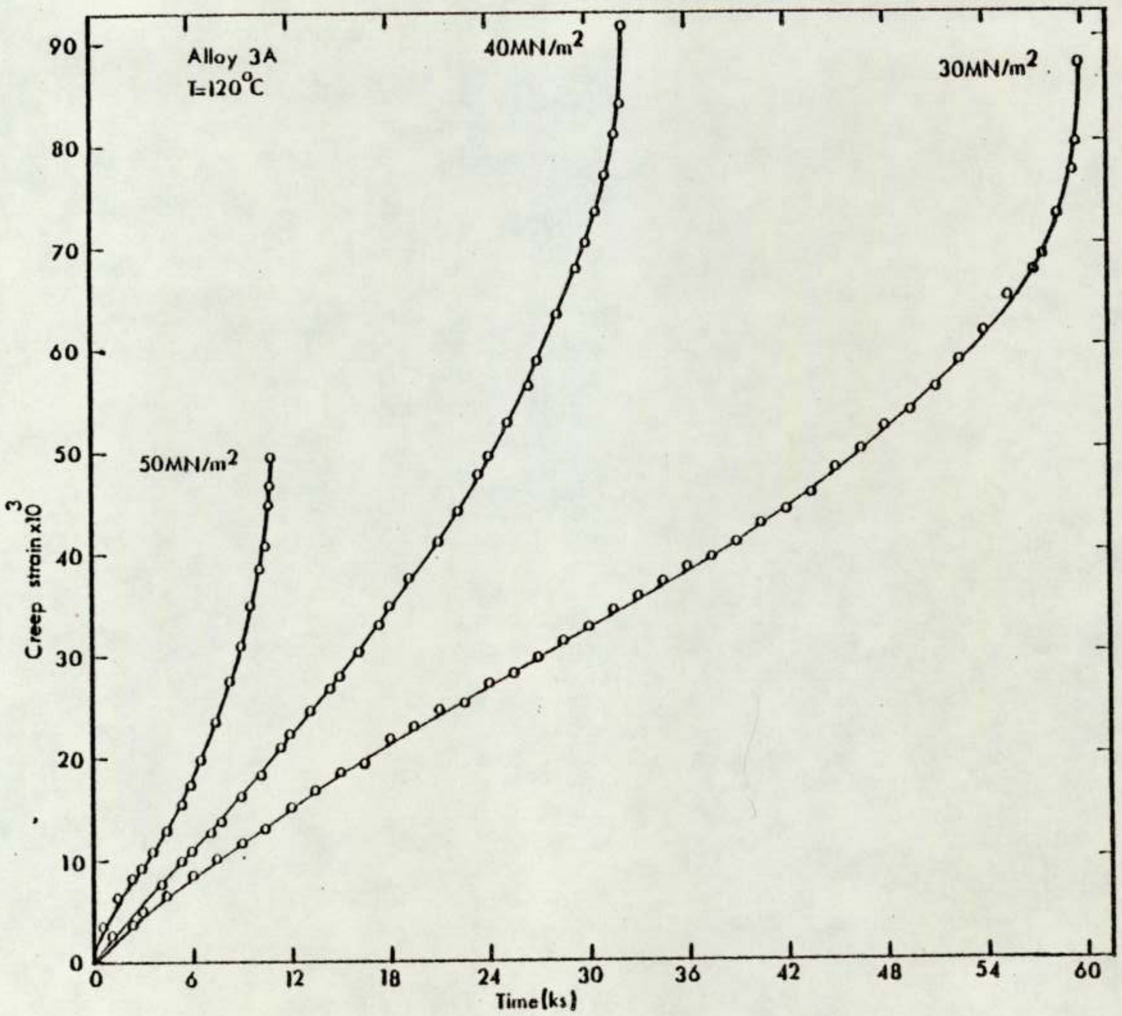

Fig. 127 Creep strain versus time curves for alloy 3A at 120°C and under stresses of 30, 40 and 50 MN/m^2

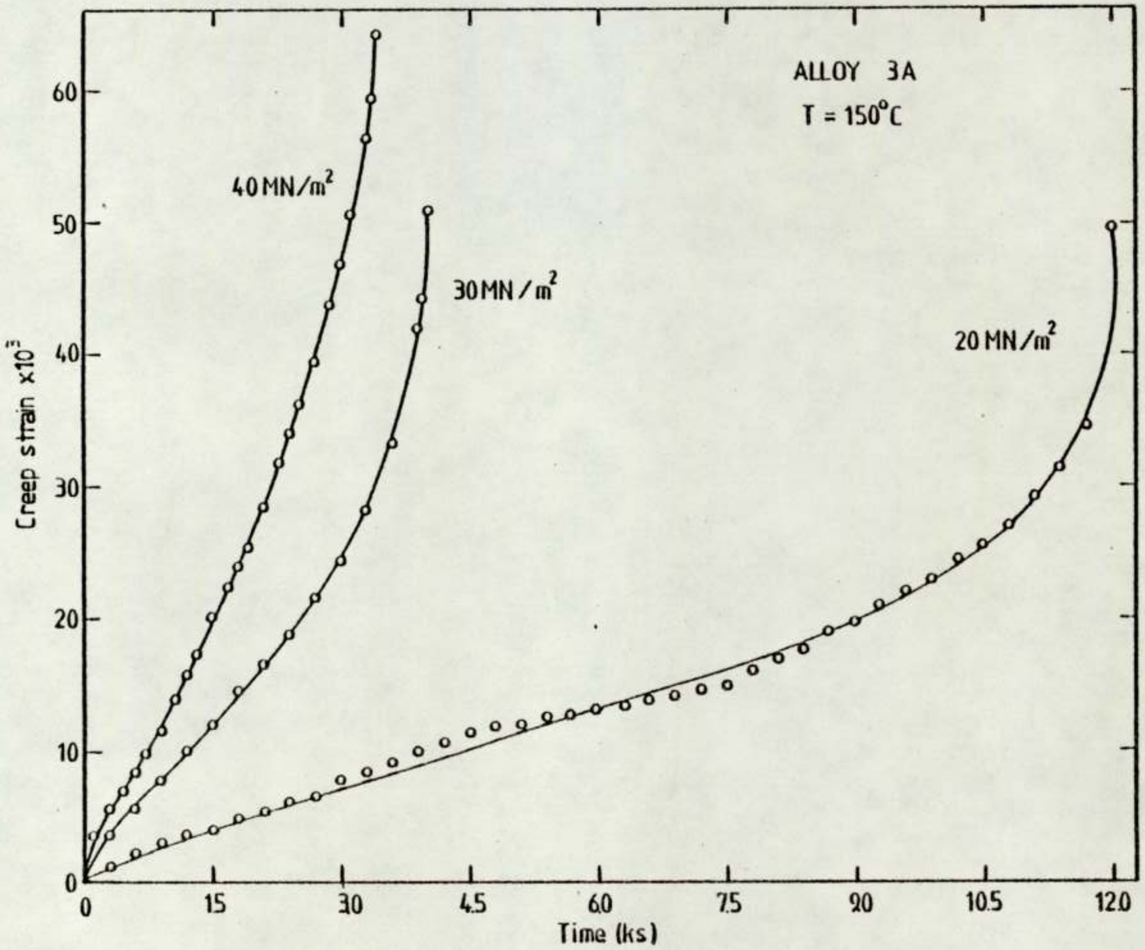

Fig. 128 Creep curves for alloy 3A at 150^{o}C and under stresses of 20, 30 and 40 MN/m^2

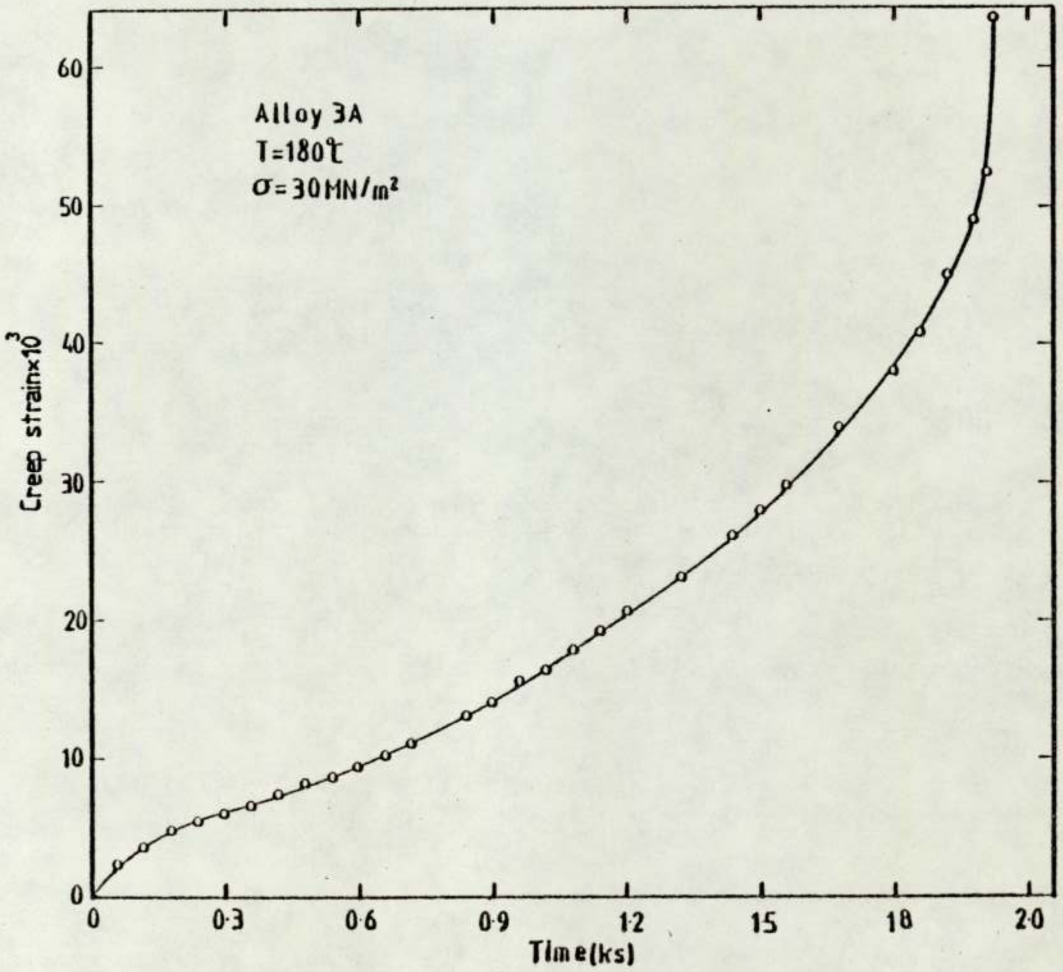

Fig. 129 Creep curve for alloy 3A at 180^{o}C and 30 MN/m^2

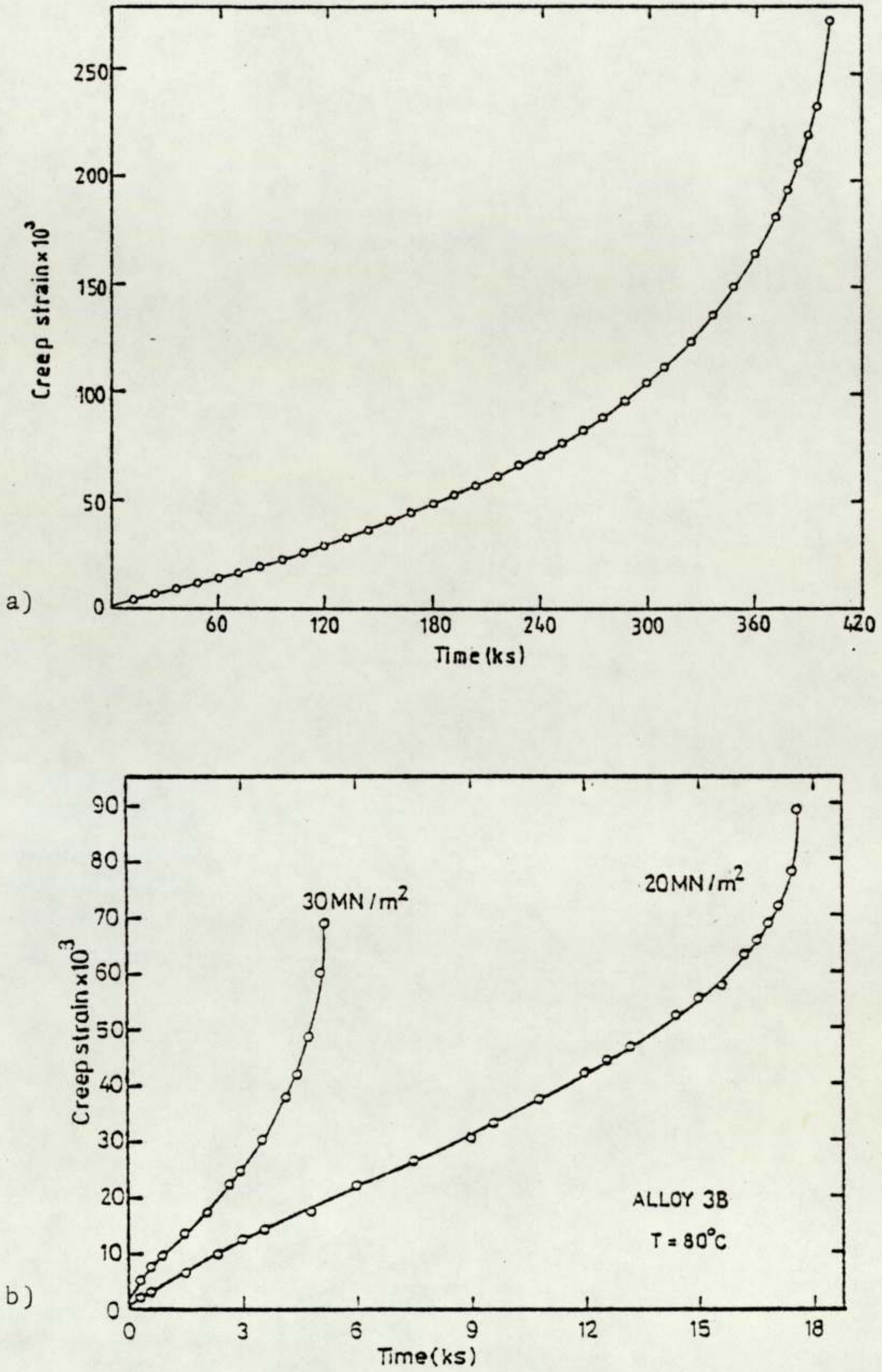

Fig. 130 Creep curve for alloy 3B at 80°C and under stress of

a) 10 MN/m²

b) 20 and 30 MN/m²

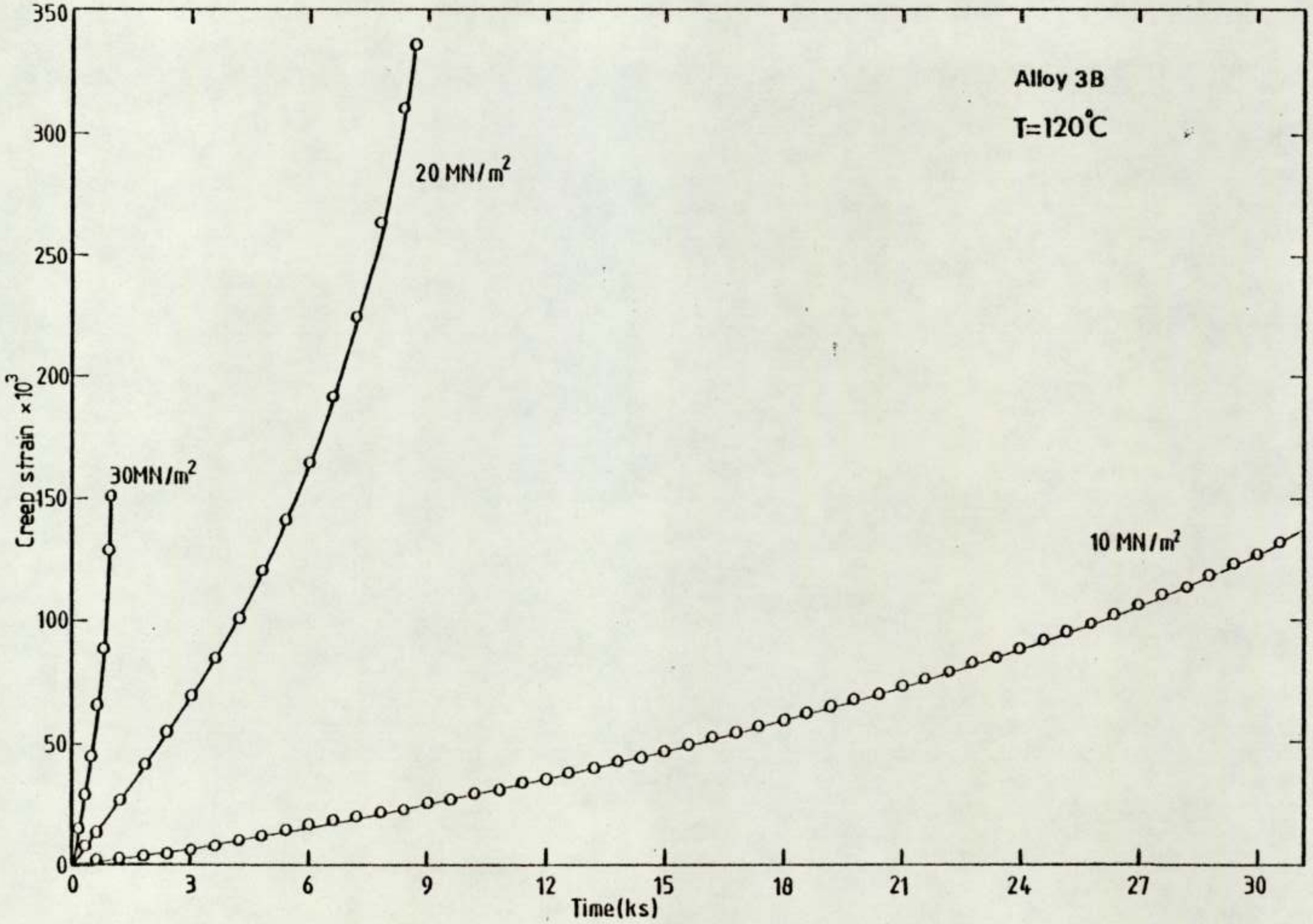

Fig. 131 Creep curves for alloy 3B at 120^{o}C and under stresses of 10, 20 and 30 MN/m^2

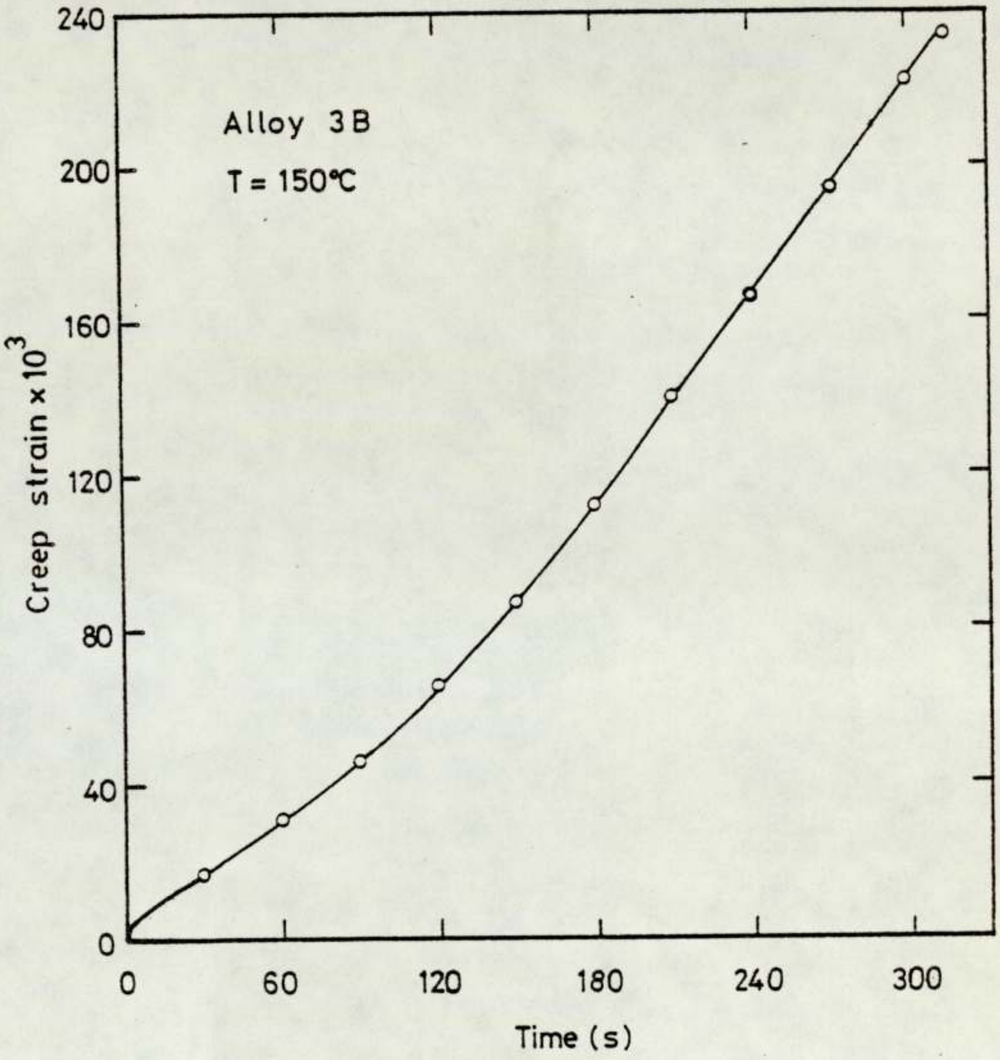

Fig. 132 Creep strain (ε) versus time curve for alloy 3B at 150^{O}C and 30 MN/m^{2}

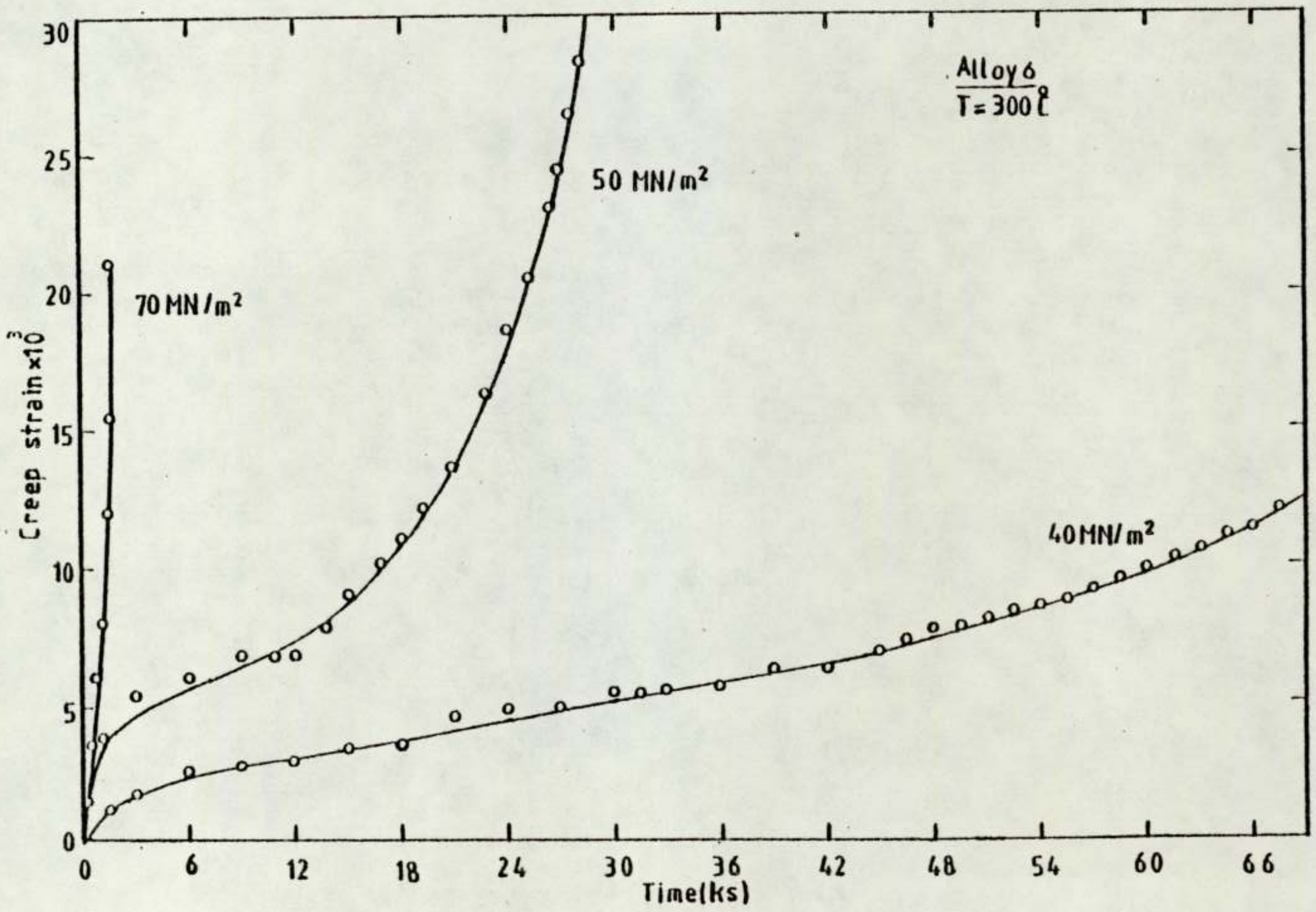

Fig. 133 Creep curves for alloy 6 at 300^{o}C and under stresses of 40, 50 and 70 MN/m^2

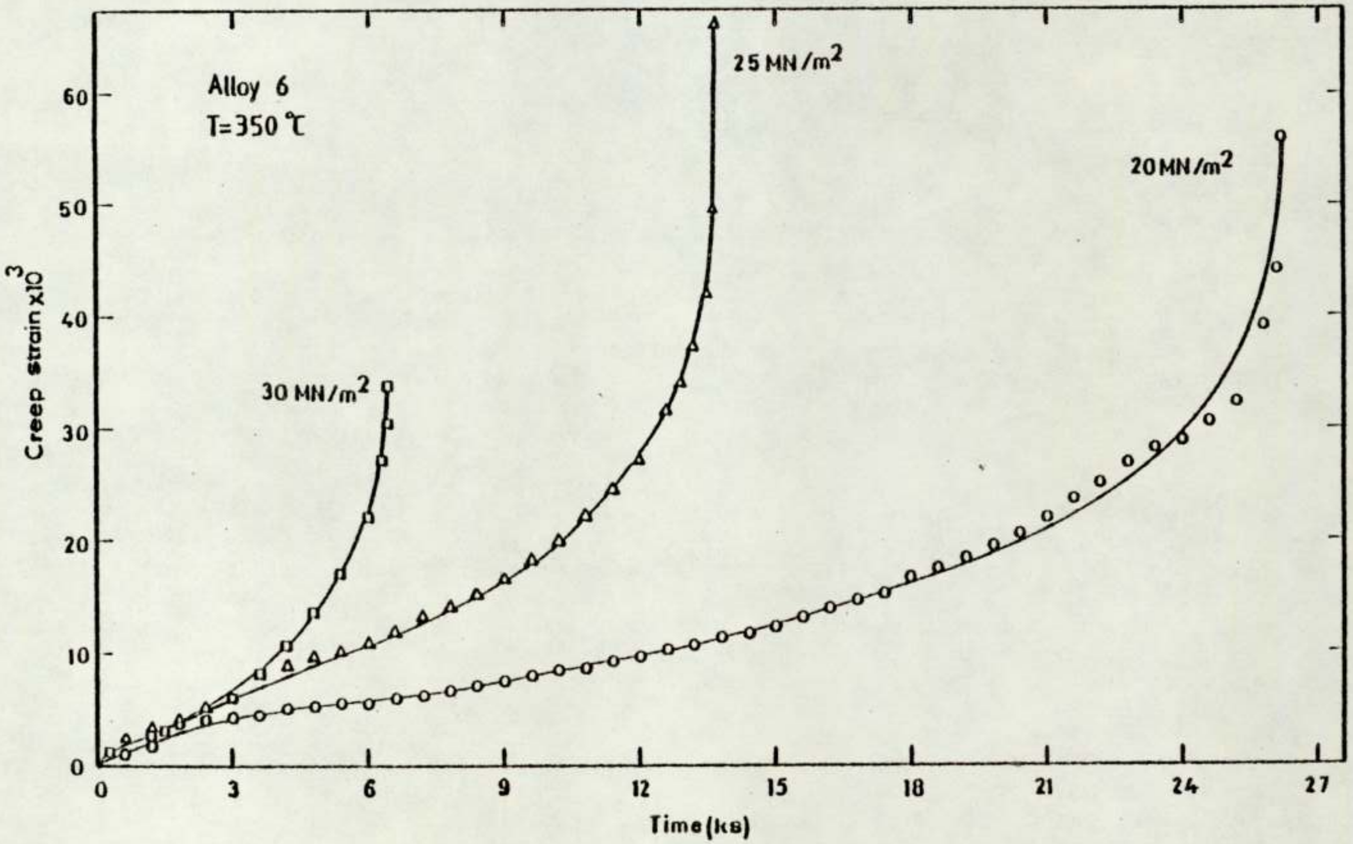

Fig. 134 Creep curves for alloy 6 at 350^{o}C and stresses of 20, 25 and 30 MN/m^2

TABLE 13

Creep Results for the Alloys Tested

Alloy	Temperature (^{o}C)	Stress (MN/m^2)	Secondary Creep Rate $\dot{\varepsilon}_s$ (s^{-1}) x 10^{-6}
1A	80	30	0.125
		40	0.465
		50	0.800
	120	20	2.32
		30	12.1
1B	60	20	2.38
		30	11.8
	80	10	2.43
		15	4.96
		20	26.0
		25	33.3
		30	63.7
		40	192
	120	10	31.1
		15	71.1
		20	140
2A	120	30	0.936
		40	1.54
		50	4.11
	150	20	4.80
		30	8.37
		40	14.8
	180	30	95.2
2B	80	20	0.650
		30	2.82
		40	5.23
	100	20	6.11
	120	10	3.87
		20	22.3
		25	43.4
		30	69.4

TABLE 13 (Continued)

Alloy	Temperature (^{o}C)	Stress (MN/m^2	Secondary Creep Rate $\dot{\varepsilon}_s$(s^{-1}) x 10^{-6}
3A	120	30	0.950
		40	1.92
		50	2.81
	150	20	2.00
		30	7.45
		40	12.3
	180	30	19.1
3B	80	10	0.323
		20	3.16
		30	8.05
	120	10	4.14
		20	24.4
		30	102
	150	30	505
6	300	40	0.111
		50	0.30
		70	6.33
	350	20	0.672
		25	1.65
		30	2.39

TABLE 14

Creep Rupture Data for the Alloys Tested

Alloy	Temperature ($^{\circ}$C)	Stress (MN/m^2)	Time to Rupture (ks)	Total Extension (mm)	Total Strain (ε) x 10^{-3}
1A	80	30	287.1	4.5	90
		40	135.0	5.7	114
		50	58.8	4.1	82
	120	20	9.7	3.9	78
		30	2.5	2.7	54
1B	60	20	33.8	10.6	212
		30	11.1	15.1	302
	80	10	>22.5	>3.2	>64
		15	36.0	10.5	210
		20	>2.1	>6.4	>127
		25	2.3	7.5	149
		30	2.2	9.5	189
		40	0.14	6.4	127
	120	10	5.6	19.2	384
		15	>3.7	>22.5	>450
		20	>1.6	>13.7	>274
2A	120	30	48.1	3.4	68
		40	23.6	3.3	66
		50	7.1	2.1	42
	150	20	6.1	2.9	58
		30	2.7	2.1	42
		40	1.3	1.6	32
	180	30	0.2	1.9	38
2B	80	20	92.8	5.5	110
		30	13.6	3.3	66
		40	6.4	2.7	54
	100	20	7.7	3.4	68
	120	10	21.6	7.5	150
		20	2.7	5.6	112
		25	1.5	5.5	110
		30	0.8	4.5	90

TABLE 14 (Continued)

Alloy	Temperature ($^{\circ}C$)	Stress (MN/m^2)	Time to Rupture (ks)	Time Extension (mm)	Total Strain (ε) x 10^{-3}
3A	120	30	59.9	4.4	88
		40	32.3	4.6	92
		50	10.9	2.5	50
	150	20	12.0	2.5	50
		30	>4.0	>2.5	>50
		40	3.4	3.5	70
	180	30	2.0	3.2	64
3B	80	10	>404.6	>13.7	>274
		20	17.6	4.5	90
		30	5.2	3.4	68
	120	10	37.8	12.9	258
		20	>9.5	>20.7	>414
		30	1.0	7.5	150
	150	30	0.3	11.7	234
6	300	40	86.4	1.2	24
		50	29.0	1.9	38
		70	1.7	1.1	22
	350	20	26.2	2.8	56
		25	13.7	4.1	82
		30	>6.7	>1.7	>34

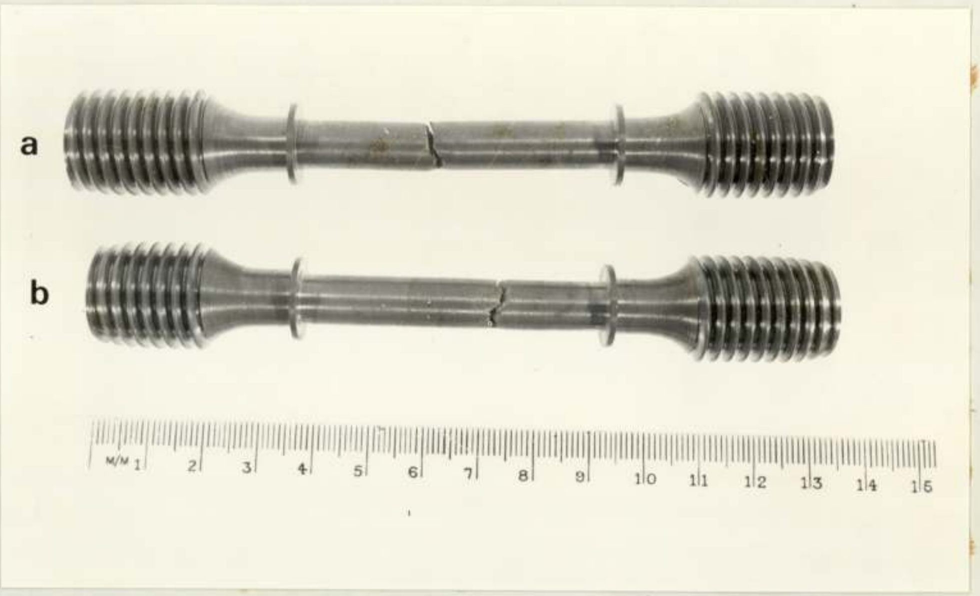

Fig. 135 Creep specimens of alloy 3A failed at 120°C and a) 40 MN/m^2, b) 50 MN/m^2

Fig. 136 Creep specimens of alloy 3B fractured at (a) 80°C, 10 MN/m^2 and (b) 150°C, 30 MN/m^2

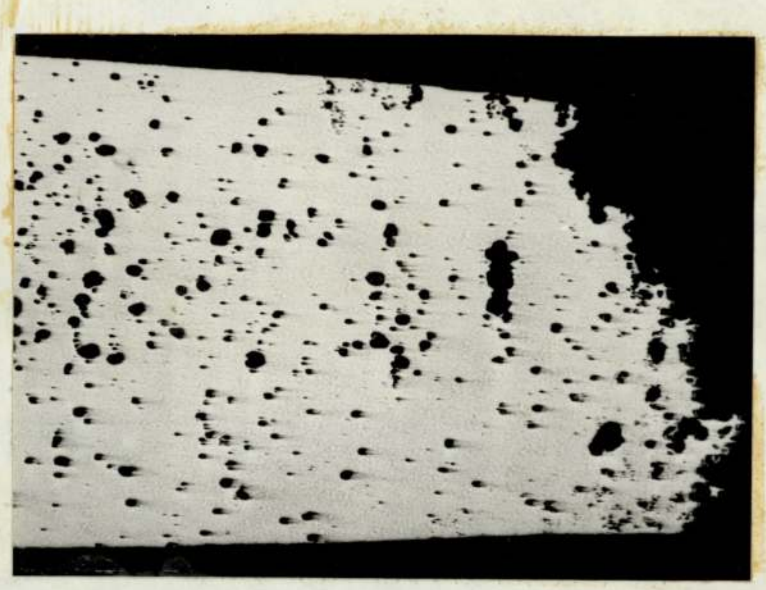

Fig. 137 Polished longitudinal section of creep specimen of alloy 2A fractured at 120°C and 30 MN/m^2 x 10

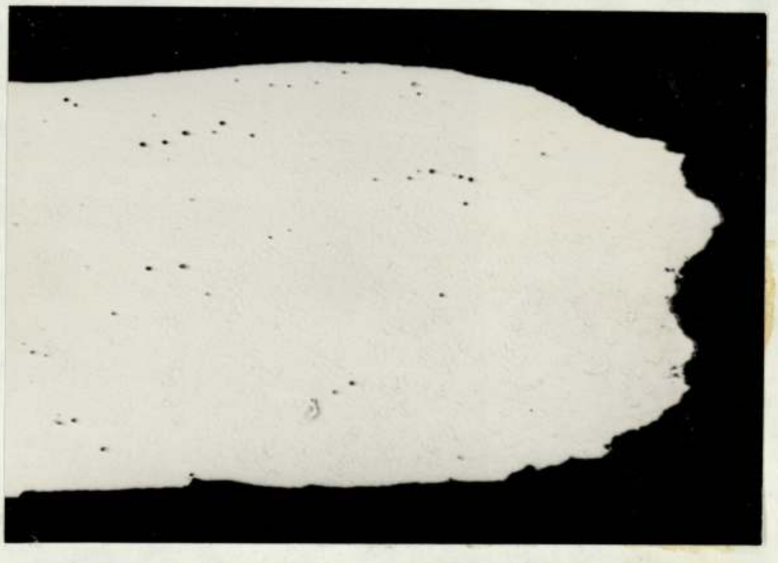

Fig. 138 Longitudinal section of creep test piece of alloy 3A failed at 120°C and 30 MN/m^2 x 10

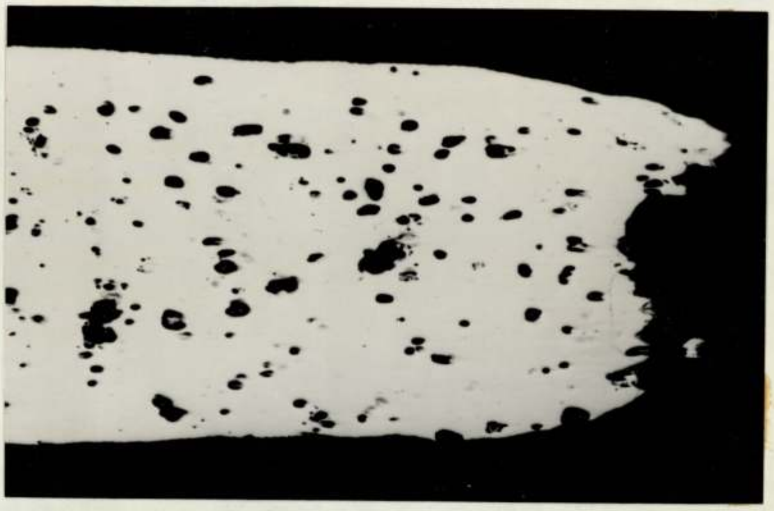

Fig. 139 Longitudinal section of creep specimen of alloy 1B failed at 120°C and 20 MN/m^2, unetched x 10

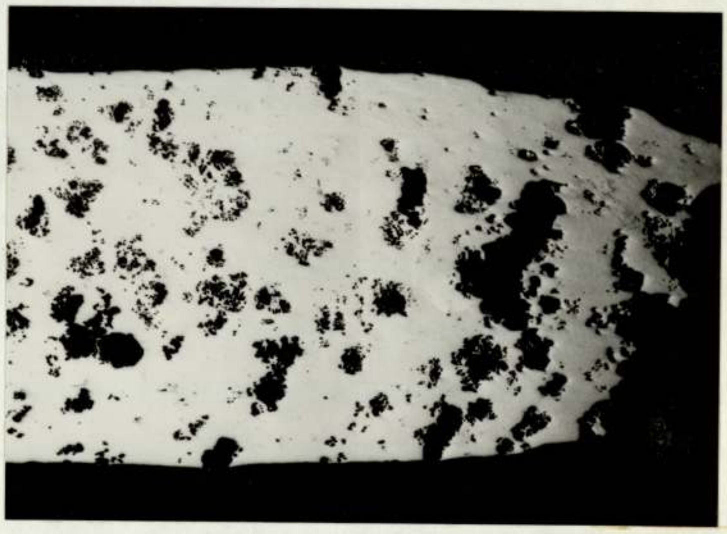

Fig. 140 Longitudinal section of creep specimen of alloy 2B failed at 120°C and 10 MN/m^2 x 10

(a)

(b)

Fig. 141 Longitudinal sections of creep specimen of alloy 3B fractured at 80°C and 20 MN/m^2

(a) fracture tip

(b) necking and cavities away from the fracture tip x 10

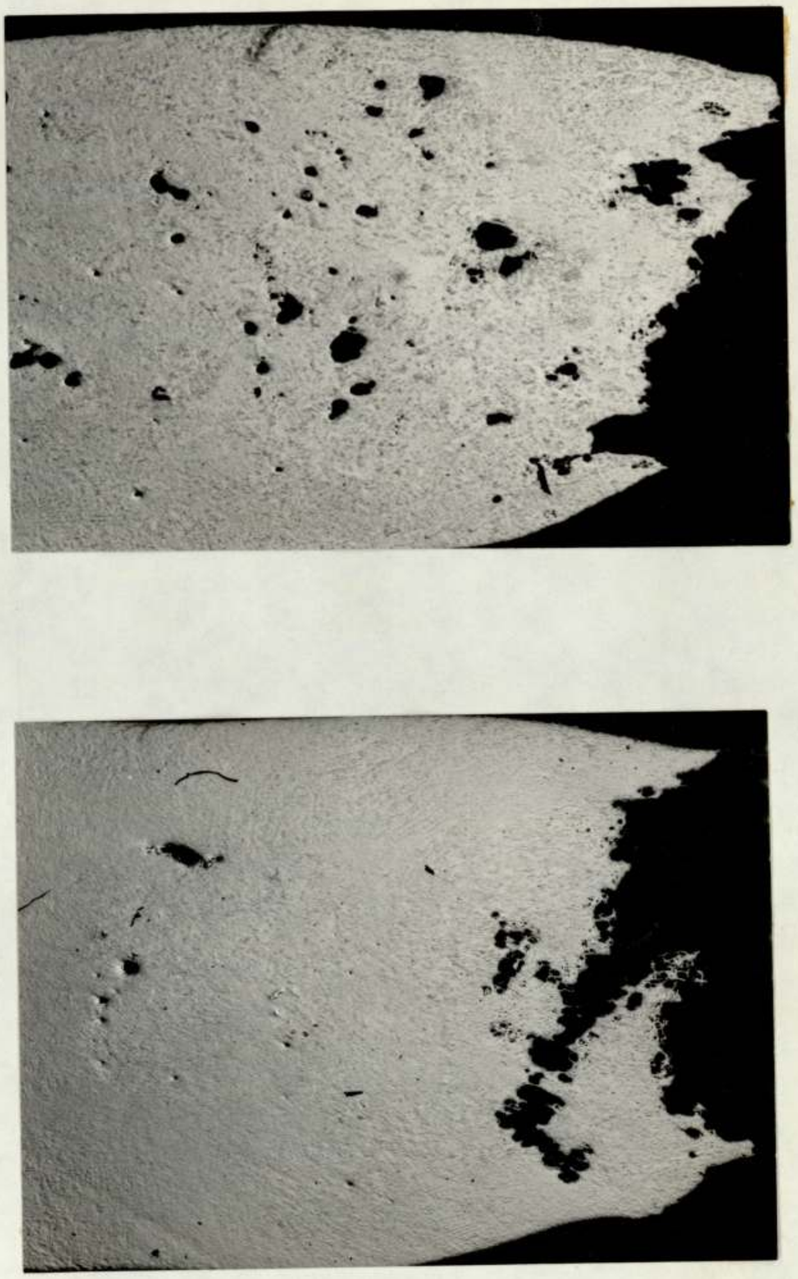
(a)

(b)

Fig. 142 Longitudinal sections of creep specimens of alloy 3B failed at 120°C and

(a) 10 MN/m^2,

(b) 30 MN/m^2. x 10

Fig. 143 Creep fracture of alloy 2A occurred at 120°C and 30 MN/m^2 x 360

Fig. 144 Microstructure of alloy 1B failed at 120°C and 20 MN/m^2 x 600

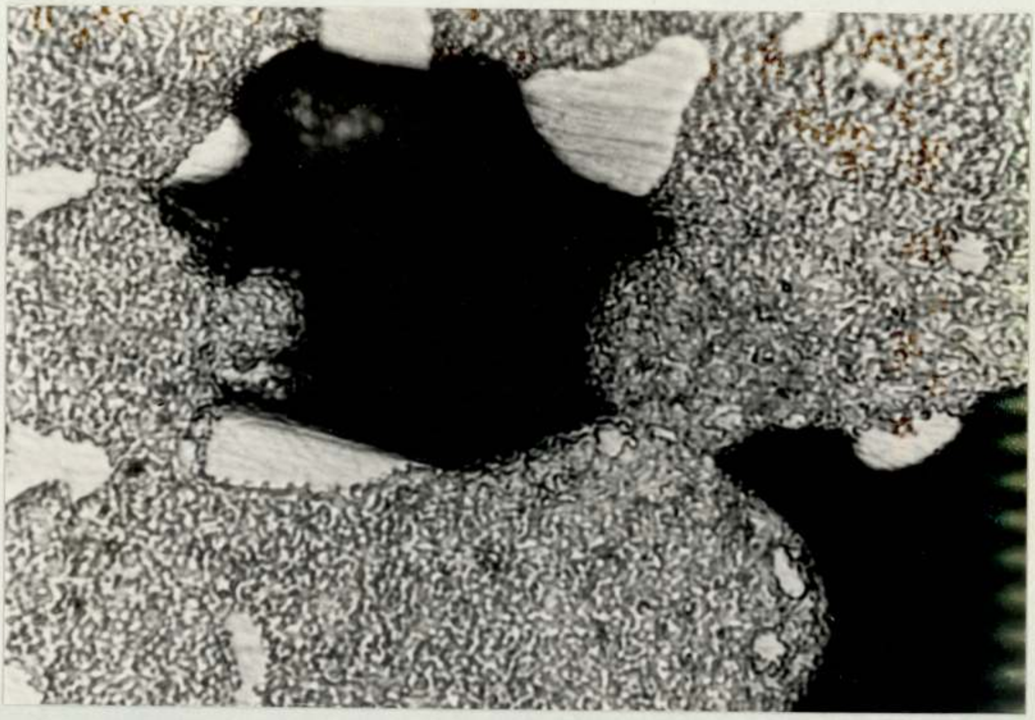

Fig. 145 Microstructure of alloy 3B after creep failure at 120^{o}C and 20 MN/m^2 x 1200

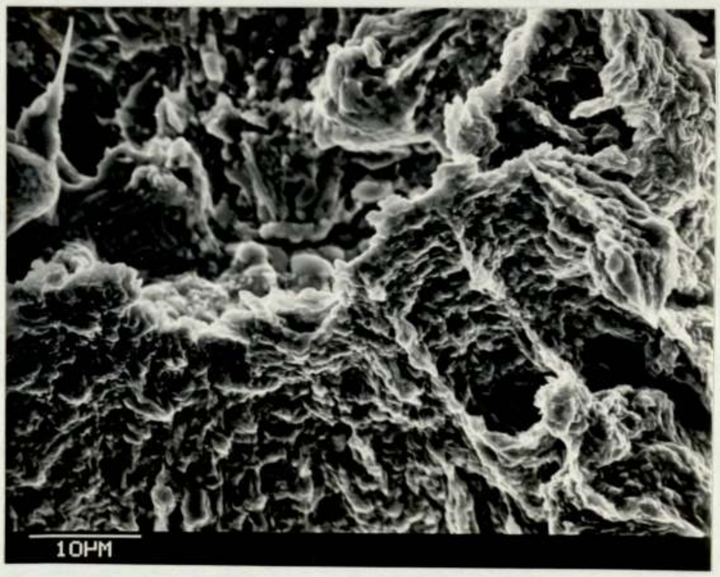

Fig. 146 Creep fracture surface of alloy 3A obtained at 150^{o}C and 20 MN/m^2

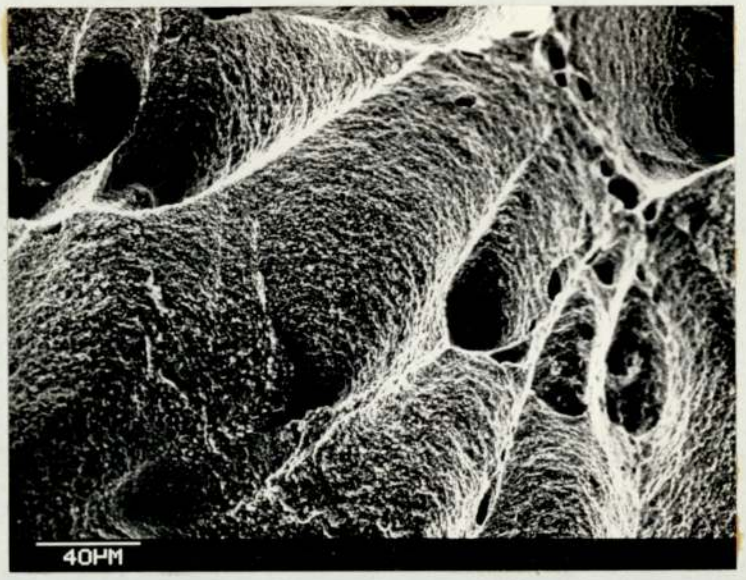

Fig. 147 Creep fracture surface of alloy 1B obtained at 120^{o}C and 20 MN/m^2

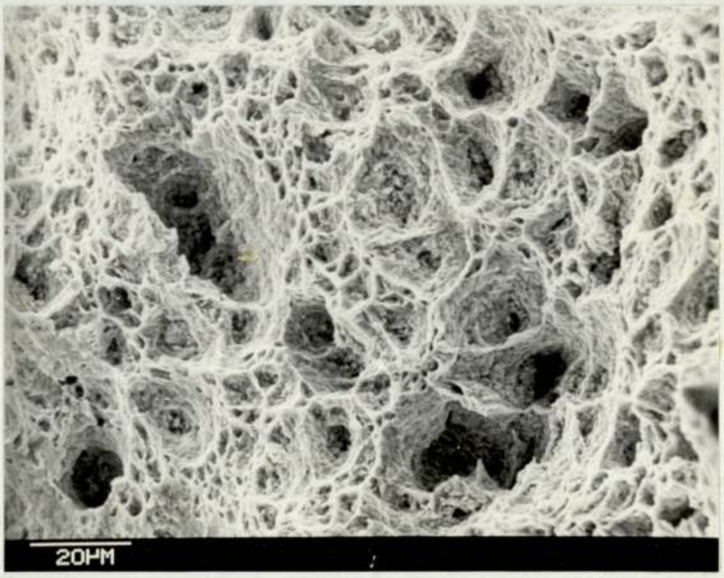

Fig. 148 SEM micrograph of creep fracture surface of alloy 3B produced at 120^{o}C and 20 MN/m^2, showing the coalescence of cavities

3.5 Wear

The results of the wear test obtained from the selected alloys are given in Table 15. The weight loss was plotted against the distance travelled to show the wear behaviour of these alloys in this bushing application, Fig. 149. The initial wear rate of the alloys in general was high, but decreased as the distance increased. However phosphor bronze and alloy 4A showed a lower and uniform wear rate initially, which extended over a large distance. The above figure also shows that, with the exception of one alloy (2A), the zinc-aluminium based ternary alloys exhibited higher wear resistance than cast iron, the normal bearing material for this application.

The best wear performance for this bushing application was obtained with the zinc-aluminium-silicon alloy in both as-cast (5A) and heat-treated (5B) condition.

Phosphor bronze and alloy 4A also exhibited good bushing properties. The wear behaviour of these two alloys was found to be quite similar as they showed steady and close wear rates.

The wear rate of zinc-aluminium-silicon alloy in both conditions was initially higher than that of phosphor bronze, but reduced gradually so that the total wear loss was eventually smaller. The wear rate of the zinc-aluminium-copper alloys (2A, B and 4A, b) was always greater than that for the phosphor bronze. Alloy 4 showed considerably higher wear resistance than alloy 2 in both as-cast and heat-treated conditions.

These results suggest that the wear behaviour of the copper-containing monotectoid zinc-aluminium alloys (4) is similar to that of phosphor bronze. Hence both alloys can be considered in the same category for this lightly stressed, low-temperature application.

Alloy 2 in the as-cast condition (2A) exhibited the lowest wear resistance, but when heat-treated (2B) showed higher wear resistance than cast iron. A very slight increase was found in the weight of alloy 2B, after a certain running distance (between 10389 and 18554 km). This unexpected result may arise from some foreign particles, suspended in the lubricant, becoming embedded in the bush. Since the oil supply was fully filtered it is considered that this was a chance event which was unlikely to affect the other results.

It appears that the monotectoid zinc-aluminium based ternary alloys containing copper or silicon are more wear resistant than the eutectoid based alloys. The hard load-carrying phase has an important effect on the wear behaviour of these bushing materials, as the silicon-containing alloy showed higher wear resistance than the copper-containing alloys.

TABLE 15

Results of Wear Test

Material	Weight (g)				
	0	2706 km	6214 km	10389km	18554km
Cast-Iron	77.2368	77.2046	77.1961	77.1910	77.1885
Phosphor bronze	80.7616	80.7597	80.7524	80.7439	80.7310
Alloy 2A	78.3370	78.2932	78.2827	78.2761	78.2142
Alloy 2B	74.2697	74.2460	74.2343	74.2232	74.2248
Alloy 4A	74.1709	74.1678	74.1588	74.1526	74.1376
Alloy 4B	76.6297	76.6243	76.6070	76.5968	76.5950
Alloy 5A	73.6042	73.5978	73.5870	73.5820	73.5818
Alloy 5B	73.0403	73.0367	73.0323	73.0296	73.0270

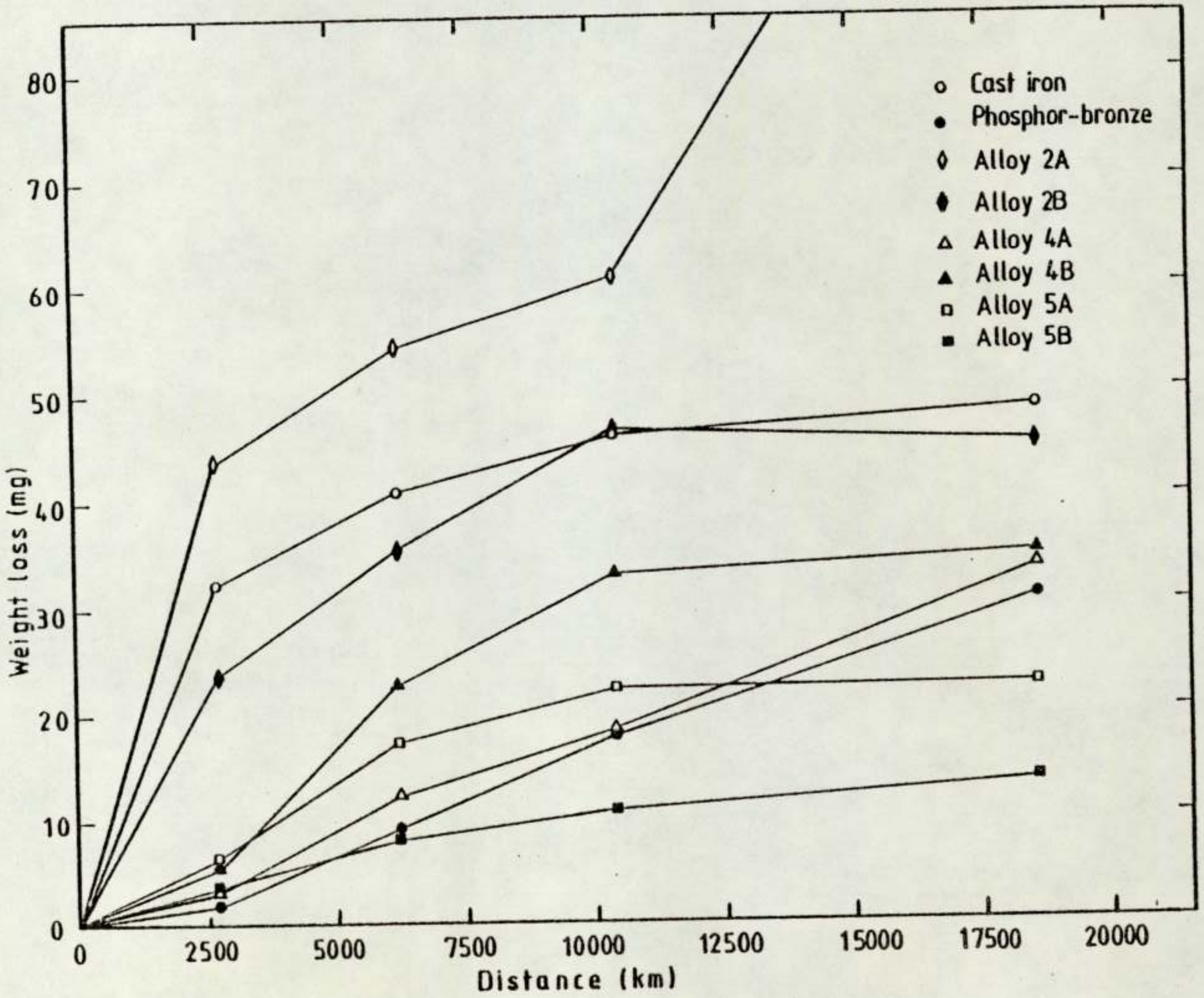

Fig. 149 Plots of weight loss versus distance for wear behaviour of the experimental alloys

4. Discussion

Bearing alloys must satisfy certain requirements which are related to their physical, mechanical and service properties. Since all of these properties are governed by the structure, it is therefore necessary to study both the structure and properties of the alloys in order to assess them for bearing applications. The structure of an alloy is mainly controlled by its composition and any applied thermochemical treatments. Therefore in order to obtain a suitable structure for bearing purposes, it is necessary to select an appropriate composition and apply the requisite heat-treatments.

In the present work, a number of zinc-based binary and ternary alloys have been investigated in order to obtain a suitable combination of conditions (structure and properaties) for bushing applications. These investigations were carried out on eutectoid (1, 2 and 3) and monotectoid (4 and 5) alloys in the as-cast and heat-treated conditions.

Metallographic examination showed that the zinc-based alloys possessed three principal structures:

(1) cored-dendritic,
(2) lamellar, and
(3) fine-grained equiaxed.

These structures were produced by casting, homogenization followed by slow cooling (furnace or air), and quench-ageing respectively. The cored-dendritic and equiaxed fine-grained conditions were selected for investigation of mechanical and wear properties, as they represent the extremes of the range of microstructures.

Primary solidification of these alloys produced a cored-structure consisting of aluminium-rich dendrites with a zinc-rich interdendritic phase. This cored cast structure is metastable and creates an instability problem in the physical and mechanical properties of these alloys during service (3,4,142,146). In particular, dimensional changes due to long-term phase transformations (3,4) become a serious problem for bearing applications, where housing fits and running clearances are critical. This undesirable metallographic structure was completely eliminated in the experimental alloys by homogenization at 350°C for 48 hours. The homogenized structure of the eutectoid alloys, after a slow cooling had a lamellar morphology, the spacing of which increased as the cooling rate decreased. The lamellar morphology is typical of an eutectoid decomposition and is also produced by either isothermal transformation or by quench-ageing above 100°C after solution treatment. The lamellae were nucleated on the former β grains. However slow cooling of the monotectoid alloys after homogenization, produced a mixture of aluminium-rich and zinc-rich rounded or U-shaped small particles, which were formed by the eutectoidal decomposition of the α' and β solid solutions.

Decomposition of the eutectoid alloys at room temperature after a rapid water-quench, produced a fine (∿1 μm) mixture of equiaxed zinc-rich (η) and aluminium-rich (α) grains. This change in the morphology of transformed products, was attributed to the occurrence of spinodal decomposition (56,62). However decomposition of the quenched β solid solution on isothermal ageing at 200°C for 2 hours, produced a mixed structure consisting of both aluminium and zinc-rich grains together with lamellar products. This change from discontinuous (lamellar) to spinodal decomposition has been reported to take place at various temperatures; 0 - 100°C (53), around 100°C (61) or around room temperature (56). Present microscopic examination showed that this change occurred above room temperature, and the hardness results suggest that it takes place at approximately 100°C.

Solution treatment followed by water-quenching produced a large grained structure of α/α' solid solution in the monotectoid alloys (1B). On ageing this produced fine precipitation products (i.e. zinc and ε phase) which initiated at the grain-boundaries and within grains. Ageing of the quenched monotectoid alloy at 200°C produced a mixed structure of fine and coarse precipitation particles together with fine and coarse lamellae very similar to that in the eutectoid alloys.

Metallographic examination showed the presence of ε phase (Zn_5Cu) in alloy 3 in the as-cast and heat-treated conditions. This was confirmed by X-ray diffraction and electron-probe analysis. Metallography, X-ray or electron diffraction results showed that ε was also formed as a transitional phase during decomposition of eutectoid and monotectoid based zinc-aluminium-copper alloys (2B and 4B). This is consistent with the results obtained by previous Polish workers (68,147). The orientation relationship between this phase and the aluminium matrix in alloy 4B was determined as:

$$[0\bar{1}0]_{\alpha} // [0001]_{\varepsilon}$$
$$(001)_{\alpha} // (1\bar{1}00)_{\varepsilon}$$
$$(100)_{\alpha} // (\bar{1}\bar{1}20)_{\varepsilon}$$

This is different to the orientation relationship between hexagonal close packed and face centred cubic metals which is normally observed, for example that between zinc and aluminium determined by previous workers (36,44)

$$\text{i.e. } [111]_{Al} // [0001]_{Zn}$$
$$(1\bar{1}0)_{Al} // (2\bar{1}\bar{1}0)_{Zn}$$

It was suggested that this zinc-rich ε phase was mainly responsible for the good anti-friction properties of the commercial alloy Alzen 305 (4). However in a recent investigation (35) the ε phase was reported to be metastable in alloys of these compositions, and the present work showed that it decomposed on quench ageing at 200°C for approximately 90 hours, Fig. 70.

The copper-rich T phase reported earlier (14,15,32) could not be identified in the experimental copper-containing alloys (2, 3 and 4). The T phase in the zinc-aluminium-copper alloys was reported (35,68) to form according to the phase transformations;

$$\beta \rightarrow \alpha + \eta + \varepsilon \text{ and } \alpha + \varepsilon \rightleftharpoons T + \eta$$

These transformations require from several months to several years to be completed at room temperature and increase the volume of the sample up to 4% (17).

It is possible that formation of T phase required a longer ageing time than the 2 hours allowed for in the electron microscopic examination, since the coarse ε phase decomposed only after ageing 90 hours at 200°C. The presence of the extremely hard T phase (4) in these alloys is of great importance, since it could provide the load carrying phase of the bearing and minimise wear during operation.

It appears that a long heat-treatment, at temperatures below 268°C, is essential in order to complete all the phase transformations and hence to avoid any dimensional changes in the quenched zinc-aluminium-copper alloys.

The transformation behaviour of these alloys on quench-ageing was investigated by metallography, hardness and quantitative X-ray diffraction methods to establish a suitable heat-treatment which produces the desired structure, and determine the effect of composition on the kinetics of the $\alpha/\acute{\alpha}'$ or β phase decomposition.

The hardness change on isothermal ageing of supersaturated solid solutions occurs due to their transformation into two or more different phases. Transformation is thus a nucleation and growth process and is controlled by diffusion. The shape of the hardness curve is primarily a function of two variables; the temperature at which ageing occurs and the composition of the alloy, since these alter the rate of transformation and chemical supersaturation.

Hardness and quantitative X-ray diffraction results showed that the quenched β phase of the binary eutectoid alloy (1B) decomposed spontaneously at room temperature due to rapid diffusion in solid solution. Consequently precipitation of new phases occurred quickly causing a rapid increase in hardness. Again due to rapid diffusion in this solid solution coarsening of the transformed products also occurred quickly and caused a sudden decrease in hardness of this alloy as shown in Fig. 92.

At higher temperatures the transformation was faster because the diffusion rate in the solid solution increases with increasing temperature according to the equation

$$D = D_o \exp(-Q/kT) \quad (148) \quad \ldots\ldots\ldots\ldots \quad (10)$$

Precipitation and overageing thus overlap and gives rise to a lower peak hardness at shorter times. In the binary eutectoid alloy, precipitation occurred so rapidly above room temperature that the peak in the hardness curve was not detectable. Consequently the hardness curves obtained on this alloy at temperatures above ambient, only showed the overageing behaviour when the precipitates were coarsening and decreasing the hardness.

However in the zinc-aluminium based ternary alloys (2B, 3B, 4B and 5B) the peak hardnesses were reached in a much longer time than in the binary eutectoid alloy at the same temperature. This demonstrates the effect of additional alloying elements on the transformation behaviour of the zinc-aluminium alloys during ageing. It is obvious that in the ternary alloys diffusion is a far slower process than in the binary eutectoid alloy, and is a combined effect of zinc/aluminium ratio and ternary alloying additions.

Alloy 4B reached its peak hardness after a much longer time than the binary zinc-aluminium (1B) and other zinc-aluminium-copper (2B and 3B) alloys as seen in Figs. 93, 94 and 95. This clearly demonstrates the effect of zinc/aluminium ratio on the transformation characteristics of the zinc-based binary (Zn-Al) and ternary (Zn-Al-Cu) alloys during quench-ageing, since α solid solution of alloy 4B has the lowest zinc content.

The hardness curves, in general, show that the decomposition rate of the quenched zinc-aluminium solid solutions on isothermal ageing increases with increasing temperature and zinc-content.

The hardness results of Figs. 93, 94 and 95 show that alloy 3B reached its peak hardness earlier than the other zinc-aluminium-copper alloys (2B and 4B), although it had the highest copper content (4%). This effect can be explained in terms of the composition of the as-quenched supersaturated solid solutions of these alloys; β (2B), β+ε (3B) and α (4B).

The β solid solution of alloy 3B contains more zinc and slightly less copper than the β phase of alloy 2B. This is because some of the copper content of alloy 3B is consumed in the formation of ε phase. The hardness change of this alloy mainly results from the decomposition of its β phase, because this phase is the matrix of the structure, Figs. 67 and 68, and the amount of ε present is less than 15%. In addition although ε is not stable at temperatures below 268°C (35) it is a much more stable phase than β at any temperature. The quantitative X-ray diffraction and metallographic examinations on quench-ageing of this alloy suggest that the incubation period for decomposition of ε phase is longer than the period of time allowed for the hardness measurements. Hence the effect of ε phase on the hardness curves of this alloy is negligible.

Therefore it appears that on quench-ageing the β solid solid solution of alloy 3B, due to its higher zinc and lower copper contents, transforms faster than the β phase of alloy 2B, as seen in Figs. 93 and 94. This is in full agreement with the results of quantitative X-ray diffraction, obtained from the β phase of both alloys (2B and 3B), as shown in Figs. 102 and 104.

The hardness curves, in general, also show that the magnitude of the peak hardnesses and the hardness value in the quenched condition (before ageing) and at a given time during overageing of the zinc-aluminium solid solutions (α and β) increased with increasing aluminium and copper. However this is not necessarily the case during prepeak-ageing to a fixed time at constant temperature, because the hardness value depends on the transformation rate of the quenched solid solution. The hardness value measured during ageing prior to peak hardness, is not very significant for comparing the alloys, since they are normally used in the overaged condition. It may be concluded that hardness results provide useful information in order to establish suitable heat treatments which produce the required structure and strength for the applications of these alloys.

The hardness curves also indicate that the magnitude of the hardness increase on ageing increased with increasing zinc content. This effect can easily be seen when the hardness curves of alloys 4B and 5B are compared with the curves obtained on the eutectoid-type higher zinc alloys (1B, 2B and 3B). The monotectoid or lower-zinc alloys such as 4B and 5B showed less hardening than the eutectoid alloys. A typical example of this is shown in the hardness curve of alloy 5B obtained on room temperature ageing, which shows very little hardening, as seen in Fig. 96. The reason for this effect is that less zinc is available in solid solution in alloys 4B and 5B, for precipitation on ageing and hence less precipitation gives rise to smaller hardening.

The hardness curves of alloys 2B and 3B (Figs. 93 and 94) show that up to $60^{o}C$ hardness change decreased with increasing ageing temperature, but above $60^{o}C$ hardness change increased with increasing temperature, as the peak hardness at 100°C is higher than the values obtained at lower temperatures (20°C and 60°C). This result is contradictory to the usual transformation behaviour on ageing of solid solutions where both the rate of transformation and coarsening of the products increase with increasing temperature. Precipitation and overageing thus overlap and give rise to a lower peak hardness. Normally the hardness of the decomposed solid solutions increases as the ageing temperature decreases, because at low temperatures nucleation rate is high but growth rate is low. Therefore as the temperature decreases the number of nuclei increases, and the mean interparticle spacing of the precipitates is smaller. According to established theories of precipitation strengthening (149) this gives rise to higher hardness. Additionally, in alloys such as those investigated, where the solubility of the second component increases rapidly with temperature, the supersaturation rapidly decreases at high temperatures. This effect reduces the nucleation rate and further lowers the peak hardness. Such an effect was observed with alloy 4B as shown in Fig. 95.

The contradictory results to the above principles, obtained on alloys 2B and 3B suggest that a different transformation mechanism operates during quench-ageing of the β solid solution above 60°C (i.e. at 100°C). This could be due to the change in the type of precipitate or zone formed above 60°C, so that the shear strength of the precipitate is greater or its dispersion is finer, leading to higher hardnesses.

This unusual change in hardness of the β solid solution with increasing ageing temperature, was consistent with the hypothesis of Garwood and Hopkins (61), who proposed a change in the mode of decomposition of this solid solution at ∿100°C on the basis of kinetic measurements. This change was also confirmed metallographically by Ardell et al (56) during investigation of the decomposition of the binary zinc-aluminium alloy on quench ageing, but they suggested that the change in decomposition mechanism occurred at room temperature.

It may be concluded that although the zinc-aluminium system has favourable solubility and precipitation characteristics, it is not a useful age-hardening system, since diffusion is rapid and over-ageing occurs very quickly even at room temperature.

Comparison of the hardness and quantitative X-ray diffraction results showed that in the binary eutectoid alloy (1B) hardness reached the maximum value much earlier than completion of full transformation, Figs. 92 and 101. This can be explained in terms of diffusion control. If diffusion is rapid, coarsening of the transformed products can occur before decomposition is completed, therefore the softening effect produced, offsets to some extent the hardening increment due to transformation. Peak hardness is then reached before full transformation is completed, and the magnitude of the hardening is reduced.

However in the ternary zinc-aluminium-copper alloys (2B and 3B) the diffusion is much slower at room temperature and hence the peak hardness is reached when full transformation is completed. This can be seen from the hardness and transformation curves of alloys 2B and 3B obtained at room temperature, Figs. 93, 94, 102, 104.

Transformation curves of fraction transformed (f) versus Ln time of alloy 2B obtained on both $(200)_{\beta}$ and $(10\bar{1}1)_{Zn}$ X-ray diffraction peaks show slight difference in transformation rate as seen in Figs. 102 and 103ab. The time required for the $(200)_{\beta}$ to reach a certain f value is found slightly less than the time necessary for $(10\bar{1}1)_{Zn}$. This is more evident in the early stage of transformation but decreases as the transformation proceeds. The difference can be explained by postulating that when the β phase breaks down it does not initially transform directly into zinc. Instead it produces a transitional zinc-rich phase which is too fine or insufficient in quantity to be detected by the X-ray method used. This phase then decomposes into zinc and zinc peak appears. The separation in the f versus Ln time curves for β and zinc are this accounted for.

The transformation curves obtained from the $(10\bar{1}1)_{Zn}$ diffraction peaks of alloys 1B and 2B showed a similar consistent deviation from the usual pattern of a transformation curve, as seen in Figs. 101 and 103ab. This deviation apparently corresponds to a change in the transformation rate of these alloys on quench-ageing. However this change is not evident in the transformation curves obtained from $(200)_{\beta}$

diffraction peaks of alloys 2B and 3B, as shown in Figs. 102 and 104. Therefore it must be related to the mode of zinc formation. A similar, but un-noted kink in the zinc formation curve is evident in the results of Ciach et al (145) who investigated the decomposition of the binary eutectoid alloy on quench-ageing, using the $(10\bar{1}1)_{Zn}$ diffraction peak, shown in their diagram of Fig. 8.

This observation suggests that zinc forms by two different mechanisms. Two possible decomposition mechanisms are continuous and discontinuous precipitation of zinc-rich phases. It is probable that zinc forms by both continuous and discontinuous modes, until the free energy of the remaining β is lowered to such an extent that there is insufficient energy change across the discontinuous phase-boundary to drive it forward. As a result discontinuous precipitation slows down or stops and continuous precipitation proceeds, and hence the transformation rate decreases. If the product of discontinuous precipitation is zinc and the products of continuous precipitation are transitional phases which revert to zinc, then the differences in the transformation curves can be explained. However in the alloys which show the effect such mixed precipitation modes were only observed at temperatures above ambient. Therefore a further examination may be needed to find evidence for the mixed precipitation products on quench-ageing at about room temperature, since a transition from lamellar mode of decomposition to a spinodal structure has been reported to take place at either room temperature (56) or about 100°C (61).

Quantitative X-ray diffraction results suggest that, on ageing, the transformation characteristics of the quenched β phase in the binary zinc-aluminium (1B) and ternary zinc-aluminium-copper (2B) eutectoid alloys are identical. The main difference is in the transformation rate, as the transformation rate of the ternary alloys is much lower than that of the binary alloy. This similarity can easily be seen when the transformation curves (f vs. Lnt) obtained from $(10\bar{1}1)_{Zn}$ diffraction peaks of both binary (1B) and ternary (2B) alloys are compared, Figs. 101 and 103ab.

The X-ray diffraction results obtained from the binary (1B) and ternary (2B and 3B) eutectoid alloys, in good agreement with the hardness measurements, show that the transformation rate of the quenched β phase on isothermal ageing is controlled by;

(a) ageing temperature,
(b) zinc/aluminium ratio, and
(c) presence of copper and its quantity.

The transformation rate of the quenched β phase increased with increasing zinc content and decreased as the copper content is increased.

The activation energies for transformation of alloy 2B on quench-ageing, determined from hardness and quantitative X-ray diffraction results were found to be very close, as seen in Tables 4b and 10. This indicated that both methods provided identical information on the kinetics of transformation in these alloys. The activation energies for transformation of these alloys (70 - 90 kJ/mol) were found to be between the activation energies for grain boundary diffusion, ∿61 kJ/mol (150), and for lattice self-diffusion, 91.3 kJ/mol (151), in pure zinc, but lower than the activation energy for lattice self-diffusion in pure aluminium, 143.2 kJ/mol (152).

It has been found that the transformation of metals or alloys which involves the nucleation and growth of a second phase, often obeys the Avrami relationship, represented by an equation of the form

$$f = 1-\exp(-kt)^{n} \quad \ldots\ldots\ldots\ldots\ldots\ldots (11)$$

where f is the fraction transformed and n and k are constants (153). If this is so, then a plot of LnLn[1/(1-f)] versus Ln t will be linear, and from it values of k and n may be determined.

The data for LnLn[1/(1-f)] versus Ln t plots obtained from either $(200)_\beta$ or $(10\bar{1}1)_{Zn}$ diffraction peaks of the alloys 1B, 2B and 3B are given in Tables 6, 7abc, 8ab and 9 and the plots are shown in Figs. 150, 151, 152ab and 153 in order of alloy number. The plots determined using the data obtained from the $(10\bar{1}1)_{Zn}$ diffraction peaks of these alloys were not found to be linear. However the plots obtained with the data from $(200)_\beta$ diffraction peak of alloy 2B were mostly found to be good straight line fits, particularly at room temperature, Fig. 151. The same plot for alloy 3B, obtained again with the data from $(200)_\beta$, showed good linearity but with two or more distinct slopes Fig. 153.

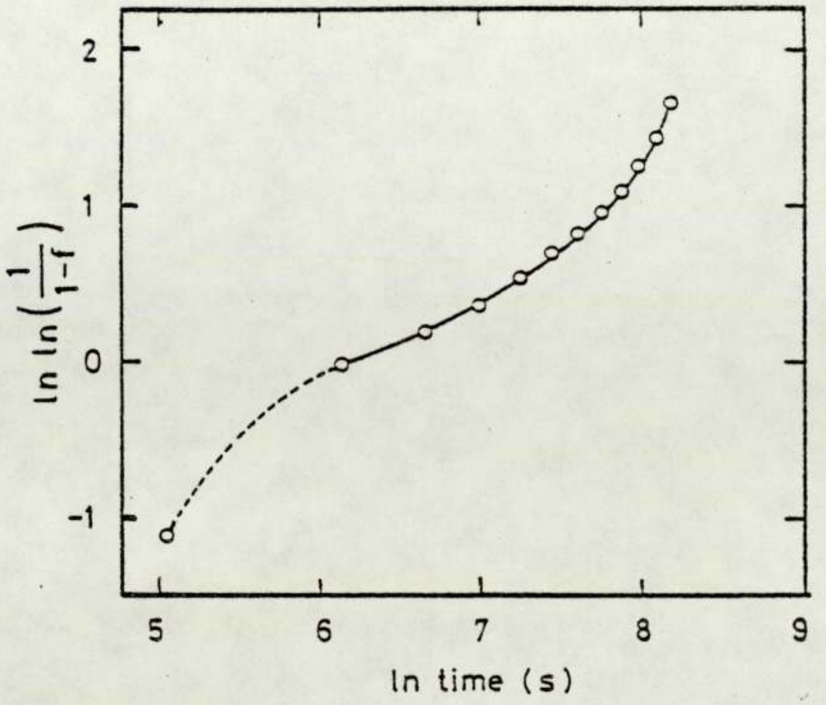

Fig. 150 Avrami plot for transformation of alloy 1B at room temperature determined from the $(10\bar{1}1)_{Zn}$

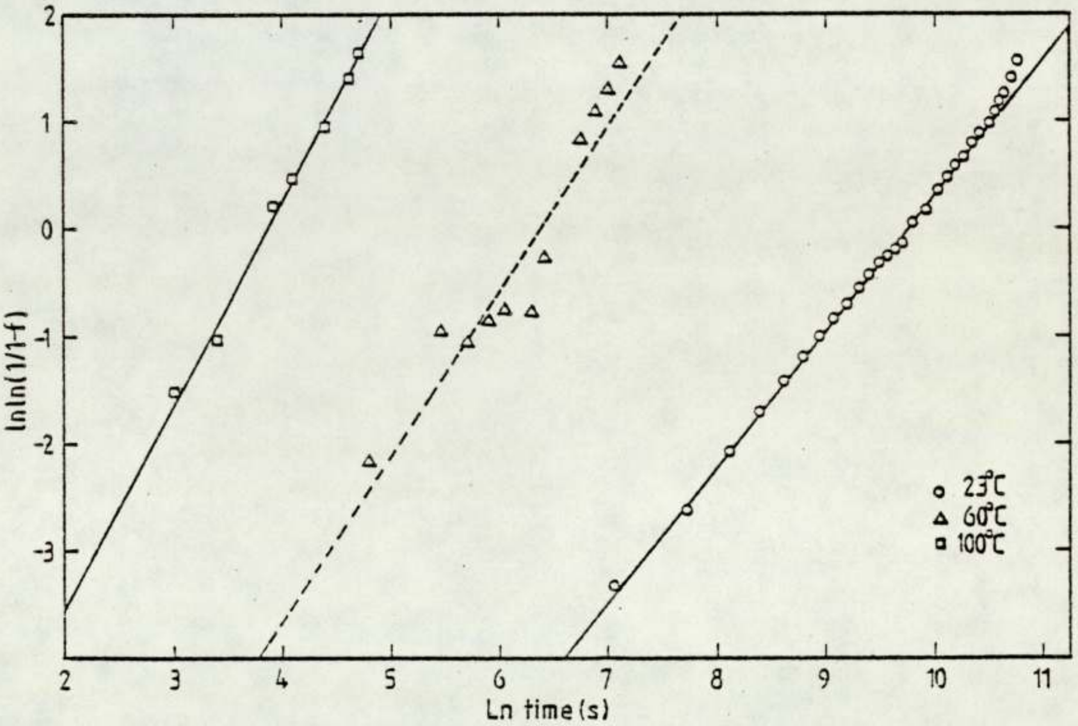

Fig. 151 Avrami plots for transformation of alloy 2B at different temperatures determined with the data obtained from $(200)_\beta$ diffraction peaks

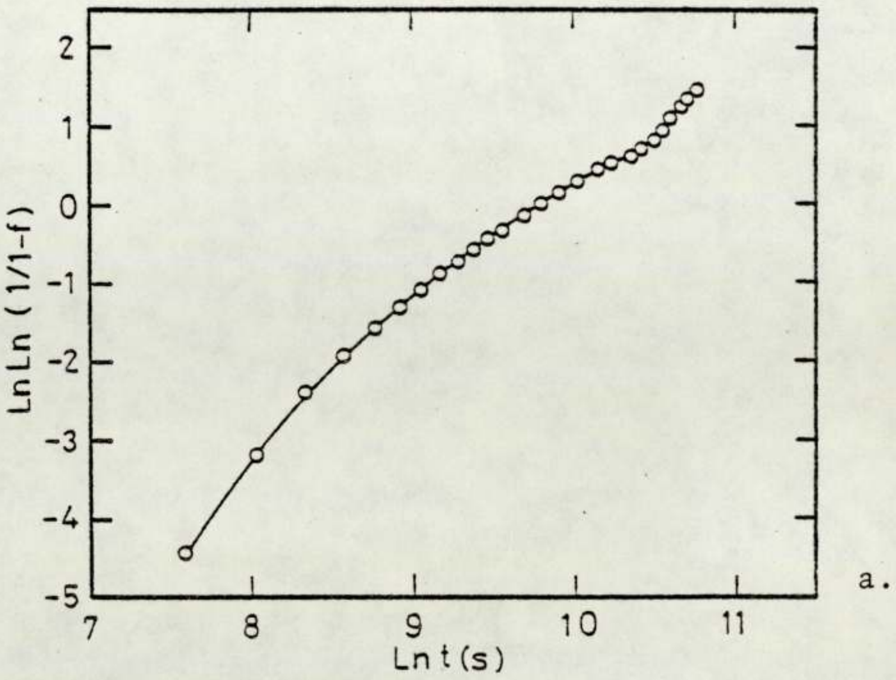

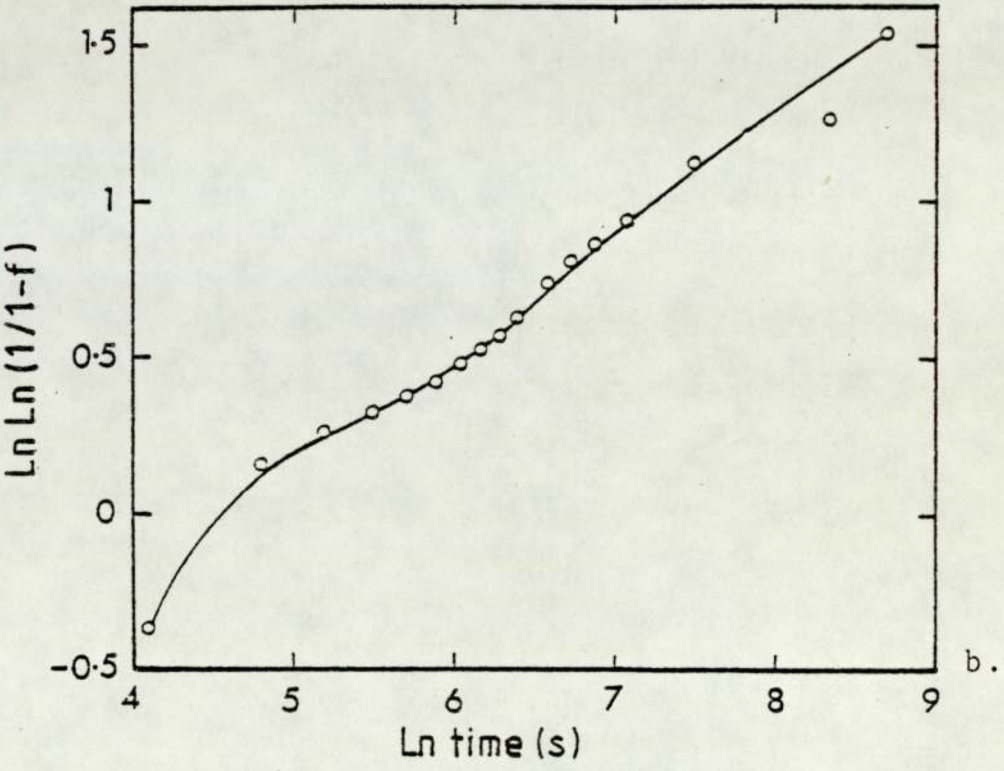

Fig. 152 Avrami plots for decomposition of alloy 2B on quench-ageing a) at room temperature and b) at 100°C, determined from the $(10\bar{1}1)_{Zn}$

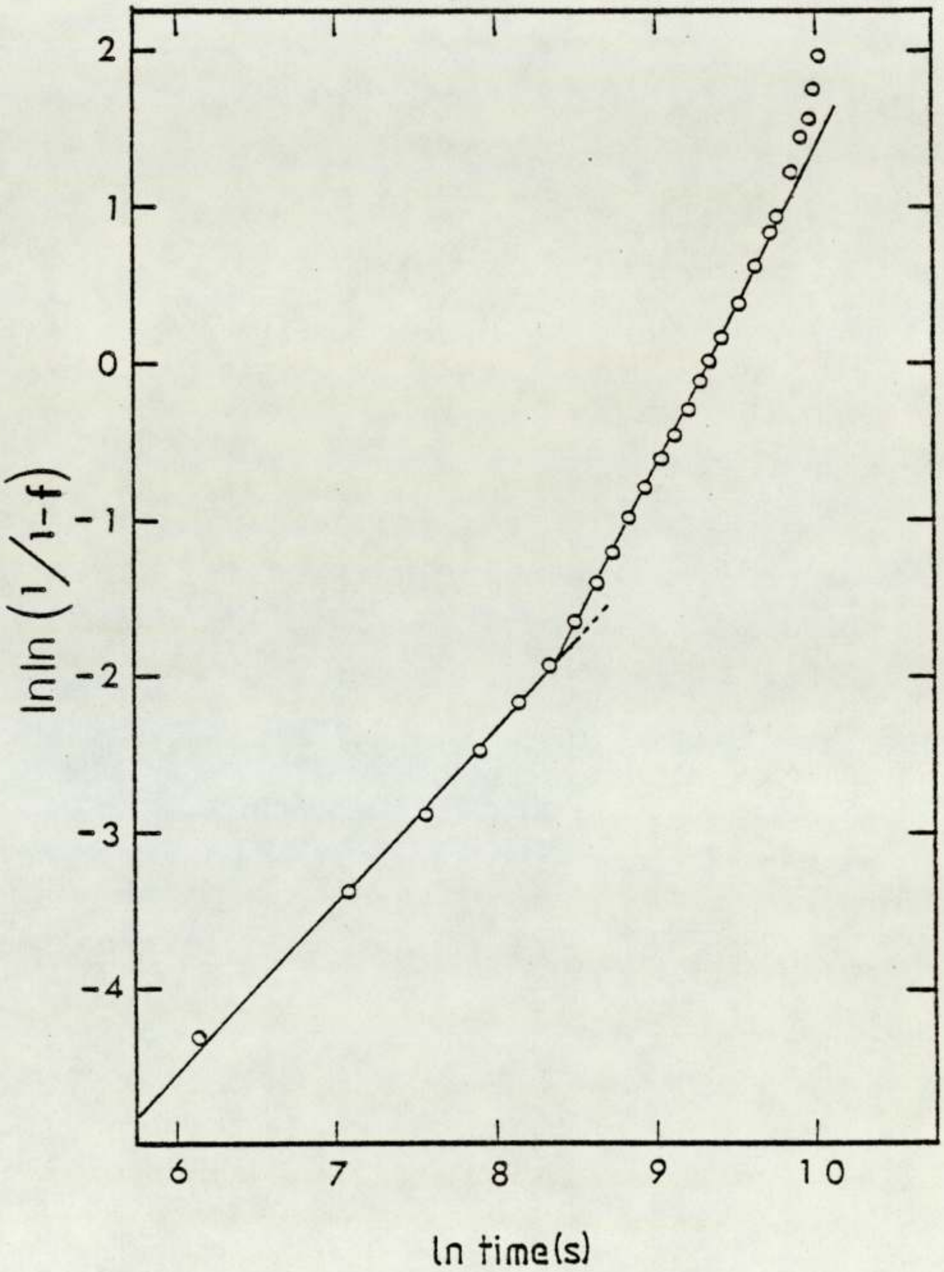

Fig. 153 Avrami plot for transformation of alloy 3B at room temperature, determined from the $(200)_\beta$

The values of n and k obtained for alloys 2B and 3B, by fitting straight lines to the data points from the $(200)_{\beta}$ diffraction peak, are listed in Table 16. This table shows that n is between 1 and 2, and the values of both n and k for alloy 2B increase with increasing temperature.

TABLE 16

Values of n and k in the Avrami Relation

Alloy	Temperature (^{o}C)	n	k (s^{-1})
	23	1.3	5.8×10^{-5}
2B	60	1.6	1.5×10^{-3}
	100	1.9	2.1×10^{-2}
3B	20	1.1	4.0×10^{-5}
		2.0	8.5×10^{-5}

When the Avrami or Johnson-Mehl (154) graph of $\mathrm{LnLn}[1/(1-f)]$ against Ln t shows a pronounced negative curvature as in Figs. 150 and 152ab better agreement is frequently obtained by replacing (1-f) by $(1-f)^2$ in equation $df/dt = k^n t^{n-1}(1-f)$ (152). In this case the rate equation becomes

$$df/dt = (1-f)^2 \, k_A^{n} \, t^{n_A-1} \quad \ldots\ldots\ldots.(12)$$

which, assuming k_A and n_A to be constants, integrates to

$$^{f}/_{1-f} = (k_A t)^{n_A} \quad \ldots\ldots\ldots\ldots\ldots.(13)$$

with the term in n_A taken into the constant. This integrated rate equation was first used by Austin and Ricketts (155) to analyse the kinetics of austenite decomposition. This equation defines another exponent n_A and the rate constant

k_A, which are different from n and k. n_A is determined from a graph of $Ln[f/(1-f)]$ against Ln t which is linear of slope n_A in equation (13).

The transformation data obtained from either $(10\bar{1}1)_{Zn}$ or $(200)_\beta$ diffraction peaks of the zinc-based eutectoid alloys were replotted in the form of $Ln[f/(1-f)]$ versus Lnt. The results for alloys 1B, 2B and 3B are given in Figs. 154, 155, 156ab and 157 respectively, showing that these plots in general are not good straight line fits. Since such poor linearity shows that the equation does not hold for these results the Austin-Rickett equation was not considered of any practical use and was not used further.

However the presence of two or more distinct slopes to the plots of $LnLn[1/(1-f)]$ or $Ln[f/(1-f)]$ versus Lnt which were found for alloys 2B and 3B, Figs. 151, 153, 155 and 157 may be taken as an evidence of two or more distinct types of decomposition reaction. This explanation was proposed to account for differences in the fraction transformed calculated from the $(200)_\beta$ and $(10\bar{1}1)_{Zn}$ peak measurements for alloy 2B.

Deviations from linearity of the $LnLn[1/(1-f)]$ versus Lnt plots of Figs. 150-153 are explicable in terms of the assumption made in deriving the transformation equation. Although developed as an empirical equation some success has been obtained in applying it to transforming systems where growth rate, nucleation rates and transformation geometry are known (148, 149, 153). Hence values of the exponent n are found to give information on the above variables. The theory leading to the equation consists of two parts; the first develops an expression for the fraction which would be produced by transformation, if no impingement of the growing regions occurred. The second part provides a correction for impingement which combined with the first, allows calculation of the true fraction transformed.

In the Avrami relationship it is assumed that the hypothetical fraction f_x is a simple function of the form

$$f_x = (kt)^n \quad \ldots\ldots\ldots\ldots\ldots\ldots(14)$$

Correction is provided by an equation of the form

$$f = 1-\exp(-f_x) \quad \ldots\ldots\ldots\ldots\ldots(15)$$

substitution for f_x this gives

$$f = 1-\exp\left[-(kt)^n\right] \quad \ldots\ldots\ldots\ldots(16)$$

f_x can then be derived if assumptions are made about the nucleation rate of new transformed volumes ($\dot{N}$) and their linear growth rate ($\dot{G}$).

It has been shown (155) that unless $\dot{N}$ and $\dot{G}$ vary in a very simple way with time, linear forms of the $\mathrm{Ln}\,\mathrm{Ln}[1/(1-f)]$ vs. Ln time plot would not be expected. Values of n less than 3 can only be obtained if $\dot{G}$ decreases rapidly with time or the geometry of the growth front is essentially two dimensional (153,154,157). Metallographic examination suggests that transformation is three dimensional, Figs. 61, 62, 73, 88, 89. Therefore the low n values are possibly due to reduced growth rate with time caused by changes in the matrix ahead of the transformed volume. Alternatively if it is assumed that decomposition occurs by the nucleation of the zinc-rich phase and the expansion of a zinc-denuded volume around it, then the increased diffusion path brought about by growth might have a similar effect.

Quantitative assessment of the creep behaviour of the different alloys under different conditions can only be effected if the creep properties can be correlated in a satisfactory manner according to useful mathematical relationship.

According to Mukherjee et al (86) creep data may be correlated using an empirical equation of the form:

$$\dot{\varepsilon}_s = A\sigma^n \exp(-Q/kT) \quad \ldots\ldots\ldots\ldots\ldots\ldots(1)$$

On integration, this becomes

$$\varepsilon = A.t.\sigma^n \exp(-Q/kT)+K \quad \ldots\ldots\ldots\ldots\ldots(17)$$

where K is an integration constant.

This equation implies a linear dependence of ε on time at constant temperature and stress and is therefore only truly applicable in the secondary creep region.

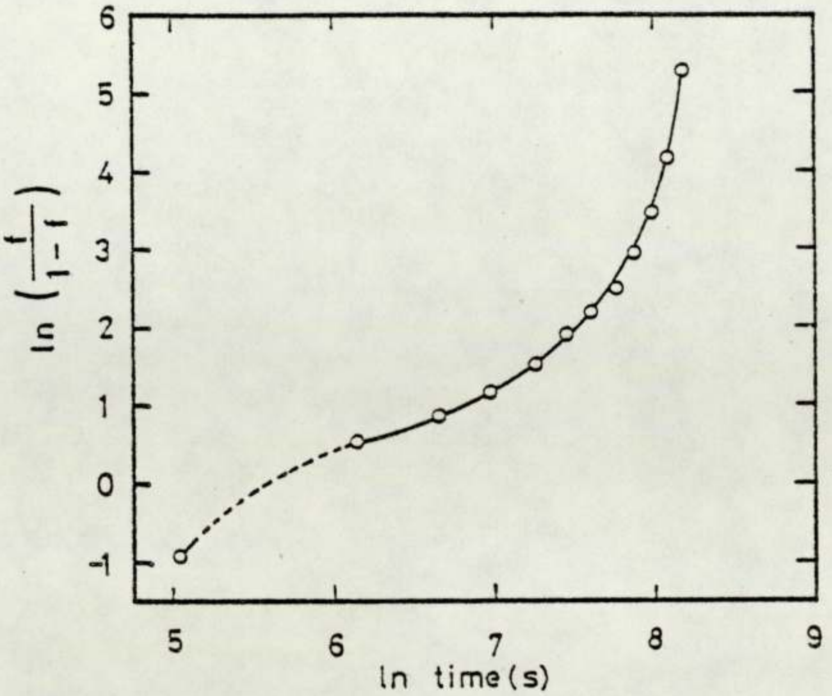

Fig. 154 Ln[f/(1-f)] vs. Ln(time) plot for transformation of alloy 1B at room temperature

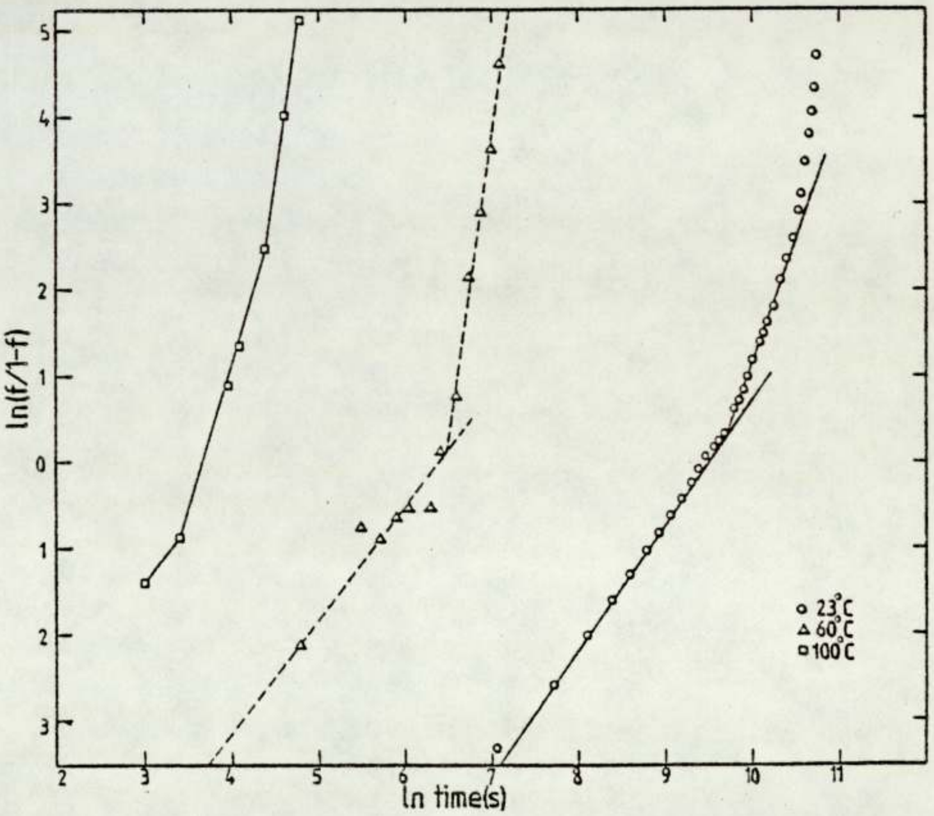

Fig. 155 Ln[f/(1-f)] vs. Ln(time) plots for transformation of alloy 2B at different temperatures, determined from the $(200)_\beta$

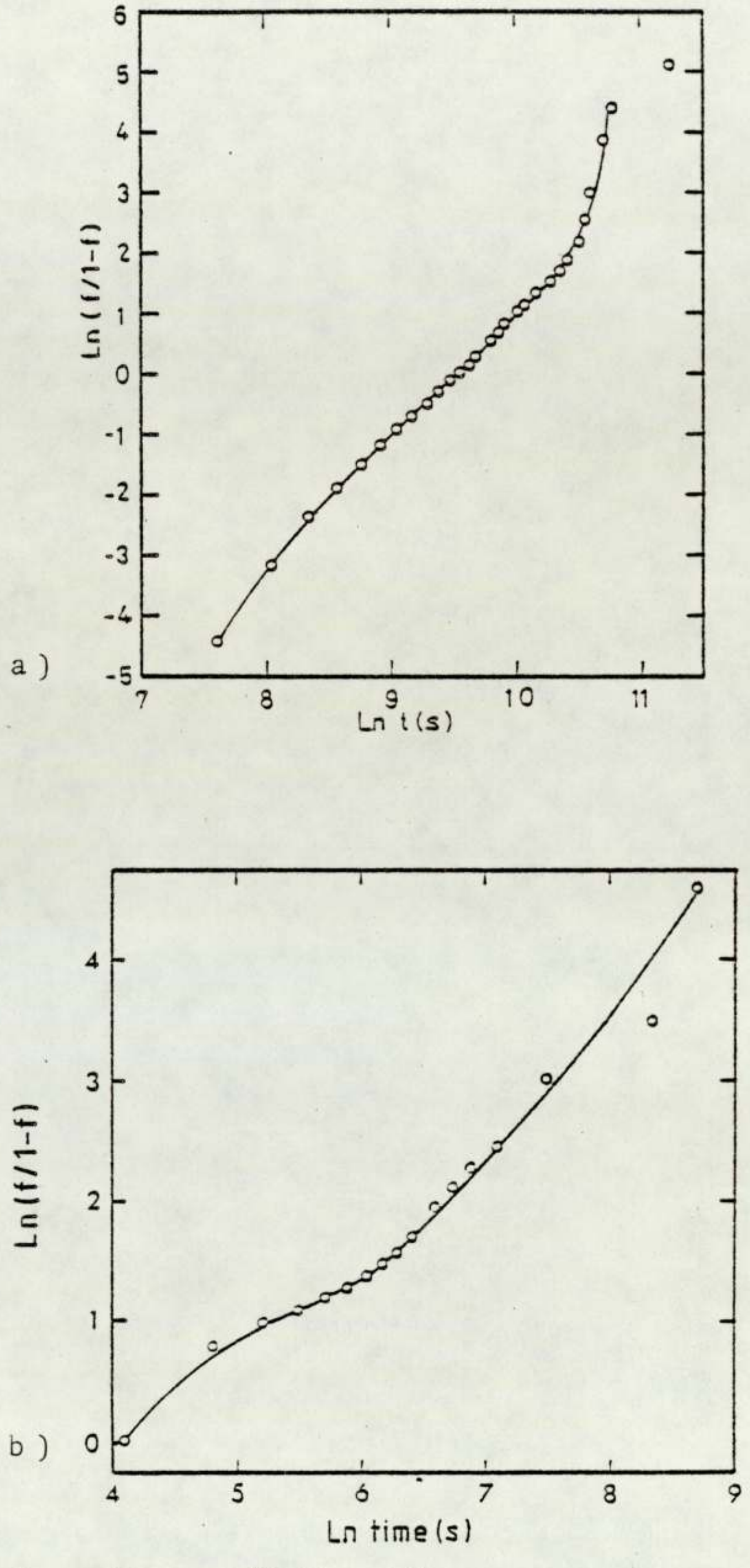

Fig. 156 Ln[f/(1-f)] vs. Ln(time) for transformation of alloy 2B

a) at room temperature and

b) at 100°C,

determined from the $(10\bar{1}1)_{Zn}$

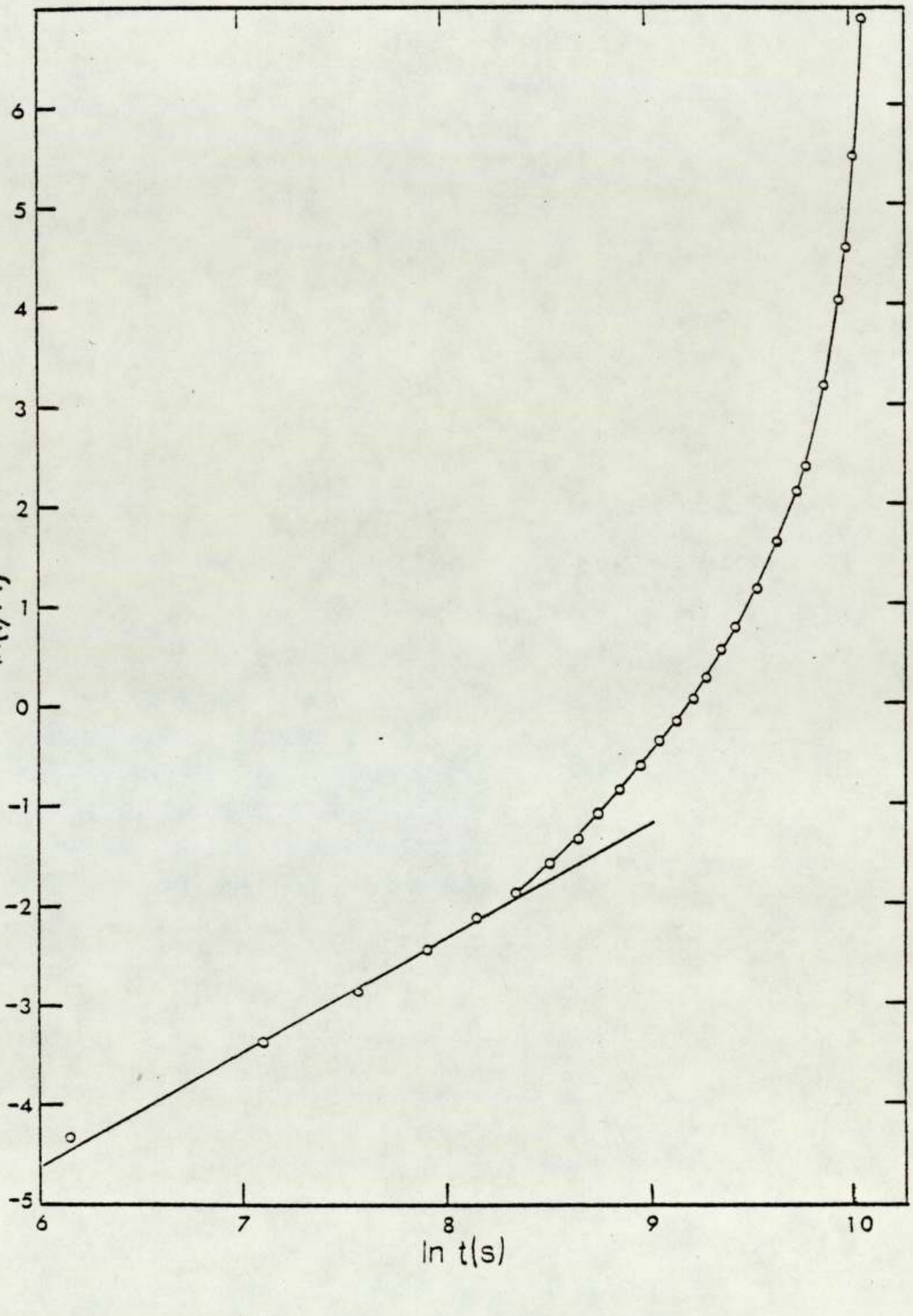

Fig. 157 Ln[f/(1-f)] vs. Ln(time) for transformation of alloy 3B at room temperature

According to the above equation, a plot of $\mathrm{Ln}\dot{\varepsilon}_s$ against the reciprocal of the absolute temperature should give a straight line of slope -Q/k and intercept (LnA + nLnσ), since:

$$\mathrm{Ln}\dot{\varepsilon}_s = n\mathrm{Ln}\sigma + \mathrm{Ln}A - \frac{Q}{k} \cdot \frac{1}{T} \;......(18)$$

The data for these plots were calculated from the creep results in Table 13 for all the zinc-based alloys. The plots produced from this data, showing the variation of $\mathrm{Ln}\dot{\varepsilon}_s$ with $^1/T$ at different constant stress levels are shown in Figures 158 to 163 in order of alloy number. Only a single stress level was used for alloy 1A since other results were invalid due to the presence of excessive porosity in the test piece. Fig. 159 for alloy 1B shows parallelism of the plots at three different stress levels. However only two points were available for each line so the real linearity of the curves is unknown. However similar parallelism of the curves is shown in the plot for alloy 3A, and 3B within a certain scatter, although alloys 2A and 2B may show real variations in the slopes of the lines. In all cases where three points were available for each line, the plots were linear within an acceptable degree of scatter.

The straight lines and their slopes and intercepts were determined by a linear regression method, and the calculated activation energies were determined for each alloy at each stress level. These results are listed in Table 17.

Again from the creep rate equation, plots of $\mathrm{Ln}\dot{\varepsilon}_s$ versus the Ln applied stress (σ) should yield straight lines of slope n and intercept (LnA-Q/kT). The data for such plots are calculated from the results in Table 13, and the plots are shown in Figures 164 to 170. In general, good straight line plots were obtained for each alloy, although the fit was possibly better for the heat-treated alloys than the as-cast alloys. However at high temperatures for certain alloys, e.g. 1B (Fig. 165), 2A (Fig. 168) and 6 (Fig. 170), the slopes of the straight line is markedly lower than for other temperatures, showing that n is not truly constant over the range of experimental conditions used. The values of n were calculated together with the intercept by linear regression method and are listed in Table 18. This table includes the reciprocal of n, i.e. the strain rate sensitivity factor m.

Since linearity of the above plots is in accordance with the form of the creep equation used, a plot of the creep strain (ε) versus the parameter $[t\sigma^n \exp(-Q/kT)]$ should also be a single straight line of slope A and intercept K for each alloy condition. Such a parametric plot should allow the total creep strain in the secondary region to be calculated for any combination of temperature, applied stress and time. The values of the constants n and Q/k are the mean values of these presented in Tables 17 and 18 respectively. The intercept ($\mathrm{Ln}A + n\mathrm{Ln}\sigma$) and ($\mathrm{Ln}A - Q/kT$) also allow A to be calculated once the mean values of n and Q/k are known. However a considerable degree of extrapoltation is made to obtain A in this way, hence A is better obtained from the slope of the parametric plots.

The results of the plots of creep strain (ε) versus the parameter $\left[t\tilde{\sigma}^n \exp(-Q/kT)\right]$ for the alloys 1A, 1B, 2A, 2B, 3A and 3B are shown in Figures 171 to 176 respectively.

Figure 171 shows a reasonable correlation of the data for alloy 1A. The intercept on the strain axis is zero showing that the integration constant K is insignificant compared with the magnitude of the parameter term. Little scattering was shown up to 20×10^{-3} strain values, above this figure a considerable degree of scatter arises. This scatter is not random but arises from the presence of a number of distinct creep curves. For example at 80°C testing temperature the separate curves are moved to lower strains for higher stress levels. The parameter does not compensate sufficiently for the stress variation. However overall the plot is approximately linear. The value of A calculated from the slope of the line is 29×10^7. This compares well with the values obtained from the individual curves for different temperatures (Table 19).

The plot for alloy 1B is shown in Fig. 172. A large scatter is evident in the results, but the overall curve is approximately linear and passes through the origin. Again data obtained at the same temperature but different stress levels are not effectively superimposed by the parametric plot but lie on separate curves. The sense of the displacement is not the same for different temperatures. For example 80°C is displaced with higher strain levels with increasing stress whilst for 120°C the displacement is to lower strain levels. This suggests that the stress dependence of the creep strain (ε) is more complicated than given by the parameter. A is calculated from the slope of the line as 1.6×10^2.

The remaining plots for alloys 2A, 2B, 3A and 3B are shown in Figs. 173, 174, 175 and 176 respectively. In all cases the plots are approximately linear and pass through the origin. All show similar behaviour in that scatter is due to failure of the parametric plot to superimpose the separate creep curves exactly.

The plots for alloys 2A and 2B give significantly better correlation than 3A and 3B. No consistent correlation of displacement of the curves with either stress or temperature could be found.

The A values calculated for alloys 2A, 2B, 3A and 3B are 6.6×10^4, 11.4×10^4, 5.7 and 8.8 respectively.

It may be concluded that the expression

$$\varepsilon \;=\; At\sigma^n \exp(-Q/kT) \;\ldots\ldots\ldots\ldots (17a)$$

can be used to correlate the creep data for all of the zinc-based alloys but with a variable and generally large scatter. The maximum error involved in calculating the creep strain (ε) is of the order of $\mp 10^{-2}$.

It is possible that some of the scatter is due to the use of the applied stress instead of the effective stress $(\sigma-\sigma_o)$ according to the argument of Willshire and his co-workers $^{(92, 9, 94)}$. The modified form of this equation takes into account the presence of a friction stress which effectively reduces the applied stress by a constant amount. The equation becomes:

$$\dot{\varepsilon}_s = A^*(\sigma-\sigma_o)^p \exp(-Q/kT) \text{ ....(4)}$$

The values of the friction stress (σ_o) were measured as described in section 2.5.3 and are presented in Table 12. The friction stresses for the heat-treated zinc-based alloys were found to be zero, and for these alloys the above equation is identical to the previous form. For the as-cast alloys, the friction stress has a positive value which is significantly large compared with the applied stress.

To examine the effect of the friction stress on correlation of the data, values of $\mathrm{Ln}\dot{\varepsilon}_s$ were plotted against $\mathrm{Ln}(\sigma-\sigma_o)$ in Figs. 177, 178 and 179. Such plots should be linear with a slope p and intercept $[\mathrm{Ln}A^*-Q/kT]$. The values used in the plots and the measured p values are given in Table 20.

Figure 177 shows the results of this plot for alloy 2A at 120°C and 150°C. Comparison of this with Fig. 166 shows that an increased scatter is obtained, but the p values are more similar. Figure 178 shows the results for alloy 3A. In this case, comparison with Figure 168 shows that a better correlation of the data is obtained and again the p values are more constant than the n values of the previous relationship. For alloy 6 also a slightly better correlation of the data obtained at 350°C was found, Fig. 179.

Using a similar approach to the data correlation, the values of p deduced from Figs. 177 to 179 were used to calculate values of the parameter $[t(\sigma-\sigma_o)^p\exp(-Q/kT)]$. Hence creep strains for alloys 2A and 3A were plotted against this parameter. Friction stresses at all the testing temperatures were not available for alloy 1A, and σ_o for the heat-treated alloys are zero therefore the parameters for these alloys are the same as the previous ones.

The data for alloy 2A are plotted in the Fig. 180. Comparison of this with Fig. 173 shows that the scatter is very much larger. Similar Figure 181 for alloy 3A shows less scatter and slightly better correlation than the previous plot, although the data obtained at 180°C are not included.

It appears that allowing for the friction stress does not materially affect the correlation of the creep data in these alloys. Since the displacement of the individual curve from the average line is approximately constant, it is possible that the expression for ε should be of the form:

$$\varepsilon = At\sigma^n\exp(-Q/kT) + f(T,\sigma). \quad .....(19)$$

Another creep equation which is stated to be universally applicable $^{(95)}$ is of the form:

$$\dot{\varepsilon}_s = B\left(\frac{\sigma-\sigma_o}{\sigma_{0.05}}\right)^{3.5} \quad \ldots\ldots\ldots\ldots\ldots(5)$$

where B has the value ≃2.5 x 10^{-5}/s and independent of material. The effective stress $(\sigma-\sigma_o)$ and the 0.05% proof stress $(\sigma_{0.05})$ take into account the effects of temperature and material condition. Taking logarithms,

$$\mathrm{Ln}\dot{\varepsilon}_s = \mathrm{Ln}B + 3.5\mathrm{Ln}(\sigma-\sigma_o) - 3.5\mathrm{Ln}(\sigma_{0.05}) \quad \ldots(20)$$

So a plot of $\mathrm{Ln}\dot{\varepsilon}_s$ versus $\mathrm{Ln}(\frac{\sigma_o-\sigma_o}{\sigma_{0.05}})$ should be a straight line of slope 3.5 and intercept LnB. All the data from alloys for which σ_o and $\sigma_{0.05}$ are known are plotted in this way in Fig. 182. The continuous straight line corresponds to the results of Evans and Harrison $^{(95)}$ in their Fig. 7. It can be seen that although the data points lie approximately in the region near to this line, there is a great deal of scatter. A large scatter is seen even for a single alloy in some cases and others seem to correlate well but with their own individual B and n.

Overall, the scatter is too great to allow values of the strain rate in secondary creep to be estimated with sufficient accuracy from the universal creep equation.

Although either of these approaches will correlate creep data to a limited degree, a more accurate estimation of the creep strain under any combination of applied stress and temperature can be obtained by the less ambitious approach of using experimentally determined families of creep curves. In Figs. 183 to 189 for example, the Ln time to selected strains is plotted against the Ln applied stress (σ) for working temperatures of 80, 120 and 150°C for the zinc-based alloys, and 350°C for alloy 6. The slopes of these curves are equal to -n, if the basic equation is accepted, and the values of n derived from these logarithmic plots (Table 21) were found to be similar to these calculated from Figs. 164 to 170. Examination of these plots shows that they are mostly good straight line fits and variation found for some alloys may be real or due to experimental scatter. However, the plots for alloy 1B showed two different sets of straight lines, Fig. 184, which may be interpreted in terms of two distinct slopes reported earlier (110,158) for the plots of stress dependence of strain rate (Ln$\dot{\varepsilon}$ vs Lnσ) of this alloy. Extrapolation of the Ln(time) versus Ln(applied stress) curves allows the prediction of stress or time taken for a certain creep strain at a certain temperature.

On the other hand the general parametric equation allows the results to be extrapolated to different temperatures. For example in Table 22 stresses for creep strain of 10×10^{-3} and 20×10^{-3} at temperatures of 20, 80 and 120°C are listed for each alloy. These temperatures correspond to approximately ambient temperature, machinery working temperature, and an overheated condition in the latter. In the last column of Table 22 the stresses (σ_2) estimated from the separate curves of Ln time versus Lnσ plots for the alloys including alloy 6.

Comparison of the stress values (σ_1 and σ_2) calculated from each method show that fair agreement occurs at the higher stress levels. However low stress levels produced wide discrepancies, differing by a factor of 2 or 3 in extreme cases.

It may be concluded that the parametric method allows the estimation of stress to a certain strain under different conditions to be estimated. The errors involved were possibly large; nevertheless it would be acceptable to a design engineer and allow a reasonable classification of the alloys according to their creep behaviour. Thus from Table 22 the order in which the alloys fall in respect to their creep behaviour is 6, 2A, 1A, 3A, 2B, 3B and 1B.

According to this order alloy 1A is more creep resistant than alloy 3A. This is contrary to the creep results obtained from both alloys under the same test conditions, because alloy 3A showed a much lower creep rate than alloy 1A at 120°C, as seen in Table 13. This unexpected result may arise from the Q/k value for alloy 1A, since it was calculated from only two data points, and found to be considerably higher than the values obtained from three data points for the other as-cast alloys. However this is not important for classification of the alloys, since the binary alloy was not considered to be useful for bearing applications.

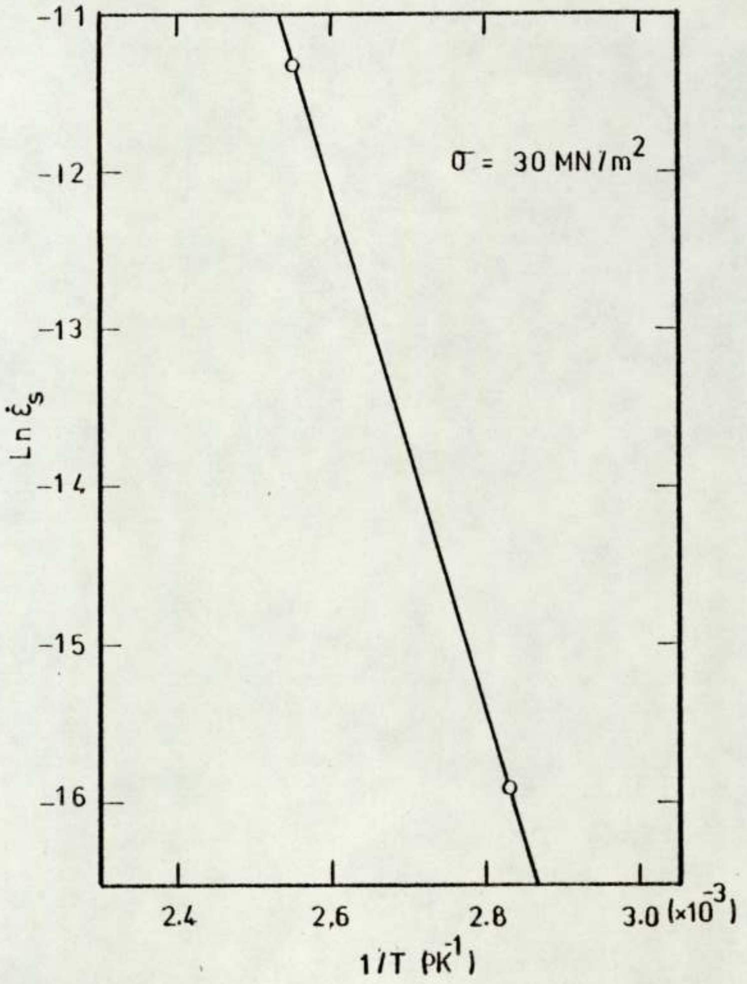

Fig. 158 Temperature-dependence (Ln$\dot{\varepsilon}_s$ vs $^1/T$) of secondary creep rates at 30 MN/m^2 for alloy 1A

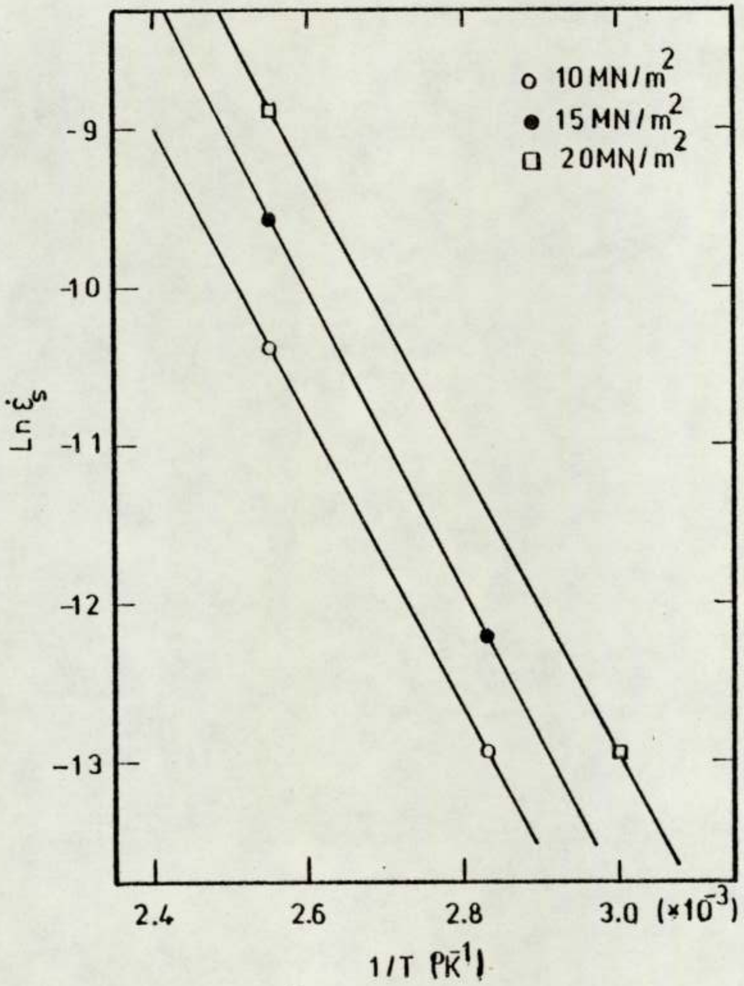

Fig. 159 Ln$\dot{\varepsilon}_s$ vs $^1/T$ plots at constant stresses for alloy 1B

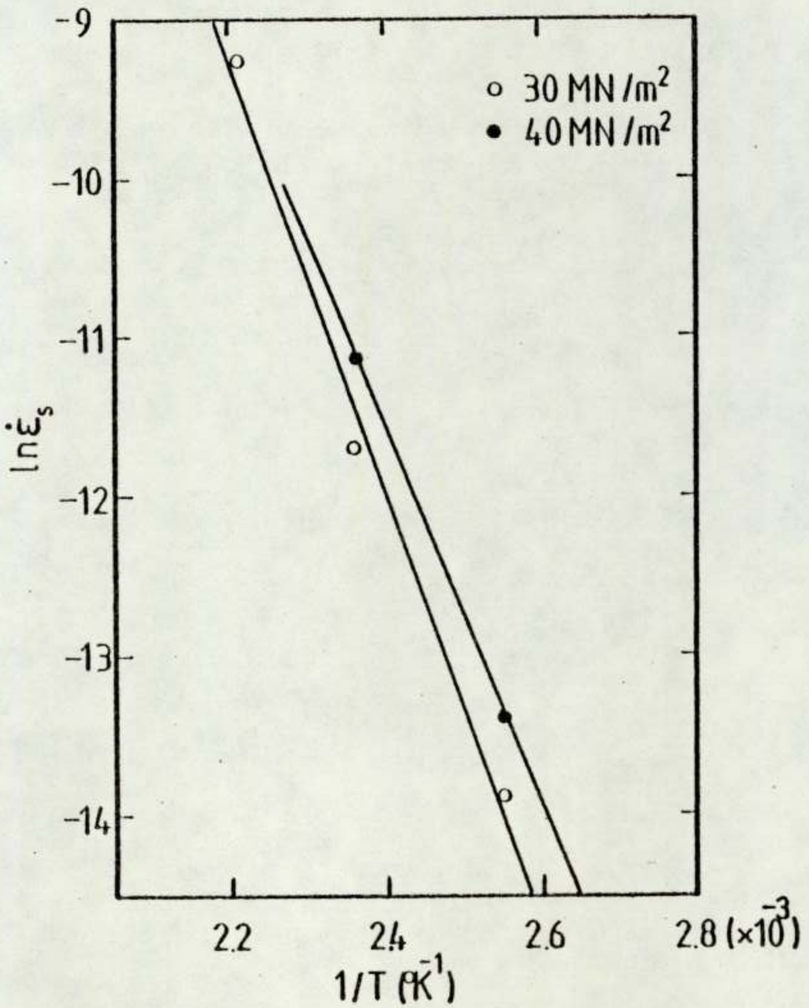

Fig. 160 Temperature-dependence of secondary creep rates at 30 and 40 MN/m^2 for alloy 2A

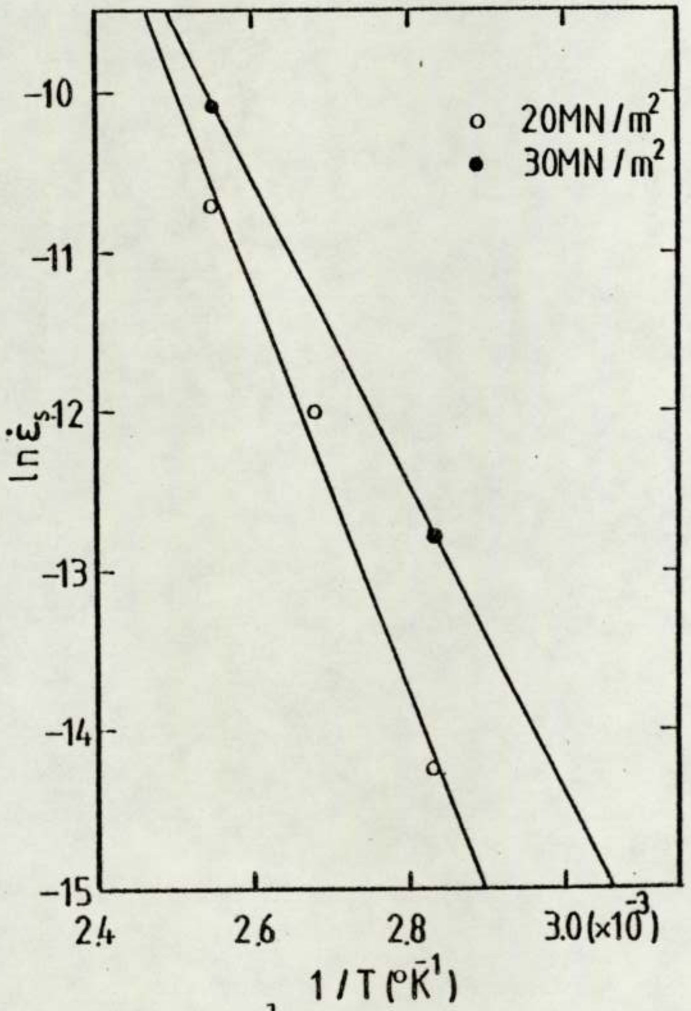

Fig. 161 Ln$\dot{\varepsilon}_s$ vs $^1/T$ plots at constant stresses for alloy 2B

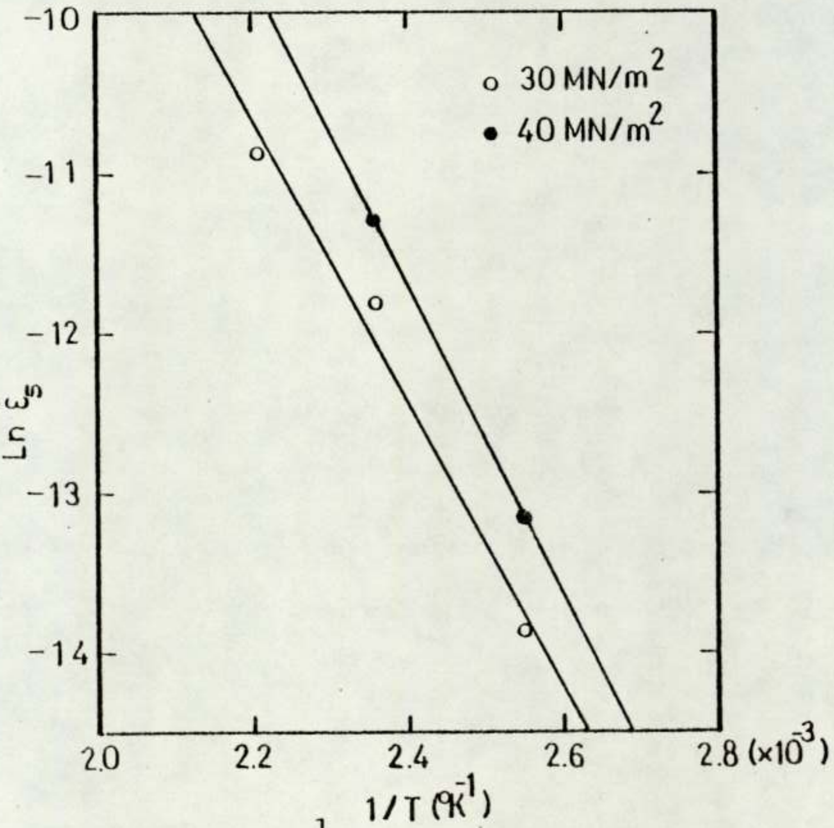

Fig. 162 Ln$\dot{\varepsilon}_s$ vs $^1/T$ plots at 30 and 40 MN/m^2 for alloy 3A

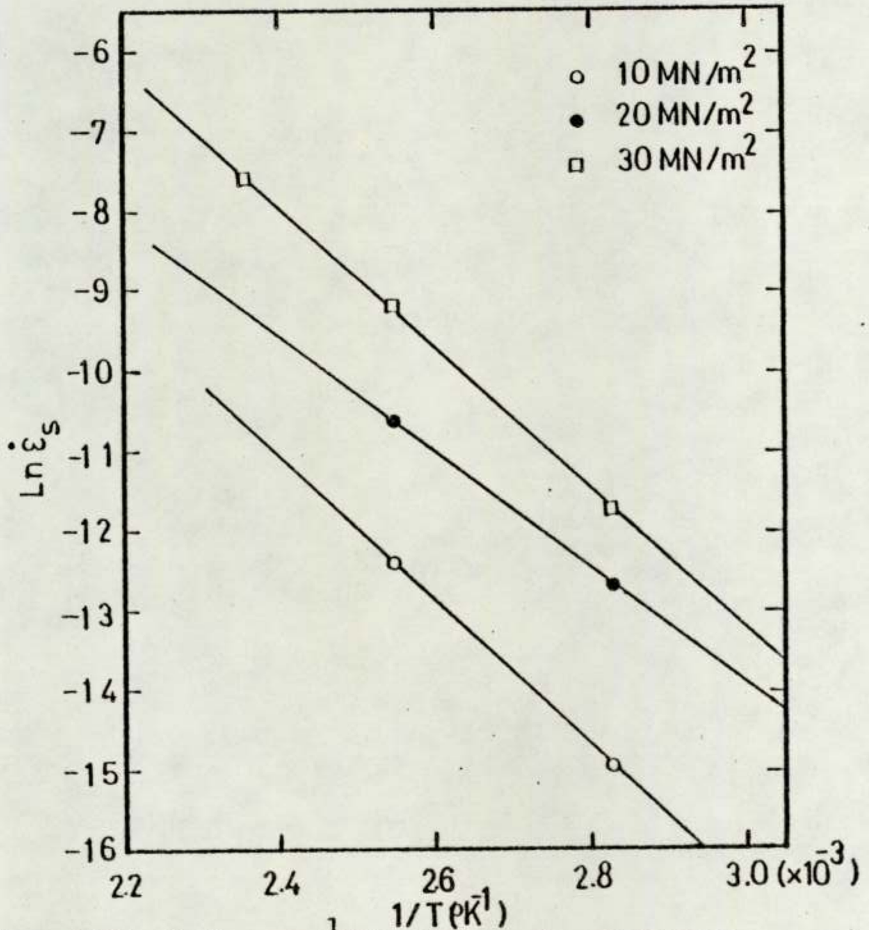

Fig. 163 Ln$\dot{\varepsilon}_s$ vs $^1/T$ plots at constant stresses for alloy 3B

TABLE 17

Activation energies for creep of the alloys determined from the slopes of the $\mathrm{Ln}\dot{\varepsilon}_s$ versus $^1/T$ plots

Alloy	Stress (MN/m^2)	Slope (Q/k) x 10^3	Activation Energy Q(kJ/mol)
1A	30	16.36	136
1B	10	9.11	76
	15	9.50	79
	20	9.07	75
2A	30	13.50	112
	40	11.90	99
2B	20	12.70	106
	30	11.43	95
3A	30	8.91	74
	40	9.74	81
3B	10	9.11	76
	20	7.32	61
	30	8.83	73

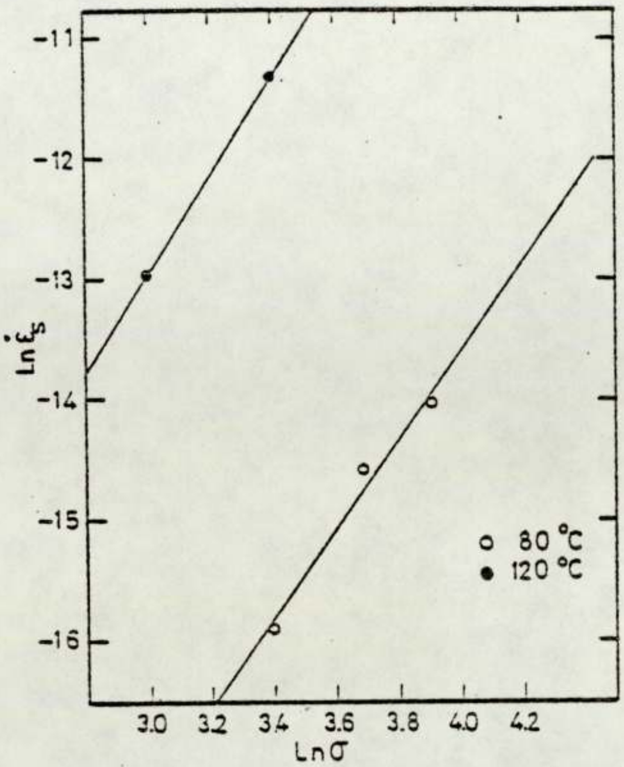

Fig. 164 Stress-dependence of secondary creep rates at 80 and 120^{o}C for alloy 1A

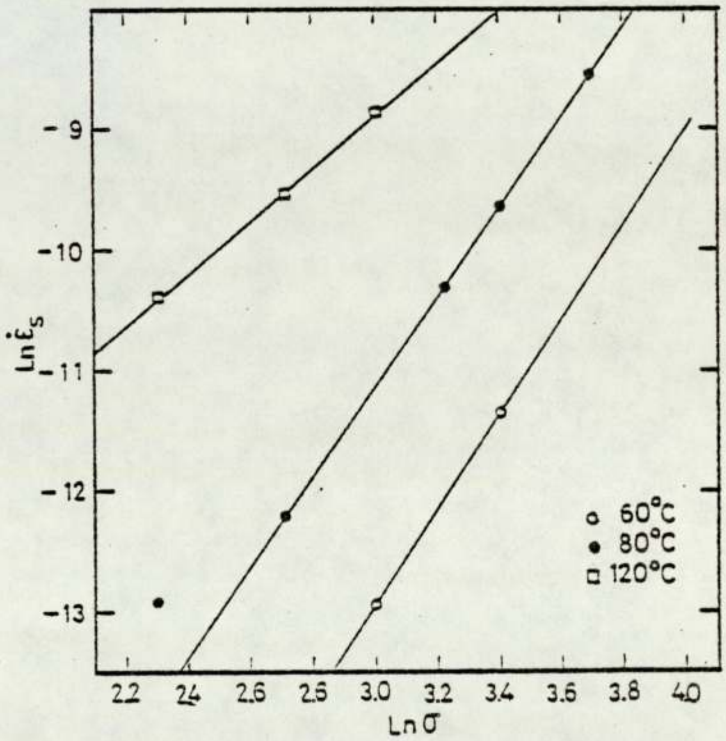

Fig. 165 Stress-dependence of secondary creep rates ($\mathrm{Ln}\dot{\varepsilon}_s$ vs $\mathrm{Ln}\sigma$) at different temperatures for alloy 1B

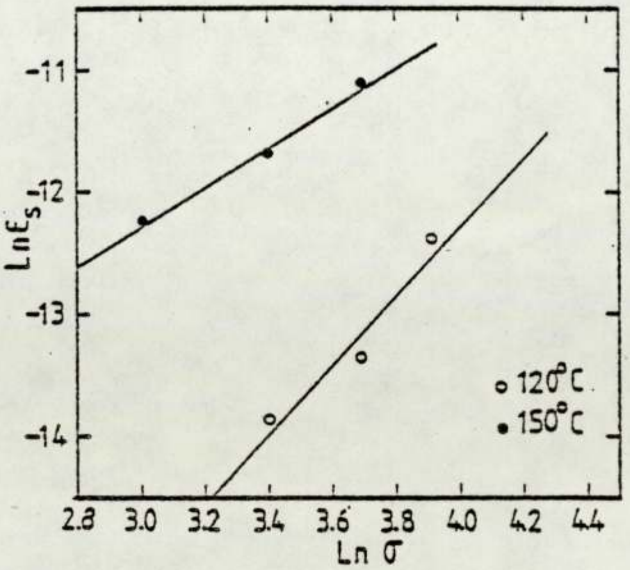

Fig. 166 $\mathrm{Ln}\dot{\varepsilon}_s$ vs Ln stress plots at 120 and 150°C for alloy 2A

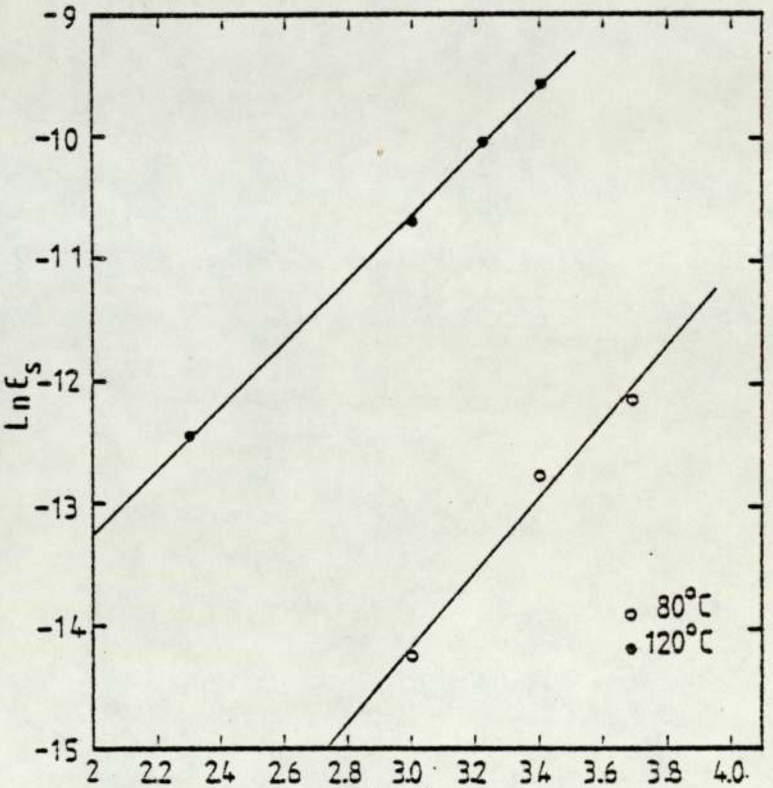

Fig. 167 $\mathrm{Ln}\dot{\varepsilon}_s$ vs $\mathrm{Ln}\sigma$ plots at 80 and 120°C for alloy 2B

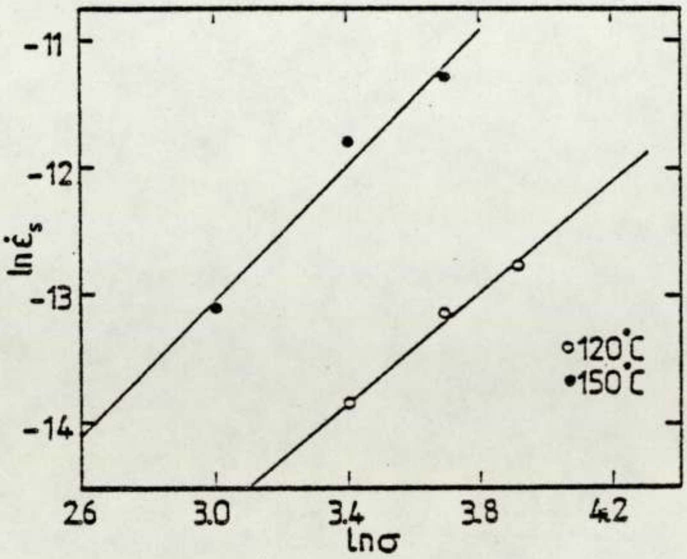

Fig. 168 Stress-dependence of secondary creep rates ($\ln\dot{\varepsilon}_s$ vs $\ln\sigma$) at 120°C and 150°C for alloy 3A

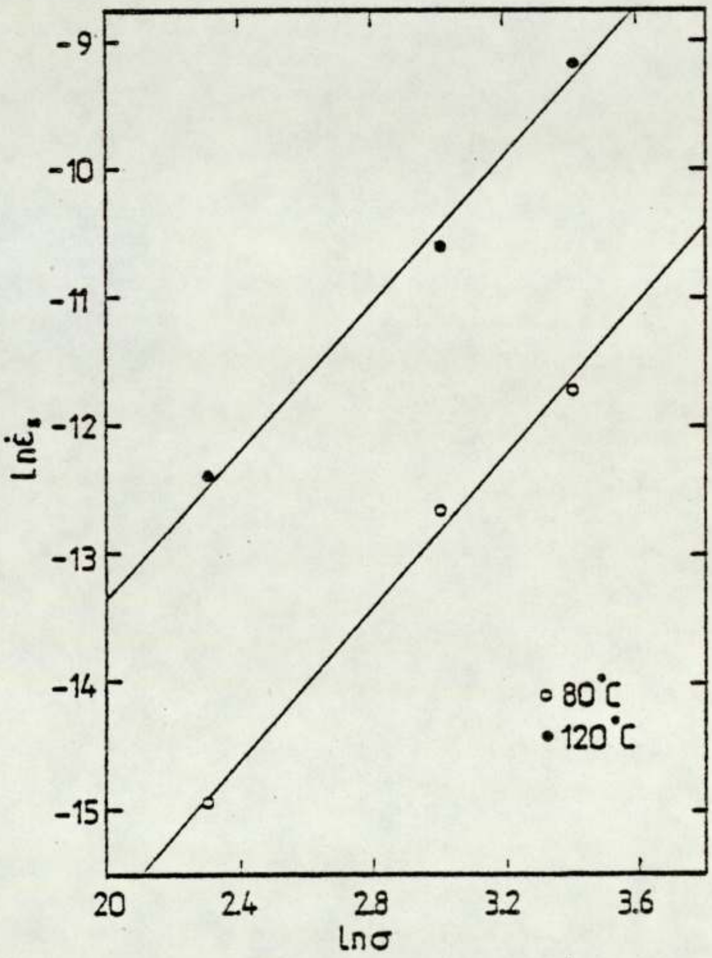

Fig. 169 $\ln\dot{\varepsilon}_s$ vs $\ln\sigma$ plots at constant temperature for alloy 3B

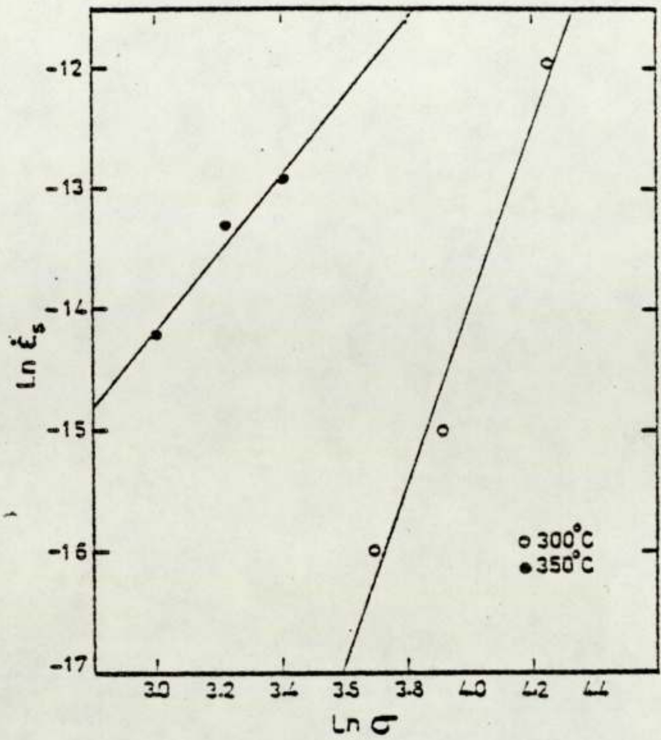

Fig. 170 Ln$\dot{\varepsilon}_s$ vs Lnσ plots at 300°C and 350°C for alloy 6

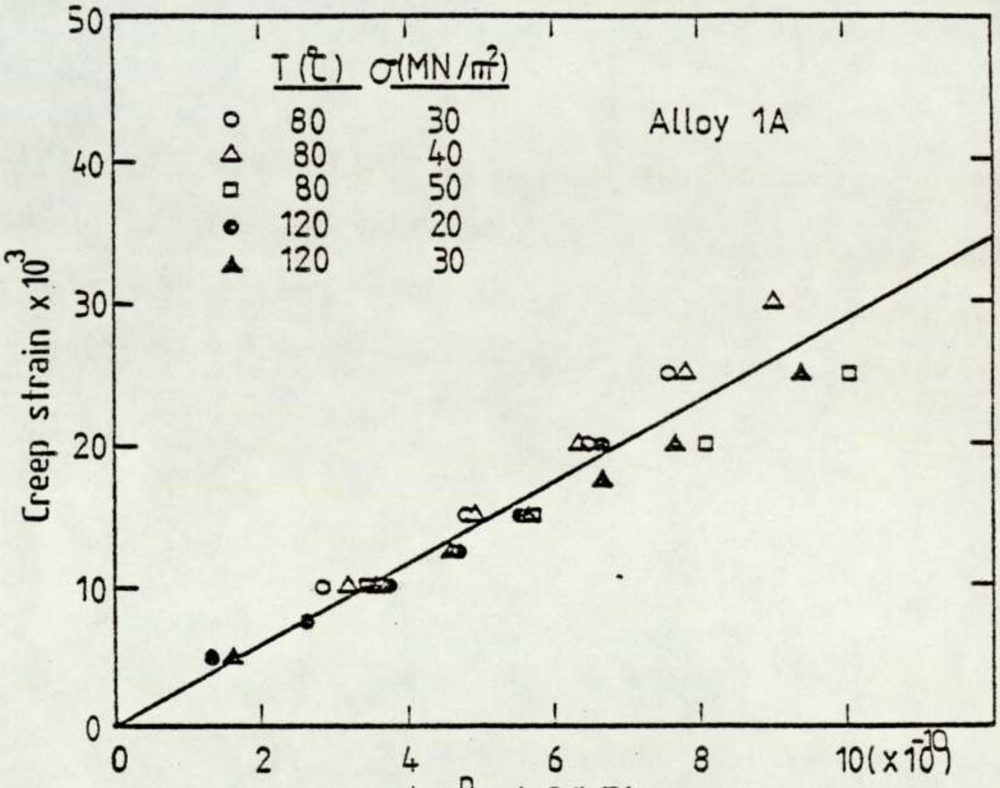

Fig. I71 Creep strain (ε) versus parameter ($t\sigma^n\exp(-Q/kT)$) plot at different temperatures and stresses for alloy 1B

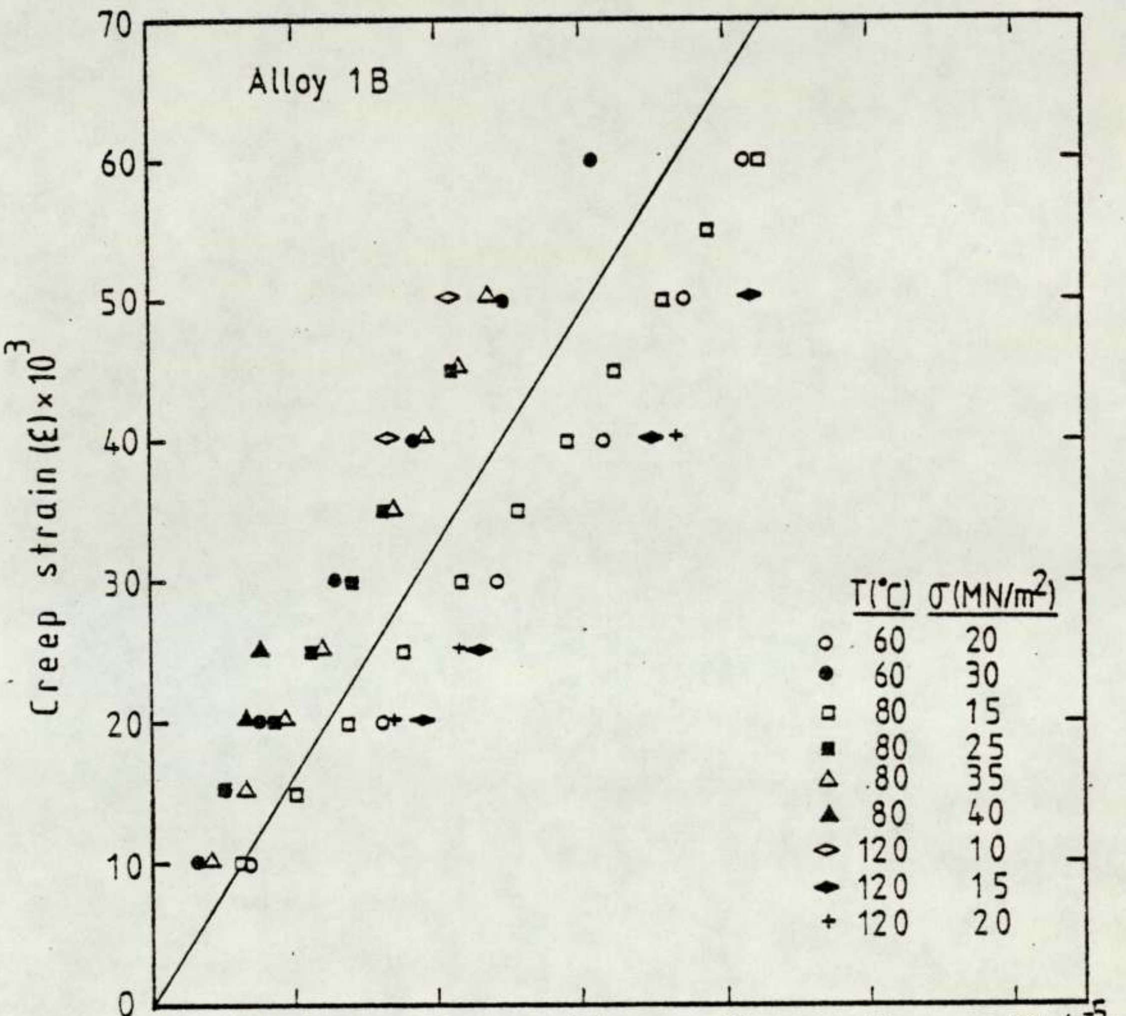

Fig. 172 Creep strain (ε) versus $t\sigma^n\exp(-Q/kT)$ plot for alloy 1B

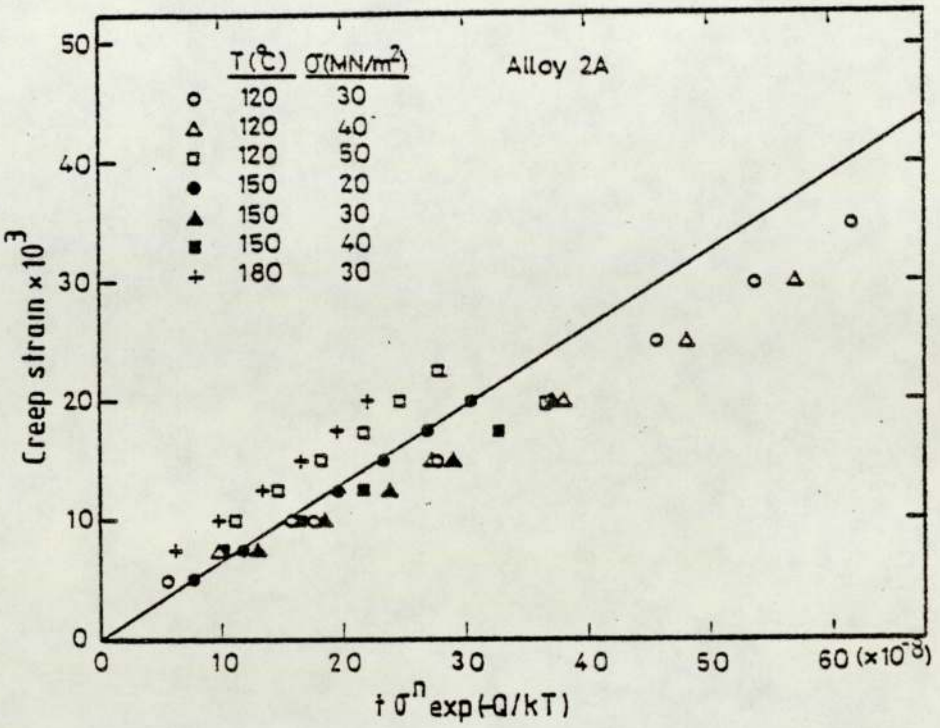

Fig. 173 Creep strain (ε) versus parameter ($t\sigma^n\exp(-Q/kT)$) plot for alloy 2A

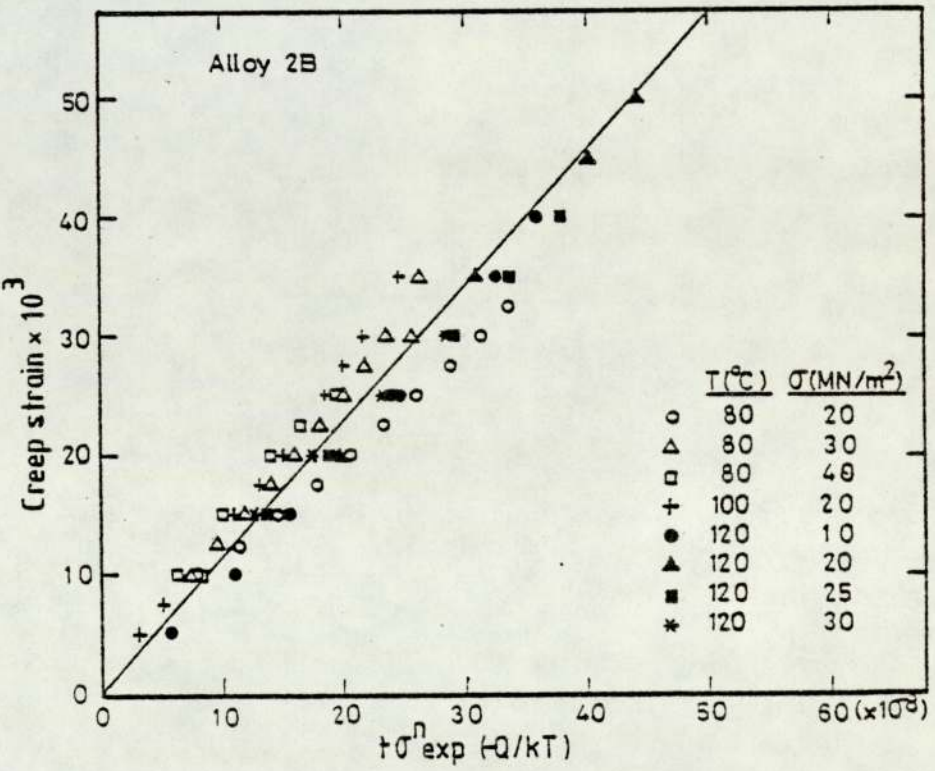

Fig. 174 Creep strain (ε) versus parameter $[t\sigma^n\exp(-Q/kT)]$ plot for alloy 2B

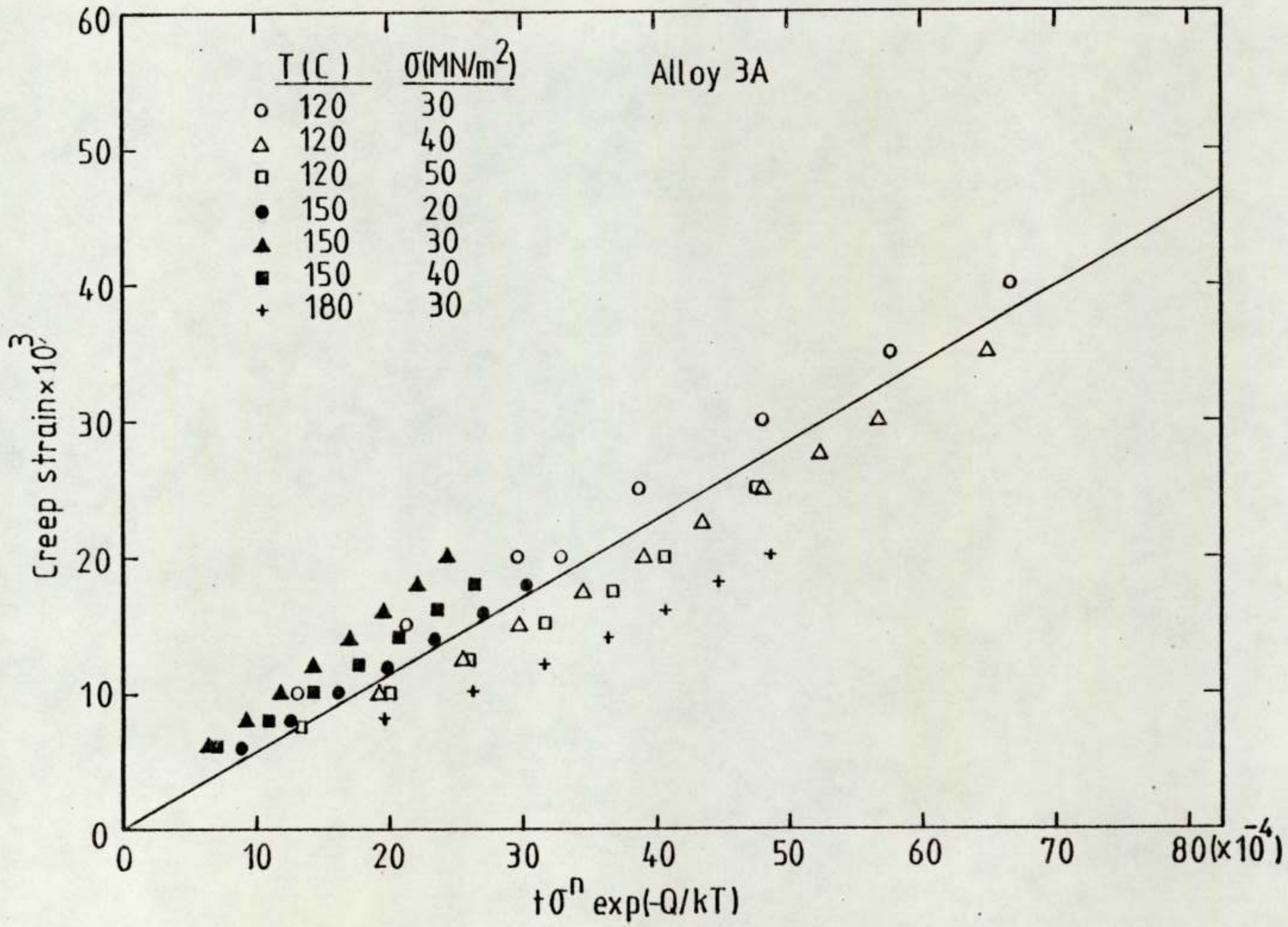

Fig. 175 Creep strain (ε) versus parameter $[t\sigma^n \exp(-Q/kT)]$ plot for alloy 3A

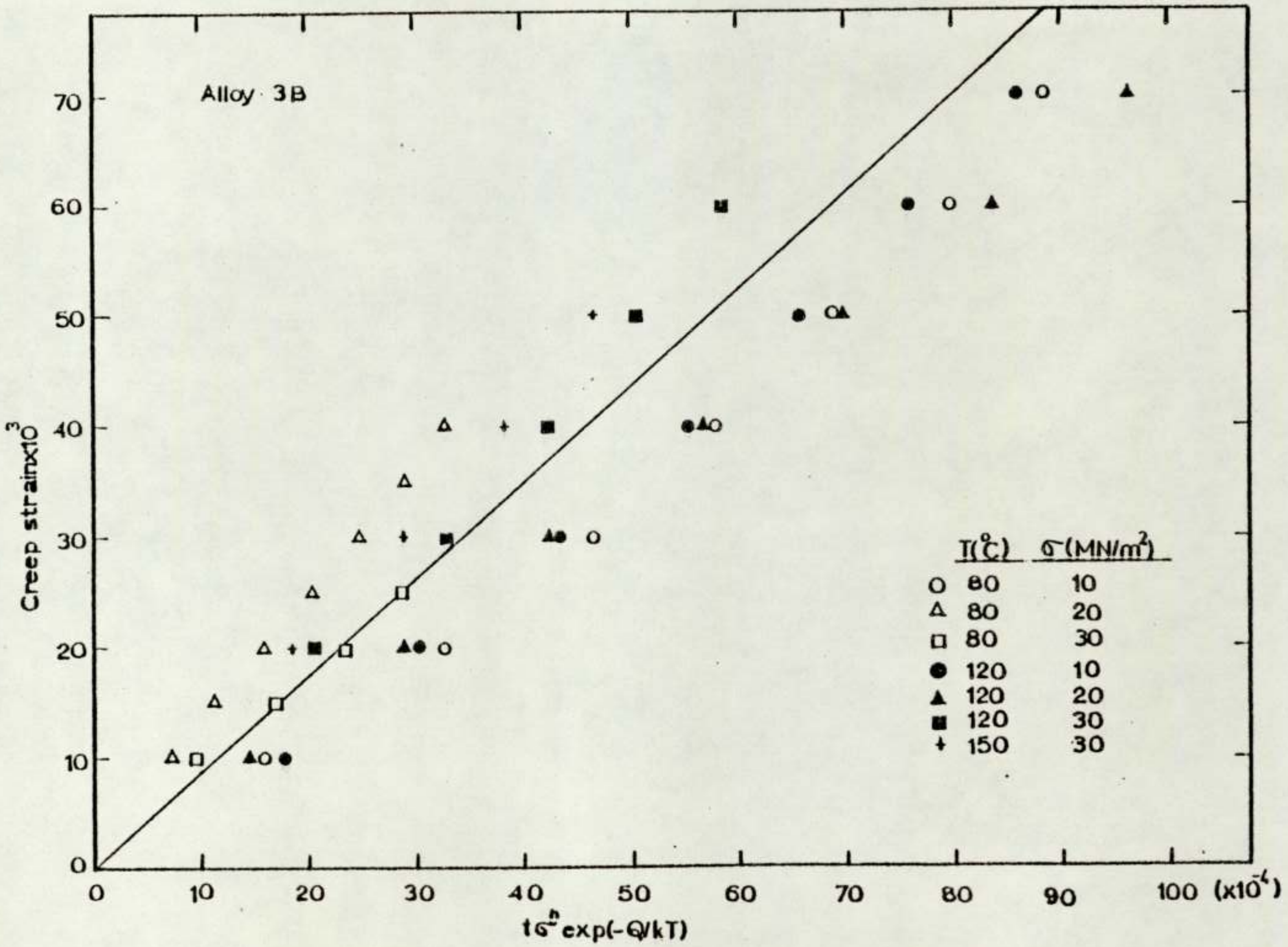

Fig. 176 Creep strain (ε) versus parameter $\left[t\sigma^n \exp(-Q/kT)\right]$ plot for alloy 3B

TABLE 18

The values of stress exponent (n), strain rate sensitivity (m) and intercepts of the $Ln\dot{\varepsilon}_s$ vs $Ln\sigma$ plots for the alloys

Alloy	Temperature (^oC)	n	m	-(LnA-Q/kT)
1A	80	3.69	0.27	28.36
	120	4.13	0.24	25.36
1B	60	4.00	0.25	24.95
	80	3.72	0.27	22.29
	120	2.15	0.47	15.34
2A	120	2.84	0.35	23.64
	150	1.62	0.62	17.15
2B	80	3.07	0.33	23.38
	120	2.62	0.38	18.50
3A	120	2.15	0.47	21.17
	150	2.66	0.38	21.04
3B	80	2.97	0.34	21.71
	120	2.88	0.35	19.08
6	300	7.36	0.14	43.42
	350	3.21	0.31	23.77

TABLE 19

The values of A for the zinc-based alloys

Alloy	A	
	Calculated	Slope
1A	3.5×10^7	2.9×10^7
1B	1.9×10^2	1.6×10^2
2A	19.1×10^4	6.6×10^4
2B	21.3×10^4	11.4×10^4
3A	8.7	5.7
3B	11.1	8.8

TABLE 20

Data for $\ln\dot{\varepsilon}_s$ versus $\ln(\sigma-\sigma_o)$ plots and calculated slopes (p) for the as-cast alloys

Alloy	T (^oC)	$\sigma-\sigma_o$ (MN/m^2)	$-\ln\dot{\varepsilon}_s$ (s^{-1})	p
1A	120	12.3	12.97	2.75
		22.3	3.11	
2A	120	11.0	13.88	1.37
		21.0	13.38	
		31.0	12.40	
	150	12.2	12.25	1.14
		22.2	11.69	
		32.2	11.12	
3A	120	12.0	13.87	1.11
		22.0	13.16	
		32.0	12.79	
	150	7.0	13.12	1.36
		17.0	11.81	
		27.0	11.31	
6	300	21.5	16.01	4.72
		31.5	15.02	
		51.5	11.97	
	350	8.0	14.21	1.59
		13.0	13.32	
		18.0	12.94	

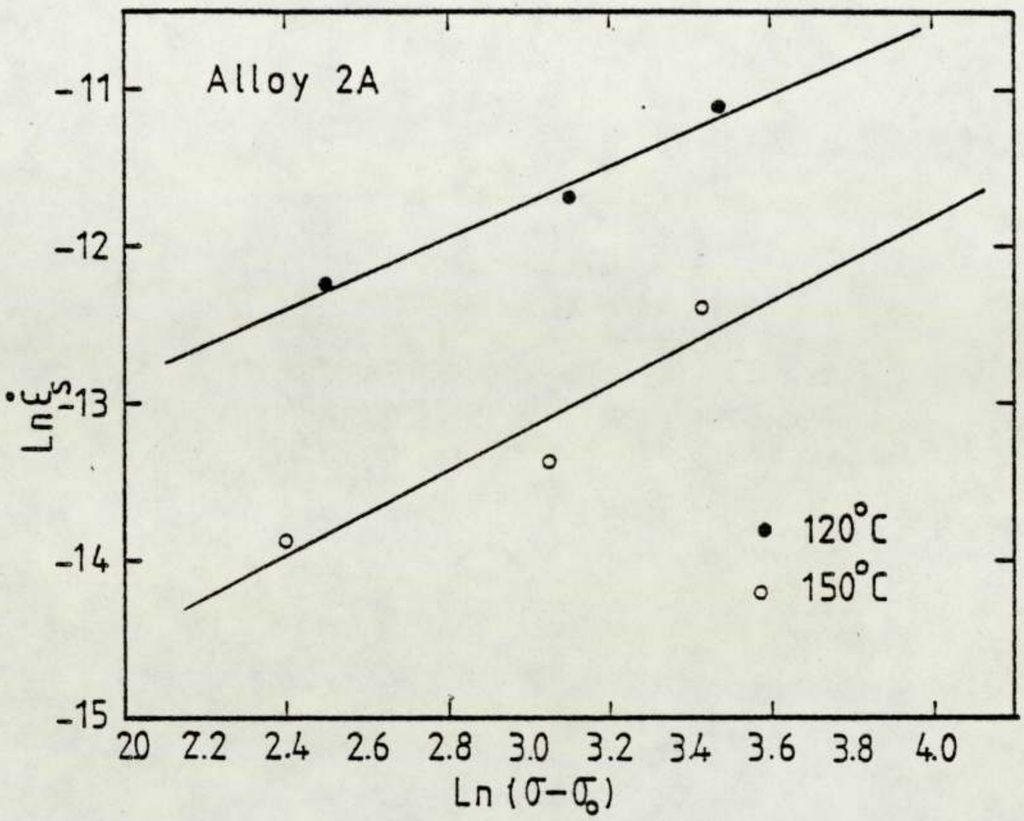

Fig. 177 $\ln\dot{\varepsilon}_s$ vs $\ln(\sigma-\sigma_o)$ plots at 120°C and 150°C for alloy 2A

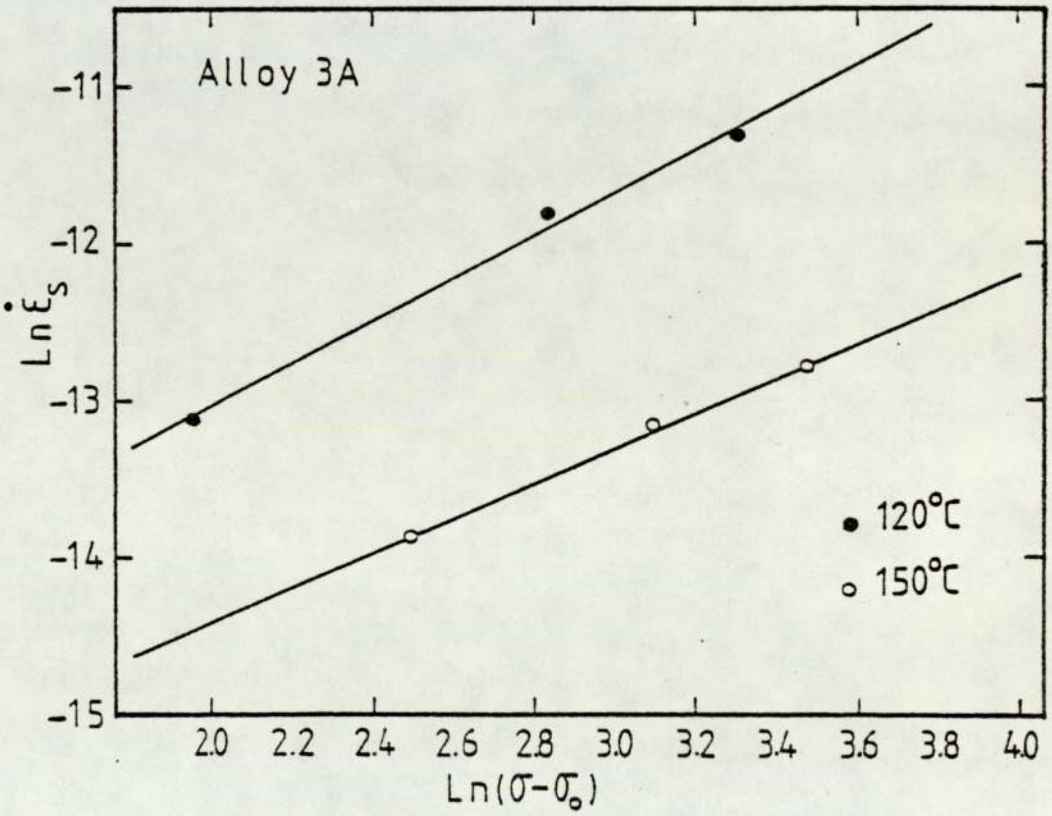

Fig. 178 $\ln\dot{\varepsilon}_s$ vs $\ln(\sigma-\sigma_o)$ plots at 120°C and 150°C for alloy 3A

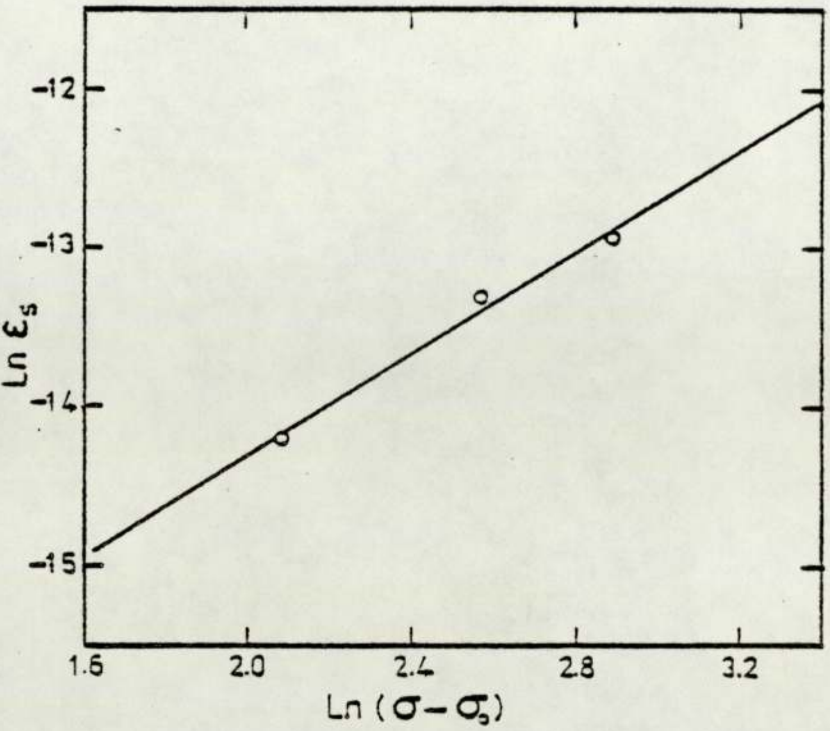

Fig. 179 Ln$\dot{\varepsilon}_s$ vs Ln$(\sigma-\sigma_o)$ plot at 350°C for alloy 6

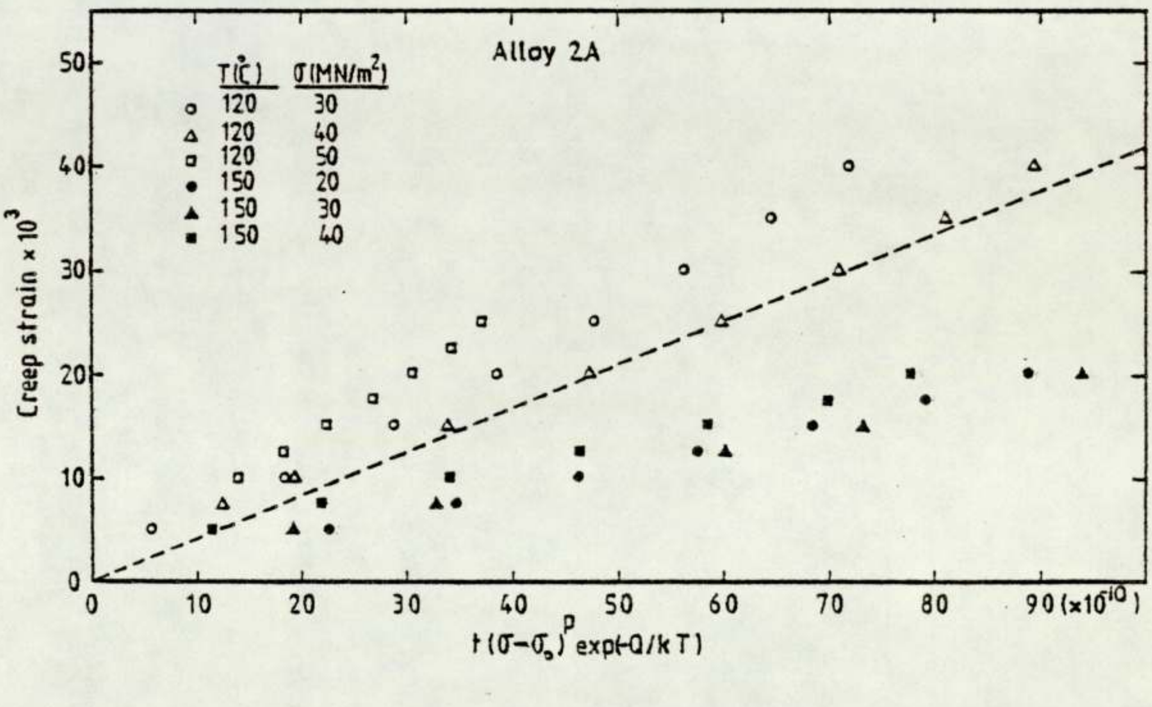

Fig. 180 Creep strain (ε) versus parameter $[t(\sigma-\sigma_o)^p\exp(-Q/kT)]$ plot for alloy 2A

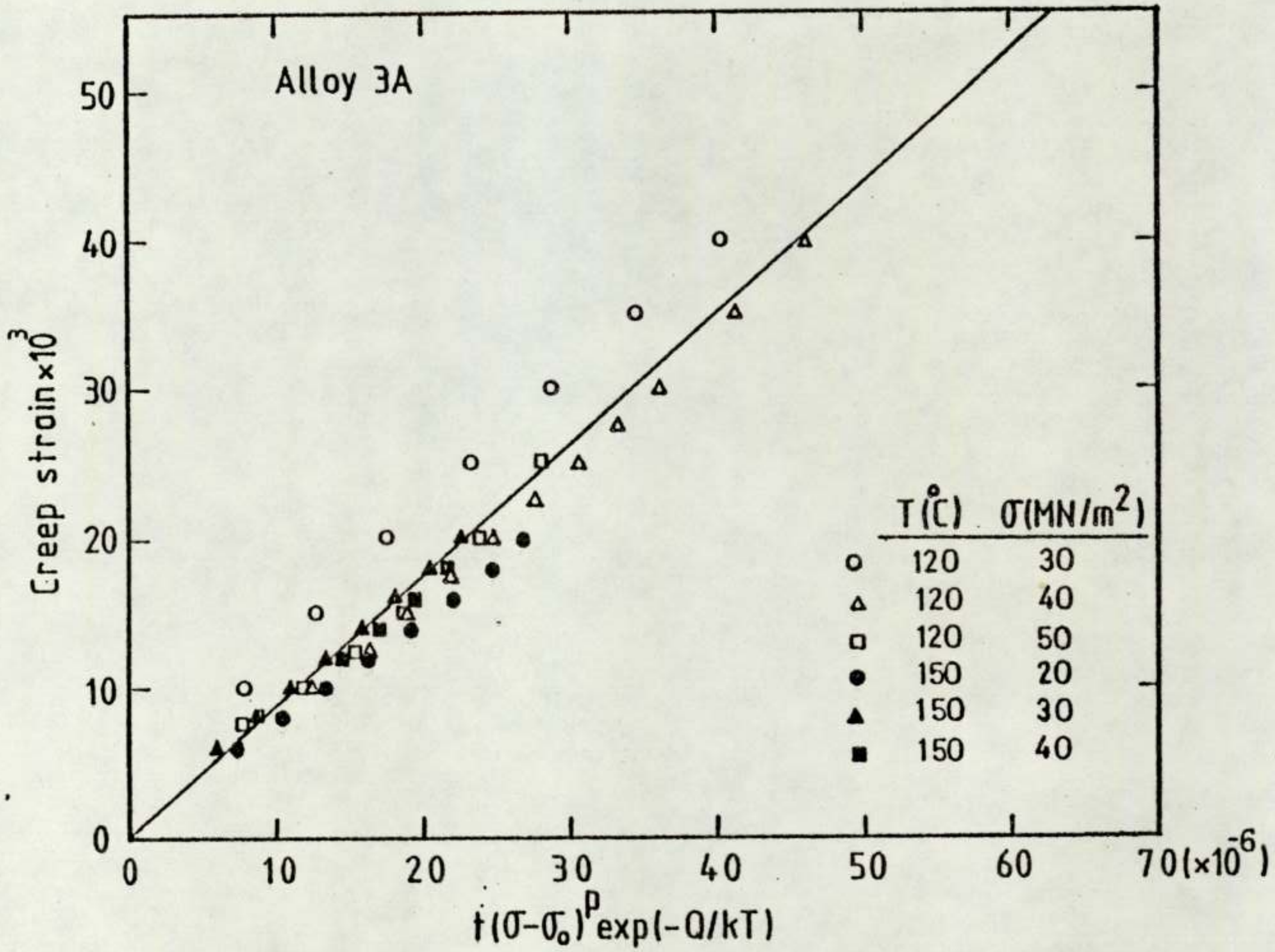

Fig. 181 Creep strain (ε) versus parameter $[t(\sigma-\sigma_o)^p\exp(-Q/kT)]$ plot for alloy 3A

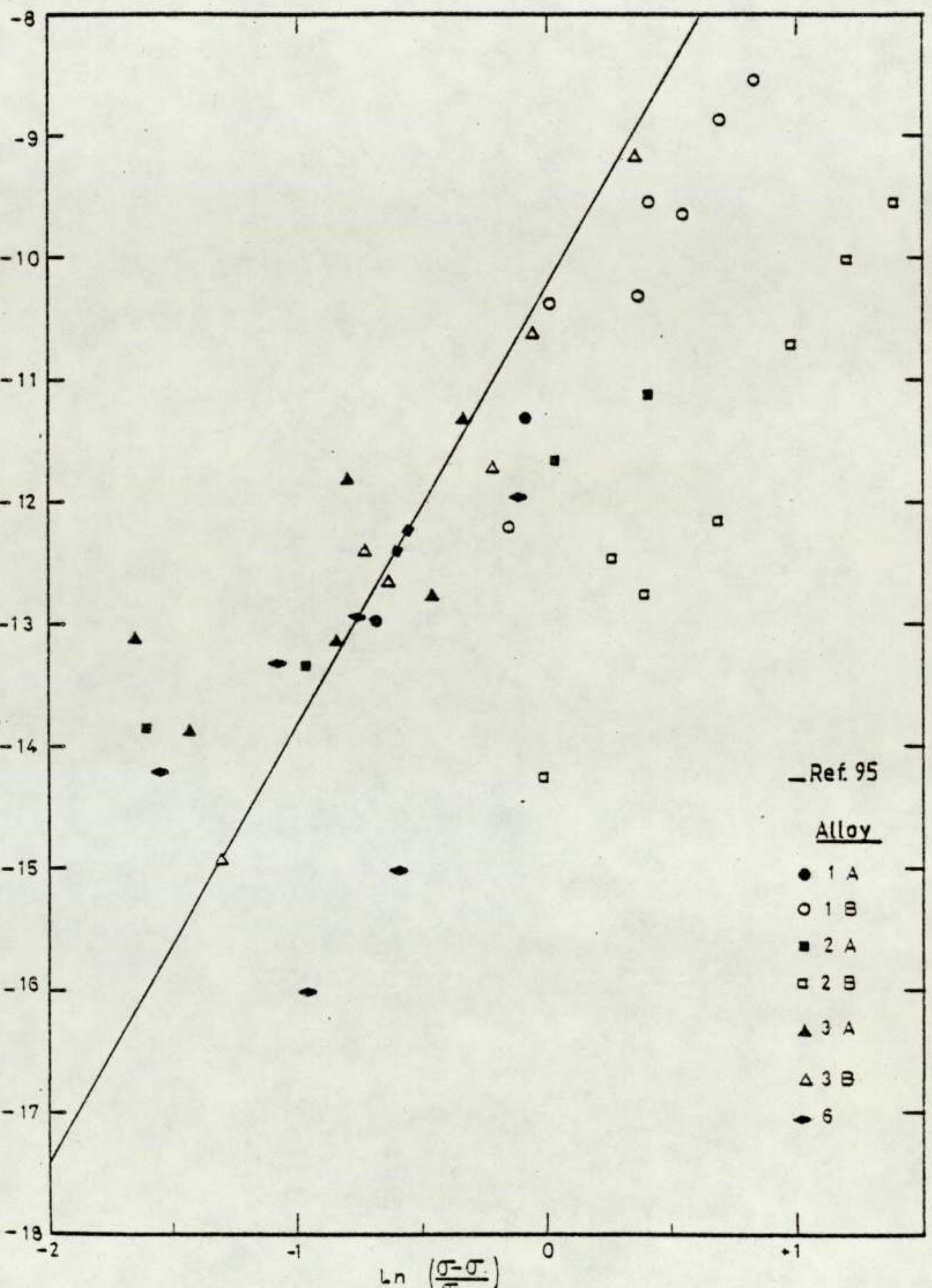

Fig. 182 $\text{Ln}\dot{\varepsilon}_s$ versus $\text{Ln}(\sigma-\sigma_o/\sigma_{0.05})$ plot for the alloys tested

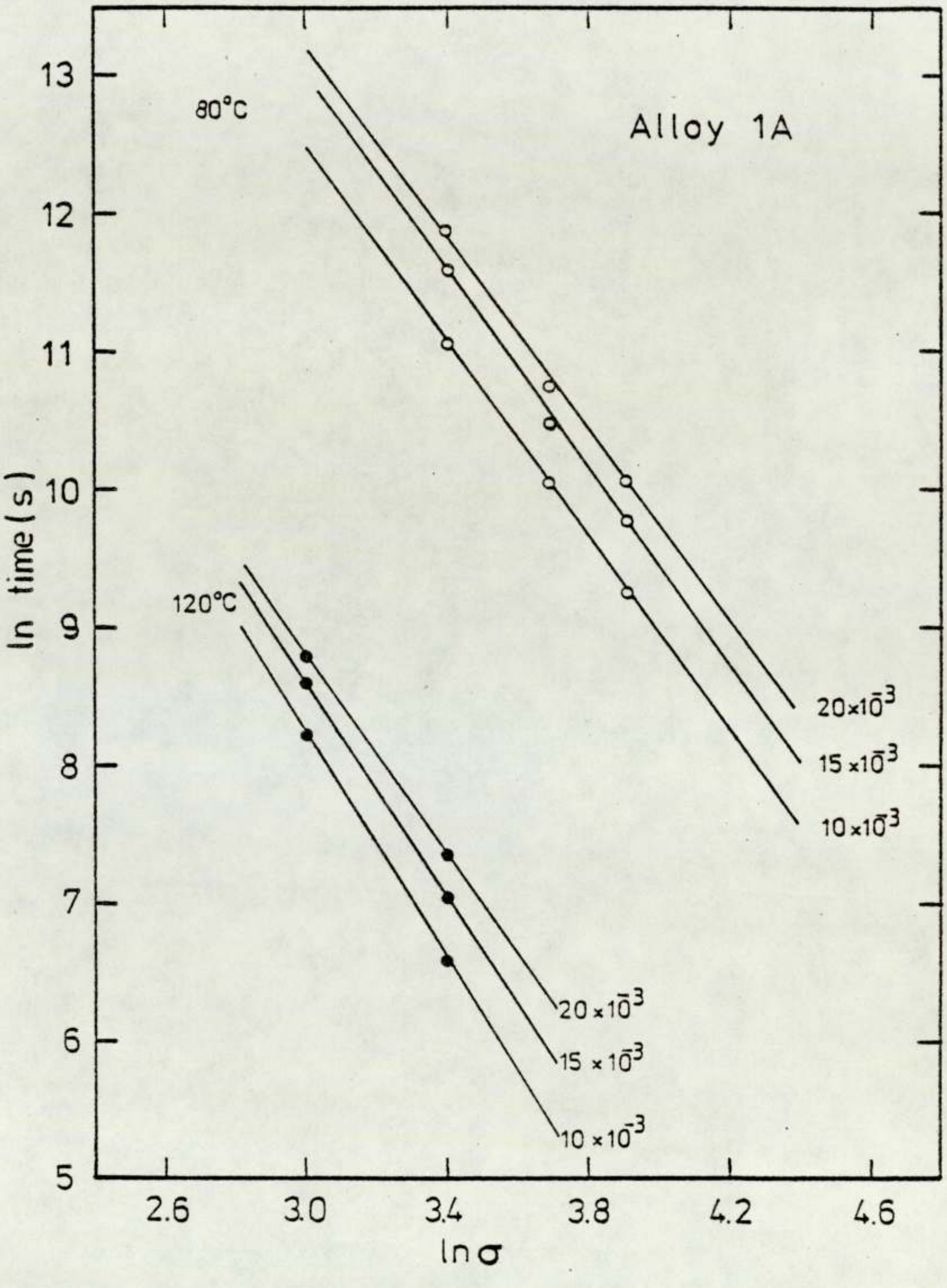

Fig. 183 Ln (time to selected strains) versus Ln stress (σ) plots at 80 and $120^{\circ}C$ for alloy 1A

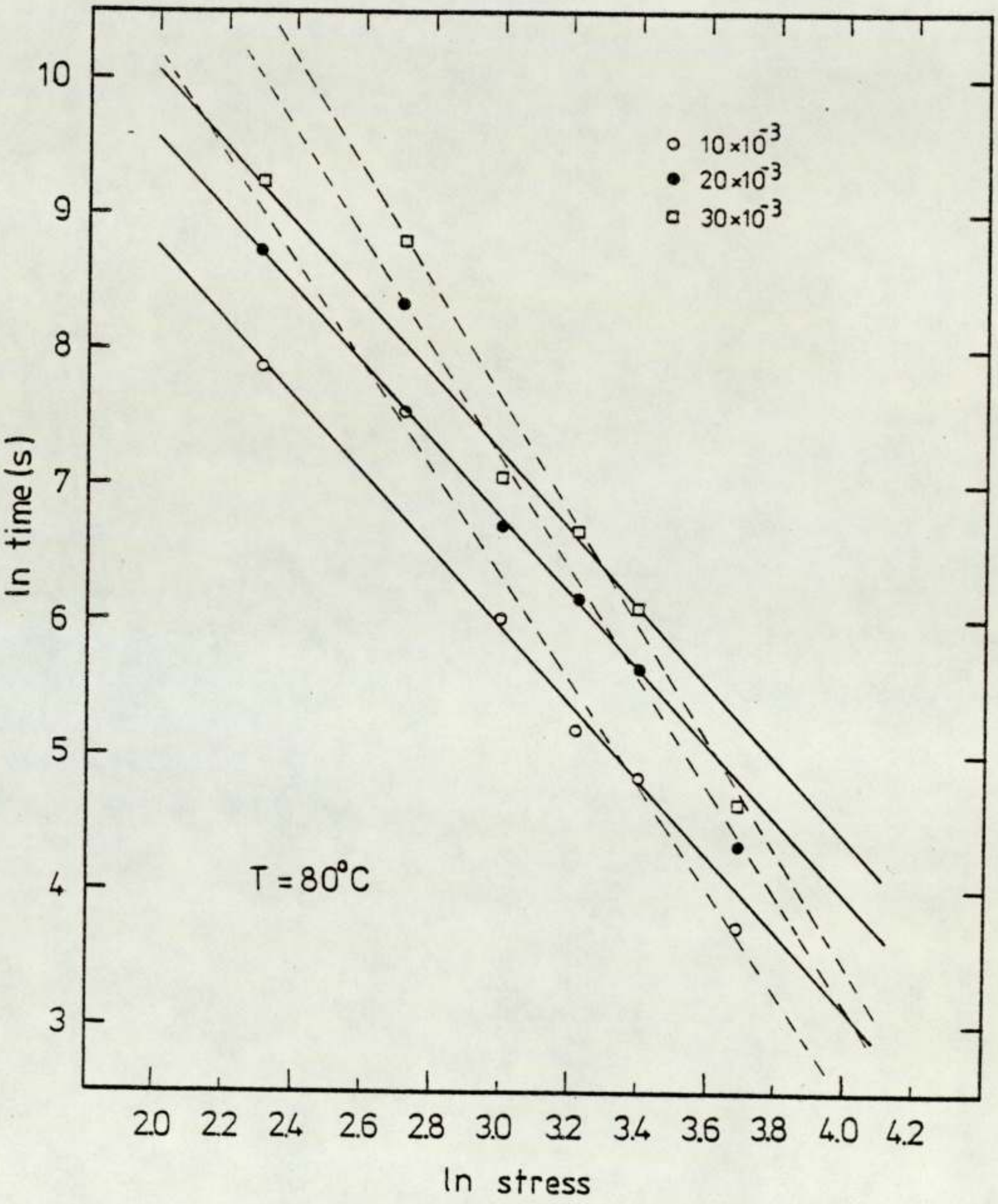

Fig. 184 Ln (time to selected strains) versus Ln stress (σ) plots at $80^{\circ}C$ for alloy 1B

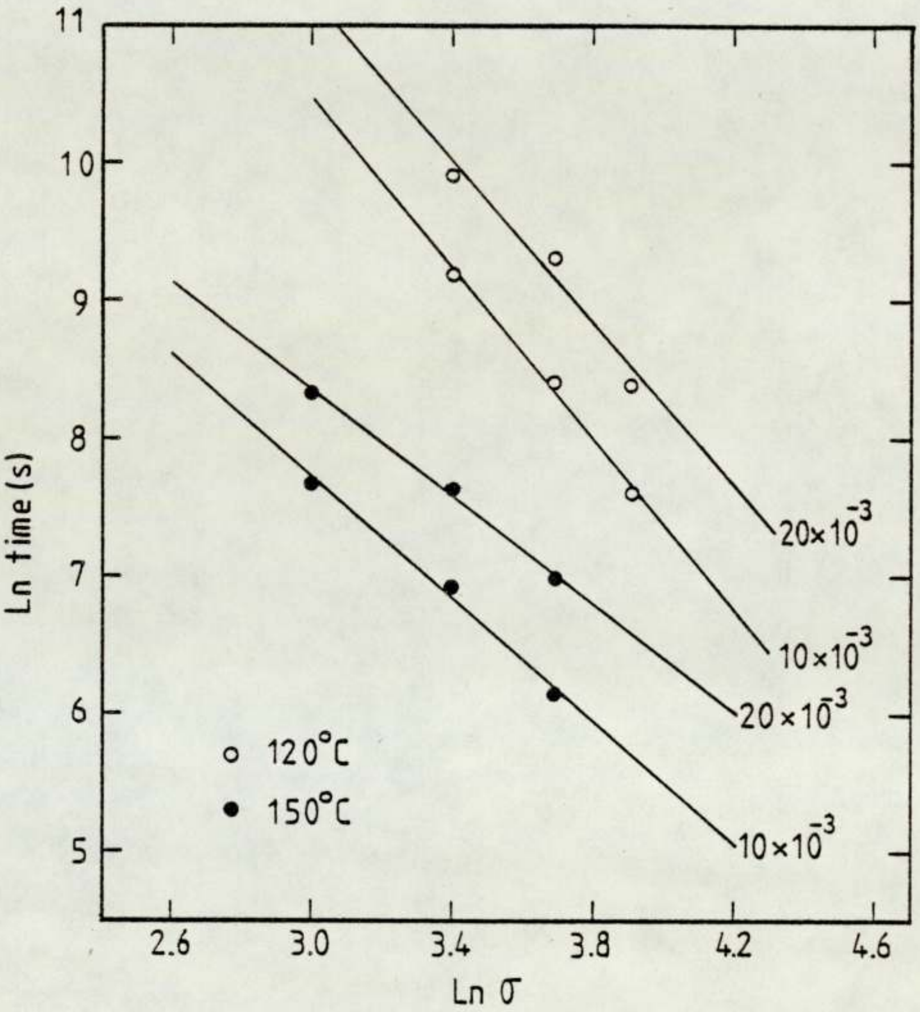

Fig. 185 Ln (time to selected strains) versus Ln stress (σ) plots at 120 and 150°C for alloy 2A

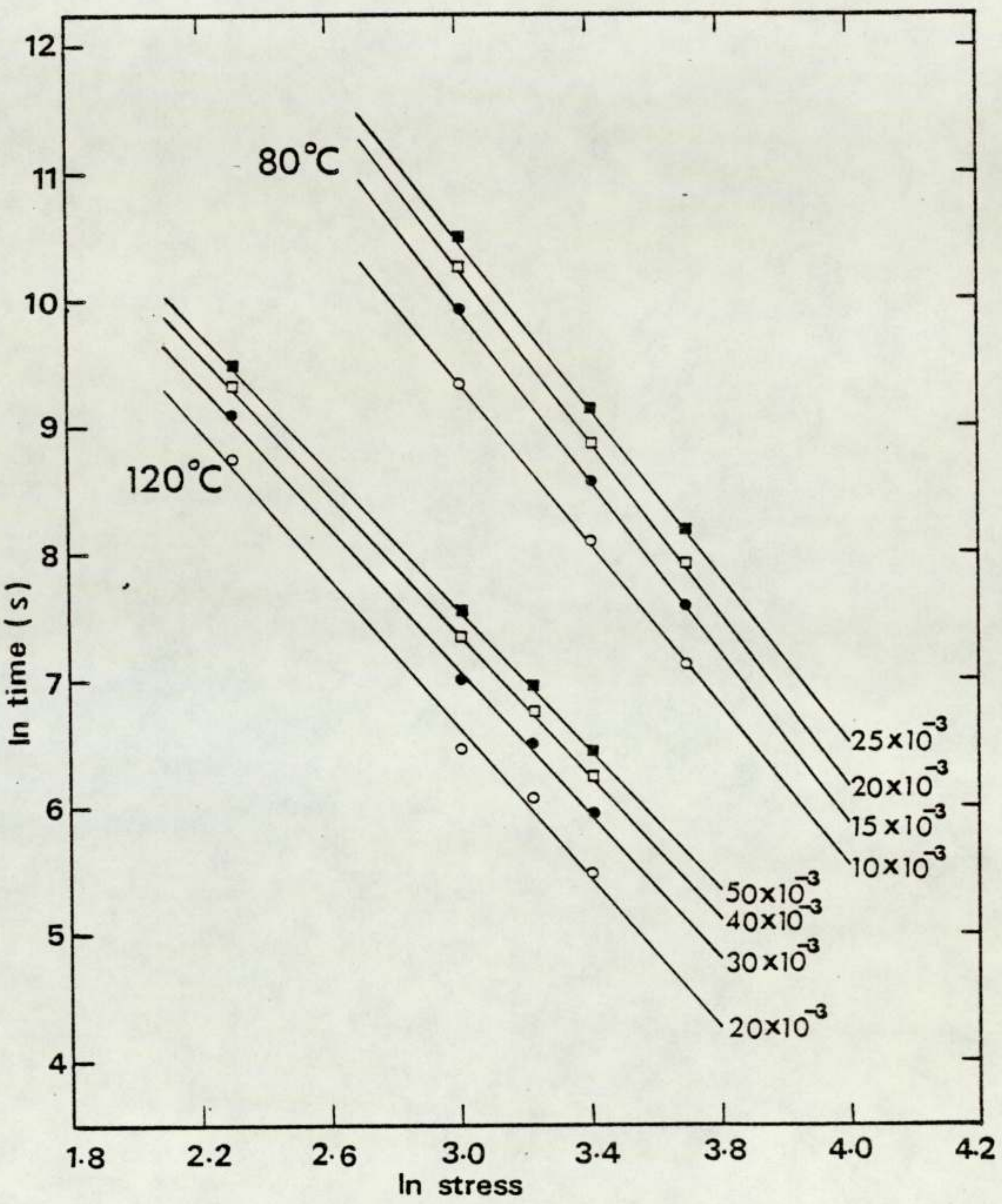

Fig. 186 Ln (time to selected strains) versus Ln stress (σ) plots for alloy 2B at 80 and 120°C

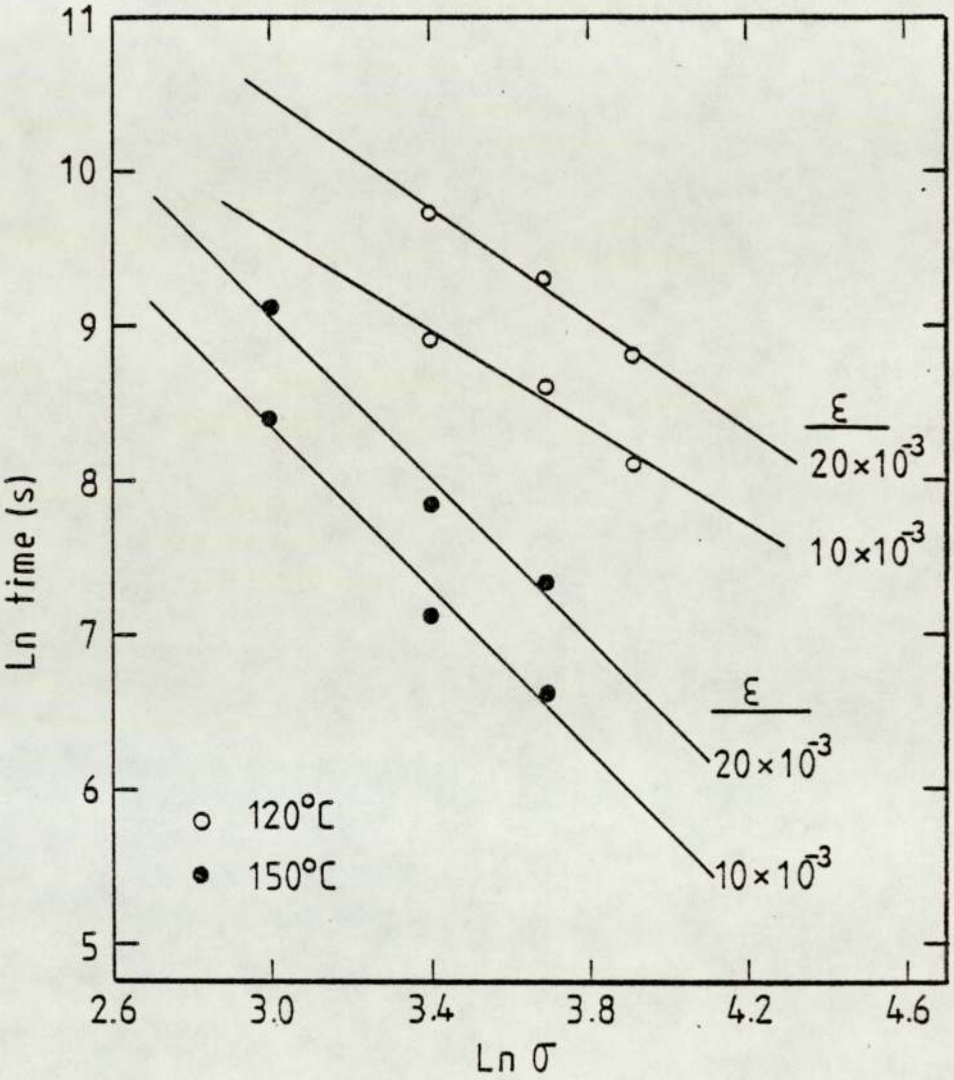

Fig. 187 Ln (time to selected strains) vs Ln (applied stress, σ) at 120 and 150°C for alloy 3A

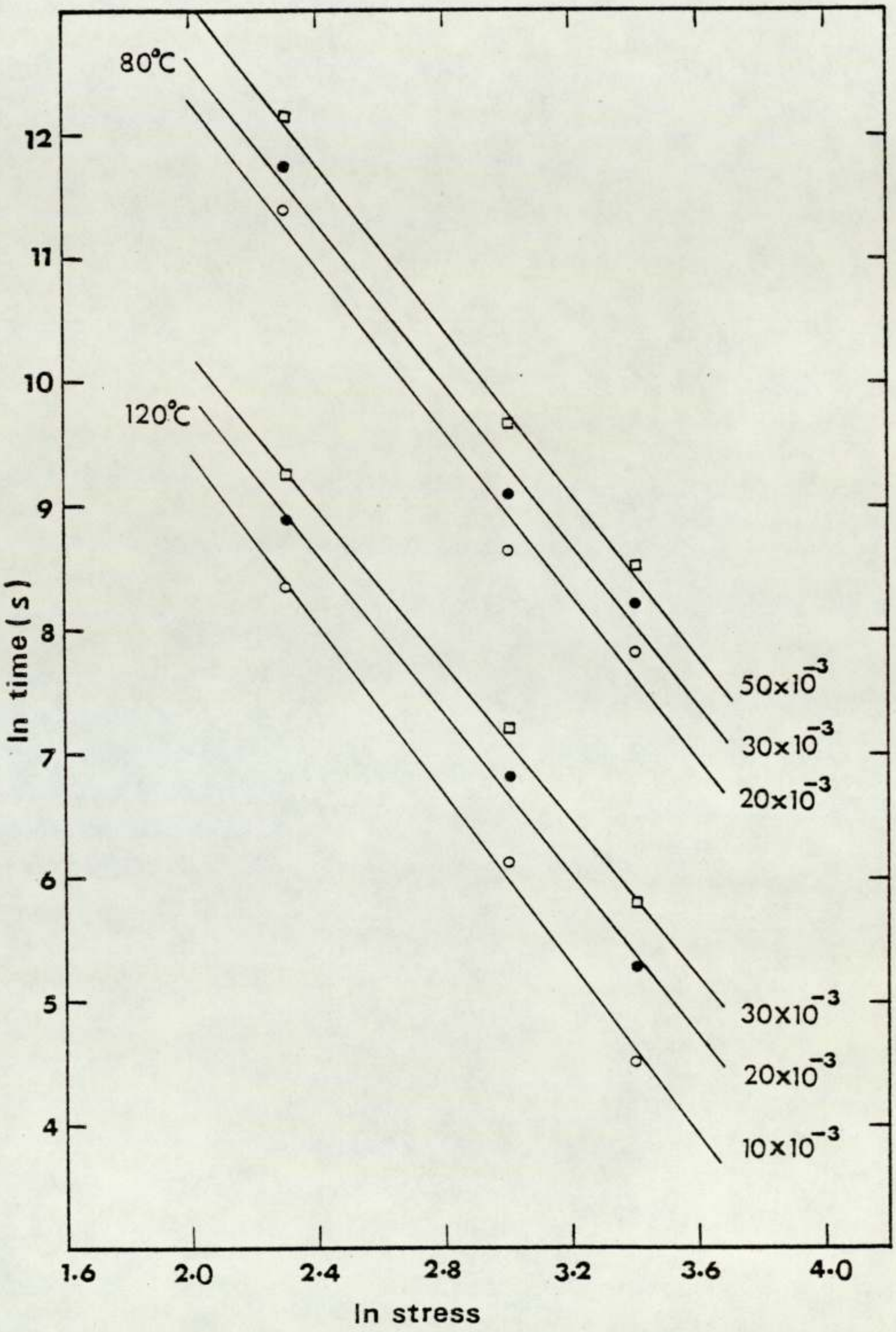

Fig. 188 Ln (time to selected strains) vs Ln (stress, σ) at 80°C and 120°C for alloy 3B

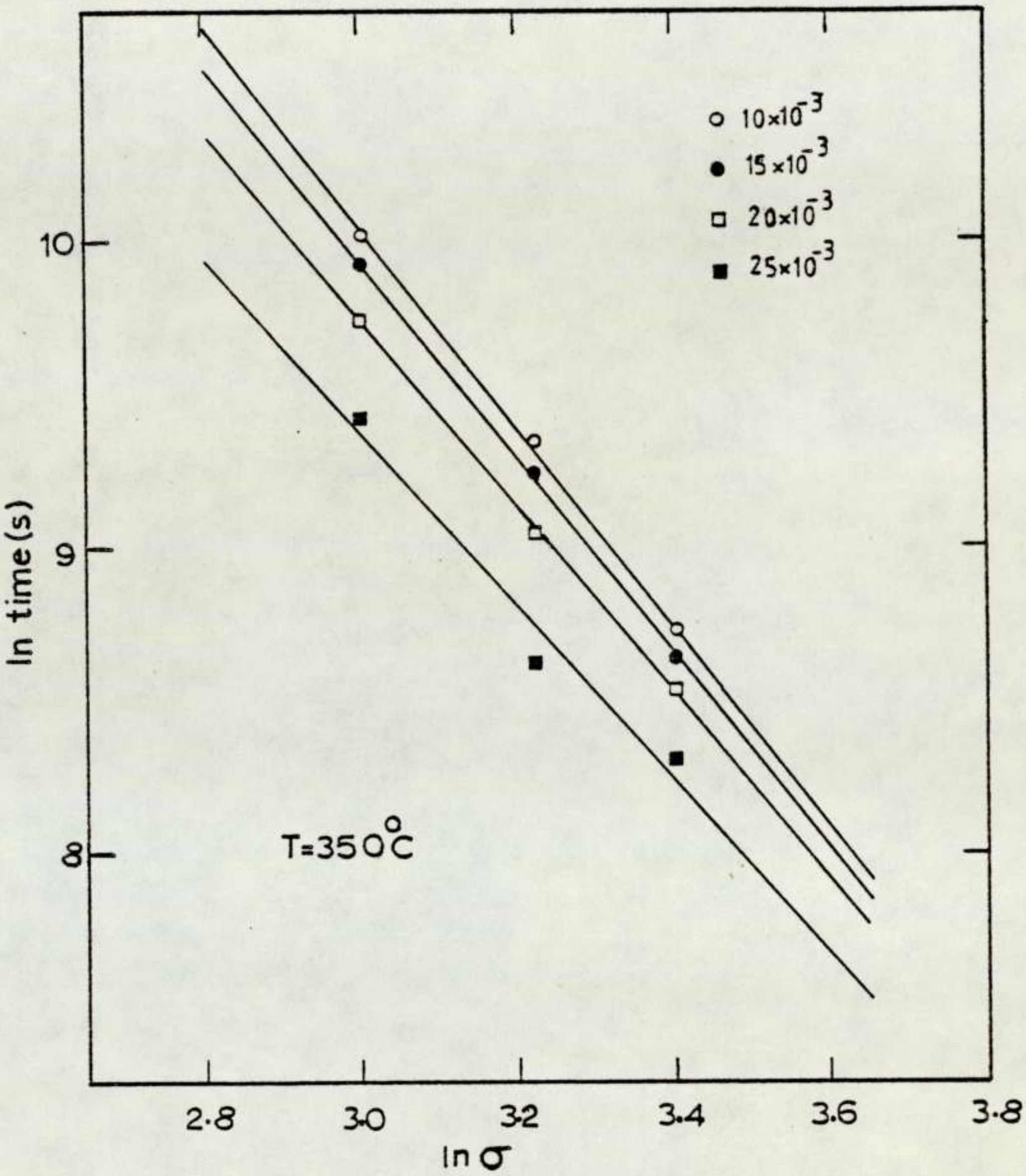

Fig. 189 Ln (time to selected strains) versus Ln (applied stress, σ) at 350°C for alloy 6

TABLE 21

The slopes (-n) of Ln time versus Ln stress straight line plots of the alloys at a given creep strain and temperature

Alloy	T (^oC)	ε x10^{-3}	slope (-n)
1A	80	10	3.55
		20	3.49
	120	10	4.10
		20	3.60
1B	80	10	2.81-3.86
		20	2.79-4.04
2A	120	10	3.10
		20	2.95
	150	10	2.21
		20	1.94
2B	80	10	3.20
		20	3.41
	120	20	2.96
		30	2.85
3A	120	10	1.56
		20	1.79
	150	10	2.63
		20	2.63
3B	80	20	3.32
		30	3.28
	120	10	3.46
		20	3.25
6	300	10	6.87
	350	10	2.83
		20	3.17

TABLE 22

Stresses for creep strain of 10×10^{-3} and 20×10^{-3} at 20, 80 and 120°C for 2000 hours working time

Alloy	Temperature (°C)	Strain $\times 10^{-3}$	σ_1 (MN/m^2)	σ_2 (MN/m^2)
1A	20	10	105.9	
		20	127.0	
	80	10	9.4	7.8
		20	11.2	9.7
	120	10	2.8	3.2
		20	3.4	
1B	20	10	6.2	
		20	7.7	
	80	10	1.2	0.6-1.7
		20	1.5	0.8-2.3
	120	10	0.5	
		20	0.7	0.2
2A	20	10	208.8	
		20	285.3	
	80	10	7.6	
		20	10.3	
	120	10	1.5	3.5
		20	2.0	4.1
2B	20	10	24.8	
		20	31.6	
	80	10	2.1	2.7
		20	2.7	4.0
	120	10	0.6	0.9
		20	0.8	1.0

TABLE 22 (continued)

Alloy	Temperature (^oC)	Strain x 10^{-3}	σ_1 (MN/m^2)	σ_2 (MN/m^2)
3A	20	10	57.0	
		20	75.8	
	80	10	5.9	
		20	7.8	
	120	10	2.6	0.4
		20	2.6	1.0
3B	20	10	8.2	
		20	10.4	
	80	10	1.6	2.2
		20	2.0	2.6
	120	10	0.7	1.2
		20	0.9	1.2
6	300	10		20.2
	350	10		2.1
		20		3.2

The mechanical behaviour of the alloys is directly related to their metallographic structures. The zinc-based binary and ternary eutectoid alloys in the as-cast condition showed higher creep and hot-tensile strengths than in the heat-treated condition. This can be explained in terms of grain size of both structures. The heat-treated alloys have a fine-grained equiaxed structure which was produced by the decomposition of β phase on quench-ageing. It has been well established (62,72,74) that a fine-grained structure, is mainly responsible for the superplastic behaviour of the zinc-aluminium eutectoid alloys which extends over a wide range of temperatures above ambient. Therefore it can be expected that these alloys in the superplastic condition will exhibit large extensions but poor mechanical strength.

However these alloys in the as-cast condition have a dendritic structure of aluminium-rich solid solution with interdendritic zinc-rich material. The dendrites in particular possess a much larger effective grain-size and hence, as-cast alloys exhibit higher strength and smaller extensions.

It appears that the strength of zinc-based alloys is reduced by the heat-treatment which is essential to avoid the dimensional changes.

Hot-tensile and creep results, Tables 12 and 13, show that the addition of copper increased the creep resistance and tensile strength of the zinc-aluminium eutectoid alloys in both as-cast and heat-treated conditions. This is consistent with the results of previous workers (65,83, 84,114). However, the results obtained from alloy 2B suggest that copper has little or no effect on the strength of this alloy although alloy 3B clearly demonstrated the effect of copper additions on the hot-tensile strength of the heat-treated alloys in the expected manner.

It appears that copper additions have more effect on the creep behaviour than they have on the hot-tensile properties of the zinc-aluminium eutectoid alloys. Similar results were reported for 1 and 4% copper-containing eutectoid alloys (83,84).

The copper additions also increased the hardness of zinc-aluminium alloys in both as-cast and heat-treated conditions, Table 24. Hence the hardness measurements confirmed the improvement obtained in the mechanical properties of these alloys by copper additions, since the higher hardness usually corresponds to higher yield strength.

TABLE 23

Hardnesses of the zinc-based alloys in different conditions

Alloy	Hardness (V.P.N.)		
	As-cast	As-quenched	Aged at 200°C for 2 hours
1	76	74	75
2	123	109	108
3	122	99	110
4	122	160	-
5	133	158	-

At present, there is little data available for the effect of zinc/aluminium ratio on the mechanical properties (creep and tensile) of these alloys. However previous work (69,70), and present hardness and creep results suggest that the strength of these alloys increases with increasing aluminium content. Wadia and Prasad (159) reported that the hardness of the zinc-aluminium-5% copper alloys increased linearly with increasing aluminium content up to about 60%, after which it decreased linearly. Therefore it is expected that zinc-aluminium monotectoid based alloys, such as alloys 4 and 5, have higher mechanical strength than the eutectoid alloys.

It is found that the friction stresses of the heat-treated alloys approached zero after a certain period of relaxation time. This period of time was found to be dependent upon temperature, strength of the alloy and initial stress level from which the relaxation started. However these alloys in the as-cast condition showed the expected measurable finite friction stresses as given in Table 12.

In structural terms this observation can be explained as a grain size effect, since the main difference between the structures of as-cast and heat-treated alloys, is the grain size. It appears that the fine-grained structures of the heat-treated alloys provide little resistance against creep deformation which takes place during stress-relaxation tests. The friction stress was regarded as the relaxed stress to sustain secondary creep at a very low strain rate.

The friction stress (σ_o) is characteristic of secondary creep, and implies a back-stress created by substructural factors other than the dislocations taking part in the creep deformation (92-94). For example in pure metals σ_o might arise from subcells or tangles (92), while in precipitation hardened systems a major factor would be the precipitates themselves (93,94).

Since it is assumed that σ_o is characteristic of the substructure, it must depend on subgrain size and total dislocation density. It also appears that for a given substructure deformation cannot occur below the friction stress.

Therefore it becomes obvious that the substructure of the zinc-based heat-treated alloys cannot create enough long-range back stresses to oppose the applied stress. The reason for this must result from the mechanism which operates during creep deformation of these alloys.

It has been reported (72) that grain-boundary sliding and grain rotation are the predominant modes of deformation during extensive superplastic flow of the fine-grained zinc-aluminium eutectoid alloys. Dislocation motion within grains cannot provide a significant effect on the deformation of the heat-treated alloys, since their grain size is smaller than the dislocation-cell structure that would normally form under the temperature and stress conditions of deformation (72).

However these alloys in the as-cast condition have much larger grain size, especially in the dendritic areas, and therefore at least in some areas dislocation motion may be an important factor in creep deformation. The fact that a definite, but small friction stress was observed for the as-cast alloys reinforces this suggested reason for the zero friction stress in the heat-treated alloys.

The stress exponent values (n) for the zinc-based alloys were found to be in the range 2-4, Tables 18 and 21, which are slightly lower than the n values, 4-5, reported for the most common metals and alloys (95, 148). However the present results are in agreement with the values reported for the strain-rate sensitivity (m) of zinc-aluminium alloys (74,75,84,158). The n values for most of the experimental zinc-based alloys slightly increased with increasing temperature, Table 18. This is also in agreement with the results obtained earlier for m values of zinc-aluminium alloys (69,70,74,83). Previous and present work suggest that n or m values of zinc-based alloys are not truely constant, but depend on temperature and strain rate.

The activation energies for creep of the zinc-based alloys were found to be in the range of 70 to 130 kJ/mol, Table 18. These values are lower than the activation energy for lattice self-diffusion in pure aluminium, 143.2 kJ/mol, (152), approximately equal to that reported for pure zinc, 91.3 kJ/mol (151), but slightly higher than the activation energy for grain boundary diffusion in pure zinc, 60.7 kJ/mol (150).

The activation energies for creep of the heat-treated alloys (70-105 kJ/mol) were approximately equal to the activation energies calculated for their transformation (70-90 kJ/mol). These values are approximately in the same range as the activation energies reported for superplastic creep of the binary eutectoid alloy, 95.9-69.9 kJ/mol (158). These two activation energy values were reported to be associated with two distinct regions of constant stress dependence with stress exponents 1 and 2.2 respectively (158). A close activation energy value of

~65 kJ/mol was also reported (72) for superplastic tensile deformation of the binary eutectoid alloy. It appears that the activation energies for deformation of the heat-treated zinc-aluminium eutectoid alloys usually found to be between the activation energies for grain boundary diffusion and for lattice self-diffusion in pure zinc.

The activation energies for creep of the as-cast alloys (1A and 2A) were found to be higher than those for the heat-treated alloys. This suggests that although the grain boundary sliding is the predominant deformation mechanism of these alloys, some lattice-diffusion control is exerted by the aluminium-rich dendrites, as the activation energy for lattice self-diffusion in pure aluminium is higher than that in pure zinc.

It appears that the diffusion is an important rate controlling factor during creep deformation of these alloys. It may therefore be concluded that grain-boundary sliding and diffusional creep are inseparable and both mechanisms operate during deformation of zinc-aluminium eutectoid alloys.

A creep-resistant material is required to support stresses for a long period at high temperatures relative to the melting point, without deforming unduly or breaking. For bearing applications as bushings excessive creep deformation cannot be tolerated, because the linear dimensions of bushes are important during service. If more than a certain amount of deformation takes place, depending on the application, the bushings need to be replaced. Therefore the creep of the bearing bushings must be prevented or minimised in order to increase their service life. However, in some applications such as for tubes, pressurised water jackets, etc., the fracture is the main limiting factor, rather than excessive deformation. For these applications creep rupture data, Table 14, is useful to the design engineer.

Metallographic examination showed the presence of extensive cavitation in the fractured creep specimens. This observation is consistent with the results obtained from the zinc-aluminium eutectoid alloy in the superplastic condition, which failed under a tensile stress at a low strain-rate(81).

The present investigation showed that cavitation occurred during creep and tensile deformation of the alloys in both as-cast and heat-treated conditions, and was more extensive in the latter.

The literature (97,98) suggests that when a material deforms under creep conditions, it can fail either by cavitation or by triple-point fracture, or an apparent combination of both. However metallographic examination revealed that the deformation of the zinc-based alloys occurred without any evidence of triple-point cracking. At high temperatures relative to melting point, and low stresses, triple-point cracking gives way to cavitation fracture, in which small spheroidal holes form all along certain boundaries and then slowly grow and coalesce. Grain-boundary sliding is usually necessary to nucleate these cavities, probably at non-adherent foreign particles or at small steps in the boundaries (148).

It may be assumed that in the zinc-based alloys the cavities nucleate at the α/η phase boundaries due to local stress. The cavities grow during deformation, and fracture occurs by their interlinkage in the necked region along a direction normal to the stress axis. Cusps formed by the interlinkage of cavities were a typical feature of the fracture surfaces examined in the scanning electron microscope. The growth rate of these cavities depends on the deformation or strain rate. Once the cavities form, they can grow by vacancy creep. Vacancy creep removes atoms from the surfaces of the cavity holes and deposits them on nearby parts of the grain boundary or second phase particles where they become attached to the adjoining grains (148).

Present work has shown that the number of cavities increased as the secondary creep rate decreased. This is probably because at the lower creep rates which were obtained at lower stress and temperature, more time is available for the cavities to form, grow and coalesce. This observation is consistent with the results obtained from the fractured tensile specimens of the binary eutectoid alloy in superplastic condition (76,81).

It has been established that the total extent of cavitation increases with increasing strain (160,161). However this was not the general case for the experimental alloys. For example, cavitation was more extensive in alloy 3B when it exhibited lower total strain (Fig. 141).

It appears that although the number of cavities in the zinc-based alloys can be related to the creep strain rate the relation between the number of cavities and total strain was not regular, as the latter is dependent on a number of factors (76) including strain rate and grain size, etc.

Optical microscopy showed that the fine grains of the heat-treated alloys remained essentially equiaxed after very large extensions, Figs. 144a and 145. However the excessive grain growth and grain clustering reported earlier (158) in a deformed superplastic eutectoid alloy was not revealed by optical microscopy in these alloys, possibly due to their very fine grain size. Electron microscopy may be necessary to show the occurrence of grain growth in these alloys during deformation but the effect cannot be very large. However this was not essential for the purpose of this work.

Since the very fine zinc and aluminium-rich grains are irregular in shape, and interlocked, large relative motion necessitates either void formation or local changes in grain shape.

Previous work (72,162) showed that grain-boundary sliding is frequently accompanied and possibly controlled by dislocation motion within the grains. Thus, grain boundary diffusion could control the rate of absorption of these dislocations into grain boundaries.

Ball and Hutchison (72) proposed that, during deformation, groups of grains slide as a unit until favourably oriented grains obstruct the process. The resultant stress concentration is then relieved by dislocation motion in the blocking grains. These dislocations pile-up against opposite grain boundary until the back stress prevents further generation of the source and stops sliding. The leading dislocation in the pile-up can thus climb into and along the grain boundaries to annihilation sites. The progressive rotation of grains in sympathy with the motions and thus changes in the most favourable plane for slip, is held to account for the absence of detectable grain elongation (72). Mukherjee (163) has proposed a modification of the above model in which grains rotate individually rather than in groups.

Since cavitation is the main cause of creep failure of zinc-based alloys, it would be desirable to control it. However cavitation is an inherent feature of these materials, much of it due to void formation incurred during grain boundary sliding in decomposed β regions.

It has been established that the binary zinc-aluminium eutectoid alloy can be made superplastic either by phase transformation (62) or by hot working (131, 164, 165). The final structures of both binary and ternary eutectoid alloys, formed by decomposition of β phase on quench-ageing, were closely similar and consisted of very fine and equiaxed grains of both zinc and aluminium-rich phases. Hence the zinc-aluminium eutectoid-based copper-containing ternary alloys in the heat-treated condition showed superplastic behaviour with improved strength.

As has been discussed earlier, the grain-boundary rolling which occurs in the stressed superplastic alloys of this type gives rise to very considerable damping capacity. Many vibration problems are due to dynamic unbalance of rotating shafts. If such shafts are supported by bushings with substantial damping capacity, a great deal of vibration can be absorbed almost at source. This relieves the machine housing of oscillating stresses which can lead to fatigue failures elsewhere.

Thus a high damping capacity is a very desirable property of these bushing materials. No measurements of damping capacity were carried out in this work, but earlier work(121) has shown that heat-treated alloys have a significantly better damping capacity than other more common materials.

The superplastic properties of these alloys could also be utilised in production of bearing components, since forming in the superplastic condition would give important commercial advantages (114,165).

The zinc-aluminium-copper alloys showed poor impact strength but this is not a great disadvantage for their applications as bearing bushings where impact is not a significant service factor. On the contrary, this can be a positive advantage for machining, since impact brittle material can give the very good surface finish which a bearing bushing requires.

It appears that these alloys in the superplastic condition have some advantage in damping capacity, forming and machining.

The zinc-based monotectoid alloys containing up to 50% aluminium can also be made superplastic by hot-extrusion(69). The main advantage of superplastic zinc-aluminium alloys with high aluminium content is that they show improved room-temperature tensile strength (69,70) and boiling water corrosion resistance (140). However present and previous work (146) has shown that the monotectoid based alloys require a longer heat-treatment (ageing) to stabilize their structure.

From the foregoing discussion it would be expected that the monotectoid zinc-aluminium based ternary alloys should be best for bearing bushings, especially in the heat-treated condition where dimensional changes will be minimised.

The zinc-aluminium based alloys, in general, exhibited higher wear resistance than cast iron, which is the normal bearing material used in this commercial application as rockers, Fig. 149. The best wear performance of the zinc-aluminium-copper alloys was obtained with the monotectoid alloy (4) and its bushing behaviour was found to be similar and comparable to that of phosphor-bronze. Its good tribological properties were attributed to its suitable multi-phase structure formed after adequate ageing and formation of zinc and aluminium oxides on the surface of the alloy as alternating films$^{(142)}$. Present metallographic examination confirmed the suitability of the structure for bearing applications of this alloy, in the heat-treated condition, as consisted of uniformly distributed zinc and aluminium-rich phases probably formed by spinodal decomposition, ε-phase and possibly copper-rich T-phase particles.

Among the experimental alloys the poorest wear resistance was obtained with alloy 2 in the as-cast condition. This result may arise from the instability problem, since in the heat-treated condition this alloy exhibited better, but not outstanding, wear resistance. The sudden large increase in weight loss of alloy 2A may be due to break up of the bush and the loss of large particles. This could not be confirmed since no more time was available for further measurements.

The zinc-aluminium-silicon alloy in the as-cast and heat-treated conditions (5A and 5B) has promising bushing properties as it showed the highest wear resistance among the experimental alloys. This may be explained in terms of its structure since there is a close relationship between microstructure and wear properties of the bearing alloys. This alloy possesses a suitable multi-phase structure consisting of a hard silicon phase in a zinc-aluminium matrix. The better wear resistance of the silicon-containing alloy which had similar zinc/aluminium ratio to that of alloy 4, shows that the nature of the load-carrying intermetallic can exert a powerful effect on the wear resistance even under slightly stressed conditions. This conclusion is at variance with the suggestion of Marczak and Ciach (142) that the wear behaviour is previously determined by the matrix chemistry.

However little work has been carried out on this alloy during the present research which was mostly concerned with the copper-containing alloys. It may be necessary to further investigate its structure and properties in order to exploit this alloy system for bearing and other engineering applications, since the present work showed that it has good wear properties. An added advantage of this alloy is that, replacement of copper with silicon can prevent the instability problem which occurs due to formation of copper-rich intermetallic phases and hence reduces the heat-treatment time necessary to produce a stable structure.

It appears that the monotectoid zinc-aluminium based ternary alloys have higher mechanical strength and wear resistance than the eutectoid-based alloys.

Phosphor bronze is a well-known bushing material and has the advantage that it is less sensitive to operating temperature than the zinc-based alternatives. The eutectoid copper-containing alloys had a lower wear resistance than this alloy but the monotectoid alloy equalled it and the silicon-containing alloy proved superior. The zinc-based bearing alloys have the important advantages of considerably better anti-seizure behaviour and are much cheaper than phosphor bronze (4).

It may be concluded that the zinc-aluminium based ternary alloys are a viable alternative to conventional bearing materials, they have the advantages of considerably better anti-seizure behaviour, higher damping capacity, better forming, machining and wear properties, and they are also much cheaper and lighter.

5. CONCLUSIONS

1. The zinc-aluminium based alloys possess three principal structures:
    - (a) The cored dendritic produced by casting,
    - (b) lamellar morphology by slow cooling or by isothermal ageing above 100°C,
    - (c) fine-grained equiaxed structure by quench-ageing.

2. Binary and ternary alloys have closely similar structures after the same heat-treatment.

3. In the high-zinc copper containing alloys such as alloy 3, the ε-phase ($Zn_5 Cu$) was present in all conditions examined, and it also formed as a transitional phase on quench-ageing of lower zinc eutectoid and monotectoid alloys, and its orientation relationship has been determined.

4. The transformation rate of the zinc-aluminium solid solutions on quench-ageing, increases as the zinc content increases.

5. Additions of copper greatly retard the decomposition of the quenched eutectoid alloys (β-phase) without seriously affecting their transformation mechanism.

6. A transition takes place in the decomposition mechanism of the eutectoid alloys on quench-ageing, at approximately 100°C.

7. All the zinc-based alloys overage within a relatively short time at temperatures near ambient. Hence from the commercial point of view differences in peak hardness are unimportant as the alloys must be heat-treated to the stable, overaged condition to limit dimensional changes in service.

8. Strength of the zinc-aluminium eutectoid alloys increases as the zinc content decreases.

9. Addition of copper increases the mechanical properties (hardness, creep resistance and hot tensile strength) of the zinc-aluminium alloys, but the improvement in the creep resistance is greater than that obtained in the hot tensile strength.

10. Creep and tensile strength of the zinc-based binary (Zn-Al) and ternary (Zn-Al-Cu) alloys are severely reduced by the necessary stabilising heat-treatment.

11. The zinc-aluminium based alloys in the heat-treated condition exhibited much higher extensions than the as-cast alloys due to their superplastic behaviour.

12. Correlation of the creep data by a parametric method allowed the estimation of stress to a certain strain under different conditions, and this was found to be a very useful method to assess the zinc-aluminium based alloys for bearing applications.

13. Activation energies for creep of these alloys were found to be approximately equal to the activation energies calculated for their transformation, and the values are approximately equal to the activation energy for lattice self-diffusion in pure zinc.

14. Diffusion is an important rate controlling factor during creep deformation of these alloys.

15. It is likely that the deformation in these alloys takes place by a combination of grain boundary sliding, diffusion creep and dislocation motion. However, especially in the heat-treated alloys grain rotation and grain boundary sliding are the predominant modes of deformation.

16. Cavity formation is the main cause of creep failure and the fracture of the heat-treated alloys occurs by a combination of external necking and internal void formation (coalescence of cavities).

17. The zinc-aluminium-copper alloys have poor impact strength, but this is not a great disadvantage for bearing applications where impact loading is not a significant service factor.

18. The monotectoid zinc-aluminium based ternary alloys have higher strength and wear resistance than the eutectoid based alloys.

19. Comparison of the wear behaviour of these alloys with that of phosphor bronze showed that the eutectoid copper-containing alloy (2), was inferior, the monotectoid alloy (4) was approximately equivalent, and the silicon-containing alloy (5) proved to be superior.

20. The hard load-carrying phase has an important effect on the bushing behaviour of these alloys.

21. The zinc-aluminium based bearing alloys are a viable alternative to conventional bearing materials and have important advantages in wear resistance and other properties.

6. FUTURE WORK

The present research work has shown that the zinc-aluminium based copper or silicon-containing alloys are viable as bushing materials. This is said to be due to their ideal multiphase structure produced by heat-treatment, and the formation of zinc and aluminium oxides. However this work has shown that the hard, load-carrying phase has an important effect on its bearing behaviour.

The best bushing performance was obtained with the monotectoid based ternary alloys. It is therefore believed that a further investigation of structure and properties of the monotectoid (55-65) % zinc-aluminium based alloys, containing copper or silicon, or a combination of both, would be a useful research topic in order to select the most suitable alloy composition and condition for bearing applications. In addition, zinc-aluminium based ternary or higher alloys containing manganese or magnesium may show better wear resistance, since they were reported to be stronger than the copper-containing alloys.

An investigation of the properties of these alloys in the slow-cooled condition, may provide useful information about their bearing and other commercial applications.

7. REFERENCES

1. World Metal Statistics, World Bureau of Metal Statistics, (monthly 1975-1980)

2. Foseco Foundry Services Limited, Information sheet No. 59, (3rd September 1958)

3. W. Köster, private communication, (1979)

4. A. Kaye, Internal report, Fry's diecastings Limited, (September 1973)

5. E.C. Wakefield, Design Engineering, (December 1973)

6. A.K. Nayak, Journal of the Institute of Metals, Vol. 101, pp.309-314, (1973)

7. G.V. Raynor, "Annoted Equilibrium Diagram Series No. 1", 1944: London (Institute of Metals)

8. A.A. Presnyakov, Yu.A. Gorban, and V.V. Chervyakova, Zhur. Fiz. Khim., Vol. 35, p. 1289, (1961), or Russian Journal of Physical Chemistry, Vol. 35, No. 6, pp.632-633, (1961)

9. E.A. Owen and L. Pickup, Philosophical Magazine, Vol. 20, pp. 761-777, (1935)

10. M.L.V. Gayler and E.G. Sutherland, Journal of the Institute of Metals, Vol. 63, pp. 123-147, (1938)

11. E.C. Elwood, ibid,, Vol. 66, pp. 87-96, (1940)

12. E.C. Elwood, ibid., Vol. 80, pp. 217-224, (1951-52)

13. G.R. Goldak and J. Gordon Parr, Journal of the Institute of Metals, Vol. 92, pp. 230-233, (1963-64)

14. W. Köster and K. Moeller, Zeitschrift für Metallkunde, Vol. 33, pp. 278-283, (1941)

15. Ibid., pp. 284-8.

16. Ibid., Vol. 34, pp. 206-207 (1942)

17. W. Köster, Zeitschrift für Metallkunde, Vol. 33, pp. 289-296, (1941)

18. E. Gebhardt, Zeitschrift für Metallkunde, Vol. 32, pp. 78-85, (1940)

19. O. Bauer and M. Hansen, Zeitschrift für Metallkunde, Vol. 24, pp. 1-6, (1932)

20. Ibid., pp. 73-78

21. A.J. Fletcher and D.L. Thomas, Journal of Institute of Metals, Vol. 98, pp. 188-192, (1970)

22. E. Gebhardt, Zeitschrift für Metallkunde, Vol. 33, pp. 297-305, (1941)

23. Ibid., Vol. 34, pp. 208-215, (1942)

24. Ibid., Vol. 40, pp. 136-140, (1949)

25. D.J. Strawbridge, W. Hume-Rothery and A.T. Little, Journal of Institute of Metals, Vol. 74, pp. 191-225, (1947-1948)

26 A. Burkhardt, Zeitschrift für Metallkunde, Vol. 28, pp. 299-308, (1936)

27. K. Löhberg, Z. Metallk., Vol. 32, pp. 86-90, (1940)

28. K.E. Bingham and J.L. Houghton, Journal of the Institute of Metals, Vol. 29, pp. 71-115, (1923)

29. A.J. Bradley and H. Lipson, Proc. Roy. Soc., (A), Vol. 167, pp. 421-438, (1938)

30. M.G. Bown ; Acta Crystallographica, Vol. 9, pp. 70-74, (1956)

31. S.S. Lu and T. Chang, Reported by W.B. Pearson in "Handbook of Lattice Spacings and Structures of Metals and Alloys ", Vol. 2, p. 552, (1957): London (Pergamon Press)

32. S. Murphy, Metal Science, Vol. 9, pp. 163-168, (1975)

33. H.H. Arndt and K. Moeller, Zeitschrift für Metallkunde, Vol. 51, pp. 596-600, (1960)

34. Ibid., pp. 656-662

35. S. Murphy, Zeitschrift Metallkunde, Vol. 71, pp. 96-102, (1980)

36. R.D. Garwood and A.L. Davies, Journal of the Institute of Metals, Vol. 88, pp. 311-317, (1959-1960)

37. A. Kelly and R.B. Nicholson, Progress in Materials Science, Vol. 10, Pergamon Press, p. 153, (1963)

38. G. Ll. Richards and R.D. Garwood, Journal of the Institute of Metals, Vol. 93, pp. 393-97, (1964-65)

39. G.J.C. Carpenter and R.D. Garwood, Journal of the Institute of Metals, Vol. 94, pp. 301-303, (1966)

40. G.J.C. Carpenter and R.D. Garwood, Metals Science Journal, Vol. 1, pp. 202-210 (1967)

41. W. Merz and Gerald, Z. Metallkunde, Vol. 57, pp. 607-615, (1966)

42. M. Simerska and V. Sunecek, Acta Met., Vol. 15, pp. 223-230, (1967)

43. M.H. Jacobs and D.W. Pashley, "The Mechanism of Phase Transformations in Crystalline Solids", (Monograph and Report Series No. 33), Institute of Metals, London, (1969), pp. 43-48

44. M.H. Jacobs, Metals Science Journal, Vol. 6, pp. 143-148, (1972)

45. J. Lasek, Journal of the Institute of Metals, Vol. 95, p. 320 , (1967)

46. T. Niklewski, P. Spiegelberg, and K. Sunbulli, Metals Science Journal, Vol. 3, pp. 23-25, (1969)

47. R.P. Wahi and T.R. Anantharaman, Current Science, Vol. 38, p. 1, (1969)

48. T.R. Anantharaman, Scripta Metallurgica, Vol. 3, pp. 899-904, (1969)

49. T.R. Anantharaman and K.G. Satyanarayana, Scripta Met., Vol. 7, pp. 189-192, (1973)

50. K.G. Satyanarayana and Ken-ichi Hirano, Trans. J.I.M., Vol. 18, pp. 403-410, (1977)

51. R. Graf and M. Lenormand, Comptes Rendus, Vol. 259, pp. 3494-3497, (1964)

52. M. Hillert, M. Cohen and B.L. Averbach, Acta Met., 9, pp. 536-546, (1961)

53. K.B. Rundman and J.E. Hilliard, ibid., 15, pp. 1025-1033, (1967)

54. V. Gerald and W. Merz., Scripta Metallurgica, Vol. 1, pp. 33-35, (1967)

55. J.E. Hilliard and K.B. Rundman, ibid, pp. 37-39, (1967)

56. A.J. Ardell, K. Nuttal, and R.B. Nicholson, "The Mechanism of Phase Transformations in Crystalline Solids", Monograph No. 33, Institute of Metals, pp. 22-26, London, (1969)

57. K.K. Rao, H. Herman and E. Parthe, Metals Science and Engineering, Vol. 1, pp. 162-166, (1966)

58. V. Ramaswamy, E.P. Butler and R.R. Swan, Journal of Microscopy, Vol. 97, pp. 259-268, (1973)

59. D. Turnbull, Theory of cellular precipitation, Acta Metallurgica, Vol. 3, pp. 55-63, (1955)

60. T.R. Anantharaman, V. Ramaswamy, and E.P. Butler, Journal of Materials Science, Vol. 9, pp. 240-244, (1974)

61. R.D. Garwood and A.D. Hopkins, Journal of the Institute of Metals, Vol. 81, pp. 407-415, (1952-53)

62. K. Nuttal and R.B. Nicholson, Phil. Mag., Vol. 17, pp. 1087-1091, (1969)

63. V.A. Toldin, G.V. Kleshchev, D.V. Shumilov, and A.I. Sheynkman, Fiz. Metal. Metalloved, 40, No. 6, pp. 1223-1226, (1975)

64. D. Cheetham and N. Ridley, Journal of the Institute of Metals, Vol. 99, pp. 371-376, (1971)

65. A.E.W. Smith and G.A. Hare, Journal of the Institute of Metals, Vol. 101, pp. 320-328, (1973)

66. A. Krupkowski and R. Ciach, Archiwum Hutnictwa, 3, pp. 199-205, (1966)

67. R. Ciach, J. Krol and K. Wegrzyn-Tasior, Bulletin De L'academie Polonaise Des Sciences, Serie des Sciences Techniques, Vol. XVII, No. 4, pp. 13 (371)-20 (378), (1969)

68. J. Krol, K. Wegrzyn-Tasior, Archiwam Hutnictwa, Tom XVI, Zeszyt 2, pp. 199-218, (1971)

69. K.N. Melton and J.W. Edington, Metal Science Journal, Vol. 7, pp. 172-175, (1973)

70. K.N. Melton and J.W. Edington, Scipta Metallurgica, Vol. 9, No. 5, pp. 559-562, (1975)

71. K. Nuttall, Journal of the Institute of Metals, Vol. 100, pp. 114-120, (1972)

72. A. Ball and M.M. Hutchinson, Metal Science Journal, Vol. 3, pp. 1-6, (1969)

73. O.A. Kaybyshev and I.V. Kazachkov, Dokl. Akad. Nauk SSSR, Ser. Fiz. Metal. Metalloved, 34, No. 2, pp. 396(163)-400(167), (1972)

74. H. Naziri, R. Pearce, M. Henderson Brown and K.F. Hale, Journal of Microscopy, Vol. 97, Pts. 1/2, pp. 229-238, (1973)

75. K. Nuttall, Journal of the Institute of Metals, Vol. 99, pp. 291-292, (1971)

76. F.A. Mohamed, M.M.I. Ahmed and T.G. Langdon, Metallurgical Transactions A, Vol. 8A, pp. 933-938, (1977)

77. L.T. Feng, Soc. Automotive Engineers Booklet, 700133, (1970)

78. G.D. Gemmell and N.J. Grant, Trans. Amer. Inst. Min. Met. Eng., Vol. 209, pp. 417-423, (1957)

79. J.A. Williams, Acta Met., 15, (6), pp. 1559-1562,(1967)

80. J.A. Williams, Journal of the Institute of Metals, Vol. 96, pp. 154-156, (1968)

81. H. Ishikawa, D.G. Bhat, F. Mohamed, and T.G. Langdon, Metallurgical Transactions A, Vol. 8A, pp. 523-525, (1977)

82. S.N. Komnik, L.T. Ponomarenko and V.I. Startsev, Fiz. Metal. Metalloved, 42, No. 2, pp. 388(141)-396(148), (1976)

83. H. Naziri and R. Pearce, Internat. J. Mech. Sci., Vol. 12, pp. 513-21, (1973.

84. K. Nuttall, Journal of the Institute of Metals, Vol. 101, pp. 59-61, (1973)

85. G.R. Loosemore, Journal of the Institute of Metals, Vol. 101, pp. 59-61, (1973)

86. A.K. Mukherjee, J.E. Bird and J.E. Dorn, Trans. ASM, Vol. 62, pp. 155-163, (1969)

87. D. McLean and H.F. Hale, "Structural Processes in Creep", p. 19, 1961: London (ISI/Met.Soc.)

88. O.D. Sherby, Acta Met., Vol. 10, pp. 135-147, (1962)

89. O.D. Sherby and P.M. Burke, "Mechanical Behaviour of Crystalline Solids at Elevated Temperature", Progress Mat. Sci., 13, 325, (1967)

90. C.R. Barrett and O.D. Sherby, Trans. AIME, 233, pp. 1116-1119, (1965)

91. J. Hancock, I.L. Dillamore and R.E. Smallman, Metal Science Journal, Vol. 6, pp. 152-156, (1972)

92. P.W. Davies, G. Nelmes, K.R. Williams and B. Wilshire, ibid, Vol. 7, pp. 87-92, (1973)

93. K.R. Williams and B. Wilshire, ibid., Vol. 7, pp. 176-179, (1973)

94. J.D. Parker and B. Wilshire, ibid., Vol. 9, pp. 248-251, (1975)

95. W.J. Evans and G.F. Harrison, Metal Science, Vol. 10, pp. 307-313, (1976)

96. W.J. Evans and G.F. Harrison, Metal Science, Vol. 13, pp. 641-649, (1979)

97. A.H. Cottrell, "Structural Process in Creep", (I.S.I. Special Report No. 70). The Iron and Steel Institute, London (1961)

98. D. McLean, Mechanical Properties of Metals, J. Wiley, New York, 327, (1962)

99. R.C. Boettner and W.D. Robertson, Trans. A.I.M.E., Vol. 221, pp. 613-622, (1961)

100. R.T. Ratcliffe and G.W. Greenwood, Phil. Mag., Vol. 12, pp. 59-69, (1965)

101. A.N. Stroh, Proc. Roy. Soc., Series A, Vol. 223, pp. 404-414, (1954)

102. E. Smith and J.T. Barnby, Metal Science Journal, Vol. 1, pp. 1-4, (1967)

103. J. Congleton and R.N. Parkins, Journal of the Institute of Metals, Vol. 97, pp. 134-139, (1969)

104. N.F. Mott, Phil. Mag., Vol. 43, pp. 1151-1178, (1952)

105. J.A. Williams, Scripta Metallurgica, Vol. 2, pp. 273-278, (1968)

106. H.C. Chang and N.J. Grant, Trans. A.I.M.E., 206, pp. 544-551, (1956)

107. J.C. Marshall, T.J. Stewart, and T.C. Babcock, Metals Engineering Quarterly, pp. 12-16, November (1973)

108. B.A. Chin, G.M. Pound, and W.D. Nix, Metallurgical Transactions A, Vol. 8A, pp. 1517-1522, (1977)

109. Ibid., pp. 1523-1530, (1977)

110. M.L. Vaidya, K. Linga Murty and J.E. Dorn, Acta Metallurgica, Vol. 21, pp. 1615-1623, (1973)

111. C.J. Swanson, British Patent 1 227 000, (31 March 1971)

112. E. Pelzel, U.S. Patent 3 754 904, (28 Aug. 1973)

113. E. Pelzel, U.S. Patent 3 785 811 (15 Jan. 1974)

114. L.E. Mulvania, R.D. Weltzin, and P.A. Talcott, Metals Engineering Quarterly, pp. 55-60 (1974)

115. C.H. Zener, Elasticity and Anelasticity of Metals, University of Chicago Press, (1948)

116. C.F. Burdett and T.J. Queen, Metals and Materials, 4 (5), pp. 47-65, (1970)

117. T.S. Ke, Journal of Applied Physics, Vol. 20, pp. 274-280, (1949)

118. V.S. Postnikov and I.V. Zolotukhin, Fiz. Metal. Metalloved, 16, No. 6, pp. 937-939, (1963)

119. K. Nuttall, Journal of the Institute of Metals, Vol. 99, pp. 266-270, (1971)

120. A.S. Nowick, Journal of Applied Physics, Vol. 22, pp. 925-933, (1951)

121. M.T. Welch, M.Sc. Project, "The Damping Capacity of Engineering Alloys and Their Application in Automotive Engineering", (1975), The University of Aston in Birmingham

122. D. Birchon, Engineer, pp. 207-209, Aug. 5, (1966)

123. D. Birchon, Eng. Matls. and Des., Vol. 7, pp. 606-608 and 692-696, (1964)

124. Vereinigte Osterreichische Eisen-und Stahlwerke AG., British Patent 1, 326, 777, (3 Dec. 1970)

125. Noranda Mines Ltd., U.S. Patent 3, 793, 091, (20 Aug. 1971)

126. E. Pelzel, U.S. Patent 3, 785, 811, (9 July 1969)

127. M.J. Stewart, Canadian Metallurgical Quarterly, Vol. 12, No. 2, pp. 159-169, (1973)

128. J.A. Belk, R.M.C.S. Tech. Rep., Met. 25/6, (1973)

129. E. Gervais et al., U.S. Patent, 3, 793, 091, (19 Feb. 1974)

130. British Patent, 1, 328, 125, (30 Aug. 1973)

131. W. Johnson, T.Y.M. Al-Naib, and J.L. Duncan, Journal of the Institute of Metals, Vol. 100, pp. 45-50, (1972)

132. R. Hawkins and J.A. Belk, Metals Technology, pp. 516-521, (November 1976)

133. T. Oshita and H. Takei, J. Japan Inst. Metals, Vol. 36, p. 1081, (1972)

134. Noranda Mines Ltd., U.S. Patent, 3, 798, 028, (21 July 1971)

135. D.L. Dollar, R.E. Giuliani, M.J. Mirra, J.W. Headrick, U.S. Patent, 3, 972, 743, (3 Aug. 1976)

136. E.C.W. Perryman and J.C. Blade, Institute of Metal Science, 1251, Vol. 77, pp. 263-285, (1950)

137. W. Truszkowski, R. Ciach, and A. Pawlowski, Bulletin De L'academie Polonaise Des Sciences, Serie des Sciences techniques, Vol. XVIII, No. 2, pp. 13 (143) - 18 (148), (1970)

138. C.B. Tennant, TMS/AIME Annual Meeting, A 70-48, (1970)

139. D.L. Dollar, J.A. Clum, and R.E. Miller, Corrosion, Vol. 28, No. 8, pp. 296-298, (1972)

140. K.N. Melton and J.W. Edington, Corrosion-Nace, Vol. 31, No. 4, pp. 146-147, (1975)

141. W.A. Pollard and J.O. Edwards, Metallurgical Transactions B, Vol. 8B, pp. 157-168, (1977)

142. R.J. Marczak and R. Ciach, Proc. 1st European Tribology Congr., London, (1973), Institition of Mechanical Engineers, pp. 223-227, (1973)

143. Vereinigte Osterreichische Eisen-und Stahlwerke AG., U.S. Patent 3, 773, 502, (1 Dec. 1970)

144. Oiles Kogyo K.K., German Patent (Offenlegungsschrift) 2, 364, 087, 25 Dec. 1972, (11 Jul. 1974)

145. J.C. Gibelling and W.D. Nix, Metals Science, Vol. 11, pp. 452-457, (1977)

146. R. Ciach, B.D. Zawadzka and J. Dutkiewicz, Heat Treatment '76, Proceedings of the 16th International Heat Treatment Conference, The Metals Society, pp. 111-115, (1976)

147. W. Truszkowski and J. Dutkiewicz, Bulletin de L'academie Polanaise des Sciences, Vol. XIX, No. 11-12, pp. 821-827, (1971)

148. A. Cottrell, "An Introduction to Metallurgy", second edition, Edward Arnold (Publishers) Ltd., (1975)

149. R.E. Reed-Hill, "Physical Metallurgy Principles", International Student Edition, VNR Company, (1972)

150. E.S. Wajda, Acta Met., Vol. 2, pp. 184-193, (1954)

151. G.A. Shirm, E.S. Wajda, and H.B. Huntington, Acta Met., Vol. 1, pp. 513-518, (1953)

152. T.S. Lundy and J.F. Murdock, Journal of Applied Physics, Vol. 33, pp. 1671-1673, (1962)

153. J. Burke, "The Kinetics of Phase Transformations in Metals", 1965: Oxford & C. (Pergamon Press)

154. W.A. Johnson and R.F. Mehl, Trans. Amer. Inst. Min. Met. Eng., Vol. 135, p. 416-441, (1939)

155. J.B. Austin and R.L. Rickets, Trans. A.I.M.E., Vol. 135, pp. 396-415, (1939)

156. S. Murphy and C.J. Ball, Journal of the Institute of Metals, Vol. 100, pp. 225-232, (1972)

157. M. Avrami, J. Chem. Phys., Vol. 7, p. 1103, (1939); Vol. 8, p. 212, (1940); Vol. 9, p. 177, (1941)

158. A. Arieli, A.K.S. Yu, and A.K. Mukherjee, Metallurgical Transactions A, Vol. 11A, pp. 181-191, (1980)

159. N.J. Wadia and A.S. Prasa, TISCO, pp. 117-132, (1967)

160 S. Sagat and D.M.R. Taplin, Acta Met., Vol. 24, pp. 307-15, (1976)

161. C.I. Smith, B. Norgate and N. Ridley, Metal Science, Vol. 10, pp. 182-188, (1976)

162. D. McLean and M.H. Farmer, Journal of Institute of Metals, Vol. 85, pp. 41-50, (1956-57)

163. A.K. Mukherjee, Materials Science and Engineering, Vol. 8, pp. 83-89, (1971)

164. R.H. Johnson, C.M. Packet, L. Anderson and O.D. Sherby, Phil. Mag., Vol. 18, pp. 1309-1318, (1968)

165. J.A. Belk, Metals Technology, pp. 161-166, (1976)

8. ACKNOWLEDGEMENTS

The author wishes to express his sincerest gratitude to Dr. S. Murphy for his helpful discussions, encouragement and ceaseless enthusiasm throughout the duration of this work.

He would like to thank Professor I.L. Dillamore for his support and Professor J.T. Barnby, Dr. J.A. Wright and Dr. J.L. Aston for their helpful discussions. The author would also like to thank all the technicians in the Metallurgy Department for their valuable assistance.

The author is grateful to the Reliant Motor Company for providing test facilities.

Thanks are given to Mr. J. Roberts and Mr. S. Bainbridge for their help. The author would also like to thank Mr. Z. Koçer, Mr. N. Uğur, Mr. M. Yildirim and other friends for their help in drawing the graphs.

Thanks are given to Karadeniz Technical University (Turkey) and Aston University for their partial financial support.

The author is also grateful to his parents and brother, Mr. M. Savaşkan, for their encouragement and financial assistance.

Finally thanks are given to Mrs. H. Howell for typing this thesis.